The relationship between brain tissue properties and MRI signal

BY

Anna Izabella Blazejewska, MSc

Thesis submitted to The University of Nottingham

for the degree of Doctor of Philosophy

in the subject of Physics

August 2013

CONTENTS

ABSTRACT

Increased signal to noise ratio in high field magnetic resonance imaging (MRI) allows the acquisition of high resolution images and the development of the quantitative techniques for measuring tissue properties. This detailed information can provide a better understanding of the structure and function of the healthy brain but, more importantly, it can also provide methods for explaining pathological processes in neurodegenerative diseases. The work described in this thesis investigated iron and myelin content in the brain using 7T MRI.

Multiple sclerosis (MS) is one of the most common demyelinating disseases. White matter (WM) lesions detected in MS with conventional MRI techniques show poor correlation with the disease progression. In this work investigation of degeneration of the WM as well as cortical and deep grey matter (GM) in MS and clinically isolated syndrome (CIS) suggestive of MS was performed using high resolution quantitative MRI techniques.

Iron plays an important role in the physiological processes of the healthy brain, but its excessive accumulation in the particular brain structures accompanies neurodegeneration in Parkinson's disease (PD). Studies analysing anatomy and quantitative properties of these structures, in vivo and post mortem, comparing PD patients with healthy controls are presented in this thesis. Investigation related to iron is supported by the simulations aimed at understand the effects of tissue microstructure related to iron on the MR signal.

The presented analyses provide a better understanding of the complex dependencies of different MR contrasts on myelin and iron content.

ACKNOWLEDGEMENTS

I would like to thank my supervisors, Professor Penny Gowland and Professor Richard Bowtell, for the constant guidance and motivation, and a lot of patience for working to the very last minute.

Thanks to all my colleagues, whose advice helped me complete this work and allowed me to learn new things.

Thanks to all of my friends, especially to Agnieszka and Aleks, for being always there for me, regardless of the distance.

Dziękuję moim rodzicom za nauczenie mnie rozpoznawania właściwych celów i wsparcie w dążeniu do nich moją włąsną drogą. Dziękuję mojemu rodzeństwu, Oli i Jachowi.

1

INTRODUCTION

The nuclear magnetic resonance (NMR) phenomenon, was first discovered in 1945 by Purcell [5] and Bloch [1], who were awarded the Nobel Prize in 1952. The application of magnetic field gradients for distinguishing between NMR signal from different locations within the sample was proposed by Lauterbur [3] and Mansfield [4] in 1973. In 1974 the technique of using the NMR signal for image formation by applying gradients for slice selection was invented by Mansfield [2]. These discoveries led to the development of MRI, the method of non-invasive imaging of a human body, which in 2003 brought the Nobel Prize for Physiology or Medicine to Mansfield and Lauterbur.

Over the years MRI has become a widely applied diagnostic technique in medicine. While for the MR systems used clinically the most popular magnetic field strengths

remain 1.5T and 3.0T (considered a high field), there is a substantial advantage of using the ultra high fields (7T and higher) for research purposes and potentially clinically, especially in the neuroimaging domain. The signal to noise ratio (SNR) increases with an increase in field strength allowing a higher spatial resolution to be achieved in MRI and the development of new quantitative imaging techniques for measuring detailed properties of tissue. This precise information can lead to better understanding of the physiological processes occurring in the healthy and diseased brain, and eventually to the establishment of new methods for diagnosing and monitoring the progression of various neurodegenerative diseases.

1.1 THESIS OVERVIEW

This thesis presents several studies focusing on the investigation of tissue properties in healthy control (HC) subjects and in patients with Parkinson's disease (PD) or multiple sclerosis (MS), related to iron and myelin.

Chapter 2 introduces the principles of NMR and MRI, including the advanced techniques used in the following experimental chapters and safety aspects of MR imaging.

Simulations described in Chapter 3 investigate the effect of shape and concentration of oriented inclusions of high magnetic susceptibility on the MR signal generated by the sample, providing a better insight into the mechanisms underlying T_2^*-w image contrast used for the estimation of iron content in the experimental chapters of this thesis.

Chapter 4 gives an overview of the different forms of iron that are present in the human brain and their functions in physiological processes. It also provides information about the role of iron in the pathology underlying PD and MS, and about the use of MRI for measuring iron content for better understanding, and possibly diagnosing and monitoring these diseases.

Two studies analysing the substantia nigra (SN) are presented in Chapter 5. The first focuses on the SN substructures and their importance in PD, using both in

vivo and post mortem (PM) MRI data compared with PM histology. The second investigates healthy brain stem tissue, PM and in vivo, in order to quantify iron and myelin content.

Chapter 6 presents three studies related to white matter (WM) and grey matter (GM) degeneration in MS and clinically isolated syndrome (CIS) suggestive of MS. The extent of the penumbra around WM lesions in CIS patients is analysed using different MRI modalities, GM lesion detection in MS is performed with high resolution MR images and iron content in the SN and red nucleus (RN) is quantified in CIS and MS patients, compared with HCs using iron sensitive MRI measures.

1.2 RELATED PUBLICATIONS

JOURNAL PUBLICATIONS

- A.I. Blazejewska, S.T. Shwarz, A. Pitiot, M.C. Stephenson, J. Lowe, N. Bajaj, R.W. Bowtell, D.P. Auer, P.A. Gowland, *Visualization of nigrosome 1 and its loss in PD: Pathoanatomical correlation and in vivo 7T MRI.*, Neurology, 81 (2013), pp. 534–540.

- A.I. Blazejewska, A.M. Al-Radaideh, S. Wharton, S. Yin Lim, R.W. Bowtell, C.S. Constantinescu, P.A. Gowland *Increase in the iron content of the substantia nigra and red nucleus in multiple sclerosis and clinically isolated syndrome: a 7T MRI study.*, submitted to Multiple Sclerosis.

CONFERENCE PROCEEDINGS

- A.I. Blazejewska, S.T. Schwarz, A. Pitiot, M.C. Stephenson, J. Lowe, N. Bajaj, R. Bowtell, D.P. Auer, P.A. Gowland, *In vivo 7T imaging of nigrosome loss in Parkinson's disease*, ISMRM 2013. A.I. Blazejewska, S.T. Schwarz, S. Wharton, R. Bowtell, D.P. Auer, P.A. Gowland, *Imaging of the nigrosomes of the substantia nigra at 3T*, ISMRM 2013.

- A.I. Blazejewska, S. Wharton, S.T. Schwarz, J. Lowe, D.P. Auer, R. Bowtell, P.A. Gowland, *Comparison with histology of quantitative MR properties of the brain stem tissue in 3T and 7T*, ISMRM 2013 (oral presentation).

- A.I. Blazejewska, S. Wharton, J. Lowe, D.P. Auer, N. Bajaj, R.W. Bowtell, P.A. Gowland, *Correlation of T2* and susceptibility mapping with histochemistry in the SN*, ISMRM 2012 (oral presentation).

- A.I. Blazejewska, A.M. Al-Radaideh, O. Mougin, S.Y. Lin, R.W. Bowtell, C.S. Constantinescu, P.A. Gowland, *Peri-lesional White Matter changes in Clinically Isolated Syndrome suggestive of Demyelination in MTR and MPRAGE at 7T*, ISMRM 2012 (oral presentation).

- A.I. Blazejewska, O. Mougin, R. Abdel-Fahim, N. Mistry, R.W. Bowtell, N. Evangelou, P.A. Gowland, *Detection of the Grey Matter Lesion in MTR and MPRAGE in 7T*, ISMRM 2012.

- A.I. Blazejewska, A.M. Al-Radaideh, S. Wharton, S.Y. Lin, C.S. Constantinescu, R.W. Bowtell, P.A. Gowland, *Increase in the Iron Content of the Substantia Nigra and Red Nucleus in Multiple Sclerosis/Clinically Isolated Syndrome using 7T MRI*, ISMRM 2012.

- A.I. Blazejewska, S. Wharton, P.A. Gowland, R. Bowtell, *Understanding the effects of oriented susceptibility inclusions on the phase and magnitude of gradient echo signals*, ISMRM 2011.

- A.I. Blazejewska, S. Wharton, P.A. Gowland, R.W. Bowtell, *Effects of susceptibility inclusions on the phase and magnitude of gradient echo signals*, British Chapter of ISMRM 2010.

References

[1] F. Bloch, W. W. Hansen, and M. Packard, *The Nuclear Induction Experiment*, Physical Review, 70 (1946), pp. 474–485.

[2] A. N. Garroway, P. K. Grannell, and P. Mansfield, *Image formation in NMR by a selective irradiative process*, J Phys C: Solid State Phys, 7 (1974), pp. L457–62.

[3] P. C. Lauterbur, *Image Formation by Induced Local Interactions: Examples Employing Nuclear Magnetic Resonance*, Nature, 242 (1973), pp. 190–191.

[4] P. Mansfield and P. K. Grannell, *NMR 'diffraction' in solids?*, J Phys C: Solid State Phys, 6 (1973), pp. 422–426.

[5] E. M. Purcell, H. C. Torrey, and P. R. V., *Resonance Absorption by Nuclear Magnetic Moments in a Solid*, Physical Review, 6 (1945), pp. 37–38.

2

Nuclear Magnetic Resonance and Magnetic Resonance Imaging

This chapter provides a brief introduction to nuclear magnetic resonance (NMR) and magnetic resonance imaging (MRI). The first section explains the theoretical principles of NMR focusing on hydrogen nuclei, the second describes how this phenomenon can be used to obtain images reflecting the properties of tissue. These topics have been widely described in the literature [1, 2, 4, 11, 16, 21–23, 29, 33, 37]. The third section characterises the advanced MRI techniques used in the experimental part of the thesis.

2.1 Nuclear Magnetic Resonance

Nuclear magnetic resonance (NMR) occurs when atomic nuclei, placed in a strong magnetic field, absorb and re-emit electromagnetic waves at the *resonant* frequency. Measurement of the generated signal can provide accurate information about the properties and molecular environment of the sample. The special role of the hydrogen nucleus arises from its high abundance in tissues (water, fat) and large magnetogyric ratio (see Table 2.1.1).

2.1.1 Spin, magnetic momentum and precession

One of the main characteristics of atomic nuclei is spin angular momentum (spin). This quantum mechanical property, classically visualised as spinning of the nucleus around its own axis, is described by a vector $\mathbf{S} = \langle S_x, S_y, S_z \rangle$ of magnitude:

$$|\mathbf{S}| = \hbar\sqrt{I(I+1)}, \tag{2.1}$$

where I is the spin quantum number taking integral or half integral values and $\hbar = 1.0546 \times 10^{-34} Js$ is Planck's constant divided by 2π. The particle can be in $2I + 1$ possible quantum states, which values of the spin angular momentum along the longitudinal axis S_z, are specified by the second quantum number $m_z = -I, -I + 1, \ldots, I$:

$$S_z = \hbar m_z. \tag{2.2}$$

For hydrogen, ^{1}H, the spin quantum number $I = \frac{1}{2}$ and m_z can take one of two values: $-\frac{1}{2}$ or $\frac{1}{2}$ as shown in Figure 2.1.1.
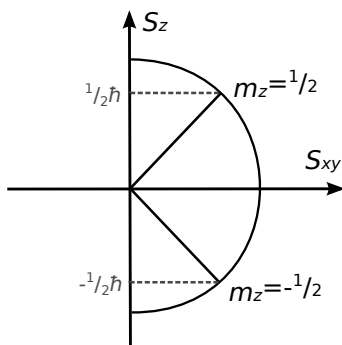
Figure 2.1.1: The z-component of the spin angular momentum, for quantum states of a nucleus with $I = \frac{1}{2}$ (^{1}H).

According to classical physics, a spinning, positively charged nucleus (containing protons) produces a magnetic field, yielding a magnetic moment $\boldsymbol{\mu} = \langle \mu_x, \mu_y, \mu_z \rangle$ parallel ($\gamma > 0$, most of the nuclei) or anti-parallel ($\gamma < 0$) to the spin:

$$\boldsymbol{\mu} = \gamma \mathbf{S}, \tag{2.3}$$

where γ is the magnetogyric ratio. The values of γ for nuclei commonly used in NMR are listed in Table 2.1.1.

nucleus	spin quantum number I	natural abundance (%)	γ (MHz/T)
^{1}H	1/2	100	42.58
^{13}C	1/2	1.1	10.71
^{14}N	1	99.6	3.08
^{31}P	1/2	100	17.25
^{23}Na	3/2	100	11.27

Table 2.1.1: Properties of commonly used nuclei, from [22].

The behaviour of the spin in the presence of an external magnetic field $\mathbf{B}_0$ is described by using the equation of motion:

$$\frac{d\boldsymbol{\mu}}{dt} = \gamma \boldsymbol{\mu} \times \mathbf{B}_0. \tag{2.4}$$

Assuming that the magnetic field $\mathbf{B}_0$ is applied in the z-direction, the change of the magnetic moment $\boldsymbol{\mu}$ is then perpendicular to both B_z and $\boldsymbol{\mu}$, so that equation 2.4

has solution:

$$\mu_x(t) = \mu_x(0)\cos(\gamma B_z t) + \mu_y(0)\sin(\gamma B_z t) \tag{2.5a}$$

$$\mu_y(t) = \mu_y(0)\cos(\gamma B_z t) - \mu_x(0)\sin(\gamma B_z t) \tag{2.5b}$$

$$\mu_z(t) = \mu_z(0). \tag{2.5c}$$

This precessional movement occurs in the clockwise direction for nuclei with $\gamma > 0$, as shown in Figure 2.1.2, at the Larmor frequency:

$$\omega_0 = \gamma \mathbf{B}_0. \tag{2.6}$$
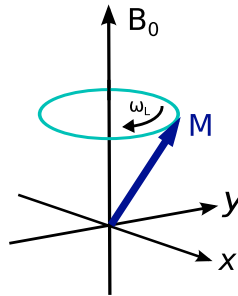
Figure 2.1.2: Precessional movement of a spin in presence of the external magnetic field $\mathbf{B}_0$

According to quantum mechanics, the applied magnetic field, $\mathbf{B}_0$, causes different quantum states to have different energies:

$$E = -\mu_z \mathbf{B}_0 = -\hbar m_z \gamma \mathbf{B}_0. \tag{2.7}$$

This phenomenon is called Zeeman splitting (Figure 2.1.3) and the energy separation between the two states given by:

$$\Delta E = \gamma \hbar \mathbf{B}_0. \tag{2.8}$$
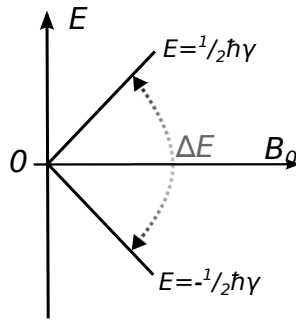
Figure 2.1.3: Zeeman Splitting, energy levels for the ^{1}H nuclei.

In the presence of an external magnetic field, $\mathbf{B}_0$, the magnetic moments of the nuclei tend to align with the field direction. Quantization of the spin only allows particular values of the z-component of the magnetic moment. From equations (2.6) and (2.8) we can derive, that in order to change the energy level proton need to absorb/lose the energy of a photon whose frequency exactly matches the Larmor frequency.

2.1.2 BULK MAGNETIZATION AND BOLTZMAN STATISTICS

In the absence of an external magnetic field, the magnetic moments $\boldsymbol{\mu}$ of the nuclei in a tissue sample have an isotropic distribution of directions (all equally possible). When placed in a magnetic field $\mathbf{B}_0$ (aligned along the z-direction), their alignment produces a net magnetization $\mathbf{M}$ along the z-direction, which is vector sum of the magnetic moments (Figure 2.1.4).
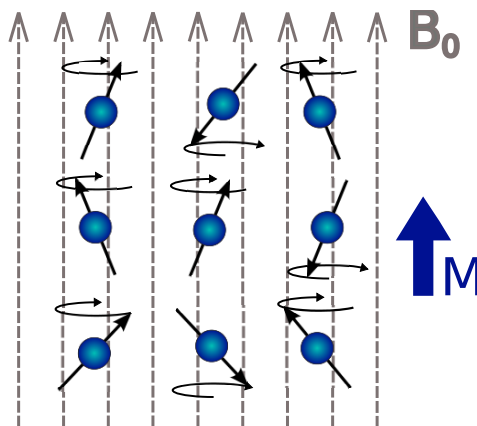
Figure 2.1.4: Net magnetization $\mathbf{M}$ of the sample placed in the external magnetic field $\mathbf{B}_0$.

The behaviour of the magnetization vector can be described by using an equation

of motion which is analogous to (2.4):

$$\frac{d\mathbf{M}}{dt} = \gamma \mathbf{M} \times \mathbf{B}_0. \tag{2.9}$$

From quantum mechanics, the relative populations of the spins in different energy states, aligned parallel (low energy) and anti-parallel (high energy) to $\mathbf{B}_0$, depend on the energy difference between the states and the thermal energy of the sample and can be described by Boltzmann statistics:

$$\frac{N \uparrow}{N \downarrow} = e^{-\frac{\Delta E}{kT}}, \tag{2.10}$$

where $k = 1.381 \times 10^{-23} J/K$ is Boltzman's constant and T is the absolute temperature of the sample in Kelvin. As the nuclei precess with different phases, transverse components of their magnetic moments cancel each other, but because there are slightly more spins with low energy (aligned parallel to the field), a net magnetization $\mathbf{M} = \langle M_x, M_y, M_z \rangle$ is generated in the z-direction. The net magnetization caused by the interaction of the spins with the external magnetic field $\mathbf{B}_0$ is known as the equilibrium magnetization $\mathbf{M}_0$ and it is given by:

$$M_0 = \frac{\rho \gamma \hbar^2 B_0}{4kT}, \tag{2.11}$$

where ρ is the proton density (number of protons per unit volume). For hydrogen nuclei in a 7T magnetic field and $T \approx 310K$ (body temperature) the population difference is equal to 7ppm. Greater magnetic field strength increases the bulk magnetization and therefore enhances the MR signal.

2.1.3   RF EXCITATION

Classical physics is sufficient to describe the behaviour of the sample containing a large number of nuclei . As a static longitudinal component of the $\mathbf{M}$ vector is generally too small in magnitude to be detected directly as a direct current (DC) field

by standard means, the MR signal is detected from the oscillating electromagnetic field caused by the transverse magnetization, which in the equilibrium state is equal to 0. A magnetic field, $\mathbf{B_1}(t)$, of much smaller magnitude than $\mathbf{B_0}$, but oscillating with the Larmor frequency ω_0, is applied to the sample to produce transverse magnetisation. In consequence some of the magnetic moments flip and start precessing with the same phase, which produces net vector, $\mathbf{M}$, rotating in the xy plane. As the Larmor frequency is in the radio frequency (RF) range, this process is called RF excitation and $\mathbf{B_1}$ forms the RF pulse. The magnetic field $\mathbf{B_1}$ can be considered as a sum of two fields counter-rotating with Larmor frequency:

$$\mathbf{B_1}(t) = B_1(\hat{\mathbf{i}}\cos\omega_0 t + \hat{\mathbf{j}}\sin\omega_0 t) + B_1(\hat{\mathbf{i}}\cos\omega_0 t - \hat{\mathbf{j}}\sin\omega_0 t) = 2B_1\hat{\mathbf{i}}\cos\omega_0 t. \quad (2.12)$$

as illustrated in Figure 2.1.5.
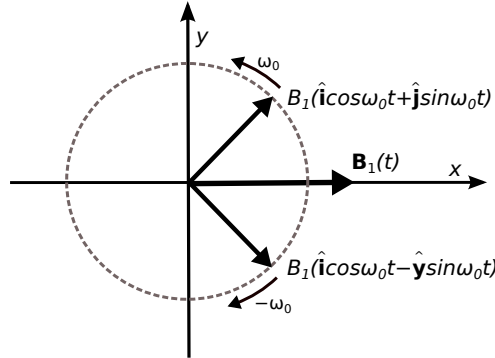
Figure 2.1.5: The two components of the magnetic field, $\mathbf{B_1}$, rotating in the clockwise and anti-clockwise directions.

Taking into account both magnetic fields, static $\mathbf{B_0}$ and time varying $\mathbf{B_1}$, and neglecting the component rotating anticlockwise as being off resonance, the equation of motion (2.13) is given by:

$$\frac{d\mathbf{M}}{dt} = \gamma\mathbf{M} \times (B_z\hat{\mathbf{k}} + B_1(\hat{\mathbf{i}}\cos\omega_0 t - \hat{\mathbf{j}}\sin\omega_0 t)). \quad (2.13)$$

In order to simplify the mathematical description of the excitation process, the rotating frame of reference can be used in place of the laboratory frame. It rotates with the Larmor frequency, so that in the rotating frame the field $\mathbf{B_1}$ becomes

stationary. The conversion of the coordinate system from the laboratory frame (x, y, z) to the rotating frame (x', y', z') is therefore performed as following:

$$x' = x\cos(\omega t) - y\sin(\omega t) \tag{2.14a}$$

$$y' = x\sin(\omega t) + y\cos(\omega t) \tag{2.14b}$$

$$z' = z. \tag{2.14c}$$

Figure 2.1.6 shows both, laboratory frame with the $\mathbf{M}$ vector under the influence of the oscillating $\mathbf{B_1}$ field and the same process simplified in the rotating frame.
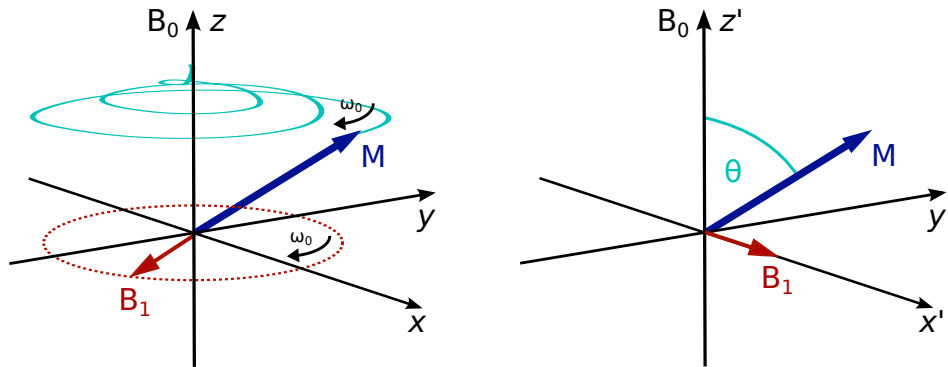
Figure 2.1.6: Behaviour of the magnetization vector $\mathbf{M}$ in the laboratory frame (left) and the rotational frame (right).

The equation of motion (2.13) converted to the coordinates of the rotating frame of reference takes the form:

$$\frac{d\mathbf{M}}{dt} = \gamma \mathbf{M} \times B_1 x'. \tag{2.15}$$

The magnetization vector rotates around the x' axis with the frequency:

$$\omega_1 = -\gamma B_1 \tag{2.16}$$

producing an oscillating magnetic field which can be detected with an RF coil. The flip angle θ through which the vector $\mathbf{M}$ is tilted relative to the z-direction depends on the duration of the RF pulse τ:

$$\theta = \gamma B_1 \tau. \tag{2.17}$$

Two special cases of the flip angle can be described: $\theta = 90°$, when $\mathbf{M}$ is fully rotated into the transverse plane, $(M_{xy} = M_0)$, and $\theta = 180°$, when $\mathbf{M}$ is inverted, $(M_z = -M_0)$.

2.1.4 Relaxation and Bloch equations

After the RF pulse is switched off, the system starts returning to the equilibrium state as a result of the interactions between nuclei and molecules. This process is called relaxation. Gradual loss of the phase coherence by the precessing nuclei causes transverse relaxation, which produces a reduction of the transverse component M_{xy} of the vector $\mathbf{M}$. Transfer of the energy from the nuclei to its surrounding results in longitudinal relaxation, recovery of the longitudinal magnetization M_z. As the relaxation rates depend on the molecular environment of the nuclei, they provide a source of tissue contrast in MR images. The equation of motion incorporating relaxation processes described by the Bloch equation is given by:

$$\frac{d\mathbf{M}}{dt} = \gamma\left(\mathbf{M} \times \mathbf{B}\right) - \frac{(M_z - M_0)\mathbf{k}}{T_1} - \frac{M_x\mathbf{i} + M_y\mathbf{j}}{T_2}, \tag{2.18}$$

where $\mathbf{B}$ is total external magnetic field. In the absence of an applied field, the solutions for the components of the magnetization vector are:

$$M_x(t) = e^{-t/T_2}\left(M_x(0)\cos\omega_0 t + M_y(0)\sin\omega_0 t\right) \tag{2.19a}$$

$$M_y(t) = e^{-t/T_2}\left(M_y(0)\cos\omega_0 t - M_x(0)\sin\omega_0 t\right) \tag{2.19b}$$

$$M_z(t) = M_z(0)e^{-t/T_1} + M_0(1 - e^{-t/T_1}) \tag{2.19c}$$

where t refers to the time after the RF pulse was switched off and T_1 and T_2 are the longitudinal and transverse relaxation constants, respectively. Just after applying the 90° RF pulse, the magnetization components have values $M_z(0) = M_y(0) = 0$, $M_x(0) = M_0$ and the solution for the equilibrium state is: $M_x(\infty) = M_y(\infty) = 0$, $M_z(\infty) = M_0$.

LONGITUDINAL (SPIN-LATTICE) RELAXATION

Applying an RF pulse disturbs the longitudinal magnetization from the equilibrium state . After switching off the $\mathbf{B}_1$-field spins start losing thermal energy gradually via exchange with surrounding atoms and molecules (the lattice). Finally the system comes back to the equilibrium state and its longitudinal magnetization reaches a value of M_0. This longitudinal relaxation process follows the exponential recovery curve described by equation (2.19c).

The time scale of the longitudinal relaxation is defined by T_1, a longitudinal relaxation constant, which differs between different types of tissue, and changes with the main magnetic field strength, as shown in Table 2.1.2. T_1 depends on the type and mobility of molecules in which the nucleus is found. It is generally short for fat and short for water that is bound to macromolecules. Table 2.1.2 shows typical values of T_1 for different types of tissue. If molecular motion is matched to the Larmor frequency then dipole-dipole interactions cause relaxation (via spin flips).

tissue	1.5T	3.0T	7.0T
white matter (WM)	656±16	1010±19	1220±36
cortical grey matter (cGM)	1188±69	1723±93	2132±103
deep grey matter (dGM)	938±34	1381±52	1633±68
cerebrospinal fluid (CSF)	4070±65	4472±85	4425±137
blood	1540±23	1914±114	2587±283

Table 2.1.2: Summary of the T_1 values in ms measured for different types of tissue of human body temperature (37°), in different field strengths, based on [35]. Values for deep grey matter nuclei (dGM) are an average of the measurements taken for: Caudate, Thalamus, Putamen and Globus Pallidus.

Figure 2.1.7 (left) presents T_1 recovery curves for different types of tissue. These differences are utilized to obtain tissue contrast in MR images.
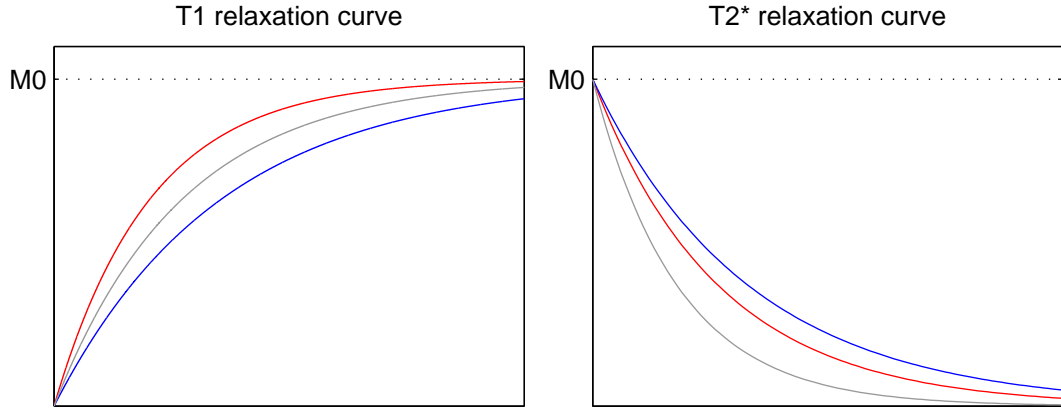
Figure 2.1.7: T_1 (left) and T_2^* (right) relaxation curves plotted for three different tissue types: white matter (WM), cortical grey matter (cGM) and deep grey matter (dGM), based on the values from Tables 2.1.2 and 2.1.3 for a 7T magnetic field.

TRANSVERSE (SPIN-SPIN) RELAXATION

As a result of applying the RF pulse, spins in the sample start to precess with the same phase and transverse magnetization is generated. The magnitude of the transverse component of the **M** vector depends on the degree of phase coherence between the spins. Therefore dephasing resulting from the local and large scale static and fluctuating magnetic field variations cause transverse relaxation.

The time scale of the relaxation related to the local magnetic field variations due to the spin interactions is described by the transverse magnetization constant, T_2. The exponential decay of the magnitude of the signal can be described by the equation:

$$M_{xy} = M_0 e^{-t/T_2} \tag{2.20}$$

derived from the solutions of the Bloch equation (2.19a) and (2.19b). This process occurs more rapidly than the longitudinal relaxation and depends on the type of tissue, the size of molecule: being shorter for protons bound to less mobile molecules (large, connected to the cell membranes). T_2 relaxation is due to oscillating fields, an exchange with location of different frequency, or static fields and diffusion. Therefore, due to the very short T_2, proteins and other macromolecules are not detectable directly in MRI (see Section 2.3.3).

16

Large-scale variations of the magnetic field caused by susceptibility differences (see section 2.3.5) and magnetic field inhomogeneities also cause signal dephasing. This effect is approximated by an exponential decay with a time constant T_2'. The summed contribution of local and large scale dephasing factors is expressed as:

$$R^* = \frac{1}{T_2^*} = \frac{1}{T_2} + \frac{1}{T_2'},\qquad(2.21)$$

where the T_2' effect is static in time and hence reversible. Values of T_2^* for different tissue types measured in different field strengths are presented in Table 2.1.3 and the T_2^* relaxation curve is plotted in Figure 2.1.7.

tissue	1.5T	3.0T	7.0T
white matter (WM)	66.2±1.9	53.2±1.2	26.8±1.2
cortical grey matter (cGM)	84±0.8	66±1.4	33.2±1.3
deep grey matter (dGM)	57.2±2.4	37.4±2.4	18±1.8

Table 2.1.3: Summary of the T_2^* values in ms measured for different types of tissue of human body temperature (37°), in different field strengths, based on [32]. Values for deep grey matter nuclei (dGM) are an average of the measurements taken for Caudate and Putamen.

2.1.5 SIGNAL DETECTION

Transverse magnetization produced when longitudinal magnetization is rotated by the application of an RF pulse starts producing an electromagnetic field oscillating around the x-axis, as described in Section 2.1.3. The induced change in the magnetic flux generates an electromotive force (according to the Faraday Law), which can be detected using a receiver coil. After switching off the RF pulse the relaxation process described in Section 2.1.4 begins, causing a *free induction decay* (FID) signal, oscillating with the Larmor frequency, ω_0, according to the Bloch equation (2.18). The FID signal is amplified to be detectable and demodulated using two phase sensitive detectors with 90° phase shift between their reference signals of frequency ω_{ref}. This allows separation of imaginary and real components of the

signal corresponding to M_x and M_y, respectively:

$$M_x(t) = M_0 \sin\theta \sin(\Delta\omega t + \phi)e^{-t/T_2^*} \tag{2.22a}$$

$$M_y(t) = M_0 \sin\theta \cos(\Delta\omega t + \phi)e^{-t/T_2^*} \tag{2.22b}$$

where $\Delta\omega = \omega_0 - \omega_{ref}$, ϕ is a reference phase and θ is the flip angle of the RF pulse. Plots of the real and imaginary components of the signal are shown in Figure 2.1.8.
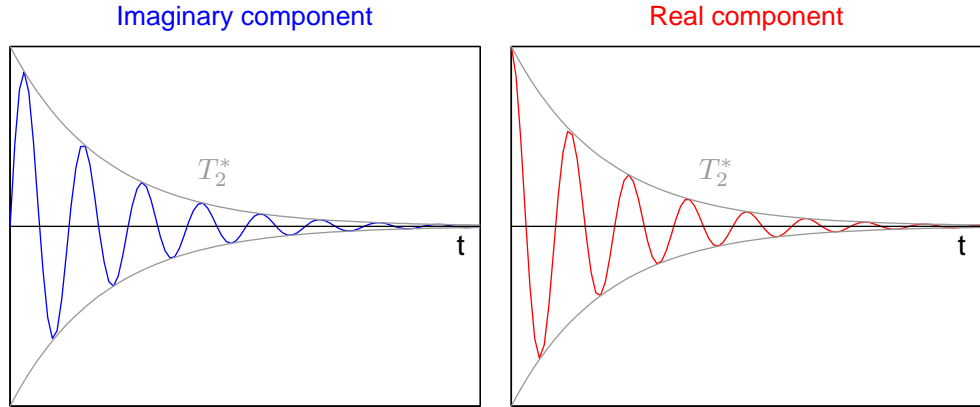
Figure 2.1.8: Imaginary and real components of the FID signal, according to the equations (2.22a) and (2.22b). The T_2^* decay envelope is plotted with grey solid line.

The complex signal is given by the equation:

$$S(t) = M_0 \sin\theta e^{-t/T_2^*} e^{i(\Delta\omega t + \phi)}, \tag{2.23}$$

assuming $M_z = M_0$ before pulse.

Combination of RF pulses into sequences allows measurement of the relaxation constants T_1 and T_2, described in Section 2.1.4, providing the information about tissue characteristics.

INVERSION RECOVERY: T_1 MEASUREMENT

The method commonly used to measure the T_1 of a sample is the inversion recovery sequence, presented schematically in Figure 2.1.9.

INVERSION RECOVERY
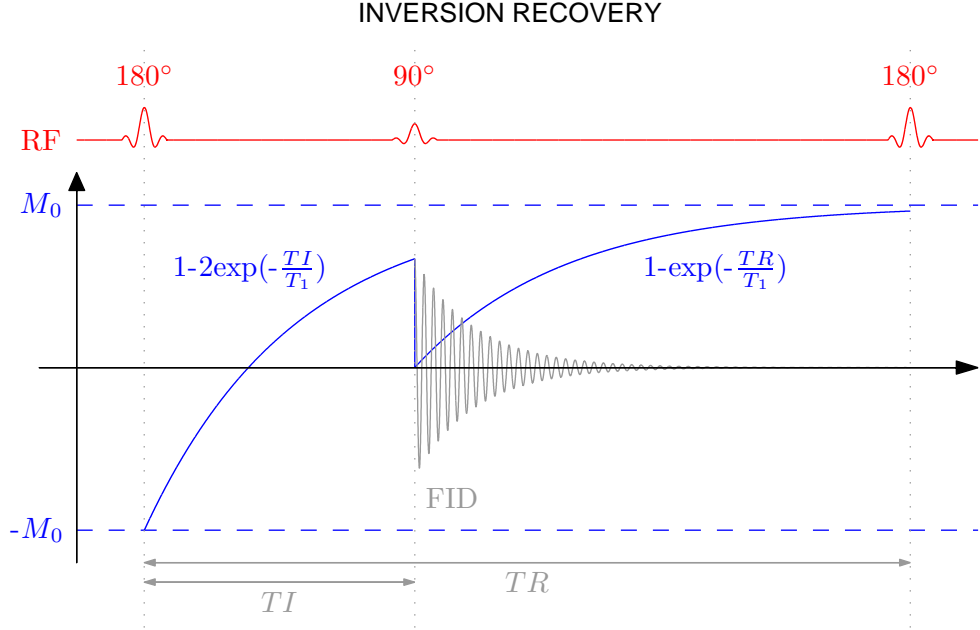
Figure 2.1.9: Diagram illustrating the inversion recovery sequence.

The 180° pulse is applied, inverting the longitudinal magnetization vector to $-M_0$. Magnetization starts recovering, but after the *inversion time* (TI) another 90° pulse flips the partially recovered magnetisation into the transverse plane, and an FID is generated. In order to measure T_1 values this sequence needs to be performed repeatedly, with varying TI values. The *repetition time* (TR) between two 180° pulses has to be long enough to allow recovery of the magnetisation. The measured signal is proportional to the product of two recovery curves which can be derived from the Bloch equation (2.19c):

$$S(TR) \propto M_0(1 - 2e^{-TI/T_1} + e^{-TR/T_1}). \tag{2.24}$$

SPIN ECHO: T_2 MEASUREMENT

As was previously described in Section 2.1.4, transverse relaxation depends not only on local properties of the sample described by the T_2 time constant, but also on large-scale static magnetic field inhomogeneities related to T_2'. However, the static T_2' effects can be reversed and hence the measurement of the T_2 value due to time varying processes is possible using the spin echo sequence introduced by Hahn in

1950 [15]. This is illustrated in Figure 2.1.10.
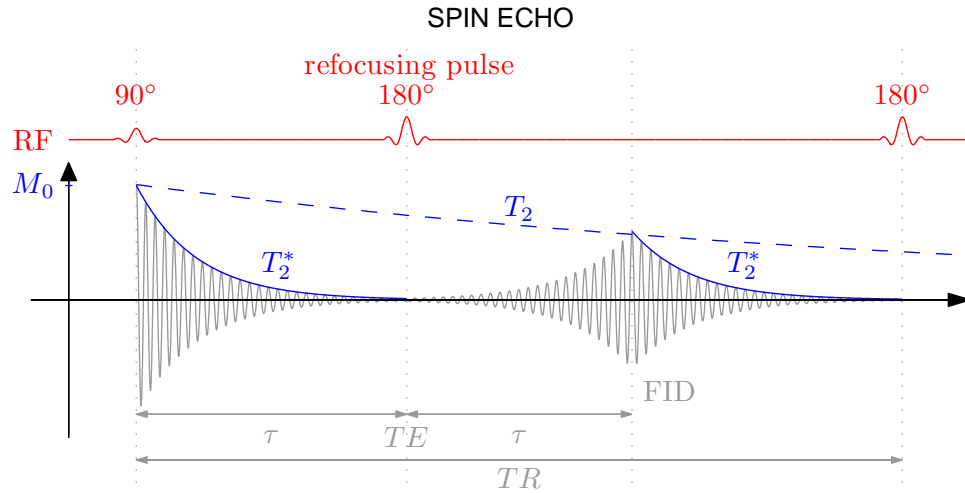
Figure 2.1.10: Diagram illustrating the spin echo sequence.

Application of the 90° pulse brings all the spins to precess in phase creating a transverse magnetization, which afterwards decays with T_2^* due to dephasing. The 180° refocusing pulse applied after time, τ, inverts the magnetisation, which start to process in the opposite direction and rephase. After the *echo time* (TE) of 2τ, the signal attenuation related to T_2' effects is fully reversed and the remaining loss of phase coherence due to the T_2 processes can not be regained. The signal measured after time TE, which is called a *spin echo* is given by:

$$S(t) \propto M_0 e^{-TE/T_2}. \tag{2.25}$$

Multiple measurements are required to measure the T_2 values of the sample, which can be performed by repeating a 90°-180° sequence with different TEs or by adding subsequent 180° pulses. The second method is less susceptible to diffusion and field inhomogeneity effects.

More introduction about the different techniques for measuring specific characteristics of tissue can be found in Section 2.3.

2.2   Magnetic Resonance Imaging

This section presents the principles underlying the use of the NMR phenomenon to acquire images of the sample, describes basic imaging techniques and introduces the MRI equipment.

2.2.1   Spatial encoding

Section 2.1 described the formation and detection of the NMR signal from an entire volume of the sample. Obtaining a 3D image requires measurement of the signal values corresponding to particular locations within the sample. This is performed using a gradient of the z-component of the magnetic field in three orthogonal directions:

$$\mathbf{G} = G_x\mathbf{x} + G_y\mathbf{y} + G_z\mathbf{z} = \frac{dB_z}{dx}\mathbf{x} + \frac{dB_z}{dy}\mathbf{y} + \frac{dB_z}{dz}\mathbf{z}. \qquad (2.26)$$

Application of the gradient affects the magnetic field experienced by the spins along the gradient's direction and the precessional frequency at the position $\mathbf{r} = (x, y, z)$ is given by:

$$\omega(\mathbf{r}) = \gamma(B_0 + \mathbf{G} \cdot \mathbf{r}). \qquad (2.27)$$

The gradients must also have transverse components (eg. $\dfrac{dB_x}{dx}$), but assuming that the $\mathbf{B}_0$ is applied in the z-direction, the transverse components of the gradient fields can be neglected due to their minor effect on the resonant frequency of the spins. Additional dephasing introduced by the gradient field can be reversed using a gradient with the opposite sign. This mechanism is used to produce a *gradient echo*, where RF pulse induced signal is dephased and subsequently rephased by a bipolar gradient and spins regaining phase coherence generate the echo. An example sequence involving gradient echo and using gradient fields for spatial encoding of the signal is presented in Figure 2.2.4.

SLICE SELECTION

Selective excitation of the sample is achieved by using a gradient field whose direction is perpendicular to the chosen slice (conventionally the z-direction) and simultaneous application of the RF pulse of appropriate bandwidth, $\Delta\omega$. Only the spins precessing with the same frequency as the applied RF pulse are excited and subsequently produce a signal, therefore a separate RF pulse is required to obtain an image of each slice. The location of the selected slice is determined by the centre frequency of the RF pulse, while the slice thickness, Δz, depends on the bandwidth of the RF pulse and the strength of the field gradient:

$$\Delta z = \frac{\Delta\omega}{\gamma G_z}. \tag{2.28}$$

The same bandwidth produces a thinner slice using a stronger gradient, but narrower bandwidth makes a thinner slice, while using the same gradient, as is illustrated in Figure 2.2.1.
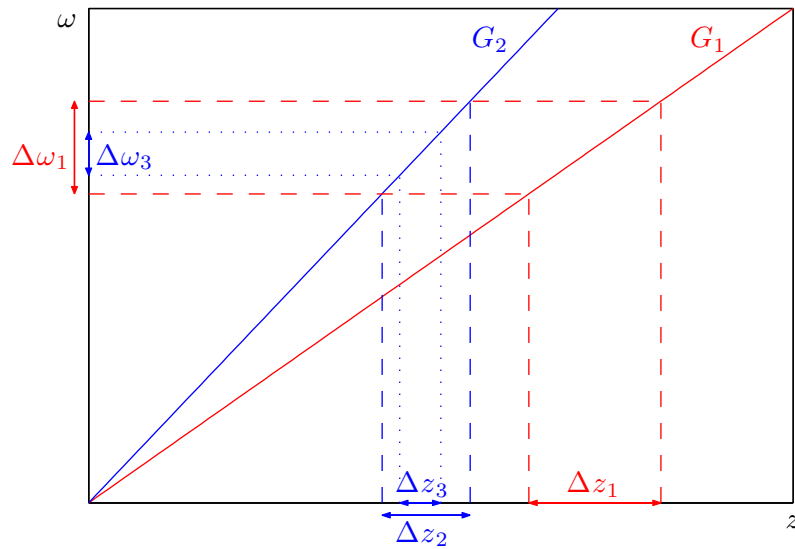
Figure 2.2.1: Plot illustrating the relation between bandwidth, gradient strength and slice thickness. The bandwidth $\Delta\omega_1$ gives a thinner slice $\Delta z_2 < \Delta z_1$ using the stronger gradient G_2, but the narrower bandwidth $\Delta\omega_3 < \Delta\omega_1$ gives a thinner slice $\Delta z_3 < \Delta z_2$ with the same gradient.

Another gradient applied after the RF pulse, conventionally in the x-direction, varies the precessional frequency of the spins according to their position along the x-axis within the excited slice:

$$\omega(x) = \gamma(B_0 + G_x x). \tag{2.29}$$

Therefore, the spins precess with the Larmor frequency only in the locations where $x = 0$. The measured signal can be decomposed using an inverse Fourier transform to identify the corresponding locations for the components of different frequencies, as described in the next sections.

Finally the third gradient is used to encode the signal position along the y-axis. It is applied after the RF pulse, before the data acquisition, for a short period of time to affect the frequency of the spins precession. It introduces a phase difference varying in the y-direction and increasing with time when the gradient is on. After the gradient has been switched off the phase shift between the precessing spins remains and the phase offset is proportional to the location of the spins along the y-axis:

$$\phi(y) = \gamma G_y y t \tag{2.30}$$

where t refers to the gradient duration. One phase encoding step corresponds to one data acquisition and the amplitude of the phase encoding gradient changes between the steps.

2.2.2 IMAGE RECONSTRUCTION

The spins' precessional frequency under the influence of three gradient fields $\mathbf{G}$ in the position $\mathbf{r}$ is given by the equation (2.27) and the phase accumulated by time t

can be calculated as:

$$\phi(\mathbf{r}, t) = \gamma \mathbf{r} \cdot \int_0^t \mathbf{G}(t')dt' \tag{2.31}$$

The signal in the absence of gradients is proportional to the proton density $\rho(\mathbf{r})$, while when gradients are applied the FID equation (2.23) is given by:

$$S(t) = \int \rho(\mathbf{r})e^{-i\phi(\mathbf{r},t)}d\mathbf{r}^3 = \int \rho(\mathbf{r})e^{-i\gamma\mathbf{r}\cdot\int_0^t \mathbf{G}(t')dt'}d\mathbf{r}^3 \tag{2.32}$$

where the relaxation terms are ignored and the reference frequency is assumed to be equal to the Larmor frequency. Substitution using the variable $\mathbf{k} \equiv (k_x, k_y, k_z)$ given by:

$$\mathbf{k}(t) = \gamma \int_0^t \mathbf{G}(t')dt', \tag{2.33}$$

leads to the signal equation:

$$S(\mathbf{k}) = \int \rho(\mathbf{r})e^{-i\mathbf{k}\cdot\mathbf{r}}d\mathbf{k}^3. \tag{2.34}$$

Finally, the inverse Fourier transform of the signal allows the original spin density value to be obtained in the particular location within the sample:

$$\rho(\mathbf{r}) = \frac{1}{2\pi^3} \int S(\mathbf{k})e^{i\mathbf{k}\cdot\mathbf{r}}d\mathbf{k}^3. \tag{2.35}$$

K-SPACE

k-space is an analog Fourier space, in which the signal is acquired, introduced as a theoretical concept in 1983 [25]. In practice it corresponds to the discrete matrix storing values of the signal sampled using an analogue to digital converter (ADC). The matrix consists of N_x columns corresponding to the frequency encoding steps (sampling points) and N_y rows, one for each of the phase encoding steps repeated with a different amplitude (see Figure 2.2.2). The strongest signals, associated with the weakest gradients, are recorded in the centre of k-space and are responsible for the coarse elements of the image (low spatial frequencies), while the weakest
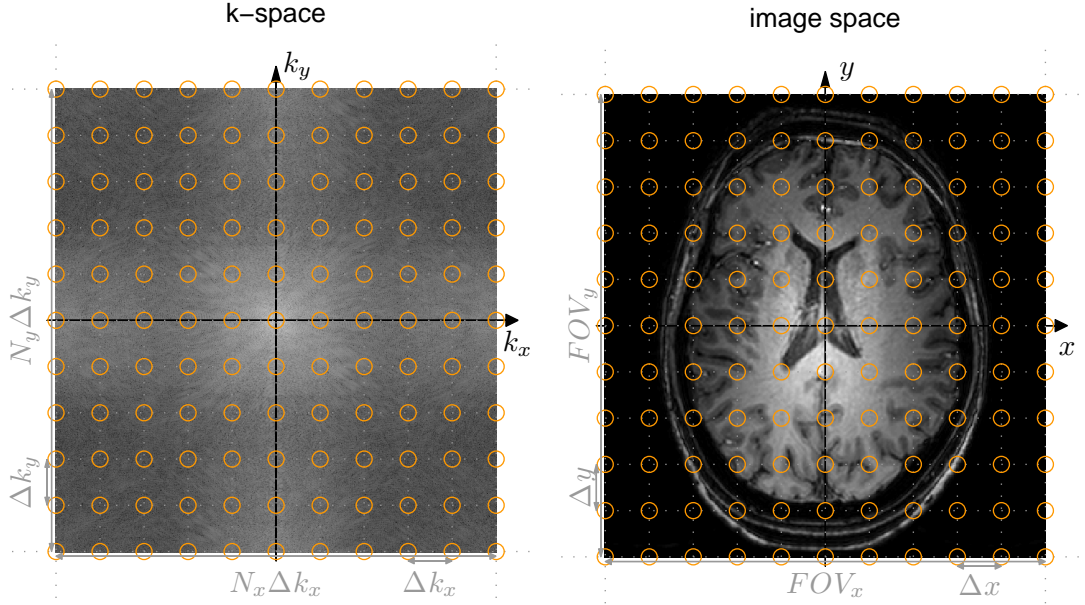
Figure 2.2.2: The signal in k-space (left) and a corresponding image (right). k-space is $N_x \times N_y$ matrix, where columns correspond to the frequency encoding steps and rows to the phase encoding steps; Δk_x and Δk_y refer to the spacing between the sampling points marked with the orange circles. Reconstructed image of size $FOV_x \times FOV_y$ contains voxels of size $\Delta x \times \Delta y$ corresponding to the sampling points.

signals correspond to the periphery and correlate with the fine details and the edges present in the image (high spatial frequencies). To obtain an image, k-space is Fourier transformed to Cartesian space according to the equation (2.35). This correspondence is presented in Figure 2.2.2. Increased image resolution (decrease of Δx and Δy) leads to a longer scanning time, as a larger number of the encoding steps are required for the fixed field of view (FOV) in a given direction:

$$\Delta x = \frac{FOV_x}{N_x}, \tag{2.36}$$

or a smaller spacing between the signal measurements:

$$\Delta k_x = \frac{1}{FOV_x}, \tag{2.37}$$

(similarly for y). Obtaining a discrete k-space matrix from an analogue k-space trajectory can involve different sampling strategies. The main pulse sequences together with their k-space sampling trajectories are presented in the following

sctions.

2.2.3 Spin versus gradient echo

Section 2.1.5 described the principles of creating a spin echo using two RF pulses 90-180 (exciting-refocusing) and measuring a generated signal. Alternatively a gradient echo can be obtained by combining an excitation pulse with a gradient. After the RF pulse of a flip angle θ a negative gradient is applied for a time, τ, to dephase the spins according to their position within the sample. Subsequently a reversed gradient is applied for the time period 2τ to rephase and then dephase the spins. The gradient echo occurs half way through the duration of the second gradient, when spins regain their phase coherence.

These two mechanisms combined with the spatial encoding gradients provide two classes of the sequences commonly used to acquire 3D MR images: spin echo (SE) and gradient echo (GE) (see Figures 2.2.3 and 2.2.4).

Spin echo imaging

In the spin echo pulse sequence, schematically presented in Figure 2.2.3 together with the corresponding k-space trajectory, the slice selection gradient G_z is switched on during both RF pulses. The de-phasing positive gradient is applied in the x direction after the excitation pulse simultaneously with the phase encoding gradient G_y, which corresponds to moving in the spatial frequency domain along both k_x and k_y axes. The refocusing pulse inverts the phase of the spins by 180° and data acquisition is performed with the frequency encoding gradient switched on in the same time. The signal intensity in the spin echo sequence depends on the T_2 relaxation constant. To fill the rest of k-space this process is repeated with varying phase encode gradient amplitudes.

Figure 2.2.3: Timing diagram of a spin echo (SE) sequence: RF pulses (red), gradients (blue) and echo signal (grey), with marked echo time (TE) and repetition time (TR) (left). Gradients positions marked in light blue correspond to the movement in k-space plotted in the same colour. The effect of the refocusing pulse is plotted in red and signal sampling trajectory is indicated by orange circles (right).

GRADIENT ECHO IMAGING

The gradient echo sequence, diagram and k-space trajectory presented in Figure 2.2.4, consists of a θ excitation pulse applied together with the slice selecting gradient G_z. Subsequently the negative pre-phasing gradient applied in the x direction and accompanied by the phase encoding gradient G_y results in a trajectory from the centre to the bottom left quarter of the k-space. Further application of the frequency encoding G_x gradient generates the gradient echo and the signal is sampled. The sequence is repeated for different θ phase encode gradient amplitudes to cover other lines across k-space.
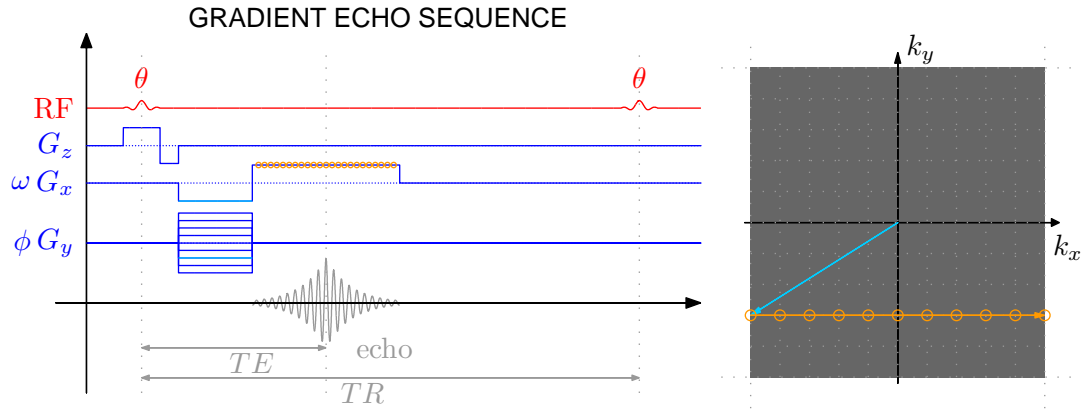
Figure 2.2.4: Timing diagram of a gradient echo (GE) sequence: RF pulse (red), gradients (blue) and echo signal (grey), with marked echo time (TE) and repetition time (TR) (left). Gradients positions marked in light blue correspond to the movement in k-space plotted in the same colour and signal sampling trajectory is indicated by orange circles (right).

As dephasing due to the large scale magnetic field variations (field inhomogeneities, susceptibility) is not be reversed by the gradient echo, the signal attenuation follows the T_2^* decay. To minimise this effect, very short TEs (in order of milliseconds) are often used and gradient echo imaging is generally faster than spin echo imaging due to the shorter duration of the GE acquisition and lack of a 180∘ RF pulse which makes it more straightforward to reduce TR and the flip angle.

2.2.4   2D MULTI SLICE VERSUS 3D VOLUME IMAGING

The slice thickness in 2D multi slice images is limited by the available gradient strength. In order to obtain thinner slices additional phase encoding gradient can be applied in the slice direction and 3D Fourier encoding of the whole volume or separate thick slabs can be performed. The slice thickness in a 3D image is equal to FOV_z/N_z, where N_z is a number of phase encoding steps in the slice selection direction. An example of a 3D GE sequence is shown in Figure 2.2.5.
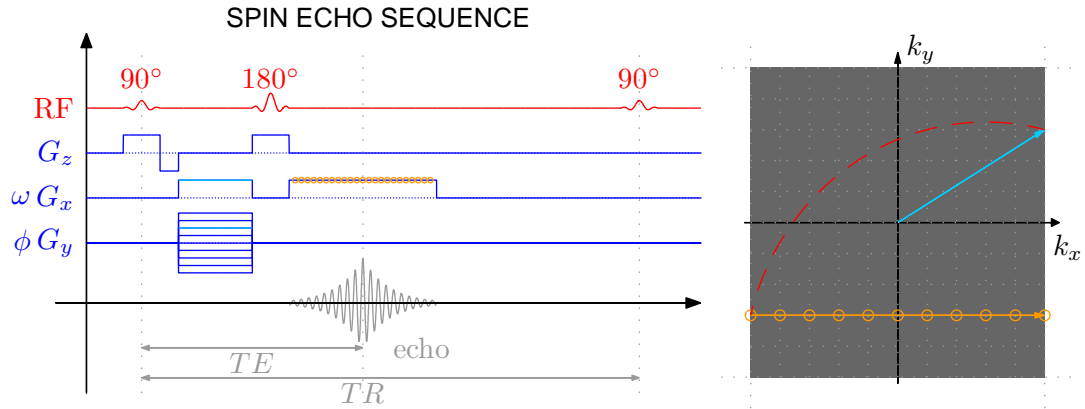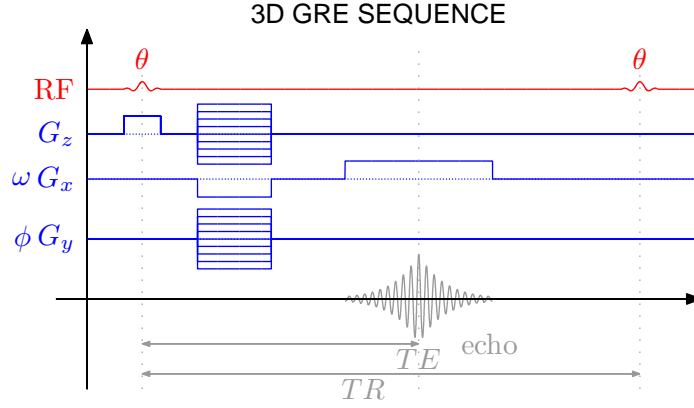
Figure 2.2.5: Timing diagram of the 3D gradient echo sequence: RF pulse (red), gradients (blue) and echo signal (grey), with marked echo time (TE) and repetition time (TR) (left).

2.2.5 Signal to noise ratio (SNR)

One of the most important quality characteristics of MRI data is the signal to noise ratio (SNR). The amount of the MR signal per voxel increases with a voxel size. The noise is higher for wider bandwidth sampling, but can be decreased by using more phase encoding steps, which effectively averages the signal in the Fourier transform. Additional improvements in SNR can be achieved by averaging the values from several acquisitions obtained under the same conditions, which also increases the scanning time. These dependences for 2D and 3D sequences are summarised in Equation (2.38) showing the 3D imaging provides higher SNR:

$$SNR_{3D} \propto \sqrt{N_z}\frac{\Delta x \Delta y \Delta z \sqrt{N_x N_y NSA}}{\sqrt{BW}} = \sqrt{N_z}SNR_{2D} \qquad (2.38)$$

where N_x, N_y and N_z are numbers of encoding steps in frequency, phase, phase slice selection direction, respectively, BW represents the bandwidth of an image and NSA stands for the number of averages.

Using wide slabs in 3D images allows the use of short excitation pulse lengths which can shorten TE and TR, although additional phase encoding steps make the total scanning time longer and the sequence is more susceptible to motion artefacts. The

29

relation between total scanning times in 2D and 3D sequence can be expressed as:

$$T_{3D} = N_z \times N_y \times TR \times NSA = N_z \times T_{2D}, \tag{2.39}$$

for constant TR. In practice in 2D imaging it is usually possible to excite more than one slice during each repetition time. The maximum number of slices to fit in one TR is given by:

$$N_{max} = \frac{TR}{TE + \Delta T}, \tag{2.40}$$

where ΔT is the additional time necessary to finish the signal acquisition and switch the gradients (approximately half of the readout time). Lengthening TR in this way generally increases the signal as it allows longer for magnetization recovery.

2.2.6   Fast imaging

This section presents several methods for decreasing the scanning time.

Partial Fourier imaging

Partial Fourier imaging is a technique introduced by Feinberg [5], which takes advantage of the conjugate symmetry of k-space:

$$S(-k_x, -k_y) = S^*(k_x, k_y) \tag{2.41}$$

where $*$ is a complex conjugate. Only the top half of k-space is sampled and is used to calculate the remaining part. As the number of the phase encoding steps is reduced to $N_y/2$, the scanning time is halved, but this also causes a reduction of the signal to noise ratio by factor of $\sqrt{2}$, because only half of the signal is acquired. In practice the condition (2.41) is not always valid due to the effects of field inhomogeneity and additional lines of k-space need to be acquired (usually 60-75% in total) to ensure the validity of the estimations of missing k-space signal. The central region of k-space (corresponding to the low spatial resolution) can be used to reconstruct the phase

image, assuming slow spatial phase variation. This method is easy to implement and is commonly used, but it can cause artefacts if the condition of slowly varying phase is not fulfilled.

Parallel imaging

Another method of shortening the scanning time is parallel imaging [34]. Reducing the number of sampled lines of k-space by increasing Δk_y would normally cause aliasing, leading to the generation of wrap around artefact (Figure 2.2.6, middle). In order to overcome this problem, multiple independent receiver coils with different spatial sensitivity profiles are used (Figure 2.2.6, right). Several methods have been developed to reconstruct the complete image from the raw data by employing the information about coil sensitivity and one of the most common is Sensitivity Encoding for Fast MRI (SENSE) introduced by Pruessmann in 1999 [34]. Parallel imaging is a hardware dependent technique, the maximum reduction of the scanning time is given by the number of channels in the receiver coil of the MR system, but in practice depends on the spatial sensitivity of the different coil elements.

Figure 2.2.6: The original image (left), wrap around artefact (middle), sensitivity profiles of the receiver coil channels used to obtain the raw data, which allows to reconstruct the complete image (right).

In 3D imaging additional reduction in the number of k-space lines in the second phase encoding direction is possible (see Section 2.3).

Echo planar imaging (EPI) is a technique proposed by Mansfield [26, 27], which uses multiple gradient echoes to acquire multiple lines of k-space after one excitation pulse. The efficiency of the sampling scheme allows the whole image to be obtained with a few excitations (multi-shot EPI) or even only one excitation (single-shot EPI).
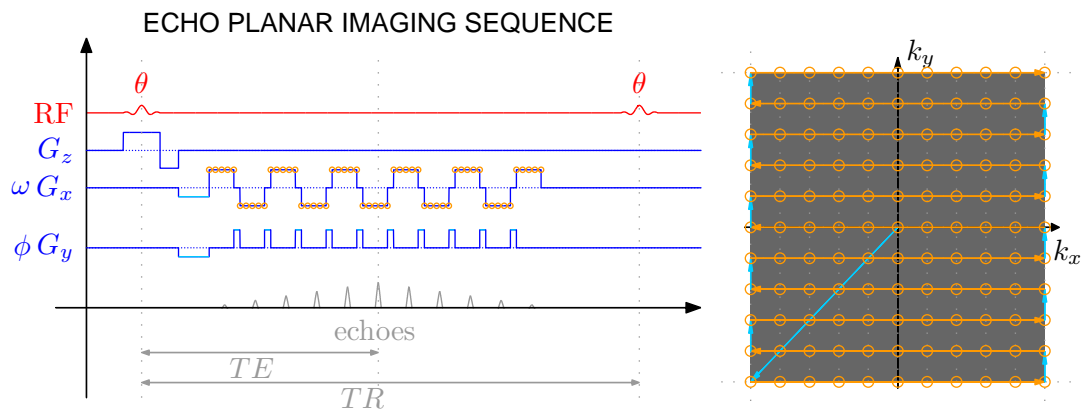
Figure 2.2.7: Timing diagram of an echo planar imaging (EPI) sequence: RF pulse (red), gradients (blue) and echo signal (grey), with marked echo time (TE) and repetition time (TR) (left). Gradients positions marked in light blue correspond to the movement in k-space plotted in the same colour and signal sampling trajectory is indicated by orange circles (right).

The pulse sequence diagram and k-space trajectory of the gradient echo planar sequence are presented in Figure 2.2.7. Each line of k-space corresponds to one of the equally spaced gradient echoes generated by G_x, which together constitute an echo train. Phase encoding is performed by applying the G_y 'blips' at the time when $G_x = 0$, which gradually moves the sampling in the k_y direction. As successive lines of k-space are sampled in opposite directions, reordering of the data is required before application of the Fourier transform. Mismatch between even and odd lines of k-space causes the Nyquist ghost artefact, which appears as a version of the object repeated and shifted by half the field of viev of the image. As all the echoes have to be acquired before the signal has decayed, rapid switching of the gradients is required to obtain an image of a single slice in a time of order of milliseconds. A relatively long readout time in EPI enforces low separation of the sampling points in the k_x direction, which causes high sensitivity to the effect of field inhomogeneity often

leading to signal mis-registration appearing in the image as a geometric distortion. The amplitudes of the successive echoes follow the T_2^* decay due to the dephasing caused by field inhomogeneities, which can also cause artefacts. Long readout times combined with the thick slices can also lead to signal drop-out due to through slice phase variation. Distortion can be reduced by increasing gradient strength (not practical) or reducing a number of the k-space lines sampled to shorten the echo train duration (parallel imaging).

In spite of being susceptible to artefacts, echo planar imaging is a popular technique, especially in the applications where fast imaging is crucial (e.g. functional MRI or diffusion weighted imaging). In addition to T_2^*-weighted contrast, by applying preparation pulses, EPI can also be used to obtain spin echo T_2-weighted or inversion recovery T_1-weighted images.

2.2.7 Hardware and safety

The architecture of an MR system is schematically presented in Figure 2.2.8 and particular elements are described below with the reference to the Nottingham 7T Philips Achieva MR scanner used to obtain most of the data in this thesis.
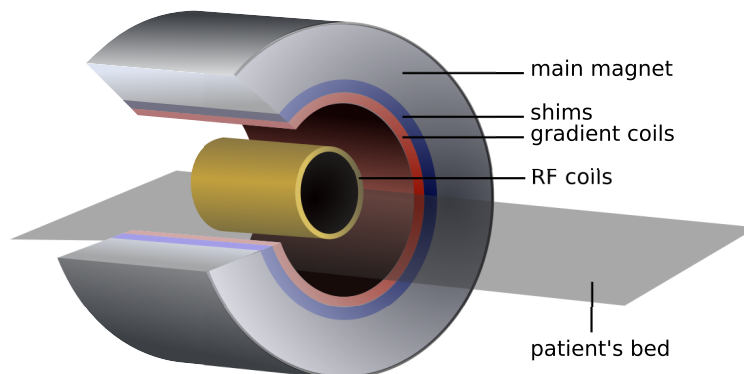
Figure 2.2.8: Schematic illustration of the MR scanner architecture.

Main magnet

The initial longitudinal magnetisation of the sample is generated by the main magnet which produces a strong, static, homogeneous, magnetic field $\mathbf{B}_0$. The strength of this field, its temporal stability and spatial uniformity are important features, as they

affect the quality of the acquired data. Permanent magnets have limited maximum strength (0.2-0.3T) and are sensitive to temperature fluctuations. Modern high field MR systems therefore use superconducting magnets built from the materials, in which the resistance drops to zero below a certain transition temperature causing the electrical current to flow indefinitely, providing a magnetic field of high stability. The required temperature and field strength depend on the material type, systems operating at fields <9.4T generally use Niobium Titanium Alloy (NbTi, 9.2K, 15T) while systems operating at fields >9.4T use Niobium Tin (Nb3Sn, 18.3K, 30T). A cooling system containing liquid helium is required to maintain a low temperature. The Nottingham 7T Phillips system contains superconducting magnet (NBTi) which produces a field with inhomogeneity of less than 0.10 ppm in a 25 cm diameter spherical volume.

Improvements in the main magnetic field inhomogeneity can be achieved by active or passive shimming. Passive shimming involves placing ferromagnetic elements within the bore, while active shimming employs coils producing additional magnetic fields, which cancel spatial variations of the main field. Active shimming can be interactively adjusted for the particular experiment by modifying the shim currents automatically or manually, based on a magnetic field map.

The magnetic field outside the bore of the magnet (fringe field) can interfere with the equipment and passive or active shielding is necessary. The Nottingham 7T scanner is passively shielded by 200 tones of iron.

Gradient coils

Linear magnetic field gradients are used for spatial localisation of the signal as described in Section 2.2.1. Efficiency and precision of the signal encoding depends on the field gradient switching time (0.1-1.0ms), strength (10-50mT/m) and linearity. The gradient in the *z*-direction can be produced using a *Maxwell Pair*, a set of two circular coils with currents flowing in the opposite directions, but the same magnitude, placed on the axis of the main magnet bore. A *Golay Coil* can be used

to generate a transverse gradient.

The waveform controller is a device responsible for generating gradient waveforms, which are then passed to the amplifiers and gradient coils afterwards.

Rapid changes in the magnetic field gradients during the imaging process produce eddy currents in scanner structures generating additional, spatially and temporary varying magnetic fields which cause image distortion and signal loss. This problem can be overcome by active shielding the conducting parts of the magnet from the gradient fields [3]. Therefore a gradient coil consists of the inner primary coil and the outer shield coil to ensure minimal gradient field outside the bore of the scanner. The gradient coils of the 7T Nottingham scanner produce gradient fields of 40mT/m and a slew rate (maximum rate of change) of 200mT/m/ms.

Radio-frequency coils

Radio-frequency coils are used to excite transverse magnetisation of the sample and to receive the resulting signal, as described in Sections 2.1.3 and 2.1.5. The waveform controller sets the frequency of the synthesiser which generates the receiver frequency and generates the envelope of the RF pulses.

Experiments presented in this thesis were performed using two different RF coils, each consisting of volume transmit coil and either a 16- or 32-channels receiver coil, which allow parallel imaging.

Safety

MRI is relatively safe imaging method in comparison to X-ray imaging. No known long term adverse effects occur due to the main magnetic field <10T, however in high field systems short term symptoms have been reported, including vertigo, nausea, and a metallic taste, particularly associated with rapid head movements close to the magnet bore [7, 8]. Objects or implants made from ferromagnetic materials experience a force moving them towards the magnet, and thus can be potentially dangerous and need special attention.

Switching the gradients generates rapidly varying, oscillating magnetic fields, which induce currents in the human body and may stimulate muscles or nerves, if exceeding a threshold for peripheral nerve stimulation (PNS, 60-100T/s) [6]. Ear protection also needs to be used to minimise the effects of the acoustic noise produced by the gradient coils due to their vibration caused by the rapidly varying current within the main magnetic field. Recommended maximum rate of change of field to limit PNS is 20T/s for pulses longer than 120μs and 140dB is considered as a maximum acoustic noise limit.

The RF field induces currents in the tissue causing heating described by the specific absorption rate (SAR), which increases with the higher field strength, where more RF power is used. The maximum allowed SAR value is 4W/kg over 5min period. It is also important to avoid loops of the cables (or skin touching itself) as this produces current loops which may lead to the skin burns.

Careful patient screening is necessary in order to exclude those with metal implants, pacemakers, claustrophobia or other possibly hazardous conditions.

2.3 ADVANCED IMAGING METHODS

This section presents an overview of the sequences and quantitative mapping methods used in the experimental part of the thesis.

2.3.1 FLASH

The Fast-Low Angle SHot (FLASH) sequence, which was introduced in 1986 [13, 14], also known as Fast Field Echo (FFE, Philips), is a GE sequence (see section 2.2.3) using very short TRs to reduce scanning time, together with low flip angle pulses to maximise the signal. If $TR \ll T_1$, the longitudinal magnetization will not fully recover between excitations, but it will reach a *steady state* after multiple RF pulses. The transverse magnetization remaining after the previous excitation is often prevented from contributing to the signal using a spoiling (crusher) gradient

before application of the subsequent RF-pulse, enabling short repetition times. Alternatively or additionally RF-spoiling can be used, involving variation of the phase of the successive RF pulses. Dephasing caused by the phase encoding gradient is refocused by a *rewinding* gradient applied after signal acquisition in the same TR-period. The diagram of a basic 2D FLASH sequence with a spoiling gradient applied in the z-direction is presented in Figure 2.3.1.
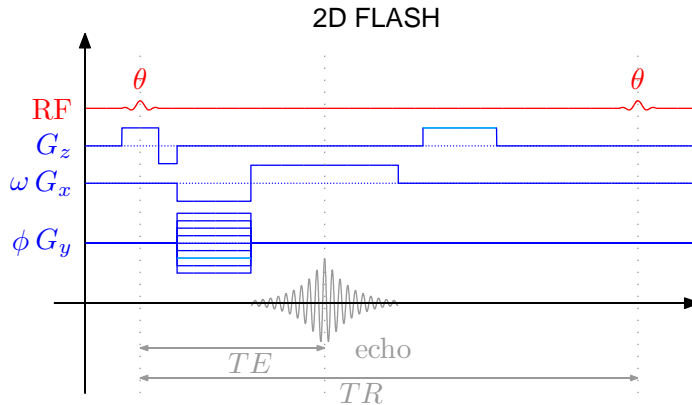
Figure 2.3.1: Timing diagram of a 2D FLASH sequence: RF pulse (red), gradients (blue) with their current positions (light blue) and echo signal (grey), with marked echo time (TE) and repetition time (TR).

The signal strength in the FLASH sequence can be written as:

$$S \propto M_0 \frac{\sin\theta(1 - e^{-TR/T_1})}{1 - e^{-TR/T_1}\cos\theta} e^{-TE/T_2^*}, \tag{2.42}$$

where θ is the flip angle. For a given TR the maximum signal is obtained by using the *Ernst angle*, θ_E which fulfils the condition: $\cos\theta_E = e^{-TR/T_1}$. Spoiling the transverse magnetization makes FLASH images T_1-weighted. In order to acquire T_2^*-weighting a relatively long $TE \geq T_2^*$ is chosen. The contrast also can be modified by adding magnetization preparation pulses at the beginning of the sequence (see Section: 2.3.2).

FLASH images can be acquired in either 2D or 3D mode. The sequence has low sensitivity to off-resonance effects, but the short TR and consequently short readout time reduces its SNR.

2.3.2 MPRAGE AND T_1 MAPPING

The mechanism of longitudinal relaxation was discussed in Section 2.1.4 and the principles of inversion-recovery-based T_1 measurement were briefly described in Section 2.1.5. Here the MPRAGE sequence, which was used in this thesis to obtain T_1-weighted images of the brain, is presented. Moreover the method to calculate maps of the actual T_1 values based on these images is described in this section.

MPRAGE

Magnetisation-Prepared RApid Gradient Echo (MPRAGE), also known as Inversion Recovery Turbo Field Echo (IR-TFE, Philips), which was proposed in 1990 [31] and is a 3D sequence consisting of a magnetization preparation step using an inversion recovery pulse and a 3D FLASH sequence. A diagram showing the structure of a version of the sequence using a spoiling gradient in the x-direction is presented in Figure 2.3.2.
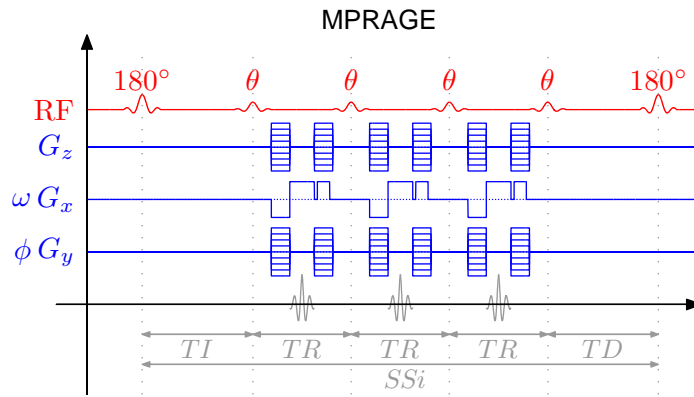
Figure 2.3.2: Timing diagram of a 3D MPRAGE sequence: RF pulse (red), gradients (blue) with their current positions (light blue) and echo signal (grey), with marked echo time (TE) and repetition time (TR); time points a-d are used in the equations for T_1 mapping in the next section.

The *inversion time (TI)* is the time after the 180° pulse when the train of FFE pulses is applied, each in a separate TR. The number of pulses is specified by the *TFE factor* (Philips). The period after the last FFE pulse during which the magnetization is recovering before application of the next inversion pulse is called the *delay time (TD)*. The total time between two sucessive 180° pulses is known as

the *Shot-to-Shot interval (SSi)* and can be calculated from:

$$SSi = TI + TR \times TFE + TD. \tag{2.43}$$

MPRAGE is a standard anatomical protocol providing T_1 weighted images with good contrast between the brain tissues: WM, GM, CSF. Timings are normally chosen to approximately null CSF signal and provide good GM/WM contrast.

T_1 MAPPING

Signal intensity in the individual T_1 weighted images can be affected by multiple factors (different relaxation times, hardware conditions, etc.) and therefore such images do not provide quantitative and reproducible measures of T_1. Approaches based on using a series of measurements obtained with varying inversion times allow more accurate mapping of the longitudinal relaxation times. For the purpose of this thesis MPRAGE-based T_1 mapping method was used [43]. The resulting data were fitted to a model, by calculating the signal as a function of M_0 and T_1 and the flip angle of the inversion pulse, taking into account all the RF pulses and recovery periods. Figure 2.3.3 presents a diagram showing three time points, before and after the RF pulse and after the recovery period
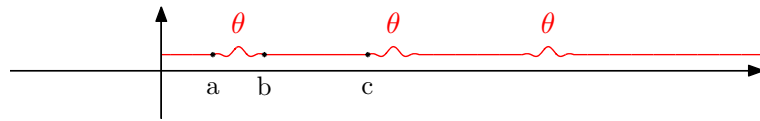
Figure 2.3.3: Simplified diagram showing RF pulses of a 3D MPRAGE sequence (red) and three different time points used in the equations below.

The magnetisation M_z^b just after the RF pulse of flip angle θ is calculated using magnetization M_z^a just before the pulse using the equation:

$$M_z^b = M_z^a \cos \theta. \tag{2.44}$$

The magnetization after the recovery period t is calculated using the formula:

$$M_z^c = M_z^b e^{-t/T_1} + M_0(1 - e^{-t/T_1}) \qquad (2.45)$$

where M_0 is the equilibrium longitudinal magnetization, M_z^c and M_z^b are values of magnetisation after and before the recovery period. Flip angles are obtained from B_1 maps [44] and the polarity restoration method [9] is applied to the data before the calculations. Fitting of the measurements acquired for different time points is performed to obtain an accurate T_1 map (for more details see [43]).

2.3.3 MTR, CEST and NOE

Conventional MRI can not detect signal directly from the protons bound in macromolecules (proteins, cell membranes, myelin) because of their short T_2 relaxation times [17]. However the water protons can interact with the bound protons leading to magnetization transfer (MT) due to either proton exchange or spin-spin interaction.
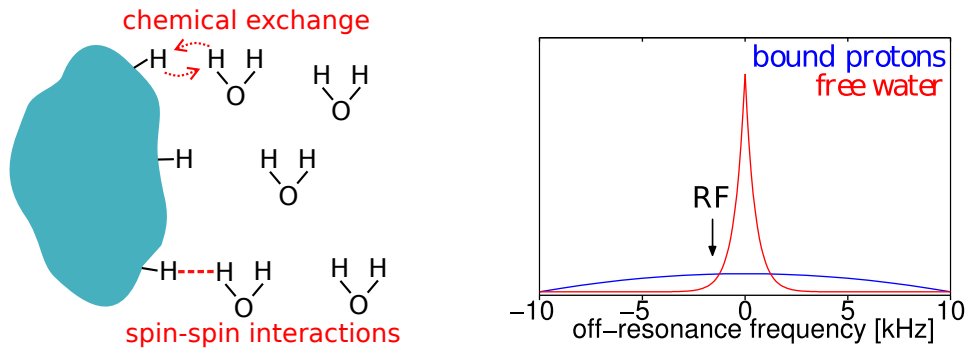
Figure 2.3.4: Magnetization exchange between the molecular and free water protons (left); the absorption lineshapes of macromolecular and water protons and the off-resonance saturation pulse (right).

The MT effect is obtained by using off-resonance RF pulses to saturate selectively macromolecular protons, which then partially saturate free water protons via magnetization exchange. This decreases the available longitudinal magnetization of the free water and results in a detectable signal change in regions where exchange occurs. This process is illustrated in Figure 2.3.4, together with the absorption

40

lineshapes of macromolecular and water protons.

Magnetization transfer is affected by tissue characteristics, allowing investigation of the concentration and distribution of macromolecules and possible exchange sites. The effect of MT on the water protons measured for different frequencies of the off-resonance saturation pulse forms the so called z-spectra [10], which can be used to study macromolecules indirectly (via the water signal) in order to evaluate relative concentrations and exchange rates.

MTR

Magnetization transfer imaging (MTI), introduced as a new source of contrast in MRI in 1989 [42], can be performed with both SE and GE sequences (in 2D and 3D). A short saturation pulse (or a train of pulses) is applied before each excitation pulse. For quantitative characterisation, the Magnetization Transfer Ratio (MTR) is calculated voxelwise based on two separate sequences with identical parameters apart from one including the MT saturation:

$$MTR = \frac{S_0 - S_S}{S_0},\tag{2.46}$$

where S_0 is the voxel intensity in the non-saturated image and S_S the intensity of the corresponding voxel in the MT-saturated one. The schematic diagram of the MT sequence used in this thesis is presented in Figure 2.3.5.
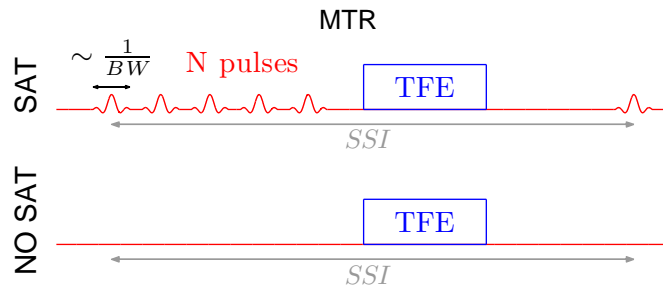
Figure 2.3.5: Schematic diagram of the pulse sequence, the pulsed saturation acquisition followed by a no saturation acquisition with the TFE imaging module.

MTR values are dependent on the tissue type and reflect the saturation of the water

protons due to the magnetization exchange and their longitudinal magnetization recovery. This method is especially useful for increasing the contrast between fluids and other tissues with significant macromolecular content. One of its major clinical applications is visualisation of MS lesions, differentiation of their types and monitoring of their evolution [18].

CEST

Chemical exchange dependent saturation transfer (CEST) is a subtype of MT measuring magnetization transfer due to the exchange of protons between free water and macromolecules. An off-resonance RF pulse is applied with frequency corresponding to the resonance of particular metabolites or chemical groups of high chemical exchange rate, such as amide protons (amide proton transfer, APT imaging). CEST often investigates asymmetries in the z-spectrum by dividing or subtracting measurements obtained with the saturation on two sides of the water spectrum balancing the effects of direct saturation of the free water, assuming that the underlying spectrum is symmetric.

NOE

The Nuclear Overhauser Effect (NOE) [20], another type of MT, occurs by dipole-dipole interaction between protons of different molecules. NOE has recently been discovered for the MRI field [19] as a method providing information about the magnetization transfer between aliphatic protons bound in proteins, peptides and lipids and the water pool [38]. Similarity of NOE to the myelin proton spectrum [19, 41] suggests it may be a good candidate for the quantitative myelin imaging technique.

HIGH FIELD

As MT experiments require high power saturation pulses, conducting them in the high magnetic field leads to the problems with reaching the SAR limits. Moreover,

increased inhomogeneity of the static magnetic field B_0 and RF B_1 field affects the effective frequency and extent of the saturation and therefore changes the contrast in the MT images. Despite the SAR limits and the issues related to field inhomogeneity, MT experiments benefit from using ultra high field due to increase in SNR, longitudinal relaxation of water and chemical shift between the water and macromolecules (especially important for CEST effects). Details of the method used for the MT measurements in this thesis are described in [30].

2.3.4 PRESTO

PRinciples of Echo-Shifting with a Train Observation (PRESTO) proposed in 1993 [24] is an Echo shifted (ES) sequence with TE>TR. Figure 2.3.6 shows a diagram of the 2D PRESTO sequence.
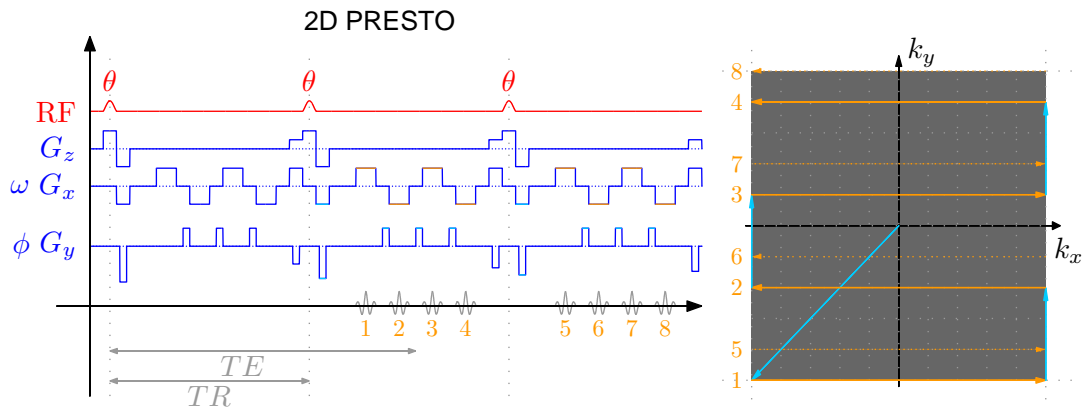
Figure 2.3.6: Timing diagram of the 2D PRESTO sequence: RF pulse (red), gradients (blue) and echo signal (grey), with marked echo time (TE) and repetition time (TR) (left). Gradients positions marked in light blue correspond to the movement in k-space plotted in the same colour and signal sampling trajectory is indicated by orange circles (right).

Multiple gradient echoes are created during a single TR and the echo train is shifted using a special configuration of the slice selection gradient pulses: a negative spoiler gradient pulse dephases transverse magnetisation after the first excitation and a positive refocusing gradient lobe before the second RF pulse. Consequently no signal is measured in the first TR and transverse magnetization created by the first RF pulse is a source of the signal in the next readout period. The same mechanism is repeated for the following TRs thus providing a sequence with TE>TR. In the

frequency encoding (readout) direction an EPI-type echo train (bipolar gradient lobes) is applied with the additional positive rephasing lobe afterwards, resulting in zero net dephasing of transverse magnetization by gradients within the TR period. The phase encoding gradient blips include: prephasing lobe of decreasing magnitude for the subsequent TRs initiating k-space trajectory, phase encoding blips and a rewinder of increasing magnitude at the end of each TR.

PRESTO provides T_2^* weighted contrast and also used when long TE is necessary (susceptibility based perfusion imaging, BOLD fMRI). It is a fast sequence as multiple k-space lines are acquired in one TR and TE>TR. PRESTO can be performed in either 2D or 3D mode.

2.3.5 Magnetic susceptibility mapping

The magnetic susceptibility χ quantifies a material's ability to magnetize and depends on the types of magnetic dipole moments due to the electrons' arrangement within the material. *Paramagnetic* materials of susceptibility values $\chi > 0$ contain atoms with unpaired electrons and have permanent magnetic moments. Weaker effects appear in *diamagnetic* materials of susceptibility $\chi < 0$ which have dipole moments induced in presence of the external magnetic field. The strongest magnetization occurs for *ferromagnetic* materials with $\chi \gg 1$ which contain permanent domains of magnetic moments. Single domain particles mixed with the background substance are called *superparamagnetics* and have magnetic susceptibility intermediate to paramagnetic and ferromagnetic materials. Brain tissues are generally diamagnetic with $|\chi| \ll 1$, but susceptibility differences occur for example for the paramagnetic deoxyhemoglobin in venous blood, iron (in form of ferritin or hemosiderin) and the air/tissue interfaces ($\chi \approx 0$ for air). Therefore, susceptibility measurement may be especially important in neurodegenerative diseases, such as Parkinson's disease or multiple sclerosis, where iron content plays a role (see Chapter 4).

MAGNETIC SUSCEPTIBILITY MEASURMENT

Local magnetic field inhomogeneities due to the dipole fields cause MR signal phase variations between the regions of different susceptibility values allowing a new type of MRI contrast. The phase of the MR signal, which corresponds to the accumulated angle of the precessing magnetization of the sample, is determined by the local magnetic field offset, ΔB, and the echo time TE:

$$\Delta\phi = -\gamma\Delta B TE, \tag{2.47}$$

where γ is the magnetogyric ratio. Since the magnetic field change depends upon local magnetic susceptibility differences, the phase of the MR signal can be used as a source of information about the magnetic properties of the imaged tissue.

For linear materials (isotropic, homogeneous and linear, i.e. where the magnetization is proportional to the field), if $\mathbf{M}$ is the additional macroscopic magnetization of the sample, the magnetic field, $\mathbf{B}$, can be written as:

$$\mathbf{B} = \frac{1+\chi}{\chi}\mu_0\mathbf{M}(\chi), \tag{2.48}$$

where χ is the magnetic susceptibility and μ_0 is the permeability of free space. The relation between the permeability and susceptibility of the substance is defined as $\mu = (1+\chi)\mu_0$.

FOURIER-BASED SUSCEPTIBILITY MAPPING

The standard method used for investigation of susceptibility differences in the brain is susceptibility weighted imaging (SWI) which involves combining phase data with modulus images to enhance the contrast [12]. However, due to the non-local relationship between the field perturbation and underlying susceptibility distribution [28] as well as the dependence of phase variations on the angle between the head and the direction of main magnetic field [36], direct susceptibility mapping approaches

provide a more accurate and precise measure [39].

The magnetic field inhomogeneity caused by susceptibility differences can be calculated using a Fourier method described in [28] and [36]. For an object of susceptibility $\chi(\mathbf{r})$ placed in an external magnetic field, B_0, aligned with the z-axis, the z-component of the induced magnetization can be expressed as:

$$M_z(\mathbf{r}) = \chi(\mathbf{r})\frac{B_0}{\mu_0\mu_r(\mathbf{r})} = \chi(\mathbf{r})\frac{B_0}{\mu_0\left(1 + \chi(\mathbf{r})\right)} \approx \chi(\mathbf{r})\frac{B_0}{\mu_0}, \qquad (2.49)$$

where the $\mu_r = \mu/\mu_0$ is relative permeability and $|\chi| \ll 1$ is assumed. The magnetic field perturbation at position $\mathbf{r}$ is the sum of dipole fields generated by the elements of the $M_z(\mathbf{r})$ distribution and can be calculated in the Fourier domain as:

$$\Delta\tilde{B}_z(\mathbf{k}) = \tilde{M}_z(\mathbf{k})\frac{\mu_0}{3}\left(1 - 3\cos^2\beta\right) = \frac{B_0\tilde{\chi}(\mathbf{k})}{3}\left(1 - 3\cos^2\beta\right), \qquad (2.50)$$

where ˜ indicates a 3D Fourier transform, $\mathbf{k}$ is a vector of coordinates in k-space and β is the angle between $\mathbf{k}$ and the direction of the magnetic field. As the value of $\cos^2\beta = \dfrac{k_z^2}{k_x^2 + k_y^2 + k_z^2}$ is undefined for $\mathbf{k} = 0$, which in fact contains the average value of the field, $\Delta\tilde{B}_z(0)$ is set to 0. Finally the inverse Fourier transform has to be applied to calculate $\Delta B_z(\mathbf{r})$.

The important advantage of this method is the fact that the Lorenz sphere effect is automatically considered. The results obtained for spherical and cylindrical objects have been consistent with analytic expression [28, 36]. Experiments using MR images of the brain and body as well as phantoms have also confirmed the accuracy of this approach [39, 40]. This Fourier-based method was used across this thesis to generate 3D susceptibility maps based on the T_2-*w FLASH images. The same approach was also applied to calculate magnetic field variations due to the susceptibility inclusions in the simulations presented in Chapter 3.

2.4 Summary

This chapter introduced the theoretical basis of the NMR phenomenon and its applications for acquiring MR images reflecting tissue properties. The following chapters will present simulations using presented theory and experiments applying described methods to study human brain.

References

[1] A. Baert, M. Knauth, and K. Sartor, *Parallel Imaging in Clinical MR Applications*, Springer, 2007.

[2] M. A. Bernstein, K. F. King, and X. J. Zhou, *Handbook of MRI Pulse Sequences*, Elsevier Academic Press, 2004.

[3] R. Bowtell and P. Mansfield, *Gradient coil design using active magnetic screening.*, Magnetic Resonance in Medicine, 17 (1991), pp. 15–19.

[4] R. B. Buxton, *Introduction to Functional Magnetic Resonance Imaging. Principles and Techniques*, Cambridge University Press, Cambridge, UK, 2nd ed., 2009.

[5] D. Feinberg, J. Hale, J. Watts, L. Kaufman, and A. Mark, *Halving MR imaging time by conjugation: demonstration at 3.5 kG*, Radiology, 161 (1986), pp. 527–31.

[6] P. M. Glover, *Interaction of MRI field gradients with the human body.*, Physics in Medicine and Biology, 54 (2009), pp. R99–R115.

[7] P. M. Glover and R. Bowtell, *Measurement of electric fields induced in a human subject due to natural movements in static magnetic fields or exposure to alternating magnetic field gradients.*, Physics in Medicine and Biology, 53 (2008), pp. 361–73.

[8] P. M. Glover, I. Cavin, W. Qian, R. Bowtell, and P. A. Gowland, *Magnetic-Field-Induced Vertigo: A Theoreticaland Experimental Investigation*, Bioelectromagnetics, 28 (2007), pp. 349–361.

[9] P. A. Gowland and M. O. Leach, *A simple method for the restoration of signal polarity in multi-image inversion recovery sequences for measuring T1*, Magnetic Resonance in Medicine, 18 (1991), pp. 224–31.

[10] J. Grad and R. G. Bryant, *Nuclear magnetic cross-relaxation spectroscopy*, Journal of Magnetic Resonance (1969), 90 (1990), pp. 1–8.

[11] E. M. Haacke, R. W. Brown, M. R. Thompson, and R. Venkatesan, *Magnetic Resonance Imaging. Physical Principles and Sequence Design*, John Wiley & Sons Ltd, Totowa, NJ, 1999.

[12] E. M. Haacke, Y. Xu, Y.-C. N. Cheng, and J. R. Reichenbach, *Susceptibility weighted imaging (SWI).*, Magnetic Resonance in Medicine, 52 (2004), pp. 612–8.

[13] A. Haase, *Snapshot FLASH MRI. Applications to T1, T2 and Chemical-Shift Imaging*, Magnetic Resonance in Medicine, 13 (1990), pp. 77–89.

[14] A. Haase, J. Frahm, D. Matthaei, W. Hänicke, and K.-D. Merboldt, *FLASH imaging: rapid NMR imaging using low flip-angle pulses*, Journal of Magnetic Resonance, 67 (1986), pp. 258–266.

[15] E. L. Hahn, *Spin Echoes*, Physical Review, 80 (1950), pp. 580–602.

[16] R. H. Hashemi, W. G. Bradley, and C. J. Lisanti, *MRI: The Basics*, Lippincott Williams & Wilkins, 2nd ed.

[17] R. M. Henkelman, G. J. Stanisz, and S. J. Graham, *Magnetization transfer in MRI: a review*, NMR in Biomdicine, 14 (2001), pp. 57–64.

[18] M. A. Horsfield, *Magnetization transfer imaging in multiple sclerosis.*, Journal of Neuroimaging, 15 (2005), pp. 58S–67S.

[19] T. Jin, P. Wang, X. Zong, and S.-G. Kim, *MR imaging of the amide-proton transfer effect and the pH-insensitive nuclear overhauser effect at 9.4 T.*, Magnetic Resonance in Medicine, 69 (2013), pp. 760–70.

[20] R. Kaiser, *Intermolecular Nuclear Overhauser Effect in Liquid Solutions*, The Journal of Chemical Physics, 42 (1965), p. 1838.

[21] V. Kuperman, *Magnetic Resonance Imaging. Physical Principles and Applications*, Academic Press, 2000.

[22] M. H. Levitt, *Spin Dynamics. Basics of Nuclear Magnetic Resonance*, John Wiley & Sons Ltd, 2nd ed., 2007.

[23] G. Liney, *MRI in Clinical Practice*, Springer-Verlag, London, 2006.

[24] G. Liu, G. Sobering, J. Duyn, and C. T. W. Moonen, *A Functional MRI Technique Combining Principles of Echo-Shifting with a Train of Observations (PRESTO)*, Magnetic Resonance in Medicine, 30 (1993), pp. 764–8.

[25] S. Ljunggren, *A Simple Graphical Representation of Fourier-Based Imaging Methods*, Journal of Magnetic Resonance, 54 (1983), pp. 338–343.

[26] P. Mansfield, *Multi-planar image formation using NMR spin echoes*, J Phys C: Solid State Phys, 10 (1977), pp. 55–58.

[27] P. Mansfield and I. L. Pykett, *Biological and medical imaging by NMR*, Journal of Magnetic Resonance, 29 (1978), pp. 355–373.

[28] J. Marques and R. Bowtell, *Application of a Fourier-based method for rapid calculation of field inhomogeneity due to spatial variation of magnetic susceptibility*, Concepts in Magnetic Resonance, 25B (2005), pp. 65–78.

[29] D. W. McRobbie, E. A. Moore, and M. J. G. nd Martin R. Prince, *MRI from picture to proton*, Cambridge, UK, 2006.

[30] O. E. MOUGIN, R. C. COXON, A. PITOIT, AND P. A. GOWLAND, *Magnetization transfer phenomenon in the human brain t 7T*, NeuroImage, 49 (2010), pp. 272–281.

[31] J. P. MUGLER AND J. R. BROOKEMAN, *Three-dimensional magnetization-prepared rapid gradient-echo imaging (3D MP RAGE).*, Magnetic Resonance in Medicine, 15 (1990), pp. 152–7.

[32] A. M. PETERS, M. J. BROOKES, F. G. HOOGENRAAD, P. A. GOWLAND, S. T. FRANCIS, P. G. MORRIS, AND R. BOWTELL, *T2* measurements in human brain at 1.5, 3 and 7 T.*, Magnetic Resonance Imaging, 25 (2007), pp. 748–53.

[33] P. V. PRASAD, ed., *Magnetic Resonance Imaging. Methods and Biologic Applications*, Humana Press, Totowa, NJ, 2006.

[34] K. P. PRUESSMANN, M. WEIGER, M. B. SCHEIDEGGER, AND P. BOESIGER, *SENSE: sensitivity encoding for fast MRI.*, Magnetic Resonance in Medicine, 42 (1999), pp. 952–62.

[35] W. D. ROONEY, G. JOHNSON, X. LI, E. R. COHEN, S.-G. KIM, K. UGURBIL, AND C. S. SPRINGER, *Magnetic Field and Tissue Dependencies of Human Brain Longitudinal ^1H_2O Relaxation in Vivo*, Magnetic Resonance in Medicine, 57 (2007), pp. 308–18.

[36] A. SCHÄFER, S. WHARTON, P. GOWLAND, AND R. BOWTELL, *Using magnetic field simulation to study susceptibility-related phase contrast in gradient echo MRI*, NeuroImage, 48 (2009), pp. 126–137.

[37] P. TOFTS, ed., *Quantitative MRI of the brain: Measuring Changes Caused by Disease.*, John Wiley & Sons Ltd, West Sussex, UK, 2003.

[38] P. C. M. VAN ZIJL AND N. N. YADAV, *Chemical exchange saturation transfer (CEST): what is in a name and what isn't?*, Magnetic Resonance in Medicine, 65 (2011), pp. 927–48.

[39] S. Wharton and R. Bowtell, *Whole-brain susceptibility mapping at high field: a comparison of multiple- and single-orientation methods.*, NeuroImage, 53 (2010), pp. 515–25.

[40] S. Wharton, A. Schäfer, and R. Bowtell, *Susceptibility Mapping in the Human Brain Using Threshold-Based k-Space Division*, Magnetic Resonance in Medicine, 63 (2010), pp. 1292–1304.

[41] M. J. Wilhelm, H. H. Ong, S. L. Wehrli, C. Li, P.-H. Tsai, D. B. Hackney, and F. W. Wehrli, *Direct magnetic resonance detection of myelin and prospects for quantitative imaging of myelin density.*, PNAS, 109 (2012), pp. 9605–10.

[42] S. D. Wolff and R. S. Balaban, *Magnetization transfer contrast (MTC) and tissue water proton relaxation in vivo.*, Magnetic Resonance in Medicine, 10 (1989), pp. 135–44.

[43] P. J. Wright, O. E. Mougin, J. J. Totman, A. M. Peters, M. J. Brookes, R. Coxon, P. E. Morris, M. Clemence, S. T. Francis, R. W. Bowtell, and P. A. Gowland, *Water proton T1 measurements in brain tissue at 7, 3, and 1.5T using IR-EPI, IR-TSE, and MPRAGE: results and optimization*, Magnetic Resonance Mater Phy, 21 (2008), pp. 121–130.

[44] V. L. Yarnykh, *Actual flip-angle imaging in the pulsed steady state: a method for rapid three-dimensional mapping of the transmitted radiofrequency field.*, Magnetic Resonance in Medicine, 57 (2007), pp. 192–200.

3

MR SIGNAL SIMULATIONS FOR
ORIENTED SUSCEPTIBILITY
INCLUSIONS

The aim of the simulations was to investigate changes of the NMR signal due to the presence of inclusions of different magnetic susceptibility (introduced in Section 2.3.5) compared to the background substance. Inclusions of ellipsoidal shape, all oriented in the same direction, were used to model microscopic biological objects present in tissue of the human brain. Spherical perturbers could correspond to iron particles or proteins carrying iron, oblate ellipsoidal perturbers to the red blood cells and prolate ellipsoidal perturbers for example to iron-rich oligodendrocytes.

Involvement of iron in the physiology of healthy and diseased brain (eg. in Parkinson's disease) is not yet fully understood and oligodendrocytes contribute to myelin creation, crucial for demyelination diseases (eg. multiple sclerosis). Therefore understanding the signal variations due to the susceptibility inclusions affecting empirical measurements of the T_2^* relaxation rate and phase evolution can be helpful for better understanding the origins of the contrast in gradient echo images of healthy and diseased brain.

Previous phase imaging studies [3] suggested, that the presence of NMR invisible microstructural features does not necessarily affect the phase of the NMR signal in a way that reflects the volume average susceptibility. Motivated by these findings, the current study investigated the effects of oriented inclusions which generate no signal.

The aim of the simulations was to investigate the phase and magnitude of the signal produced by samples containing oriented ellipsoidal perturbers, in order to understand how phase relates to average susceptibility in microstructured material containing NMR invisible oriented inclusions.

3.1 THEORY

The effects of inhomogeneities in the magnetic field generated by susceptibility differences between substances are characterised as static, if diffusion effects (related to molecular motion) are not considered. To investigate the signal behaviour in this case, two-component models containing objects immersed in a medium of different susceptibility are often used [4, 5, 8].

3.1.1 FIELD PERTURBATION DUE TO SPHERE

As an illustration of the effect of a susceptibility inclusion, the case of a sphere was first considered. Assume a spherical object of constant magnetic susceptibility, χ, is placed in a z-directed magnetic field B_0 and centred at the origin. If $\mathbf{B}_{out} \rightarrow \mathbf{B}_0$ far

from the sphere and the field is finite at the origin, the magnetic field at position $\mathbf{r}$ inside the sphere can be expressed as:

$$\mathbf{B}_{in}(\mathbf{r}) = 3B_0 \frac{1+\chi}{3+\chi}\hat{\mathbf{z}}, \tag{3.1}$$

where $\hat{\mathbf{z}}$ is a unit vector in the z-direction. Outside the sphere, the field in the z-direction is a sum of the B_0 component and a dipole field:

$$\mathbf{B}_{out}(\mathbf{r}) = B_0\hat{\mathbf{z}} + B_0 \frac{\chi}{3+\chi} \left(\frac{a}{r}\right)^3 (3\cos\theta\hat{\mathbf{r}} - \hat{\mathbf{z}}), \tag{3.2}$$

where a is the radius of the sphere, (θ, r) are spherical polar coordinates of the considered positions and $\hat{\mathbf{r}}$ is a radial unit vector [2]. The change in the magnetic field in the z-direction caused by the presence of the sphere of different susceptibility can be then calculated as:

$$\Delta B_{in} = \frac{2\chi}{3+\chi} B_0 \tag{3.3}$$

$$\Delta B_{out} = \frac{\chi}{3+\chi} \left(\frac{a}{r}\right)^3 (3\cos^2\theta - 1) B_0 \tag{3.4}$$

In reality, the susceptibility inside an object is not constant at the macroscopic scale and interactions between spins cause a vanishing of microscopic susceptibility effects, which is known as the Lorentz sphere phenomenon [1]. After taking into account this fact, and assuming that the sphere is now embedded in a medium of susceptibility, χ_e, such that $\Delta\chi = \chi - \chi_e$, the changes in the effective magnetic field seen by the nuclear magnetization inside and outside the sphere are defined as:

$$\Delta B_{in} = \frac{1}{3}\chi_e B_0 \tag{3.5}$$

$$\Delta B_{out} = \frac{\Delta\chi}{3} \left(\frac{a}{r}\right)^3 (3\cos^2\theta - 1) B_0 + \frac{1}{3}\chi_e B_0. \tag{3.6}$$

54

This indicates that the perturber generates a spatially varying external field, while a uniform field offset may be present inside the perturber.

3.1.2 SIGNAL CALCULATION

For N objects of total volume v embedded in a medium of volume V_0, the relative volume fraction is defined as $\varsigma = \dfrac{v}{V}$, where $V = V_0 + v$. If the volume fraction is very small, the signal can be calculated (ignoring contributions from the inside of the objects) as:

$$S(t) = \frac{\rho}{V} \int_{V_0} e^{-i\omega(\mathbf{r})t} d\mathbf{r}, \tag{3.7}$$

where ρ is the coefficient representing parameters of the scan (spin density, flip angle, etc.). This calculation also holds in the case where the objects generate no NMR signal. Assuming that the results will be presented with respect to the frequency of the rotating frame $\omega_0 = \gamma B_0$ and the external magnetic field, B_0, is aligned with the z-axis, the frequency at position $\mathbf{r}$ can be written as follows:

$$\omega(\mathbf{r}) = \sum_n \omega_n(\mathbf{r} - \mathbf{r}_n) = \gamma \sum_n B_{zn}(\mathbf{r} - \mathbf{r}_n) = \gamma \Delta B_z(\mathbf{r}), \tag{3.8}$$

where $\mathbf{r}_n$ is the reference vector defining the position of the n-th object and $B_{zn}(\mathbf{r} - \mathbf{r}_n)$ is the z-component of the magnetic field created by the n-th object at point $\mathbf{r}$.

For a random distribution, in which the objects are not overlapping, the average signal can be calculated using the following formula:

$$\bar{S}(t) = \rho(1 - \varsigma) \prod_{n=1}^{N} \frac{1}{V - v_n} \int_{V-v_n} e^{-i\omega_n(\mathbf{r} - \mathbf{r}_n)t} d\mathbf{r} \tag{3.9}$$

where v_n is the volume of the n-th object. As the function $\omega_n(\mathbf{r} - \mathbf{r}_n)$ depends on the geometry of the object, further analytical derivation is performed for the example case of spherical objects. For the simulations presented in the following sections, the method described in Section 2.3.5 was used instead of the analytic

$\Delta B_z(\mathbf{r})$ calculation.

3.1.3 Signal behaviour due to spheres

For the n-th sphere of radius a_n, the frequency can be calculated according to the following formula:

$$\omega_n(\mathbf{r} - \mathbf{r}_n) = \delta\omega_s \left(\frac{a_n}{r}\right)^3 \left(3\cos^2\theta - 1\right), \tag{3.10}$$

where $r = |\mathbf{r} - \mathbf{r}_n|$, θ is the angle between the z-component of the external magnetic field and the vector $\mathbf{r} - \mathbf{r}_n$. The characteristic frequency shift for the sphere is defined as:

$$\delta\omega_s = \frac{\gamma\Delta\chi B_0}{3}, \tag{3.11}$$

where $\Delta\chi$ represents the susceptibility difference between the sphere and the medium.

Calculations of the average signal presented in [8] showed that the signal is dependent on the volume fraction of perturbers, but not on the particular size distribution of the objects. For the short time limit $t\delta\omega_s \leq 1.5$ the signal is a quadratic exponentially decaying function:

$$\bar{S}(t) = \rho(1 - \varsigma)e^{-0.4\varsigma(t\delta\omega_s)^2} \tag{3.12}$$

and for the long time $t\delta\omega_s \geq 1.5$ is described as an exponential function with an oscillating part:

$$\bar{S}(t) = \rho(1 - \varsigma)e^{-i\Delta\omega_s t}e^{R2'_s|t-t_s|}, \tag{3.13}$$

where the shift from the reference frequency $\Delta\omega_s = c\varsigma\delta\omega_s$, where $c = -0.15977$,

$$t_s = \left(\frac{2\pi}{3\sqrt{3}}\delta\omega_s\right)^{-1}$$

and

$$R2'_s = \frac{2\pi}{3\sqrt{3}}\varsigma\delta\omega_s.$$

3.1.4 SIGNAL BEHAVIOUR DUE TO ELLIPSOIDS

The field perturbations produced by ellipsoidal perturbers are more difficult to calculate analytically [4], hence the use of a numerical approach for evaluating field perturbations. However some insight can be gained by considering the field offsets produced inside an ellipsoidal perturber, often known as the demagnetizing field. The dependence of the demagnetizing field on the shape of an ellipsoidal perturber can be described using a demagnetizing factor [6], which for an ellipsoid formed by revolution about the z-axis ($a = b$, $c = qa$) are defined as $D_{xe} = D_{ye} = (1 - D_{ze})/2$ and:

$$D_{ze}(q) = \frac{qln(q + \sqrt{q^2 - 1})}{(q^2 - 1)^{3/2}} - \frac{1}{q^2 - 1}, \qquad (3.14)$$

where the subscripts x, y or z indicates the direction of the applied field relative to the ellipsoid. For randomly distributed and randomly oriented ellipsoids of revolution the signal has been shown to follow a quadratic exponential decay in the short time regime ($t\delta\omega_s \ll 1$) and a linear exponential function in the long time regime ($t\delta\omega_s \gg 1$) [4].

3.2 METHODS

3.2.1 ONE PERTURBER

The simulations were first run using one perturber, separately for two ellipsoids of revolution with aspect ratios of 1:1:2 and 1:1:4, and for a sphere. The object was placed in the centre of the space, in the external magnetic field, with the longest dimension parallel to the field direction. The maximum dimension of each object was set equal to 100 voxels and the overall space was a cube of 500^3 voxels. The external magnetic field was set to a value of 7T and the magnetic susceptibility difference between the object and the surrounding medium had a value of 10^{-7}. The Fourier method described in Section 2.3.5 was used to calculate the magnetic field shifts. The complex signal was calculated in each voxel, excluding the inside of

57

the object, for TE values in the range of 1-100 milliseconds. A separate simulation was performed to examine the influence of the volume fraction (object's size relative to the total space considered) on the signal.

3.2.2 MULTIPLE PERTURBERS

The magnetic field perturbation due to the susceptibility distribution was calculated using the Fourier method described in Section 2.3.5. Simulations were run for randomly positioned inclusions consisting of ellipsoids of revolution with different aspect ratios (a:b:c), as illustrated in Figure 3.2.1, ranging from 1:1:6=*needles* to 1:1:1=*spheres* to 6:6:1=*pancakes.*
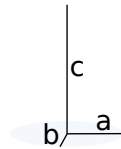
Figure 3.2.1: Illustration of the ellipsoid aspect ratio a:b:c.

Three sizes of ellipsoid were included in each case (small, medium, large), and the volume fraction ($VF = \varsigma$) of the inclusions was varied from 1-5%. Small volume fractions allowed the comparison of the simulated results with previously presented data [8] and had and additional advantage of simplifying the simulations. All of the ellipsoids had the same orientation such that axis of revolution was parallel to the field. The dimensions, sizes and volumes of the ellipsoids are summarised in Table 3.2.1; average numbers of perturbers for each volume fraction and for each variant of the perturber's dimension ratio are shown in Table 3.2.2.

	small		medium		large	
a:b:c	size	volume	size	volume	size	volume
1:1:6	$6 \times 6 \times 36$	5429	$7 \times 7 \times 42$	8621	$8 \times 8 \times 48$	12868
1:1:5	$6 \times 6 \times 30$	4524	$7 \times 7 \times 35$	7184	$8 \times 8 \times 40$	10723
1:1:4	$7 \times 7 \times 28$	5685	$8 \times 8 \times 32$	8453	$9 \times 9 \times 36$	12173
1:1:3	$8 \times 8 \times 24$	6434	$9 \times 9 \times 27$	9161	$10 \times 10 \times 30$	12566
1:1:2	$9 \times 9 \times 18$	6089	$10 \times 10 \times 20$	8309	$11 \times 11 \times 22$	11117
1:1:1	$11 \times 11 \times 11$	5575	$13 \times 13 \times 13$	9171	$14 \times 14 \times 14$	11513
2:2:1	$14 \times 14 \times 7$	5747	$16 \times 16 \times 8$	8578	$18 \times 18 \times 9$	12215
3:3:1	$15 \times 15 \times 5$	4712	$18 \times 18 \times 6$	8143	$21 \times 21 \times 7$	12931
4:4:1	$16 \times 16 \times 4$	4289	$20 \times 20 \times 5$	8378	$24 \times 24 \times 6$	14476
5:5:1	$15 \times 15 \times 3$	2827	$20 \times 20 \times 4$	6702	$25 \times 25 \times 5$	13090
6:6:1	$12 \times 12 \times 2$	1206	$18 \times 18 \times 3$	4071	$24 \times 24 \times 4$	9651

Table 3.2.1: Summary of the sizes and volumes of the perturbers of different dimensions and ratios, measured as a number of voxels.

vf	1:1:6	1:1:5	1:1:4	1:1:3	1:1:2	1:1:1	2:2:1	3:3:1	4:4:1	5:5:1	6:6:1
1%	141	174	146	138	150	97	144	148	138	164	292
2%	294	350	284	272	303	187	280	303	294	354	592
3%	430	570	423	404	444	281	438	450	432	540	854
4%	567	693	592	540	606	384	586	609	603	710	1150
5%	704	873	722	690	740	472	734	762	766	924	1485

Table 3.2.2: Average (N=5) number of perturbers for the particular volume fraction and perturber's dimension ratio.

Inclusions were placed at random positions inside a larger cylindrical region, not crossing the external boundaries and not overlapping with each other (for details regarding the overlapping condition see Appendix 1). An external shape corresponding to an infinite cylinder was chosen to avoid an otherwise necessary correction of the average phase [3]. The choice of external shape affects only the average frequency offset and in the case of dilute perturbers does not have a significant effect on the evolution of the signal magnitude. The size of the simulation space was 500^3 voxels and the external cylinder's radius was equal 230 voxels. Each ellipsoid's axis of revolution was aligned with the applied magnetic field (B_0=7T) and a susceptibility difference, χ, between the inclusions and the matrix of 0.1ppm was used, yielding a value of $\alpha = \gamma \chi B_0$ of $187s^{-1}$. The axis of the external cylinder was also aligned with the field direction. The complex MR signal from the whole region, ignoring contributions from inside the ellipsoids, was calculated for TE values in the range of 1-100ms. The variations of the phase and log of the signal magnitude

with TE were fitted using polynomials in two different time ranges (0-25ms = short) and (75-100ms = long). Linear fitting was performed for the phase of the signal in both time ranges, and for the log of the magnitude, in the long time range only. The quadratic function was used for the log of the signal magnitude in the short time range, following previously presented theory [8]. The variation of the amplitudes of the resulting polynomial coefficients with the volume fraction and ellipsoid shape was then evaluated.

3.3 RESULTS

3.3.1 ONE PERTURBER

Figure 3.3.1 presents maps of the magnetic field shift calculated using the Fourier method, together with the masks of the perturbers used. Inside the sphere and ellipsoids the field offset is uniform, outside a characteristic dipole-like field appears. With increasing aspect ratio, the regions of positive field shift above and below the ellipsoid are reduced in extent.
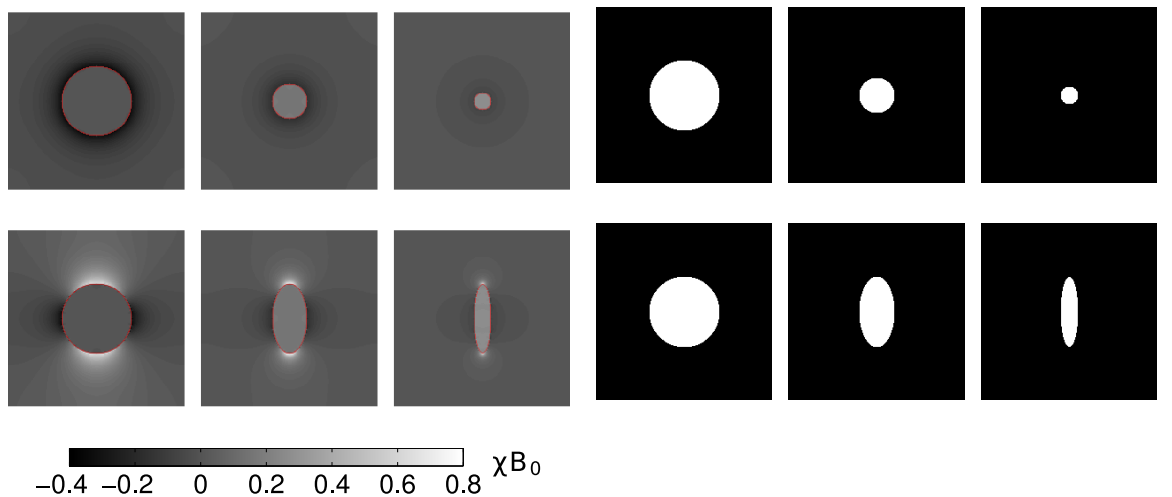
Figure 3.3.1: Magnetic field shift due to the susceptibility difference for a sphere and ellipsoids, in central x-y (top) and x-z (bottom) plane with overlaid outlines of the perturbers in transparent-red (left); masks of the corresponding perturbers (right).

Figure 3.3.2 presents maps of phase of the signal obtained for $TE = 100ms$ shown in central x-y and x-z planes with the outlines of the ellipsoidal perturbers indicated

in red. Phase wrapping occurs in the regions of large field variation.
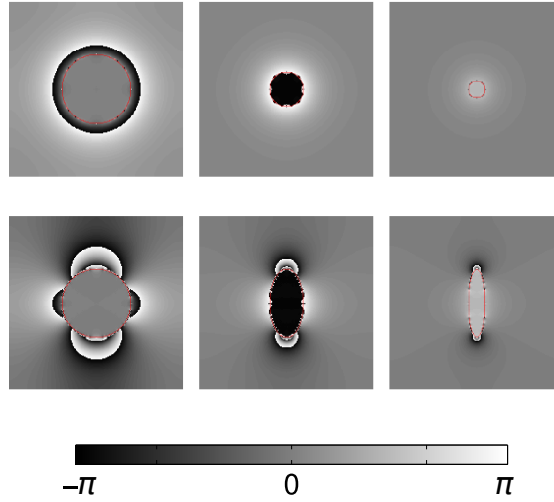
Figure 3.3.2: The map of phase (radians) of the signal obtained for $T_E = 100ms$, x-y (top) and x-z (bottom) plane.

The variation of the total signal as a function of TE is presented in the plots in Figure 3.3.3. Loss of the signal increases with TE due to increased dephasing and is fasterst for the sphere. At short TEs the phase averages to zero for the sphere.
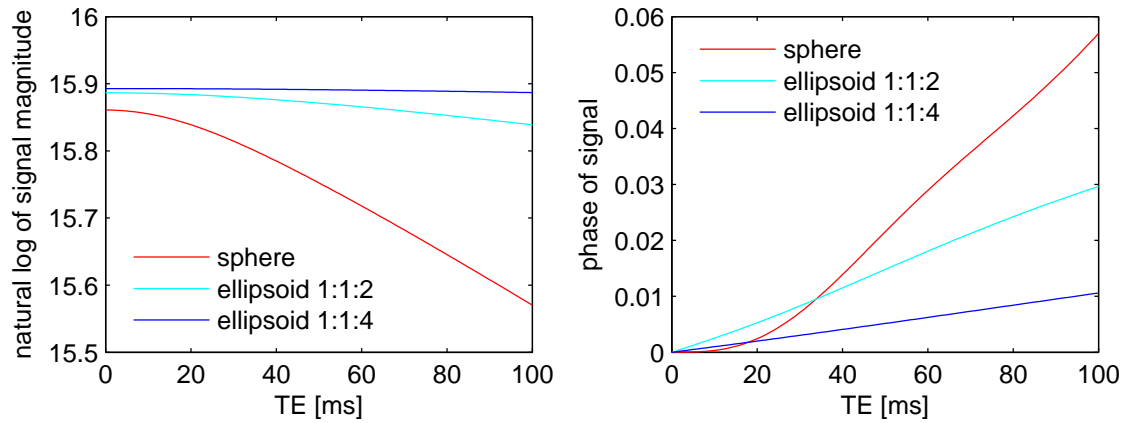
Figure 3.3.3: Magnitude (left) and phase (right) of the total signal from a cube surrounding sphere and two ellipsoids of different sizes as a function of TE .

Figure 3.3.4 shows the results calculated for spheres of different sizes (volume fractions), indicating that the signal loss and phase accumulated at long TE both increase with increasing volume fraction.

61
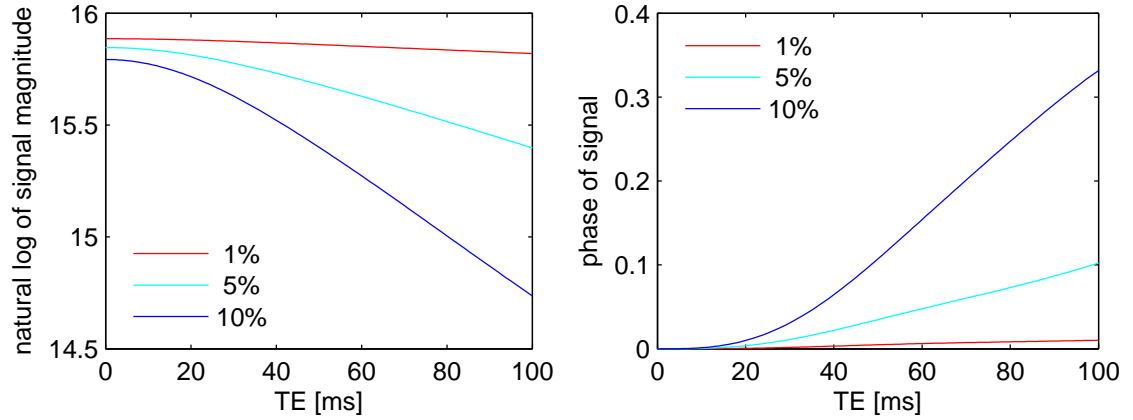
Figure 3.3.4: Magnitude (left) and phase (right) of the total signal calculated from a cube surrounding a single sphere for different volume fractions (1, 5, 10%); volume fraction changes were produced by increasing the size of the sphere.

3.3.2 MULTIPLE PERTURBERS

Figure 3.3.5 shows a cross section through the structure in the cylindrical region and the resulting field perturbation for ellipsoids of aspect ratio of 1:1:3 and volume fraction 3%.
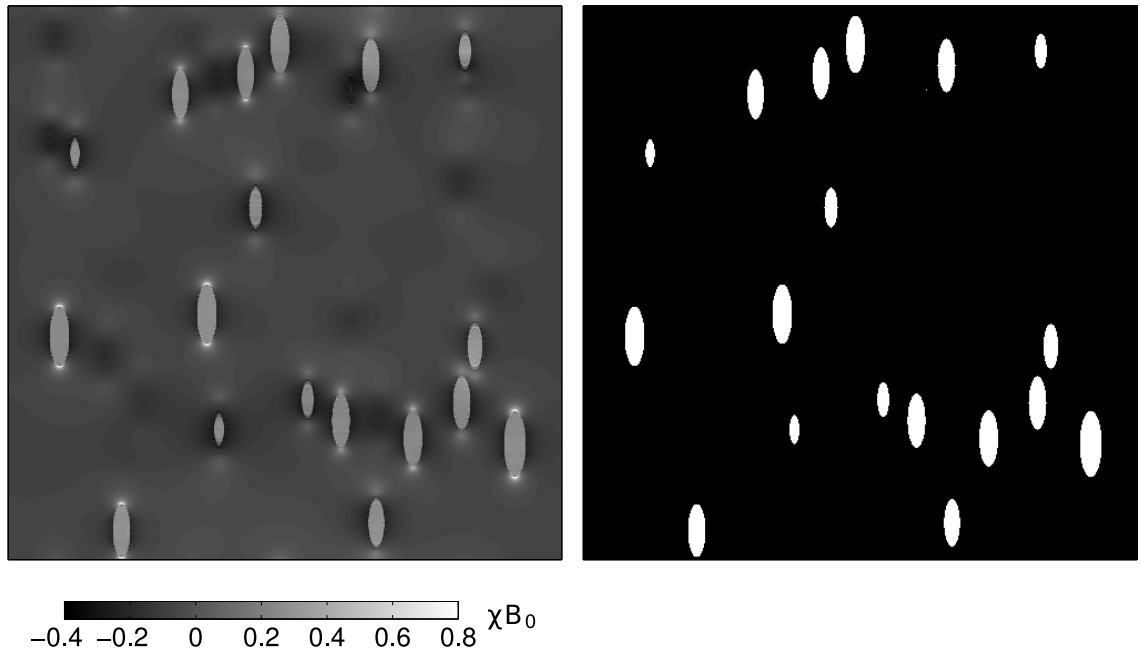
Figure 3.3.5: Coronal slice through field perturbation (left) and susceptibility distribution (right) for ellipsoids with an aspect ratio of 1:1:3 and a volume fraction of 3%.

Figure 3.3.6 presents a coronal slice of the map of phase of the signal obtained for $TE = 100ms$.
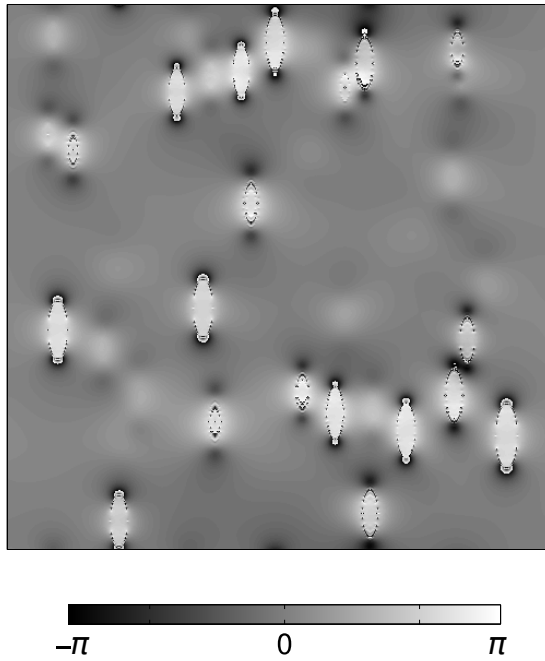
Figure 3.3.6: The map of phase of the signal obtained for $T_E = 100ms$, in a coronal slice.

Example plots of the log of the magnitude and of the phase of the signal (along with the polynomial fits in the two regimes) for χ=0.1ppm for spheres with volume fractions of 1, 3 and 5% are shown in Figure 3.3.7; similar plots for needles and pancakes with a volume fraction of 3% are presented in Figure 3.3.8.
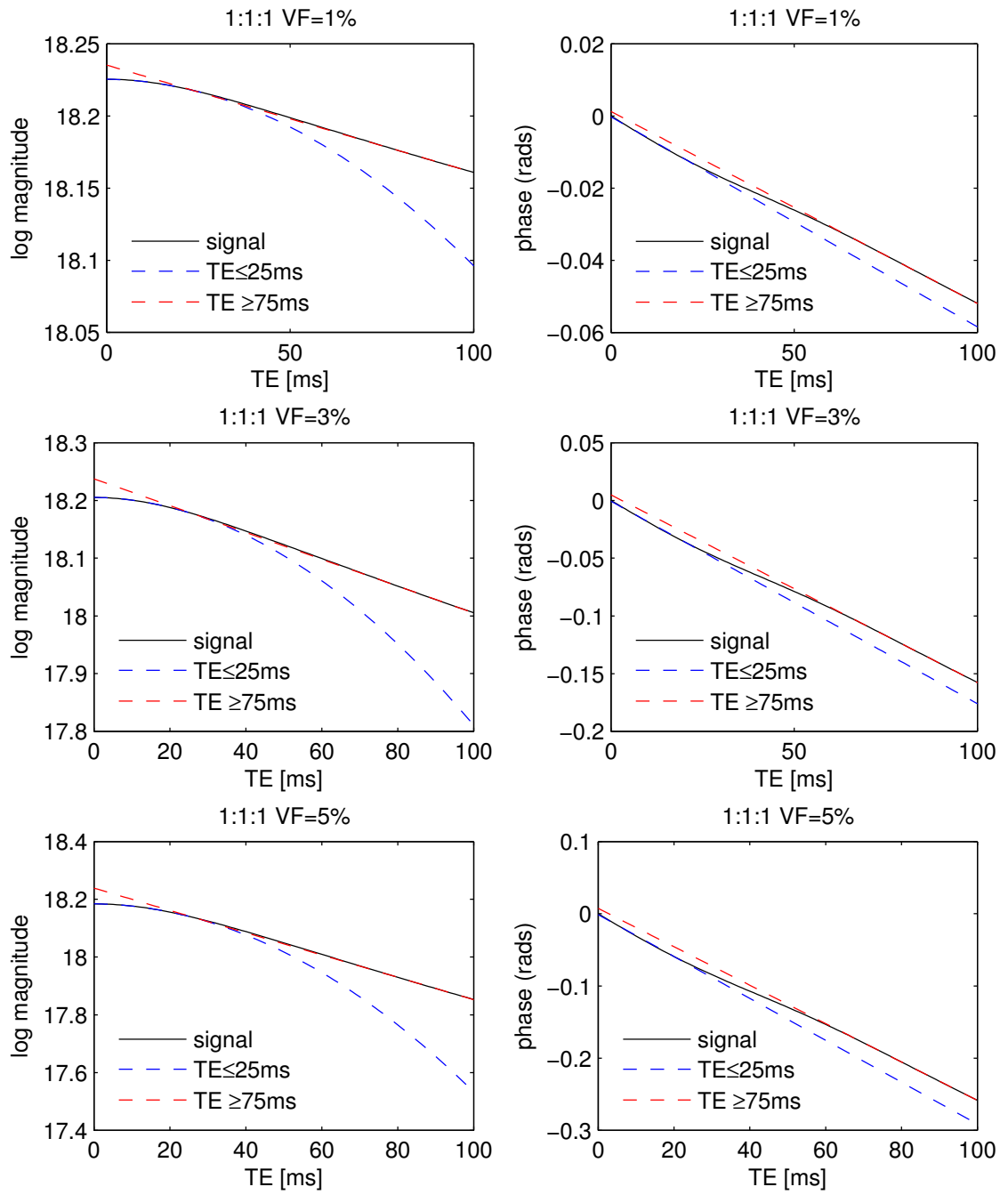
Figure 3.3.7: Signal magnitude (left) and phase (right) variation with TE for spheres with VF=1, 3, 5%. Polynomial fits are shown for the two regimes.
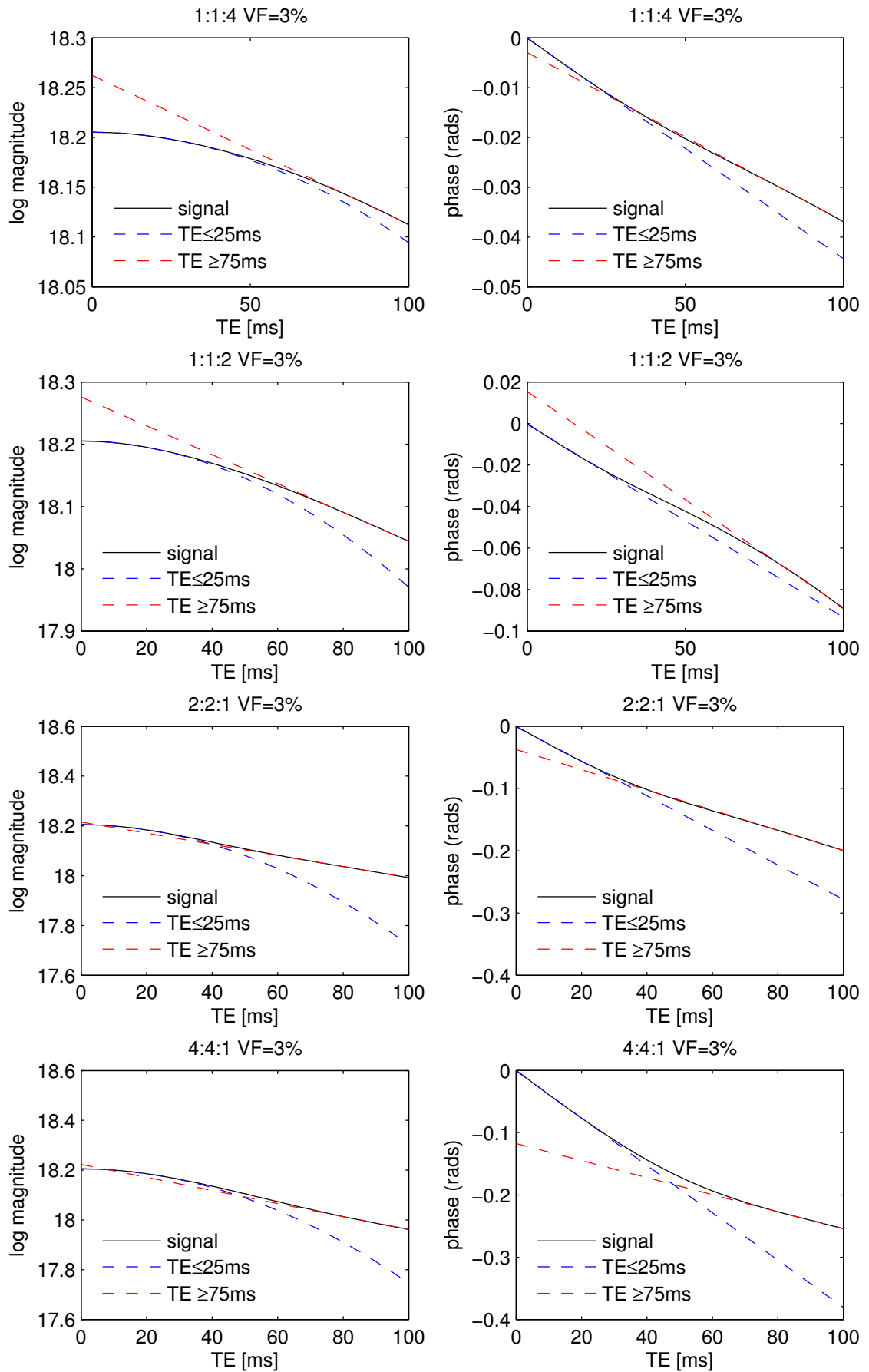
Figure 3.3.8: Signal magnitude (left) and phase (right) variation with TE for needles (1:1:2 and 1:1:4) and pancakes (2:2:1 and 4:4:1) with VF= 3%. Polynomial fits are shown for the two regimes.

In all cases the natural log of the signal magnitude varied quadratically with TE (proportional to: $\text{const} + a_2 TE^2$) in the short echo time regime and linearly with TE (proportional to: $\text{const} + b_1 TE$) in the long echo time case. The phase was found to vary linearly with TE in both regimes, but with different constants of proportionality (written as c_1 and d_1 in the short and long TE regimes, respectively). The dominant polynomial coefficients were found to scale linearly with volume fraction. Figure 3.3.9 shows the variation of $c_1/(\alpha \times VF)$ with the demagnetising factor of the ellipsoids (see Section 3.1).
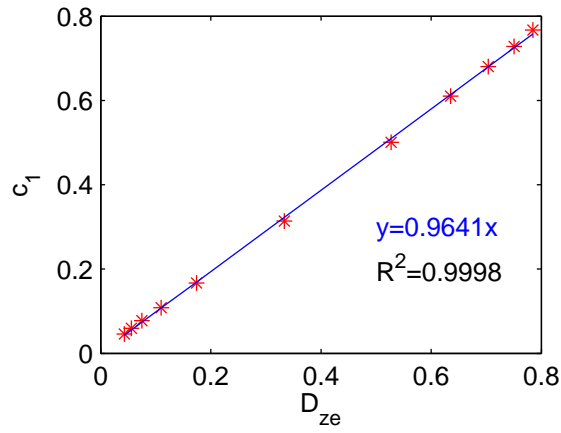
Figure 3.3.9: The variation of $c_1/(\alpha \times VF)$ with the demagnetising factor of the ellipsoids.

Figure 3.3.10 shows the variation with the ellipsoid aspect ratio, q, of the other coefficients in appropriately-scaled, dimensionless forms ($a_2/(\alpha^2 \times VF)$, $b_1/(\alpha \times VF)$ and $d_1/(\alpha \times VF)$).
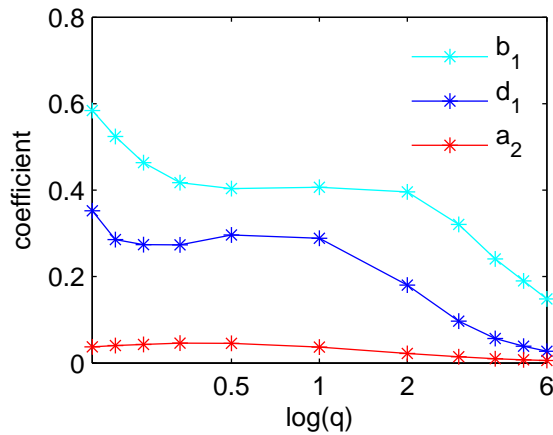
Figure 3.3.10: The variation with the ellipsoid aspect ratio, q, of the coefficients $a_2/(\alpha^2 \times VF)$, $b_1/(\alpha \times VF)$ and $d_1/(\alpha \times VF)$.

3.4 DISCUSSION

The findings presented in this chapter are in agreement with theory previously described for spherical, cylindrical [8] and ellipsoidal [4] inclusions. As reviewed in Section 3.1 the transition between the short and long time regimes occurs at $t\delta\omega_s \sim 1.5$. Therefore quadratic evolution of the natural logarithm of signal magnitude and linear evolution of signal phase were expected in the two different time ranges used for the polynomial fitting since for TE=25ms and 75ms $t\delta\omega_s$ is approximately equal to 1.56 and 4.68. Importantly, the results indicate that the measured phase scales linearly with echo time and volume fraction, even in the regime where the induced phase is $\gg 2\pi$ close to the oriented inclusions.

The linear variation of phase with D_{ze} in the short-TE regime presented in Figure 3.3.9 was previously predicted from simple analysis of the average field in the matrix [7]. These data indicate that at short TE the measured phase depends strongly on the shape of the ellipsoids and that pancakes have a larger effect than needles.

In Figure 3.3.10 the coefficient a_2, which characterises the variation of the signal magnitude at short TE, is largest when $q \sim 0.5$, indicating that slightly pancake-like ellipsoids oriented in the field direction have the strongest effect on signal decay in the short TE regime. This is in contrast to the case of randomly oriented ellipsoids for which it has been shown that spheres ($q = 1$) cause the fastest signal decay [4]. Figure 3.3.10 indicates that the coefficient, b_1, which characterises the rate of exponential decay of the signal at long TE is approximately constant for intermediate q-values (0.33 to 2) taking a value of $\sim 0.4\alpha VF$. This is the value predicted for a random arrangement of point dipoles with an equivalent volume average magnetic moment [8]. Similarly the coefficient, d_1, which describes the effective angular frequency offset at long TE takes a value of $\sim 0.28\alpha VF$ for intermediate q-values, again as predicted for point dipoles arranged in a cylindrical volume [8]. In this long-TE regime (TE=75-100 ms, intermediate q) the behaviour of the signal magnitude and phase is therefore largely independent of the shape

of the ellipsoids and reflects the average susceptibility. This behaviour can be understood by considering the variation of the signal contributions with distance from the centre of each ellipsoid. Rapid phase variation around a needle nulls the signal out to a radius that is approximately $\sqrt[3]{\alpha TE q^{-2} (2\pi)^{-1}}$, times the z-dimension of the ellipsoid (for pancakes q^{-2} is replaced with q). If this radius is larger than the extent of the ellipsoid then the region which generates a significant signal experiences a purely dipolar field and so the behaviour can be adequately described using a distribution of dipoles. For the maximum value of $\alpha TE \sim 18.7$ considered here, this condition is satisfied for $0.34 < q < 1.7$, as illustrated in Figure 3.4.1 (top row) for TE=100ms and 7 different ellipsoid aspect ratios. Additional simulations indicated that increasing αTE expands the range of q-values for which simple dipolar behaviour holds. Figure 3.4.1 shows the phase variation (middle and bottom row) for TE=100, 200 and 300ms.
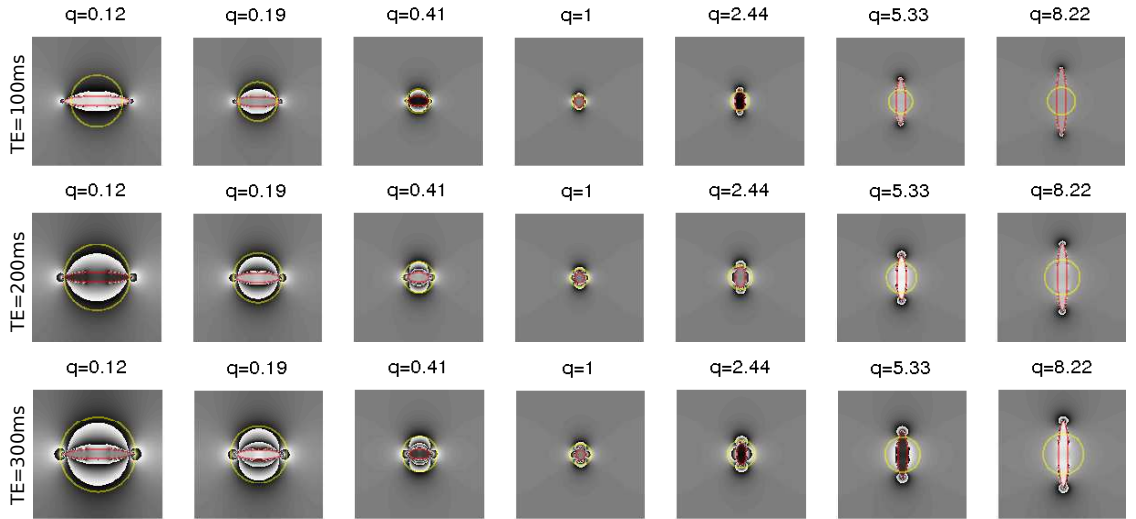
Figure 3.4.1: The map of phase of the signal obtained for ellipsoids of different aspect ratios (q values) in TE=100ms (top), TE=200ms (middle) and TE=300ms; outline of the perturber marked in red and radius of $\sqrt[3]{\alpha TE q^{-2} (2\pi)^{-1}}$ ($q > 1$) or $\sqrt[3]{\alpha TE q (2\pi)^{-1}}$ ($q < 1$) in yellow.

3.5   Conclusions

Numerical simulations of the NMR signal in the presence of ellipsoidal inclusions have provided insight into the effect of the shape and concentration of oriented, inclusions of high susceptibility, on the contrast in phase and T_2^*-weighted images.

The ellipsoidal perturbers used in the presented simulations can potentially correspond to various paramagnetic biological objects found in the human brain, such as red blood cells, iron particles and proteins carrying iron, or particulate contrast agents used in MRI. The signal simulations performed in this study may therefore improve our understanding of the T_2^*-w contrast and its dependence on the volume fraction, shape, size and distribution of these objects.

The importance of iron in the physiology of the healthy human brain and its role in the pathological processes underlying neurodegenerative diseases, such as Parkinson's disease and multiple sclerosis, are discussed in Chapter 4 of this thesis. The next two chapters of the thesis presents empirical studies of the properties of the tissue in healthy and diseased brain using MRI, with a special focus on iron content changes. The aim of the simulations presented in this chapter was to provide deeper understanding of how the images used to asses iron concentration may depend on the microscopic characteristics of the imaged iron stores. However, more work relating the simulated results to the experiments regarding microscopic structure of the tissue is required to take a full advantage of these findings.

References

[1] S. C. Chu, Y. Xu, J. a. Balschi, and C. S. Springer, *Bulk magnetic susceptibility shifts in NMR studies of compartmentalized samples: use of paramagnetic reagents.*, Magnetic Resonance in Medicine, 13 (1990), pp. 239–62.

[2] E. M. Haacke, R. W. Brown, M. R. Thompson, and R. Venkatesan, *Magnetic Resonance Imaging. Physical Principles and Sequence Design*, John Wiley & Sons Ltd, Totowa, NJ, 1999.

[3] X. He and D. a. Yablonskiy, *Biophysical mechanisms of phase contrast in gradient echo MRI.*, Proceedings of the National Academy of Sciences of the United States of America, 106 (2009), pp. 13558–63.

[4] A. L. SUKSTANSKII AND D. A. YABLONSKIY, *Theory of FID NMR signal dephasing induced by mesoscopic magnetic field inhomogeneities in biological systems.*, Journal of Magnetic Resonance, 151 (2001), pp. 107–17.

[5] A. L. SUKSTANSKII AND D. A. YABLONSKIY, *Gaussian approximation in the theory of MR signal formation in the presence of structure-specific magnetic field inhomogeneities. Effects of impermeable susceptibility inclusions.*, Journal of Magnetic Resonance, 167 (2004), pp. 56–67.

[6] R. ULRICH, R. W. GLASER, AND A. S. ULRICH, *Susceptibility corrections in solid state NMR experiments with oriented membrane samples . Part II : Theory*, Journal of Magnetic Resonance, 164 (2003), pp. 115–127.

[7] S. WHARTON, A. SCHÄFER, AND R. BOWTELL, *Susceptibility Mapping in the Human Brain Using Threshold-Based k-Space Division*, 63 (2010), pp. 1292–1304.

[8] D. A. YABLONSKIY AND M. E. HAACKE, *Theory of NMR Signal Behavior in Magnetically Inhomogeneous Tissues: The Static Dephasing Regime*, Magnetic Resonance in Medicine, 32 (1994), pp. 749–763.

4

ROLE OF IRON IN

NEURODEGENERATIVE DISEASES

Non-haeme iron present in the brain has been shown to play a role in the pathogenesis of various neurodegenerative diseases, such as Parkinson's disease (PD), Alzheimer's disease (AD), multiple sclerosis (MS), Huntington's disease (HD), Neuodegeneration with Brain Iron Accumulation Type 1 (formally known as Hallervorden-Spatz syndrome) and others. The exact role of iron in pathological processes and in normal physiology is not yet fully understood. Various reviews summarising the current state of knowledge with regards to the significance of iron in neurodegeneration [7, 36, 64] and use of MRI for iron imaging [28, 60] are available. Here, a brief summary regarding brain iron is presented, limited to the purpose of

this thesis, together with possible ways of measuring brain iron content post mortem (PM) and in vivo. A short discussion of the characteristic of PD and MS is given, including role of iron in these diseases.

4.1 BRAIN IRON

There are two subtypes of iron in the human body: haeme iron, which is found in haemoglobin providing tissues with oxygen, and in some enzymes, and non-haeme iron which plays an important role in many aspects of normal metabolism, being involved in myelination and neuro-transmission and as a co-factor for tyrosine hydroxylase (TH), an enzyme required for dopamine synthesis. About 60mg of non-haeme iron is present in the brain [30], in the form of free ions (Fe^{2+} and Fe^{3+}), as a part of low-weight molecular complexes or bound to proteins, of which the most important are transferrin and ferritin.

Transferrin, which can bind two Fe^{3+} ions, is responsible for transporting iron from blood to the brain tissue. Ferritin is a storage protein able to carry within its core up to 4500 Fe^{3+} ions in the form of ferrihydrite ($5Fe_2O_3 \cdot 9H_2O$). Storage of ferrous Fe^{2+} iron requires oxidation to the ferric Fe^{3+} form and is not only important for metabolic processes, but also plays protective role to prevent iron toxicity, as described below. Ferritin's protein shell can contain different proportions of two components: light (L)-chain and heavy (H)-chain ferritin; L-rich ferritin is associated with long term iron storage and H-rich ferritin is present in organs which utilise iron [57]. An additional iron storage protein, hemosiderin is considered to be a degeneration product of ferritin, the occurrence of which is connected to hemorrhage and iron overload diseases.

Neuromelanin (NM), a complex molecular structure forming the dark pigment present in the substantia nigra and locus coeruleus of the human brain, which also contains iron [16, 71]. NM binds ferric iron and is generally not fully loaded in vivo [16]. Iron is also involved in NM creation [71]. Binding of iron to NM may play a protective role, but may also increase the risk of oxidative damage within the

dopaminergic neurons in case of increased iron content, for example in PD [24]. Iron accumulation within the NM cells has been shown to increase in PD [24], however the amount of NM has been shown to decrease in PD and to increase in normal ageing [70].

Free ferrous iron can lead to the creation of highly reactive hydroxyl radicals ($OH^{\bullet}$) via the Fenton reaction (4.1):

$$Fe^{2+} + H_2O_2 \longrightarrow Fe^{3+} + OH^- + OH^{\bullet}. \tag{4.1}$$
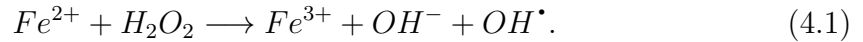
Moreover, Fe^{3+} can be reduced via the Harber-Weiss reaction (4.2):

$$Fe^{3+} + O_2^{\bullet -} \longrightarrow Fe^{2+} + O_2, \tag{4.2}$$
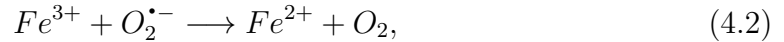
affecting redox cycling of iron [35]. Free iron is therefore considered to be highly toxic, leading to the oxidative stress, which causes damage and death of the cells [21].

Iron in the human brain is distributed non-uniformly with the highest concentration found in the basal ganglia (for detailed review see [28]) and has been shown to accumulate with age [31]. Increased iron levels were found in various neurodegenerative diseases [21], for further description regarding PD and MS see the following sections of this chapter.

4.2 IMAGING OF BRAIN IRON

The method most commonly used to study regional iron content in PM tissue involves the use of Perls' stain [54]. This stain is claimed to be sensitive to local concentration of ferric ions, however recent studies showed that in fact Perls' is not specific to the iron oxidation state, as the chemical compounds used for staining also react with Fe^{2+} [47]. This method has some disadvantages; first, staining depends on the way iron is bound and not all the iron is stained (iron bound in NM remains

unstained). Tissue fixation causes additional problems, depending on the pH of the formalin, loosely bound iron can be released from ferritin and hemosiderin [47], which leads to iron leaching [20, 61]. Alternative methods for investigating iron content in PM tissue include microscopic experiments using frozen, unfixed tissue [51], Mössbauer spectroscopy [19] or high energy X-ray absorption spectroscopy [27]. Iron content in vivo can also be studied using MRI. Of the different forms of non-haeme iron only ferritin and hemosiderin are visible in MRI due to their high concentrations [59]. Iron present in tissue as a magnetic material reduces T_2 and, to smaller extent, T_1 relaxation times and therefore appears hypointense in T_2-w and hyperintense in T_1-w images [28]. Strong linear correlation of $R_2 = 1/T_2$ with iron concentration has been found in healthy grey matter as well as linear dependence of iron related R_2 on magnetic field strength [22, 58, 67]. However other factors, such as decreased water content reduces the amount of free water and hence shortens T_2 and lead to potential mis-interpretation of the results [28]. Other studies suggested that R_2' related to local field inhomogeneities reflects iron content better than R_2 [22, 53], but its values are relatively small and therefore difficult to measure accurately. Instead T_2^* maps can be used, which contain a T_2' contribution as $T_2^*=1/R_2^*=1/R_2+1/R_2'$, such maps have been shown to have higher sensitivity to iron concentration than T_2, both post mortem [39] and in vivo [65]. T_2' and in consequence also T_2^* measurements may be affected by the background field inhomogeneity and require correction for such effects [53].

It has also been shown in previous work that phase shifts in GE images correlate with iron concentrations derived from the literature [52]. However phase shifts have a non local correspondence to the underlying susceptibility distribution. A new way of visualising iron content by combining phase and magnitude data to estimate susceptibility values has been proposed, called susceptibility weighted imaging (SWI) [30]. More recently Fourier-based methods using phase data for accurate quantitative susceptibility mapping have also been developed [43, 63, 69] giving results that correlated well with iron content [44, 62, 63, 68].

Ferritin and haemosderrin were first considered to cause MR relaxation by the outer sphere mechanism: de-phasing of the spins of the diffusing water due to the proximity of the aggregate of magnetic atoms kept away from water (iron within the protein shell). However this model did not explain the linear magnetic field strength dependence of the transverse relaxation rate, due to the presence of ferritin. A new approach was proposed, called proton-exchange de-phasing model (PEDM) explaining this effect by the exchange between structural protons of the hydroxyl groups (OH) of the surface of hydrous iron oxide (ferrihydrite) particles and protons of free water. This model predicts that relaxation rates are higher in lower pH, where more exchangeable protons exist [25].

As the interpretation of the results of quantitative MRI data acquired in vivo is non trivial and the contrast obtained depends on tissue microstructure, studies comparing PM MRI with histology data can provide valuable information about healthy and diseased human brain [37]; specifically regarding investigation of the iron content [4, 46] as presented in Chapter 5.

4.3   Iron in Parkinson's Disease

Parkinson's disease (PD) is (after Alzheimer's disease) the second most common neurodegenerative disorder [14], affecting up to 1% of the population and with onset generally occurring in people older than 60 [50]. Post mortem studies of PD demonstrate selective dopaminergic cell loss in the nigrostratial pathway, in the substantia nigra pars compacta (SNpc) [18], as well as pathology of such brain structures as nucleus basalis of Meynert and locus coeruleus [15].

The cause of neurodegeneration in PD is not fully elucidated, but it is potentially related to mitochondrial dysfunction, oxidative stress or protein mishandling [26]. The increased levels of iron that have been reported in the SN in PD patients [56, 66] support a role for iron-mediated oxidative stress in PD pathogensis. It has also been found that environmental chemicals (pesticides) may cause dopaminergic cell death in PD [3]. There is growing evidence relating the occurrence of PD to genetic factors

[11].

PD is clinically diagnosed using the UK PD Brain Bank Criteria with fatiguable bradykinesia as the obligatory criterion along with one of the following: tremor, rigidity or gait disorder [32]. Diagnosis of PD is further supported by an excellent L-dopa response, subsequent development of L-dopa related motor fluctuations and finally cortical Lewy body depositon leading to dementia and visual hallucination. Misdiagnosis is especially common in the early stages of the disease (4-17% in clinical trials and up to 25% in community studies) and a biomarker for PD is yet to be established [14]. The Unified Parkinson's disease rating scale (UPDRS) [17] is used to asses the clinical status of PD patients and can be used to monitor disease progression, albeit with limited sensitivity. The rate of confirmation of the clinical diagnosis by histopathological findings varies from 80-90% (see the review paper, [42]), but there are no generally accepted criteria; the most commonly used is the finding of degeneration of dopaminergic neurons in the SNpc along with the presence of proteinaceous inclusions, so called Lewy bodies. To differentiate PD from other tremulous syndromes, neuroimaging techniques such as (^{123}I)ioflupane (also called (123I)FP-CIT), DaTSCAN, are becoming more widely used [1, 13].

Chelation treatment has been proposed for binding the excess iron occurring in PD [49]. Difficulties with this approach include the requirement for highly selective chelators, which should only affect the intracellular reactive labile iron pool, and not the bound iron that is essential for physiological function, as that could influence systemic iron homeostasis. Moreover, chelators need to have the ability to cross the brain blood barrier (BBB) and the resulting bound products have to be non-toxic. Some studies have shown that chelation treatment can reverse PD symptoms in transgenic mice [34], as well as successful chelation treatment in patients with Friedrich ataxia, another disease where increased iron levels are present [5].

4.4 Iron in Multiple Sclerosis

Multiple sclerosis (MS) is a chronic, autoimmune, inflammatory disease of the central nervous system (CNS), leading to demyelination and axonal loss, which results in the formation of lesions (plaques) [33]. MS generally affects young adults (20-45y.o.), is twice as common in women as men, and has a high prevalence in descendants of Northern Europeans (Europe and North America) [23]. The main clinical symptoms of MS include: sensory disturbances (numbness and tingling), visual loss, loss of muscle control and weakness. Life expectancy after the onset of the disease is reduced by about 5-15 years.

MS most often starts as a clinically isolated syndrome (CIS), involving an episode of symptoms suggestive of demyelination, usually affecting the optic nerve, spinal cord, brain stem or cerebellum [48]. The second episode, occurring within 2-3 years in most cases, determines the conversion from CIS to MS [33]. The course of the disease can be progressive or relapsing. The most common type of MS is relapsing-remitting (RRMS, 85%), then primary progressive (PPMS, 10%) and progressive-relapsing (PRMS, 5%). Some RRMS patients develop secondary progressive MS (SPMS).

The diagnostic criteria, which were defined by McDonald et al. [45], and recently revised [55] include clinical assessment supported by laboratory tests (examination of cerebrospinal fluid (CSF)) and use of MRI for lesion detection. Disease progression is measured with Expanded Disability Status Scale (EDSS) [38]. There is no cure for MS, however various disease-modifying therapies are available [23].

As previously mentioned, iron plays an important role in myelination. Oligodendrocytes responsible for the creation of myelin have high levels of iron and ferritin, and iron is also found in myelin [8, 9, 41]. Dysfunction of oligodendrocytes has been proposed as being important in the pathological processes involved in MS [10]. Elevated levels of ferritin have been reported in patients with progressive MS, which may be a sign of the defence mechanism for binding iron and preventing oxidative stress [40]. It was also shown in PM work that iron accumulation occurs

in the periphery of demyelinated MS plaques [12]. MRI studies confirmed these results [29] and also found increased iron content in deep grey matter, both in MS [2] and in CIS [6] patients.

4.5 Conclusions

Considering the importance of iron in the pathogenesis of neurodegenerative diseases such as PD and MS, in vivo imaging of iron can potentially provide non-invasive tools for diagnosis, monitoring or better understanding. MRI has proved successful for both qualitative and quantitative assessment of iron content in the brain. The following chapters of this thesis will present various studies applying MRI methods to investigate pathology and possible diagnostic tools related to iron, regarding PD and MS.

References

[1] N. Bajaj, R. a. Hauser, and I. D. Grachev, *Clinical utility of dopamine transporter single photon emission CT (DaT-SPECT) with (123I) ioflupane in diagnosis of parkinsonian syndromes.*, Journal of Neurology, Neurosurgery & Psychiatry, (2013).

[2] R. Bakshi, R. H. B. Benedict, R. A. Bermel, S. D. Caruthers, S. R. Puli, C. W. Tjoa, A. J. Fabiano, and L. Jacobs, *T2 Hypointensity in the Deep Gray Matter of Patients With Multiple Sclerosis*, Archives of Neurology, 59 (2002), pp. 62–68.

[3] R. Betarbet, T. B. Sherer, G. Mackenzie, M. Garcia-osuna, A. V. Panov, and J. T. Greenamyre, *Chronic systemic pesticide exposure reproduces features of Parkinson's disease*, Nature Neuroscience, 3 (2000), pp. 1301–1306.

[4] A. I. Blazejewska, S. T. Schwarz, A. Pitiot, M. C. Stephenson, J. Lowe, N. Bajaj, R. W. Bowtell, D. P. Auer, and G. P. A, *Visualization of nigrosome 1 and its loss in PD: Pathoanatomical correlation and in vivo 7T MRI.*, Neurology, 81 (2013), pp. 534–540.

[5] N. Boddaert, K. H. Le Quan Sang, A. Rötig, A. Leroy-Willig, S. Gallet, F. Brunelle, D. Sidi, J.-C. Thalabard, A. Munnich, and Z. I. Cabantchik, *Selective iron chelation in Friedreich ataxia: biologic and clinical implications.*, Blood, 110 (2007), pp. 401–8.

[6] A. Ceccarelli, M. a. Rocca, M. Neema, V. Martinelli, A. Arora, S. Tauhid, A. Ghezzi, G. Comi, R. Bakshi, and M. Filippi, *Deep gray matter T2 hypointensity is present in patients with clinically isolated syndromes suggestive of multiple sclerosis.*, Multiple Sclerosis, 16 (2010), pp. 39–44.

[7] J. F. Collingwood and J. Dobson, *Nanoscale Iron Compounds Related to Neurodegenerative Disorders*, in Biomedical Nanostructures, K. Gonsalves, C. Halberstadt, C. T. Laurencin, and L. Nair, eds., no. chapter 18, John Wiley & Sons, 2008, pp. 461–490.

[8] J. R. Connor, K. L. Boeshore, S. A. Benkovic, and S. L. Menzies, *Isoforms of ferritin have a specific cellular distribution in the brain.*, J Neurosci Res, 4 (1994), pp. 461–5.

[9] J. R. Connor and S. L. Menzies, *Relationship of Iron to Oligodendrocytes and Myelination*, Glia, 17 (1996), pp. 83–93.

[10] J. R. Connor, S. L. Menzies, J. R. Burdo, and P. J. Boyer, *Iron and iron management proteins in neurobiology.*, Pediatric neurology, 25 (2001), pp. 118–29.

[11] I. P. D. G. Consortium, *Imputation of sequence variants for identification of genetic risks for Parkinson's disease: a meta-analysis of genome-wide association studies*, Lancet, 377 (2011), pp. 641–649.

[12] W. Craelius, M. W. Midgral, C. P. Luessenhop, A. Sugar, and I. Mihalakis, *Iron deposits surrounding multiple sclerosis plaques*, Archives of Patholgy & Laboratory Medicine, 106 (1982), pp. 397–399.

[13] R. de la Fuente-Fernández, *Role of DaTSCAN and clinical diagnosis in Parkinson disease.*, Neurology, 78 (2012), pp. 696–701.

[14] L. M. L. de Lau and M. M. B. Breteler, *Epidemiology of Parkinson's disease*, Lancet Neurology, 5 (2006), pp. 525–35.

[15] K. Del Tredici and H. Braak, *Dysfunction of the locus coeruleus-norepinephrine system and related circuitry in Parkinson's disease-related dementia.*, Journal of Neurology, Neurosurgery & Psychiatry, (2012), pp. 774–783.

[16] K. L. Double, M. Gerlach, V. Schünemann, A. X. Trautwein, L. Zecca, M. Gallorini, M. B. Youdim, P. Riederer, and D. Ben-Shachar, *Iron-binding characteristics of neuromelanin of the human substantia nigra*, Biochemical Pharmacology, 66 (2003), pp. 489–494.

[17] S. Fahn and R. Elton, *Unified Parkinson's disease rating scale*, in Recent developments in Parkinson's disease, S. Fahn, C. Marsden, M. Goldstein, and D. Calne, eds., 1987, pp. 153–63.

[18] J. M. Fearnley and A. J. Lees, *Ageing and Parkinson's disease: substantia nigra regional selectivity*, Brain, 114 (1991), pp. 2283–2301.

[19] A. Friedman, J. Galazka-Friedman, and D. Koziorowski, *Iron as a cause of Parkinson disease - a myth or a well established hypothesis?*, Parkinsonism & Related Disorders, 15 Suppl 3 (2009), pp. S212–4.

[20] K. Gellein, T. P. Flaten, K. M. Erikson, M. Aschner, and T. Syversen, *Leaching of trace elements from biological tissue by formalin fixation.*, Biological Trace Element Research, 121 (2008), pp. 221–5.

[21] B. B. Gelman, *Iron in CNS Disease*, Journal of Neuropathology and Experimental Neurology, 54 (1995), pp. 477–286.

[22] N. Gelman, J. M. Gorell, P. B. Barker, R. M. Savage, E. M. Spickler, J. P. Windham, and R. a. Knight, *MR imaging of human brain at 3.0 T: preliminary report on transverse relaxation rates and relation to estimated iron content.*, Radiology, 210 (1999), pp. 759–67.

[23] M. M. Goldenberg, *Multiple Sclerosis Review.*, P & T : a peer-reviewed journal for formulary management, 37 (2012), pp. 175–84.

[24] P. F. Good, C. W. Olanow, and D. P. Perl, *Neuromelanin-containing neurons of the substantia nigra accumulate iron and aluminum in Parkinson's disease: a LAMMA study*, Brain Research, 593 (1992), pp. 343–346.

[25] Y. Gossuin, a. Roch, F. Lo Bue, R. N. Muller, and P. Gillis, *Nuclear magnetic relaxation dispersion of ferritin and ferritin-like magnetic particle solutions: a pH-effect study.*, Magnetic resonance in medicine : official journal of the Society of Magnetic Resonance in Medicine / Society of Magnetic Resonance in Medicine, 46 (2001), pp. 476–81.

[26] J. T. Greenamyre and T. G. Hastings, *Parkinson's – Divergent Causes Convergent Mechanisms*, Science, 304 (2004), pp. 1120–1122.

[27] P. D. Griffiths, B. R. Dobson, G. R. Jones, and D. T. Clarke, *Iron in the basal ganglia in Parkinson's disease. An in vitro study using extended X-ray absorption fine structure and cryo-electron microscopy*, Brain, 122 (1999), pp. 667–673.

[28] E. M. Haacke, N. Y. C. Cheng, M. J. House, Q. Liu, J. Neelavalli, R. J. Ogg, A. Khan, M. Ayaz, W. Kirsch, and A. Obenaus, *Imaging iron stores in the brain using magnetic resonance imaging.*, Magnetic Resonance Imaging, 23 (2005), pp. 1–25.

[29] E. M. Haacke, M. Makki, Y. Ge, M. Maheshwari, V. Sehgal, J. Hu, M. Selvan, Z. Wu, Z. Latif, Y. Xuan, O. Khan, J. Garbern, and R. I. Grossman, *Characterizing iron deposition in multiple sclerosis lesions using susceptibility weighted imaging.*, Journal of magnetic resonance imaging : JMRI, 29 (2009), pp. 537–44.

[30] E. M. Haacke, Y. Xu, Y.-C. N. Cheng, and J. R. Reichenbach, *Susceptibility weighted imaging (SWI).*, Magnetic resonance in medicine : official journal of the Society of Magnetic Resonance in Medicine / Society of Magnetic Resonance in Medicine, 52 (2004), pp. 612–8.

[31] B. Hallgren and P. Sourander, *The Effect Oof Age on the Non-heamin Iron in the Human Brain*, Journal of Neurochemistry, 3 (1958), pp. 41–51.

[32] a. J. Hughes, S. E. Daniel, L. Kilford, and a. J. Lees, *Accuracy of clinical diagnosis of idiopathic Parkinson's disease: a clinico-pathological study of 100 cases.*, Journal of Neurology, Neurosurgery & Psychiatry, 55 (1992), pp. 181–184.

[33] J. E. Joy and R. B. Johnston, eds., *Multiple Sclerosis. Current Status and Strategies for the Future*, National Academy Press, Washington, DC, 2003.

[34] D. Kaur, F. Yantiri, S. Rajagopalan, J. Kumar, J. Q. Mo, R. Boonplueang, V. Viswanath, R. Jacobs, L. Yang, M. F. Beal, D. Dimonte, I. Volitaskis, L. Ellerby, R. A. Cherny, A. I. Bush, and J. K. Andersen, *Genetic or Pharmacological Iron Chelation Prevents MPTP-Induced Neurotoxicity In Vivo : A Novel Therapy for Parkinson ' s Disease*, 37 (2003), pp. 899–909.

[35] J. P. Kehrer, *The Haber-Weiss reaction and mechanisms of toxicity.*, Toxicology, 149 (2000), pp. 43–50.

[36] D. B. Kell, *Towards a unifying, systems biology understanding of large-scale cellular death and destruction caused by poorly liganded iron: Parkinson's,*

Huntington's, Alzheimer's, prions, bactericides, chemical toxicology and others as examples., Archives of toxicology, 84 (2010), pp. 825–89.

[37] J. Kolasinski, C. J. Stagg, S. a. Chance, G. C. Deluca, M. M. Esiri, E.-H. Chang, J. a. Palace, J. a. McNab, M. Jenkinson, K. L. Miller, and H. Johansen-Berg, *A combined post-mortem magnetic resonance imaging and quantitative histological study of multiple sclerosis pathology.*, Brain : a journal of neurology, 135 (2012), pp. 2938–51.

[38] J. F. Kurtzke, *Rating neurologic impairment in multiple sclerosis: an expanded disability status scale (EDSS).*, Neurology, 11 (1983), pp. 1444–52.

[39] C. Langkammer, N. Krebs, W. Goessler, E. Scheurer, F. Ebner, K. Yen, F. Fazekas, and S. Ropele, *Quantitative MR Imaging of Brain Iron : A Postmortem Validation Study*, Radiology, 257 (2010), pp. 455–462.

[40] S. M. LeVine, S. G. Lynch, C. N. Ou, M. J. Wulser, E. Tam, and N. Boo, *Ferritin, transferrin and iron concentrations in the cerebrospinal fluid of multiple sclerosis patients.*, Brain research, 821 (1999), pp. 511–5.

[41] S. M. LeVine and W. B. Macklin, *Iron-enriched oligodendrocytes: a reexamination of their spatial distribution.*, Journal of Neuroscience, 26 (1990), pp. 508–12.

[42] I. Litvan, K. P. Bhatia, D. J. Burn, C. G. Goetz, A. E. Lang, I. Mckeith, N. Quinn, K. D. Sethi, C. Shults, and G. K. Wenning, *SIC Task Force Appraisal of Clinical Diagnostic Criteria for Parkinsonian Disorders*, Movement Disorders, 18 (2003), pp. 467–486.

[43] T. Liu, P. Spincemaille, L. de Rochefort, B. Kressler, and Y. Wang, *Calculation of susceptibility through multiple orientation sampling (COSMOS): a method for conditioning the inverse problem from measured magnetic field map to susceptibility source image in MRI.*, Magnetic Resonance in Medicine, 61 (2009), pp. 196–204.

[44] A. K. Lotfipour, S. Wharton, S. T. Schwarz, V. Gontu, A. Schäfer, A. M. Peters, R. W. Bowtell, D. P. Auer, P. a. Gowland, and N. P. S. Bajaj, *High resolution magnetic susceptibility mapping of the substantia nigra in Parkinson's disease.*, Journal of Magnetic Resonance Imaging, 35 (2012), pp. 48–55.

[45] W. I. McDonald, a. Compston, G. Edan, D. Goodkin, H. P. Hartung, F. D. Lublin, H. F. McFarland, D. W. Paty, C. H. Polman, S. C. Reingold, M. Sandberg-Wollheim, W. Sibley, a. Thompson, S. van den Noort, B. Y. Weinshenker, and J. S. Wolinsky, *Recommended diagnostic criteria for multiple sclerosis: guidelines from the International Panel on the diagnosis of multiple sclerosis.*, Annals of neurology, 50 (2001), pp. 121–7.

[46] M. D. Meadowcort, J. R. Connor, M. B. Smith, and Q. X. Yang, *Magnetic Resonance Imaging and Histological Analysis of Beta- Amyloid Plaques in Both Human Alzheimer's Disease and APP/ PS1 Transgenic Mice*, J Magn Reson Imaging, 29 (2009), pp. 997–1007.

[47] R. Meguro, Y. Asano, H. Iwatsuki, and K. Shoumura, *Perfusion-Perls and -Turnbull methods supplemented by DAB intensification for nonheme iron histochemistry: demonstration of the superior sensitivity of the methods in the liver, spleen, and stomach of the rat.*, Histochemistry and cell biology, 120 (2003), pp. 73–82.

[48] D. H. Miller, D. T. Chard, and O. Ciccarelli, *Clinically isolated syndromes*, Lancet Neurology, 11 (2012), pp. 157–69.

[49] R. B. Mounsey and P. Teismann, *Chelators in the treatment of iron accumulation in Parkinson's disease.*, International journal of cell biology, 2012 (2012), pp. 1–12.

[50] R. L. NUSSBAUM AND C. E. ELLIS, *Alzheimer's disease and Parkinson's disease.*, The New England journal of medicine, 348 (2003), pp. 1356–64.

[51] A. E. OAKLEY, J. F. COLLINGWOOD, J. DOBSON, G. LOVE, H. R. PERROTT, AND C. M. MORRIS, *Individual dopaminergic neurons show raised iron levels in Parkinson disease*, (2007).

[52] R. J. OGG, J. W. LANGSTON, E. M. HAACKE, R. G. STEEN, AND J. S. TAYLOR, *The correlation between phase shifts in gradient-echo MR images and regional brain iron concentration.*, Magnetic Resonance Imaging, 17 (1999), pp. 1141–1148.

[53] R. J. ORDIDGE, J. M. GORELL, J. C. DENIAU, R. A. KNIGHT, AND J. A. HELPERN, *Assessment of Relative Brain Iron Concentrations Using T2-Weighted and T2*-Weighted MRI at 3 Tesla*, Magnetic Resonance in Medicine, 32 (1994), pp. 335–341.

[54] M. PERLS, *Nachweis von Eisenoxyd in gewissen Pigmenten*, Archiv für Pathologische Anatomie und Physiologie und für Klinische Medicin, 39 (1867), pp. 42–48.

[55] C. H. POLMAN, S. C. REINGOLD, B. BANWELL, M. CLANET, J. A. COHEN, M. FILIPPI, K. FUJIHARA, E. HAVRDOVA, M. HUTCHINSON, L. KAPPOS, F. D. LUBLIN, X. MONTALBAN, P. O'CONNOR, M. SANDBERG-WOLLHEIM, A. J. THOMPSON, E. WAUBANT, B. WEINSHENKER, AND J. S. WOLINSKY, *Diagnostic criteria for multiple sclerosis: 2010 revisions to the McDonald criteria.*, Annals of Neurology, 69 (2011), pp. 292–302.

[56] P. RIEDERER, E. SOFIC, W.-D. RAUSCH, B. SCHMIDT, G. P. REYNOLDS, K. JELLINGER, AND B. H. YOUDIM, *Transition Metals, Ferritin, Glutathione, and Ascorbic Acid in Parkinsonian Brains*, Journal of Neurochemistry, 52 (1989), pp. 515–520.

[57] P. Santambrogio, S. Levi, A. Cozzi, B. Corsi, and P. Arosio, *Evidence that the specificity of iron incorporation into homopolymers of human ferritin L- and H-chains is conferred by the nucleation and ferroxidase centres*, Biochem J, 314 (1996), pp. 139–144.

[58] F. Schenck, *Imaging of brain iron by magnetic reso nance: T2 relaxation at different field strengths*, Journal of Neurological Sciences, 134 (1995), pp. 10–18.

[59] J. F. Schenck, *Magnetic resonance imaging of brain iron*, Journal of the Neurological Sciences, 207 (2003), pp. 99–102.

[60] J. F. Schenck and E. a. Zimmerman, *High-field magnetic resonance imaging of brain iron: birth of a biomarker?*, NMR in biomedicine, 17 (2004), pp. 433–45.

[61] M. Schrag, A. Dickson, A. Jiffry, D. Kirsch, H. V. Vinters, and W. Kirsch, *The effect of formalin fixation on the levels of brain transition metals in archived samples.*, Biometals, 23 (2010), pp. 1123–7.

[62] F. Schweser, A. Deistung, B. W. Lehr, and J. R. Reichenbach, *Quantitative imaging of intrinisic magnetic tissue properties using MRI signal phase: An approach to in vivo brain iron metabolism?*, NeuroImage, 54 (2011), pp. 2789–2807.

[63] K. Shmueli, J. a. de Zwart, P. van Gelderen, T.-Q. Li, S. J. Dodd, and J. H. Duyn, *Magnetic susceptibility mapping of brain tissue in vivo using MRI phase data.*, Magnetic resonance in medicine : official journal of the Society of Magnetic Resonance in Medicine / Society of Magnetic Resonance in Medicine, 62 (2009), pp. 1510–22.

[64] J. Sian-Hülsmann, S. Mandel, M. B. H. Youdim, and P. Riederer, *The relevance of iron in the pathogenesis of Parkinson's disease.*, Journal of neurochemistry, 118 (2011), pp. 939–57.

[65] S. Siemonsen, J. Finsterbusch, J. Matschke, a. Lorenzen, X.-Q. Ding, and J. Fiehler, *Age-dependent normal values of T2* and T2' in brain parenchyma.*, AJNR. American journal of neuroradiology, 29 (2008), pp. 950–5.

[66] E. Sofic, P. Riederer, H. Heinsen, H. Beckmann, G. P. Reynolds, G. Hebenstreit, and M. B. H. Youdim, *Increased iron (III) and total iron content in post mortem substantia nigra of parkinsonian brain*, Journal of Neural Transmission, 74 (1988), pp. 199–205.

[67] J. Vymazal, R. a. Brooks, N. Patronas, M. Hajek, J. W. Bulte, and G. Di Chiro, *Magnetic resonance imaging of brain iron in health and disease.*, Journal of the neurological sciences, 134 Suppl (1995), pp. 19–26.

[68] S. Wharton and R. Bowtell, *Whole-brain susceptibility mapping at high field: a comparison of multiple- and single-orientation methods.*, NeuroImage, 53 (2010), pp. 515–25.

[69] S. Wharton, A. Schäfer, and R. Bowtell, *Susceptibility Mapping in the Human Brain Using Threshold-Based k-Space Division*, Magnetic Resonance in Medicine, 63 (2010), pp. 1292–1304.

[70] L. Zecca, R. Fariello, P. Riederer, D. Sulzer, A. Gatti, and D. Tampellini, *The absolute concentration of nigral neuromelanin, assayed by a new sensitive method, increases throughout the life and is dramatically decreased in Parkinson's disease*, FEBS Letters, 510 (2002), pp. 216–220.

[71] L. Zecca, D. Tampellini, M. Gerlach, P. Riederer, R. G. Fariello, and D. Sulzer, *Substantia nigra neuromelanin : structure , synthesis , and molecular behaviour*, (2001), pp. 414–418.

5

Substantia nigra in healthy and parkinsonian brain

There is a growing evidence supporting the hypothesis that Parkinson's disease (PD), which affects dopamine transporter system involving the substantia nigra (SN) and other midbrain structures, is related to the dysfunction of iron homeostasis (see Chapter 4). Numerous MRI studies have investigated in vivo changes of the iron content of the SN in PD using techniques such as T_2-, T_2^*-imaging or susceptibility mapping [7, 23, 37, 45]. This study attempts a quantitative, post mortem (PM) validation of R_2^* and susceptibility maps as markers of tissue iron, by comparing brain stem MR image data acquired at 7T with the histological Perls' stains as presented in Section 5.2.

According to the recent studies T_2^* and susceptibility contrast are also affected by myelin content [34, 36]. Therefore in this work PM and in vivo myelin and iron distributions in the brain stem were investigated by comparing magnetization transfer ratio MTR maps, considered to be an MRI myelin marker, but also sensitive to tissue properties caused by inflammation, R_2^* and susceptibility maps related to iron and myelin with the solochrome cyanine (SC) stain for myelin and Perls' stain for iron (Section 5.2).

Changes of the iron content in the substantia nigra (SN) reported in PD patients are not uniform [16] and death of the dopaminergic neurons of the SN in PD has previously been found to occur more rapidly in particular locations within the SN [8, 9]. These spatial variations in neurodegeneration in the SN gave rise to the motivation for studying its sub-structures in a search for a potential diagnostic biomarker of PD (Section 5.1).

5.1 IMAGING OF NIGROSOMES OF THE SUBSTANTIA NIGRA

The diagnosis of PD in the UK is based on the UK Parkinson's Disease Brain Bank criteria of fatiguable bradykinesia plus tremor, rigidity or gait impairment. Although the accuracy of diagnosis is high in clinico-pathological studies, the false positive error rate is 15-25% in community studies and is 4-15% in clinical trials [3]. Nuclear medicine techniques such as dopamine transporter scanning (single photon transmission scan following Ioflupane ^{123}I injection) have a reported sensitivity and specificity approaching 95% and are helpful in the assessment of clinically challenging cases [3]. However they are expensive and there is no direct correlation between the stage of disease and degree of abnormality on the scans, limiting their use in tracking disease progression. There is therefore a need for an alternative diagnostic marker in PD, which can provide tracking of disease progression.

The pathological hallmarks of PD are deposition of Lewy bodies and depigmentation of the substantia nigra (loss of the neuromelanin pigment). The SN is divided into the pars compacta (SNpc), which is densely packed with neuromelanin-containing dopaminergic cells, and the pars reticulata (SNpr), which is formed by loose aggregations of GABAergic medium and large neurons [27]. The majority of neurons in the SNpc project to the neostriatum (putamen and caudate nucleus) as nigrostriatal fibres [27]. The SNpr neurons mainly project to the thalamus, the superior colliculus and the parabrachial pontine reticular formation [27]. Neurons from striosomes (acetylcholinesterase-poor regions) project to the SNpc and those from the remaining matrix of striatum project to the SNpr [27]. Five distinct subgroups of dopamine-containing neurons in calbindin-negative zones within the SNpc, called nigrosomes, have been identified by immunostaining for calbindin D_{28K} [9]. The largest, nigrosome 1, is lens-shaped and situated along the rostral/caudal axis of the SN in its dorsal part, at caudal and intermediate levels (Figure 8 of Damier et al [9] and Figure 5.1.5). Post mortem (PM) studies have shown the loss of dopaminergic neurons in PD to be significantly higher in the nigrosomes than in other subregions of the SN, with the greatest loss (98%) occurring in nigrosome 1 [8]. Further evidence of nigrosome 1 involvement in early stages of the disease would allow monitoring of these neurodegenerative changes in vivo to determine whether this biomarker can provide a direct diagnostic tool and a method for studying the aetiology and progression of PD.

SN BOUNDARIES

Many magnetic resonance imaging (MRI) studies have reported PD-associated changes in the SN [35]. However, delineating the boundaries and sub-structures of the SN and assessing the features of neurodegeneration in the SN remains challenging [1]. This is partly because of the limited spatial resolution of conventional MRI, but also because of the large signal loss caused by the high iron content in the SN region.

It is sometimes erroneously assumed that the hypointense area in T_2^* weighted (T_2^*-w) images corresponds to the SN (e.g. [7, 15, 31]), and variations in the definition of the SN anatomy on MRI might explain some of the variability in literature on MRI changes in the SN of PD patients. Recently developed ultra-high field MRI systems allow the acquisition of very high spatial resolution T_2^*-w images providing detailed morphological information from within the SN. Careful correlation of high resolution MR data and histology [40] may enable a more precise definition of the boundaries and sub-structures of the SN in vivo, and an accurate demonstration of PD pathology.

MRI OF NIGROSOMES

The morphological features of the SN found in MR images acquired in vivo at 7T were investigated by comparison with post mortem MRI and histochemical data including Perls' stain which is sensitive to ferric iron and neuromelanin, tyrosine hydroxylase (TH) stain which is a marker for dopaminergic cells and calbindin stain to identify nigrosomes [9]. The results suggest that it is possible to visualise nigrosome 1 directly in healthy subjects. Given previous histological evidence of preferential dopaminergic cell loss from the nigrosomes in PD [8], the study then examined whether the in vivo appearance of nigrosome 1 at 7T could provide a diagnostic marker to distinguish PD patients from healthy controls (HC). Furthermore the possibility of visualising nigrosome 1 at 3T using different MRI techniques was investigated. This is important due to the much wider availability of these scanners.

5.1.1 MATERIALS AND METHODS

ANATOMY OF THE HUMAN BRAIN STEM

Schematic diagram in Figure 5.1.1 presents the substructures of the brain stem laying within two planes positioned perpendicularly to the brain stem axis.
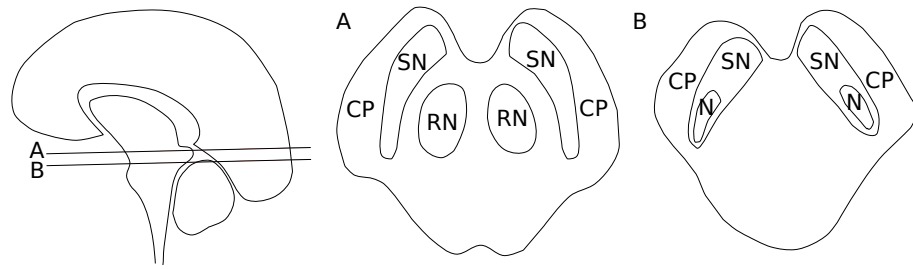
Figure 5.1.1: Diagram showing the substructures of a brain stem on the level of red nucleus (A) and below it (B); lebeled structures are: substantia nigra (SN), red nucleus (RN), cerebral peduncle (CP) and nigrosome 1 (N).

This positioning was used in all the MRI scans of the SN used in this thesis. Post mortem samples obtained to visualise nigrosome 1 were taken on level B, below the red nucleus (RN).

PROCESSING OF THE POST MORTEM MIDBRAIN SAMPLES

Complex processing of the PM tissue samples is described here, involving: scanning, staining, registration and masking images. This part was common to the methods for the two studies presented in the current and the subsequent sections of the chapter.

Three post mortem (PM) midbrains fixed in 10% formalin were obtained from the Queen's Medical Centre, Nottingham. Two from subjects with no known neurological conditions (HC, 67 and 46 y.o.) and one diagnosed with PD (PD, 75 y.o., disease duration 6 years).

The samples were washed in 0.9% saline for 24 hours and placed on an agar bed in a Perspex sphere, which was then filled with saline solution. All three midbrains were scanned on a 7T Phillips Achieva system equipped with a 32 channel receiver coil (with the exception for the images from the first brain, where a 16 channel receiver was used). Four sequences were used, a high resolution 3D FFE (here referred to as hr-T_2^*-w) sequence allowing identification of anatomical details, a lower resolution 3D FFE (here referred to as lr-T_2^*-w) sequence repeated with the sample at 4 different orientations with respect to B_0 for robust estimation of susceptibility. A second healthy midbrain and a parkinsonian one were additionally scanned with 3D FFE

multi-echo sequence (here referred to as me-T_2^*-w) used to obtain R_2^* maps and an MT sequence (here referred to as MT-TFE) allowing calculation of the MTR maps. Details of the scans carried out on each sample are presented in Table 5.1.1 and relevant parameters of all the scans are summarised in Table 5.1.2.

sample	hr-T_2^*-w	lr-T_2^*-w	me-T_2^*-w	MT-TFE	coil (channels)
HC1	✓	✓			16
HC2 (a & b)	✓	✓	✓	✓	32
PD	✓	✓	✓	✓	32

Table 5.1.1: Summary of the obtained scans and receiver coil types (16 or 32 channels) for the particular PM samples.

name	resolution	slices	TR/TE/ΔTE	FA	additional	time
hr-T_2^*-w	0.3x0.3mm	3D 133 x 0.3mm	46/15ms	15°	NSA=20, BW=67.5Hz	10h 22:00
lr-T_2^*-w	0.5x0.5mm	3D 288 x 0.5mm	26/12ms	12°	BW=337.6Hz	31:54
me-T_2^*-w	0.5x0.5mm	3D 200 x 0.5mm	44/5/5ms	16°	4 echoes, BW=335.2Hz	44:13
MT-TFE	0.4x0.4mm	3D 75 x 0.4mm	14/6.4ms	8°	NSA=8, MTC=no/off BW=101.2Hz	2h 19:12

Table 5.1.2: Summary of the parameters of the scans acquired for the PM midbrain samples.

Subsequently, midbrains were sectioned and experienced histopathologists prepared four different stains on the adjacent, 5µm thick, transverse slices cut using a Leica RM2135 microtome and put onto adhesive microscope slides. Sections were dewaxed with xylene, washed with alcohol of descending concentrations, and rehydrated in water. Table 5.1.3 presents summary of all the stains obtained.

name	precedure	used for
Perls'	Prussian blue	iron Fe^{3+}
TH	tyrosine hydroxylase	dopaminergic cells
CAL	calbindin	nigrosomes (CAL–) and matrix (CAL+) [8]
SC	solochrome cyanine	myelin

Table 5.1.3: The summary of stains obtained for the PM tissue samples.

It is important to note that, during the process of section preparation most of the Fe^{2+} present in tissue is oxidised to ferric iron (by oxygen in aqueous solutions and exposure to air) and in consequence is also visualised by Perls' staining [41]. Therefore in this thesis we will consider Perls' stain to reflect the total iron content in the tissue rather than just Fe^{3+}.

For Perls' staining, sections were washed three times, put into a solution of 25ml of

2%w/v potassium ferrocyanide and 25ml of 2%w/v hydrochloric acid and incubated at room temperature for 10 minutes. After rinsing thoroughly in water, they were flooded with 0.1%w/v nuclear fast red for 5 minutes to counterstain and washed again. For staining with solochrome cyanine (SC), sections were incubated in solution of 96ml distilled water, 4ml 10%w/v iron alum and 0.2g solochrome cyanin RS for 30 minutes and then removed and washed thoroughly in water. Afterwards they were put into a 5%w/v iron alum solution for 10 minutes (removing excess dye from tissue to accentuate the structure) and then returned to water for 10 minutes until the cream/white coloured areas within the blue could be seen. At the end of both histochemical procedures, sections were dehydrated and mounted in DPX using a Leica CV5030 cover slipper.

Two immunohistochemical staining methods were performed using a Leica Bond Max automated system and commercially produced Leica solutions. To obtain calbindin (CAL) stains, sections were heated in a citrate-based antigen retrieval solution (trade name: Novocastra Bond Epitope Retrieval Solution 1) at pH 6.0 for 20 minutes, washed, placed in a peroxidase inhibitor solution for 5 minutes and washed. Calbindin antibody was diluted to a concentration of 1/500 with Leica 'Antibody diluent' and slides were incubated in this for 20 minutes, removed and washed. For tyrosine hydroxylase (TH) staining of the dopaminergic cells sections were heated in an EDTA-based antigen retrieval solution (trade name: Novocastra Bond Epitope Retrieval Solution 2) at pH 9.0 for 30 minutes, washed and incubated in a peroxide inhibitor for 5 minutes, then washed again. Tyrosine hydroxylase antibody was diluted with Leica 'Antibody diluent' to 1/20 and sections were incubated in this for 30 minutes, removed and washed. Finally CAL and TH sections were incubated in diaminobenzidine (DAB) solution for 10 minutes, washed and then DAB-enhanced for 5 minutes, before being washed and counterstained with haematoxylin. Slides were mounted and covered using Microm DTM 6 coverslipper. Images of the stained slides were digitized using a Hamamatsu NanoZoomer microscope camera to enable further processing.

Susceptibility maps were calculated from the low resolution lr-T_2^*-w images with the k-space threshold method [59] (for more details see Section 2.3.5) and co-registered to the high resolution hr-T_2^*-w scans using the transformation matrices obtained from the lr-T_2^*-w data registration with FLIRT, FSL [30]. MTR maps were created using method described in Section 2.3.3 and R_2^* maps were generated by fitting multi echo me-T_2^*-w data, for two brain stems where me-T_2^*-w was obtained (see Table 5.1.1). For the third stem, HC1, an hr-T_2^*-w image was used to estimate an R_2^*-w image, according to the equation $m - \dfrac{\log S}{TE}$, where S corresponds to the values of the signal in the original image and m is an absolute value of the global minimum of the resulting map, to give a linear relation between R_2^*-w signals and R_2^*. MTR and R_2^* maps were then co-registered to the hr-T_2^*-w images. The hr-T_2^*-w data and digitized stains, TH, CAL and SC, were co-registered to the Perls' stain images using a semi-automatic method (Medical Imaging NetCDF tools, Montreal Neurological Institute) based on manually selected landmarks (9 degrees of freedom plus shear), which compensated for tissue deformation due to sectioning. This transformation was also applied to the susceptibility, R_2^* and MTR maps, to bring all the images into the Perls' stain space.

The CAL images were converted from RGB to grey scale (using coefficients specified by the Rec. 601 standard [4]), for other stains the best separation of positively and negatively stained regions was obtained based on one chosen channel: blue for TH and red for SC. The Perls' images were processed using colour deconvolution [48] to separate the blue contrast, corresponding to iron, from the brown contrast, corresponding to neuromelanin. For each sample, a mask outlining the brain stem was created and manually corrected to remove the background, damaged tissue, small veins visible in the Perls' image, and air bubble artefacts. Next, masks of regions that were high in iron, high in neuromelanin and TH-, SC- or CAL-positive, were obtained by thresholding the stain images and applying manual correction to remove obvious artefacts. These masks were overlaid on the MR images and quantitative MR maps to compare the characteristics of the different regions of the

SN. All the processing steps are summarized in the diagram presented in Figure
5.1.2.
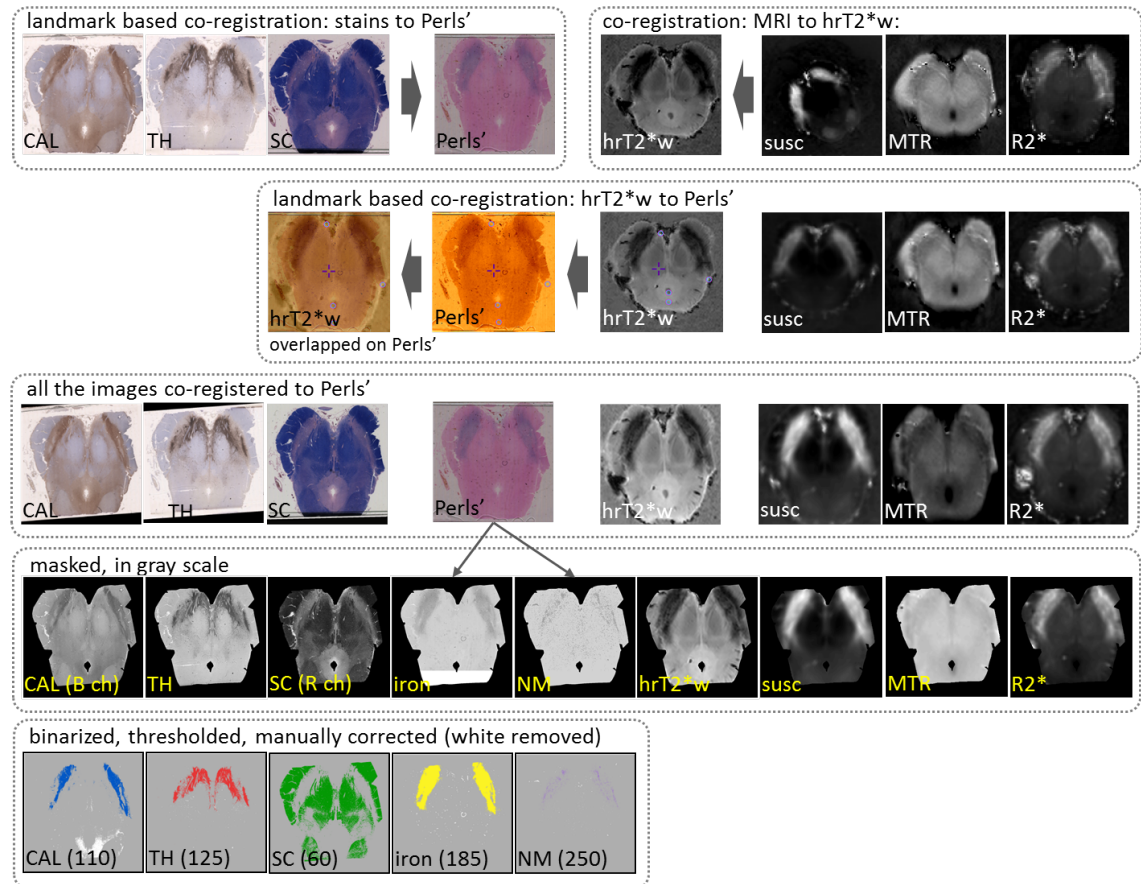
Figure 5.1.2: Image processing steps (on sample from HC2a). The stages were: co-registration (linear for MRI data and based on landmarks for stains), 'cleanup' (masking the whole stem, removing small veins, artefacts etc.), converting to grey scale, thresholding and thus binarizing the images, and hence making the masks for iron, NM, TH, CAL, SC. The final masks were also corrected to remove remaining artefacts.

IMAGING NIGROSOMES IN VIVO AT 7T

To study differences between PD patients and healthy controls (HC), 19 subjects
(10 PDs and 9 age-matched HCs, median/interquartile range: HC=65/5 y.o.,
PD=64/5y.o., sex: HC=6F:3M, PD=4F:6M; PD duration=3±2 years, mean total
UPDRS on medication =24±13) were scanned using a 2D FFE sequence with
TE/TR=16/385ms, α=40°, FOV=180x160x16mm^3, 0.35x0.35x1.0mm^3 resolution,
10 minutes acquisition. A senior neuroradiologist and neuroradiology training fellow
examined the blinded T_2^*-w datasets to classify the subjects according to the presence
or otherwise of a hyperintense ovoid sub-structure within the dorsal/posterior

hypointense midbrain region, later identified as nigrosome 1. To classify a dataset as showing this structure, it had to be visible on both sides of the SN, be present on at least two adjacent axial slices, be surrounded for more than half its boundary by hypointensity, not be part of a perivascular space and to extend below the RN.

IMAGING IRON AND NEUROMELANIN IN VIVVO

Two healthy volunteers (49 and 29 y.o.) were scanned in vivo at 7T to improve characterisation of nigrosome 1. Ultra-high resolution T_2^*-w scans were acquired using a 3D FFE sequence with TE/TR=15/25ms, flip angle=12°, SENSE factor=1, FOV=180x160x15mm^3, 0.3mm isotropic resolution in 21 minutes. A T_1-weighted fast spin echo (FSE) sequence with an off resonance magnetisation transfer pre-pulse (here referred to as mt-T_1-w) at +1100 Hz, with TE/TR=9.0/2582, NSA=4, FOV=180x180x7mm^3, 0.6mm isotropic resolution was also acquired in 7:47 minutes; the contrast in a similar scan at 3T has previously been ascribed to neuromelanin [49, 52]. Images were co-registered using FLIRT, FSL [30]) and visually examined.

IMAGING NIGROSOMES IN VIVO AT 3T

Eight healthy subjects (age: 33±11y.o., F/M=4/4) were scanned on a 3T Philips Achieva scanner using four different sequences: (i) high resolution T_2^* weighted (T_2^*-w), (ii) Fast Field Echo (FFE), (iii) PRESTO and (iv) T_1-weighted scans, with off resonance MTC which has been reported to be sensitive to neuromelanin (NM) [53] (Table 5.1.4).

name	resolution	slices	TR/TE	FA	additional	time
T_2^*-w	0.43x0.43mm^2	2D 8 x 1.5mm	300/50ms	42°	NSA=5, BW=216.8Hz	9:57
FFE	1.0x1.0mm^2	3D 40 x 1.0mm	100/35ms	10°	EPI=3, BW=23.8Hz	5:06
PRESTO	1.0x1.0mm^2	3D 200 x 1.0mm	15/21ms	10°	BW=191.2Hz	4:34
NM	0.6x0.6mm^2	2D 8 x 2.5mm	699/9ms	90°	NSA=4, MTC=off, BW=416.7Hz	9.23

Table 5.1.4: Summary of the scanning parameters.

One dataset was excluded from the analysis due to insufficient coverage. Two neuroradiologists independently rated the images using two scales: nigrosome visibility, 1-3 (definitely not visible – definitely visible) and image quality, 1-5 (very

low – very high, equal to the quality of the T_2^*-w image obtained at 7T). On the NM scan nigrosome visibility is interpreted as 'high NM in the region corresponding to N1' since the high NM area extends beyond the nigrosome, so delineation of the nigrosome 1 is not generally possible.

For quantitative comparison, all images were co-registered to the PRESTO data using FLIRT, FSL [30]. For each dataset two slices of the T_2^*-w image, in which nigrosome 1 was clearly visible, were used to define circular regions of interest (ROIs): 4 voxel diameter for nigrosome, 8 voxel diameter for remainder of SN and for a reference region in the brain stem (care was taken to avoid small veins). These are shown in Figure 5.1.7 (top middle). ROIs were used to calculate the relative contrast between the nigrosome and the SN, as well as the contrast-to-noise ratio (CNR), formed by dividing the contrast by the standard deviation of the signal in the reference region. A one-way ANOVA test with Tukey-Kramer correction for multiple comparisons was performed to examine differences between the contrast and CNR of the different images.

5.1.2 Results

Comparison of histology and 7T post mortem MRI of healthy and parkinsonian substantia nigra

The results presented in this section were obtained using the high resolution T_2^*-w images and stains (TH, CAL, Perls') processed using the methods described in Section 5.1.1. For the four histology samples containing the SN at a level below the RN (three from HC and one from PD) colour-coded maps of areas of high iron, NM, TH and CAL were overlapped (Figures 5.1.3 and 5.1.4). In HC samples superposition of the TH (red) and CAL (blue) masks allowed a CAL- region co-localised with dopaminergic cells (TH+) inside a larger CAL+ area to be identified (Figure 5.1.3, 1st row and Figure 5.1.4); a region with this staining, similar size and location was previously defined as nigrosome 1 [9].
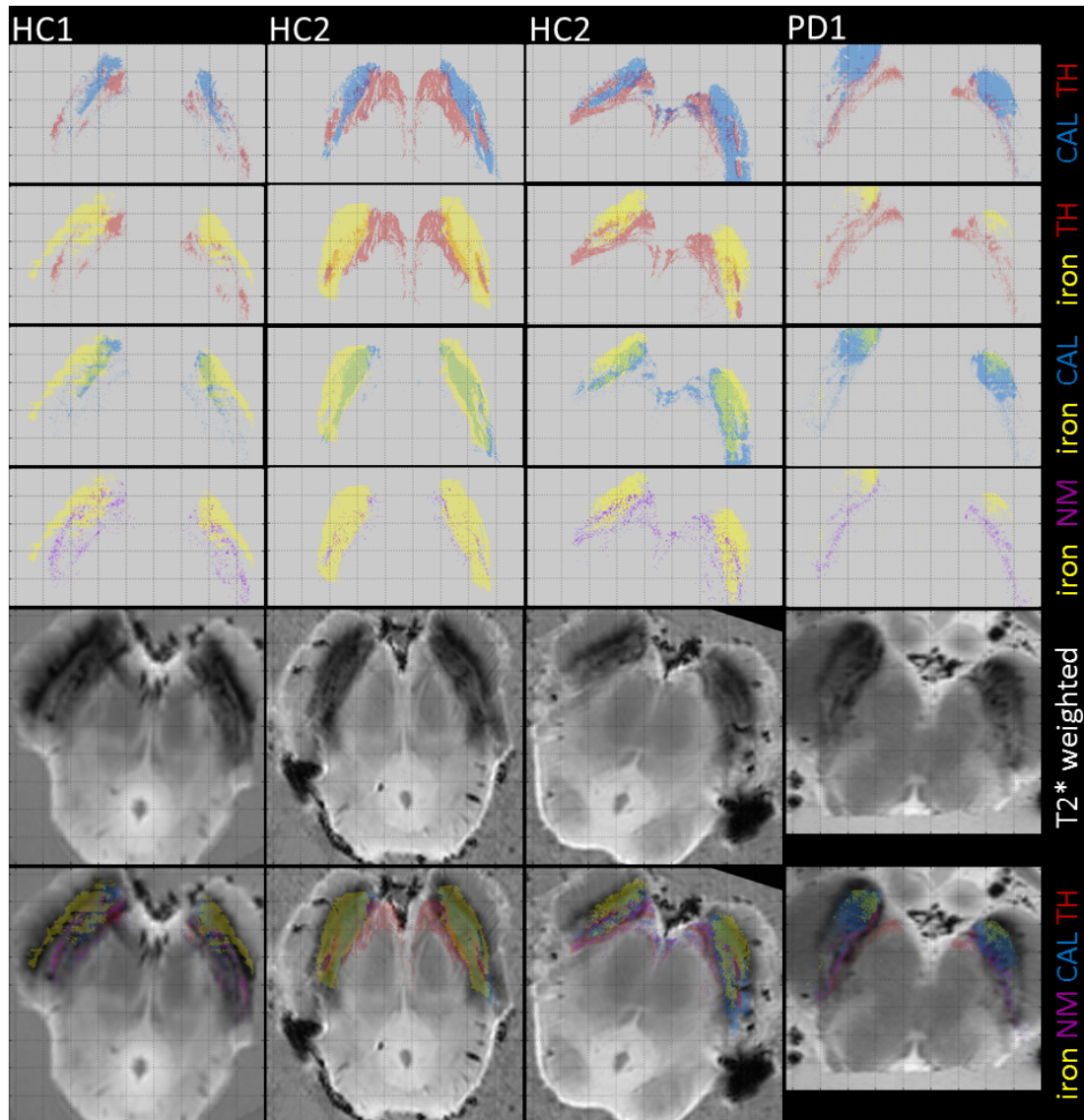
Figure 5.1.3: Four samples from three brain stems of two healthy and one parkinsonian subject (HC1, HC2, PD1) containing the SN at a level below the RN. First four rows show pairs of superimposed masks: CAL with TH (1st), iron with TH (2nd), iron with CAL (3rd) and iron with neuromelanin (4th) (the coloured text on the right hand side indicates the meanings of the colours on the masks). Slice of the 3D MR dataset (5th row, 0.3x0.3x0.3mm^3 voxels) and the same slice with overlapped masks representing the different regions (6th row). All masks and images were co-registered to the Perl's stain image.

The same area showed low iron (Figure 5.1.3, 2nd row: TH and iron, 3rd row: CAL and iron, and Figure 5.1.4), and high neuromelanin (Figure 5.1.3, 4th row: iron and neuromelanin, and Figure 5.1.4), and corresponded to the hyperintense sub-structure visible in the PM T_2^*-w data although PM MRI scans showed more laminar structure in the SN compared to the in vivo scans (Figure 5.1.3, 6th row).
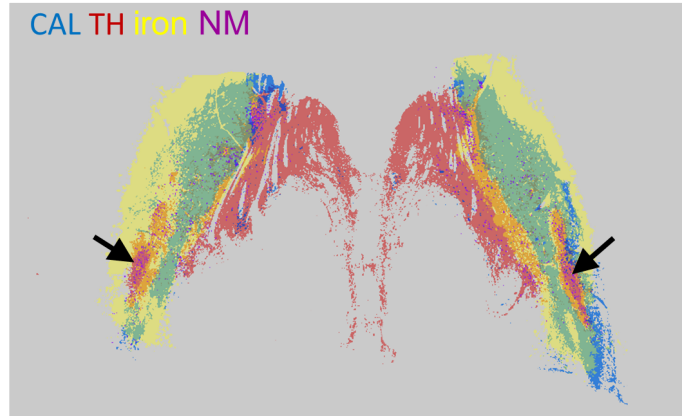
Figure 5.1.4: Superimposed masks of TH, CAL, iron and neuromelanin obtained for sample HC2a with nigrosome 1 indicated by black arrows.

The high iron on the Perls' stain area (yellow) overlapped with the T_2^*-w hypointense regions in the lateral part of the SN (Figure 5.1.3, 6th row). Regions with high neuromelanin content do not overlap with regions of high iron (comparing Perl's (yellow), TH (red) and NM (purple)), or T_2^*-wt hypointensity. For the PD sample a CAL- zone corresponding to the nigrosome 1 was again present (Figure 5.1.3, 4th column) and partially overlapped with a larger T_2^*-w hyperintense region, although it was neither TH+ nor high in NM. T_2^*-w hypointense areas were similar to, if slightly more diffuse than, those in HC, but high iron areas based on the Perls' stain were smaller. TH+ regions were co-localised with high NM and smaller compared to HCs.

NIGROSOME LOSS IN PARKINSON'S DISEASE PATIENTS IN 7T

The hyperintense sub-structure in the dorsal SN corresponding to nigrosome 1 could generally be detected in vivo in HCs using high resolution (0.35x0.35x1.0mm3), T_2^*-w images acquired in a clinically feasible imaging time (Figure 5.1.5). Neuroradiologists blinded to the clinical status of the subjects were able to independently correctly classify 7/8 HC and 10/10 PD on the basis of the presence or absence of nigrosome 1 (one dataset not of diagnostic quality due to subject motion). This translates to a sensitivity of detection of PD of 100%, specificity of 88%, with inter-observer agreement κ of 1.
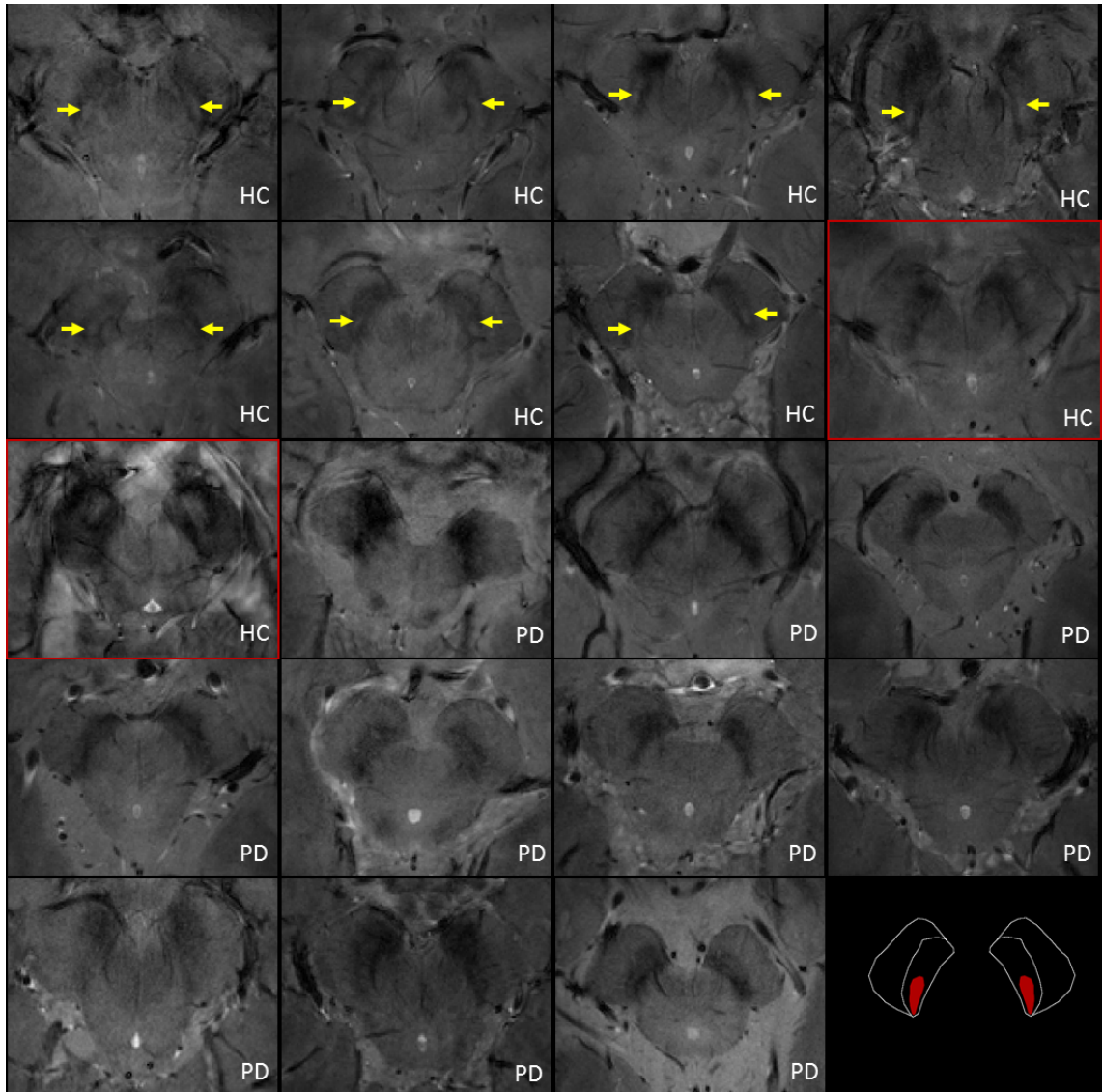
Figure 5.1.5: Example slices from all of the in vivo 7T T_2^*-w scans showing SN in HC and PD patients. Nigrosome 1 (yellow arrows) is visible in HC images as a hyperintense structure, except of two cases highlighted by the red borders, one wrongly classified (2nd row) and one bad quality dataset (3rd row), but not in any of the PD cases. The last segment shows a schematic of the substantia nigra highlighting the nigrosome in red.

IRON VERSUS NEUROMELANIN IN HEALTHY CONTROLS IN 7T

The ovoid sub-structure hyperintense in T_2^*-w images corresponded to a region of hyperintensity on mt-T_1w FSE images (Figure 5.1.6, right and left co-registered).
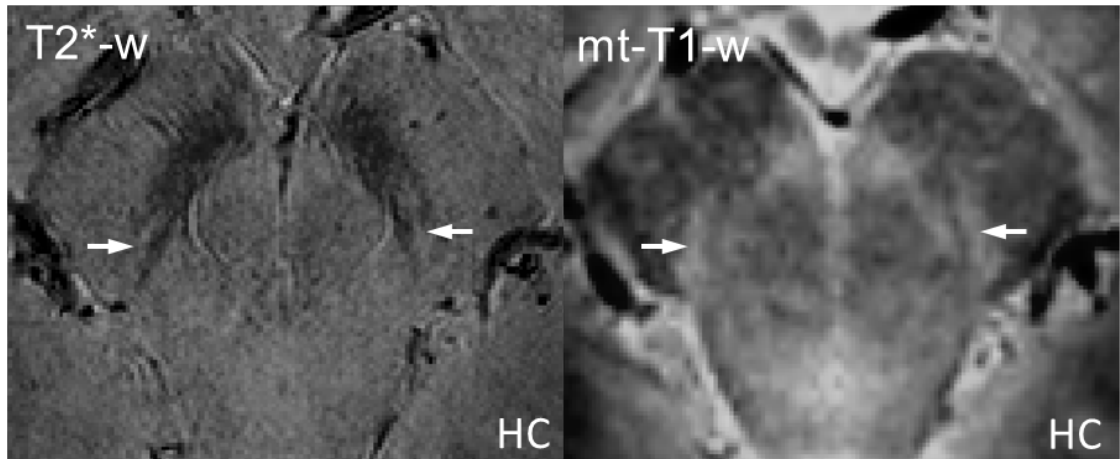
Figure 5.1.6: Example of two, co-reregistered, high resolution, in vivo 7T images of a healthy control showing the substantia nigra and nigrosome 1 (white arrow). In the T_2^*-w image (left, 0.3x0.3x0.3mm^3 voxels) the nigrosome is hyperintense due to its low iron content; in the mt-T_1-w sequence (right, 0.6x0.6x0.6mm^3 voxels) the nigrosome is hyperintense due to its high neuromelanin content.

IMAGING OF THE NIGROSOMES AT 3T

In vivo, high resolution T_2^*-w images of HCs at 7T clearly showed a hyperintense ovoid sub-structure within the dorsal hypointense midbrain region, medial to the cerebral peduncles, which was identified as nigrosome 1. However, since 7T scanners are not widely available, it is important to determine whether this structure can also be detected at 3T. Different 3T scans were therefore compared in terms of their ability to visualise nigrosome 1. Figure 5.1.7 shows example images for one subject, including the filtered phase image from the T_2^*-w scan.
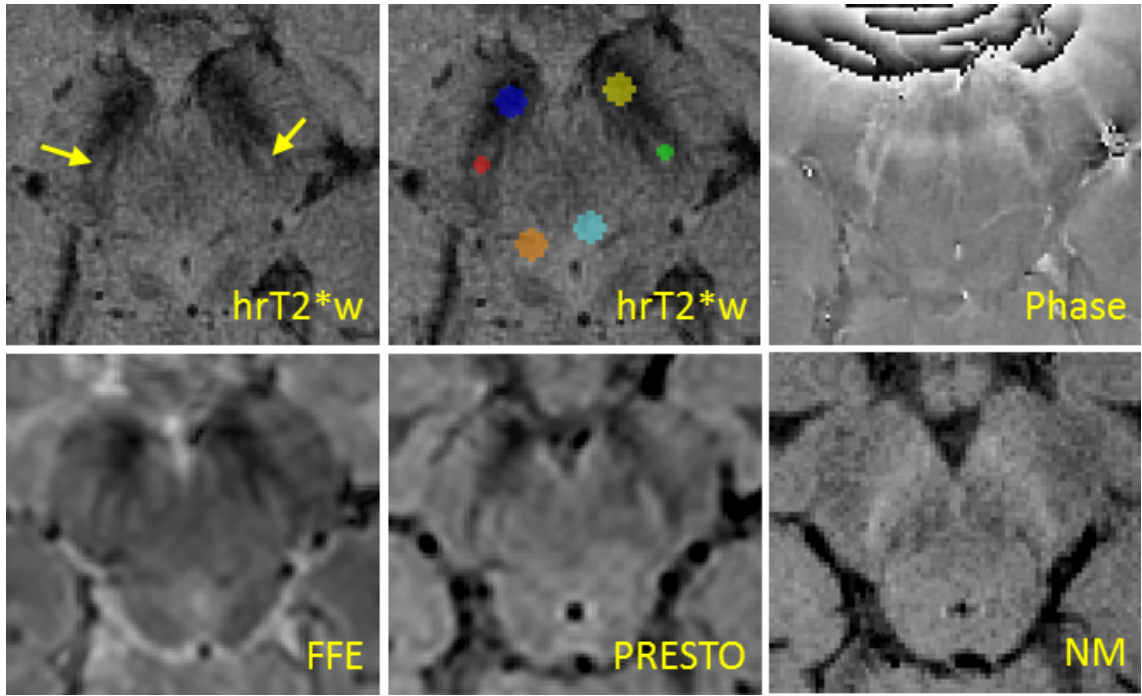
Figure 5.1.7: Example slices of all the 3T images showing the nigrosome; top middle: single slice of T_2^*-w image with ROIs: SN (blue, yellow), nigrosome (red, green), reference region (orange, cyan).

Averaged scores of nigrosome visibility and image quality from the two neuroradiologists are plotted in Figure 5.1.8, with error bars corresponding to standard deviation. FFE and PRESTO provided the best images for nigrosome detection (nigrosome visibility=2.9) and also achieved high image quality scores (2.7 and 3.0), while the NM scans obtained the highest image quality value (3.2). Note again the different definition of visibility for the NM image compared to the other scans.
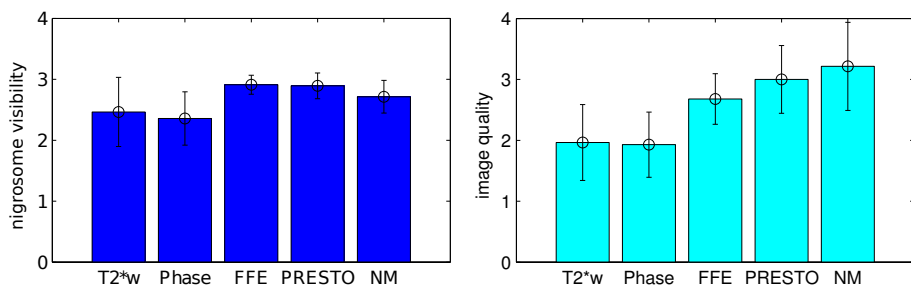
Figure 5.1.8: Nigrosome visibility (left) and quality of the images for nigrosome delineation (right), average scores from two neuroradiologists

Contrast and CNR values are plotted in Figure 5.1.9 with error bars corresponding

to the interquartile range (IQR).
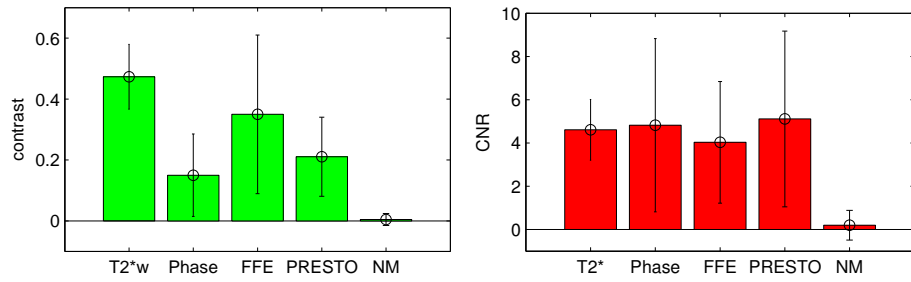
Figure 5.1.9: Contrast (left) and CNR (right) between nigrosome and the SN; error bars represent IQR values.

T_2^*-w images had significantly higher contrast between nigrosome and the SN than all of the other images, except the FFE. The FFE produced significantly higher contrast than phase and NM, while PRESTO yielded higher contrast then the NM sequence (p<0.01). There was no significant difference between CNR values for T_2^*-w, phase, FFE and PRESTO images (p<0.01).

Figure 5.1.10 presents a comparison of 7T and 3T T_2^*-w in vivo images, showing that the nigrosome can also be identified in the 3T images, though less clearly.
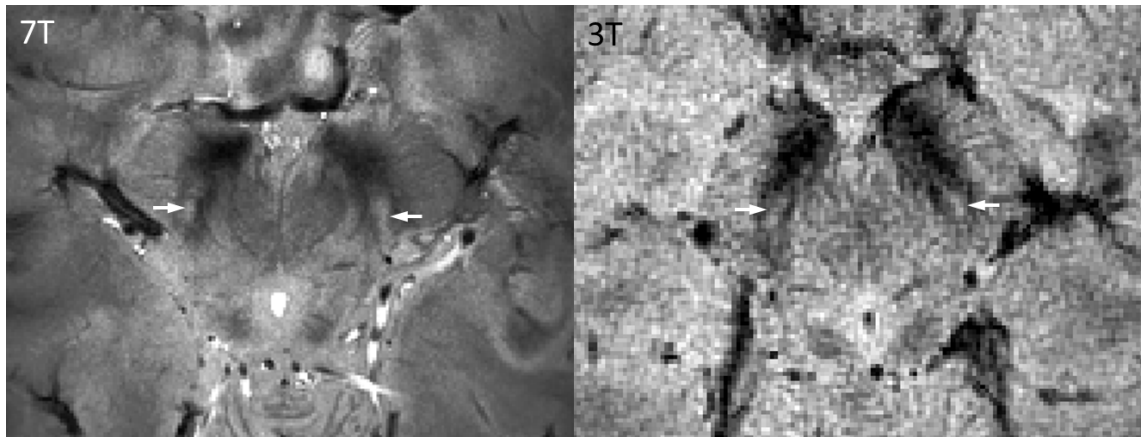
Figure 5.1.10: Example T_2^*-w images obtained at 7T (0.35x0.35x1.00mm^3 voxels, left), and at 3T (0.43x0.43x1.5mm^3 voxels, right) on a healthy subject showing the hyperintense structure that has been identified as nigrosome 1 (white arrows) within the hypointense region of the midbrain.

5.1.3 Discussion

Nigrosome as PD diagnostic marker

This study identified as nigrosome 1, an ovoid, hyperintense feature, embedded within the dorsal, hypointense, midbrain region of the SN on high resolution in vivo T_2^*-w 7T MRI scans of HCs. This MR feature was recently reported by another group, who speculated that it might correspond to a nigrosome [31]. PM MRI and histology data were co-registered to show that this sub-structure has high TH, high NM and low calbindin content, thus conforming to Damier's definition of nigrosome 1 [9]. In the PD sample this calbindin-low region was not high in neuromelanin or TH positive, confirming the loss of neuromelanin-containing cells in nigrosome 1 as previously described [8].

Importantly, this small clinical study demonstrated the consistent absence of this MRI feature in PD patients in vivo; which could be a consequence of neuronal cell loss, neuromelanin loss, an increase in iron content within the nigrosome, a change in iron oxidation state, or a combination of these effects. This could be investigated by studying other patient groups who show iron accumulation without dopaminergic cell loss in this area. The HC misclassified by both raters as 'probable PD' may have elevated iron due to other factors or may have presymptomatic PD; about 10% of elderly HCs show alterations of echogenicity in transcranial sonography consistent with PD [5].

The diagnostic accuracy achieved in this preliminary study at 7T is comparable with the dopamine transporter scan, which is used for diagnosis of difficult parkinsonian cases [11]. However, in contrast to dopamine transporter scanning, MRI-based techniques do not involve risks of radiation exposure, are more widely available and more cost efficient, particularly since the preliminary data suggests that now the nigrosome has been clearly identified at 7T, it may be possible to identify it on more widely available, 3T scanners. Motion was not a major problem in this study, affecting data only from 1/19 subjects. If the T_2^*-w scan was the primary outcome

of a scanning session then the protocol could be modified to reduce the effects of motion, for instance by motion tracking or by over acquiring the data [38].

It was also shown that nigrosome 1 can be detected at 3T, and PRESTO and FFE images were preferred by the neuroradiologists for this identification task. T_2^*-w images provided the greatest contrast between nigrosome 1 and surrounding tissue. The CNR values of FFE and PRESTO images were similar to T_2^*-w data, which in combination with the short scanning (5min) make them potentially clinically useful. Susceptibility weighted images (SWI) created by multiplying the T_2^*-w modulus image by a phase mask did not yield improved results. The low contrast and CNR values of the NM scan are explained by its specificity to NM, which is high in the nigrosome 1 area and much of the rest of the SN.

Iron content

The literature on the change of iron content in the SN in PD is inconsistent. Some PM studies reported greater age-related increases in iron content in PD than HC, for ferritin-bound iron [24], total iron and Fe^{3+} [55]. Mössbauer spectroscopy and colorimetry based studies found total iron concentration to be unchanged or lower in PD, with a possible increase in non-ferritin bound iron [17]. In vivo MRI studies tend to suggest iron accumulation in the SN with age [14] and in PD [26, 37, 44], but without distinguishing the form of iron; since it is known that the relaxivity of Fe^{3+} ferric ions is about 10 times greater than that of iron (II) [21], changes in T_2^* could simply reflect changes in the oxidation state of iron. The lower iron content in the Perls' stain of the PD sample found here, may be due to the fixation time being longer for the PD sample compared to the HC samples ($\approx$2 versus 1 year) [19, 51]. The mismatch between the hypointensity observed on the T_2^*-w MRI and Perl's stains is interesting (Figure 5.1.3). Since the Perls' stain is sensitive only to Fe^{3+}, this could be due to higher iron (II) content in PD brains, which could relate to the fixation process, but would also be consistent with increased oxidative stress due to elevated ferrous iron in PD [17].

T_2^*-w MRI provides excellent contrast in the midbrain due to the high iron content of this brain area [6, 7, 45]. Previous MR work has mainly focused on localising and measuring characteristics of the whole SN [7, 42, 43] or distinguishing the SNpc and SNpr [15, 42], although there has been some inconsistency in the definition of boundaries and sub-areas of the SN in both the MR and histological literature. In many previous MRI studies, the boundaries of the SN and changes in PD have often been defined with reference to the high-iron, T_2^*-w hypointense region [7, 15, 31]. The comparison of the Perls' stain and PM T_2^*-w scan in HC confirmed the expected sensitivity of T_2^*-w MRI to iron, but closer inspection of the histology data shows that the high-iron region cannot be used to delineate the SN boundary. This does not affect the validity of previous MRI results regarding changes in the size, shape or intensity of the high iron region in PD, but questions its interpretation as corresponding to the SN.

MRI characteristics of the SN sub-structures

Summarising, in HC, the SNpc is mainly depicted as a T_2^*-w hypointense, mt-T_1-w hyperintense region, with high iron, low TH and high calbindin, which incorporates a dorsal T_2^*-w hyperintense, low iron, high TH and low calbindin sub-region (nigrosome 1 [9]). As far as the author of this thesis is aware, this is the first study to determine that nigrosome 1 is a low iron structure. The SNpr, located lateral to the SNpc, overlapped with high iron, T_2^*-w hypointense region, but information about the neuronal projections, from diffusion tensor MRI, is needed to exactly define its boundaries [42, 43]. The signal characteristics of nigrosome were similar to an area ascribed to the VTA and depicted as a T_2^*-w hyperintense, TH positive, iron negative region lying adjacent to the RN (VTA, A10 [39]). This area is also hyperintense on T_2^*-w and mt-T_1-w scans in vivo, and lies medial to the SNpc. The subthalamic nucleus was not investigated here since the area studied was limited to the levels below the RN.

The PM characteristics of the SN in the PD sample differed in two ways. First the region of nigrosome 1 was TH negative and low in neuromelanin consistent with loss of neuromelanin-containing dopaminergic cells. Second the iron content in the Perls' stain was surprisingly low, which is probably an artefact of the longer fixation time of the PD sample [19, 51]. The T_2^*-w hypointensity was somewhat larger than the Perls' stain region, but this loss of iron may also explain why the region including nigrosome 1 was hyperintense on PM MRI in PD, in contrast to the results observed in vivo.

Visual comparison of the TH stain, neuromelanin containing cells in the Perls' stain, and the mt-T_1-w and T_2^*-w high resolution in vivo scans provides further evidence that the mt-T_1-w scan is indeed sensitive to neuromelanin [49, 52]. The 7T scan used here is less specific to neuromelanin than previously reported at 3T since it shows hyperintensity in the cerebrospinal fluid, probably due to enhanced inflow effects due to the smaller slab thickness (8mm, 5 slices). The reason why the neuromelanin rich region is hyperintense on mt-T_1-w scans is unclear, but possibly neuromelanin directly shortens the T_1 of both the bound and free proton pools leading to rapid recovery of MT saturation and an increase in T_1-w signal.

LIMITATIONS

This study had several limitations. Firstly, the assessment of diagnostic accuracy is only preliminary, due to the small sample size. Secondly, further quantitative analyses are necessary to determine whether the nigrosome could provide a non-invasive biomarker of PD progression, which might be useful in future therapeutic trials, or for distinguishing idiopathic PD from other parkinsonian conditions. Thirdly, the low iron content in the Perls' stain of the PD sample was paradoxical and indicates that future studies should use PM samples with similar fixation times [2, 19, 51].

This is the first study to identify the sub-structure of the SNpc that is visible on 7T T_2^*-w images [31] as nigrosome 1 [9] and to show that this sub-structure can also be

detected at 3T. This feature is not observed in PD patients, suggesting that it could potentially provide a simple, sensitive and specific diagnostic tool for PD, but future longitudinal, quantitative studies are needed to show if it can provide a biomarker of disease progression.

5.2   ORIGINS OF MR PROPERTIES OF THE BRAIN STEM TISSUE

In this section quantitative analysis related to the iron and myelin distribution in the brain stem are presented. Post mortem MRI properties of healthy controls were related to histology results to provide a better understanding of the MRI tissue properties. The analyses were further extended to in vivo data obtained at 7T and 3T, using ROIs corresponding to the different structures of the brain stem.

The values of R_2^* and R_2 have been shown to linearly correlate with iron content by several studies in vivo and post mortem [20, 32, 45, 46]. Comparison of these measures with Perls' stains has also been performed qualitatively [13] and quantitatively, showing good correlation between the MRI measures and Perls' stain intensity [58]. Similarly quantitative susceptibility values correspond to iron content in brain tissue [33, 62], however correlation with Perls' stain have not been yet shown. MTR is a known MRI myelin marker [50, 61] and some studies have shown correlations between MTR values and Luxol fast blue myelin stain intensities [50, 56], but no similar results exist for the solochrome cyanine stain used in this work.

The main aim of this study was to correlate R_2^*, susceptibility and MTR values of in vivo and fixed PM tissue with Perls' stain for iron and SC stain for myelin. Based on the previously published results, it was hypothesized that we would find a positive correlations between MR iron measures (susceptibility and R_2^*) and Perls' stain, and between MTR and myelin stain were expected. These findings can be potentially useful for monitoring neurodegenerative changes occurring in PD and also allow image optimization for MRI.

5.2.1 Materials and methods

Three different groups of correlations were calculated: PM MR images and stains were correlated pixel by pixel; for in vivo data ROIs corresponding to the particular structures of the brain stem were used, as direct pixel-based comparison was impossible for the images obtained from the different samples; finally similar ROIs were applied to calculate correlations of the PM data for better comparison with the results obtained in vivo.

Post mortem

Quantitative analysis regarding iron and myelin were performed using MR data and stains acquired for three samples of two healthy PM brain stems, HC1, HC2a and HC2b. Details of the acquisition and preprocessing of MRI and histology data, including obtaining iron and myelin masks, were described in Section 5.1.1. In order to normalise the range and distribution of the intensity values within the Perls' and SC images they were converted to grey scale and histogram equalisation was applied to each image separately. The number of desired grey levels was chosen to be similar to the original intensity ranges for all samples. Figure 5.2.1 presents mean and standard deviation values calculated for the brain stem region of the stains before and after normalisation. Afterwards the images were inverted so that the high intensity values correspond to high content of iron for Perls' and high myelin content for SC (Figure 5.2.2, right).
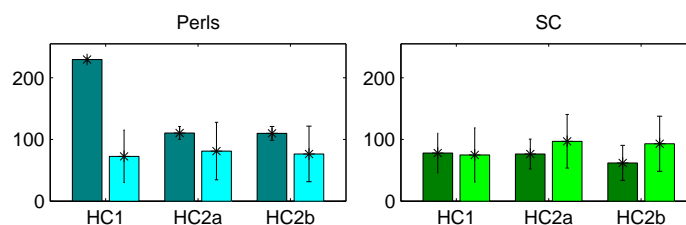

Figure 5.2.1: Bar plots corresponding to mean and standard deviation values calculated for Perls' (left) and SC (right) stains of three samples using the whole-stem region before (dark) and after (bright) normalisation.

High resolution R_2^*, susceptibility and MTR maps were correlated with Perls' and

SC stained images on a pixel by pixel basis to investigate the iron and myelin distributions within the samples. The brain stem was analysed using an outlining mask (whole-stem) to avoid areas affected by artefacts caused by air bubbles. For studying high-iron regions of the substantia nigra, additional high-Perls masks obtained by thresholding the Perls' stains were applied and for analysing high-myelin regions of a brain stem high-SC masks were used (see Section 5.1.1). Perls' and SC stains were also correlated with each other within the whole-stem regions and high-Perls masks were overlapped with the high-SC masks for comparison.

Histograms of R_2^* and susceptibility values were plotted for the iron rich region (high-Perls) and of MTR for the high myelin region (high-SC), together with additional histograms for the remaining part of the brain stem. The mean and standard deviation of the MR values within these regions were calculated.

To compare particular brain stem structures, Perls' and SC stains were analysed using circular regions of interest (structure-ROIs) drawn on the original Perls' stains and overlapped on SC images for: nigrosome 1 (N) [8, 9] (also see Section 5.1), substantia nigra (SN), ventral tegmental area (VTA), cerebral peduncle (CP) and periaqueductal tissue (PAT), as shown in Figure 5.2.2.
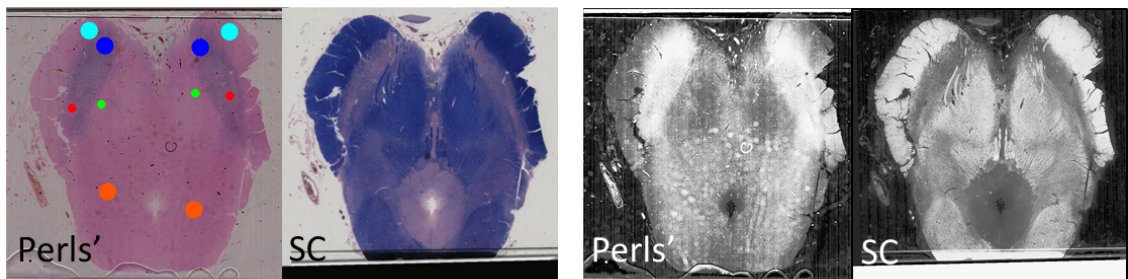
Figure 5.2.2: Perls' (iron), SC (myelin) stains of the PM brain stem, original (left) and converted to grey scale and inverted (right) with overlaid ROIs for N, SN, VTA, CP, PAT.

Mean values calculated for the stains within the structure-ROIs were compared. Structure-ROIs were overlaid on the co-registered slices of R_2^*, susceptibility and MTR maps and image values in these ROIs were correlated with Perls' and SC intensities (for sample HC1, MTR data were not acquired and the R_2^*-w image was omitted as having values incomparable with the R_2^* maps of two other samples due

to the different techniques used, as described in Section 5.1.1).

IN VIVO

Eight healthy subjects (33±11y.o.) were scanned at 3T (one dataset excluded due to insufficient coverage) and two subjects (29, 49y.o.) were imaged at 7T producing the following scans: high resolution T_2^* weighted (referred to as hr-T_2^*-w), PRESTO, multi-echo gradient echo sequence for R_2^* quantification (referred to as me-T_2^*-w), MT with one off-resonance pulse using FSE at 3T and a multi-pulse saturation train with an FFE readout at 7T. Scan details are presented in Table 5.2.1.

	name	resolution	slices	TR/TE/ΔTE	FA	additional	time
3T	hr-T_2^*-w	0.43x0.43mm	2D 8 x 1.5mm	300/50ms	42°	NSA=5, BW=216.8Hz	9:57
	me-T_2^*-w	0.7x0.7mm	2D 35 x 1.5mm	2122/7/10ms	80°	5 echoes, BW=173.6Hz	5:16
	MT-FSE	0.6x0.6mm	2D 8 x 2.5mm	699/9ms	90°	NSA=4, MTC=no/off BW=416.7Hz	2x9.23
	PRESTO	1.0x1.0mm	3D 200 x 1.0mm	15/21ms	10°	BW=191.2Hz	4:34
7T	hr-T_2^*-w	0.35x0.35mm	2D 20 x 1.0mm	525/16ms	40°	BW=67.5Hz	12:00
	me-T_2^*-w	1.0x1.0mm	3D 129 x 1.0mm	24/5/5ms	11°	4 echoes, BW=289.3Hz	7:31
	MT-TFE	0.5x0.5mm	3D 40 x 1.0mm	12/6.2ms	8°	MTC=no/off, BW=101.1Hz	11:18
	PRESTO	1.0x1.0mm	3D 200 x 1.0mm	13/18ms	10°	BW=883.3Hz	3:49

Table 5.2.1: Summary of the scanning parameters for HCs at two field strengths.

R_2^* maps were calculated by fitting the me-T_2^*-w data and MTR maps were created from the MT images using methods described in Section 2.3.3. The example images for both scans and field strengths are presented in Figure 5.2.3. Susceptibility maps were obtained from the 7T me-T_2^*-w data [59].
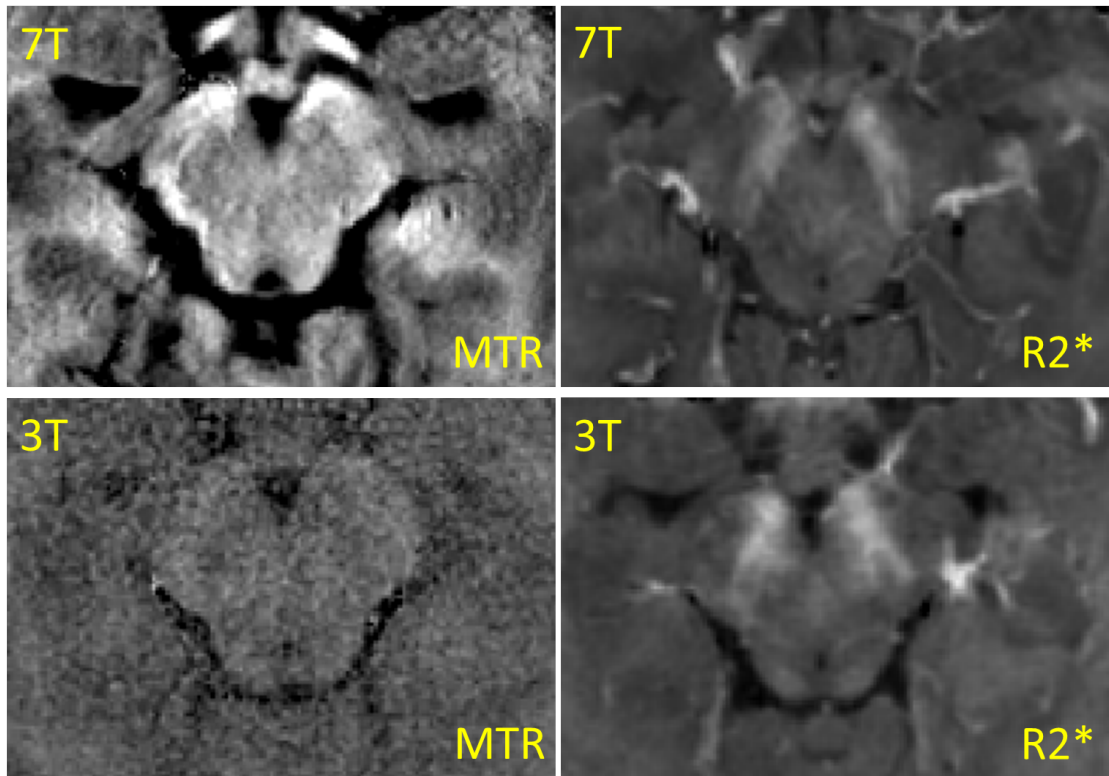
Figure 5.2.3: Example slices showing brain stem with the SN in MTR (left, so called neuromelanin scan for 3T) and R_2^* (right) images acquired in 7T (top) and 3T (bottom).

Circular structure-ROIs were drawn on the slices of hr-T_2^*-w data sets in which nigrosome 1 was clearly visible (2x1.5mm slices in 3T images and 3x1mm slices in 7T images) for the following structures: N, SN, VTA, CP, PAT, white matter (WM) and grey matter (GM) of the medial-temporal lobe; structure-ROIs for the red nucleus (RN) were placed on higher slices in the 7T data (the 3T scan did not have sufficient coverage). The diameter of the structure-ROIs was 8 voxels for SN, RN, CP, WM, GM and PAT, and 4 voxels for N and VTA. The example slices of 7T and 3T hr-T_2^*-w images with all the structure-ROIs, except of those for RN, are presented in Figure 5.2.4.
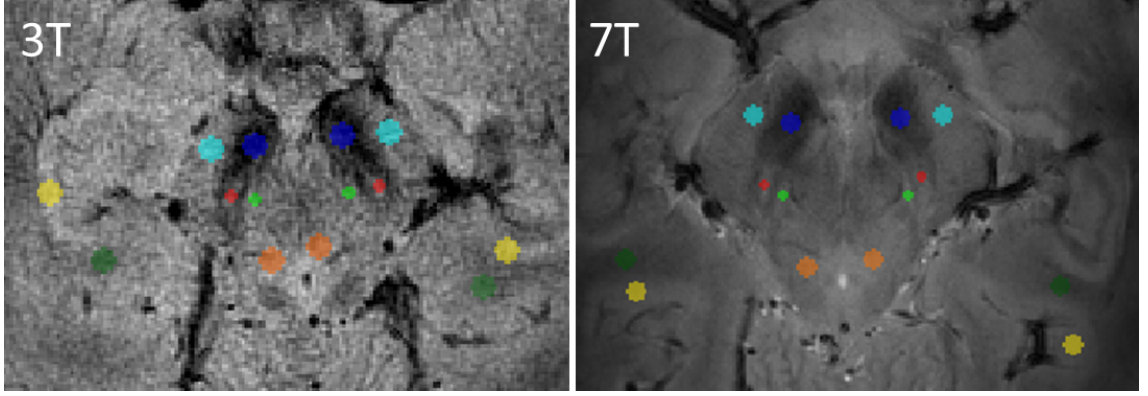
Figure 5.2.4: Two slices of hr-T_2^*-w aquired in 3T (left) and 7T (right) with overlaid ROIs: N, SN, VTA, CP, WM, GM, PAT and RN (not in the picture).

Structure-ROIs masks, R_2^*, susceptibility and MTR maps were co-registered to PRESTO images (which had greatest coverage) with FLIRT, FSL [30], to allow all the images to be transferred to the same space. Mean values calculated for the structure-ROIs, averaged across all subjects and slices, were compared for R_2^*, susceptibility and MTR maps obtained in vivo at 3T and 7T and PM at 7T magnetic field. In vivo and PM 7T R_2^*, susceptibility and MTR maps were correlated with Perls' and SC stains, and stains were correlated with each other, for the corresponding structure-ROIs.

Gradients of the linear fits for all correlations of the in vivo and PM data were compared. Those calculated PM for whole-stem were averaged across three samples (omitting values obtained for R_2^* images of the HC1 sample).

5.2.2 RESULTS

CORRELATION ACROSS WHOLE STEM, PM

Figures 5.2.5 and 5.2.6 show R_2^* and susceptibility maps (respectively) for all three PM samples with overlaid masks of whole-stem (red), high-Perls (blue) and high-SC (green). Additionally, the right column of Figure 5.2.5 shows overlap between high-SC and high-Perls. MTR maps with overlaid whole-stems (red) and high-SC (green) are presented in Figure 5.2.7.
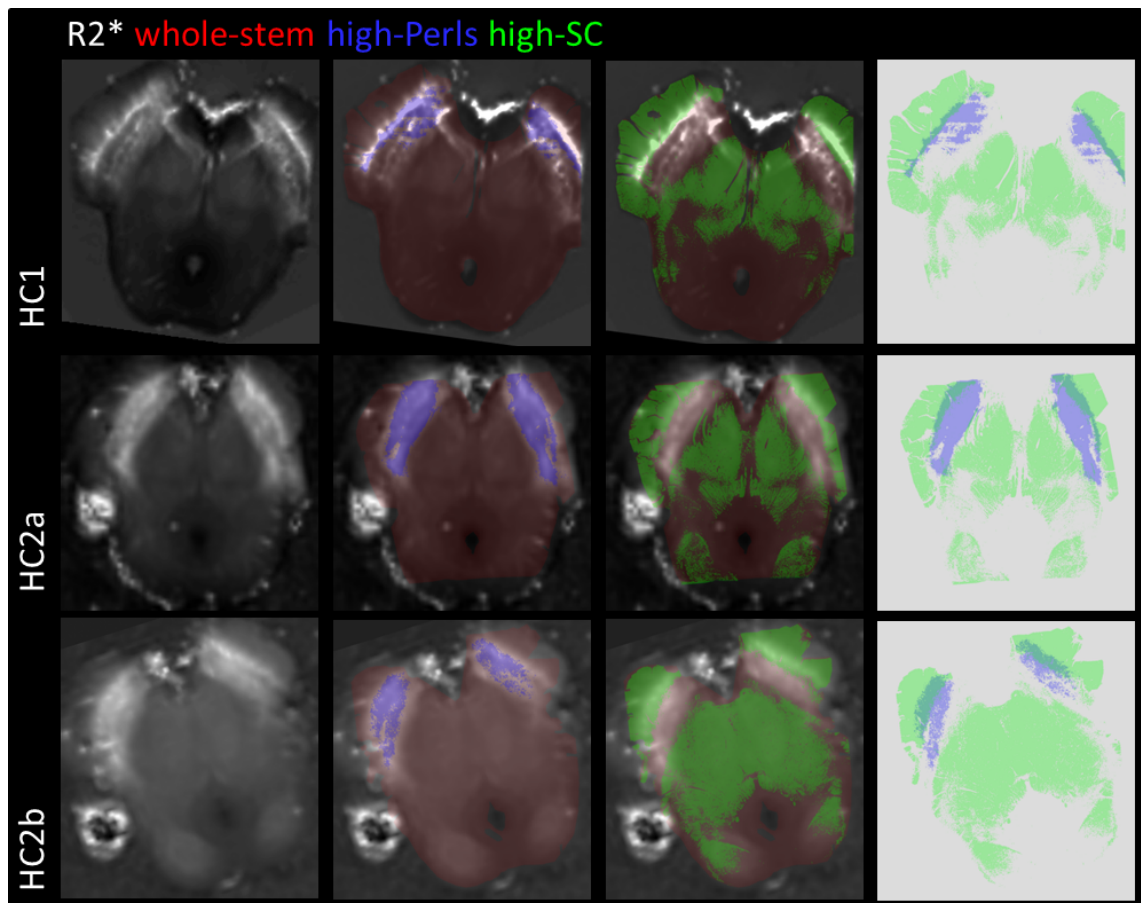
Figure 5.2.5: Images of three samples of two healthy PM brain stems (HC1, HC2a, HC2b); R_2^* maps with overlaid whole-stem, high-Perls and high-SC; 3rd column presents overlapped high-SC and high-Perls.
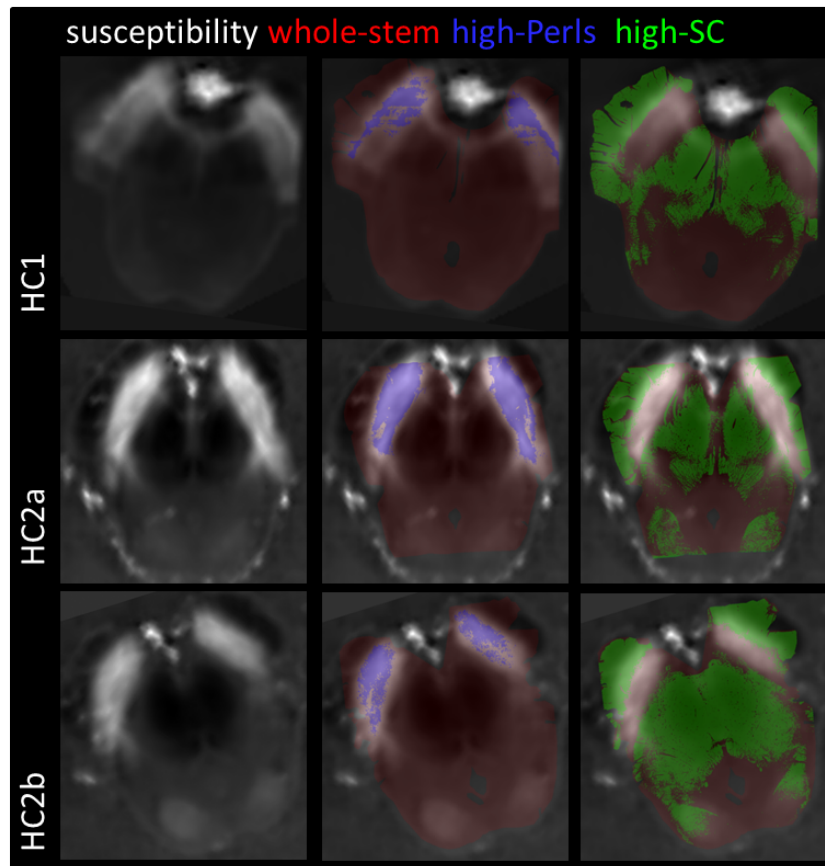
Figure 5.2.6: Images of three samples of two healthy PM brain stems (HC1, HC2a, HC2b); susceptibilty maps with overlaid whole-stem, high-Perls and high-SC.
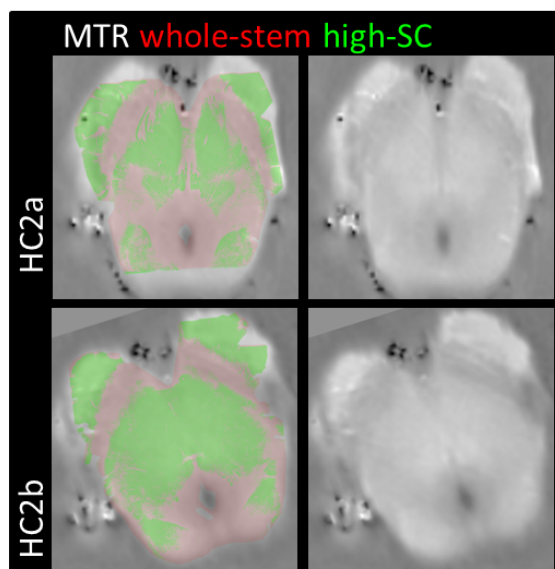
Figure 5.2.7: Images of two samples from a healthy PM brain stem (HC2a, HC2b); MTR maps with (1st column) and without (2nd column) overlaid high-SC and whole-stem;

Scatter-plots showing the correlations between R_2^*, susceptibility and MTR versus Perls' and SC with linear fits and outliers ($\pm 2 \times$standard deviation) marked in grey

are presented for one example sample in Figure 5.2.8 and the correlation coefficients for all the samples are summarised in Table 5.2.2. Similar scatter-plots obtained for range of values limited by the high-Perls and high-SC masks are presented in Figure 5.2.9.
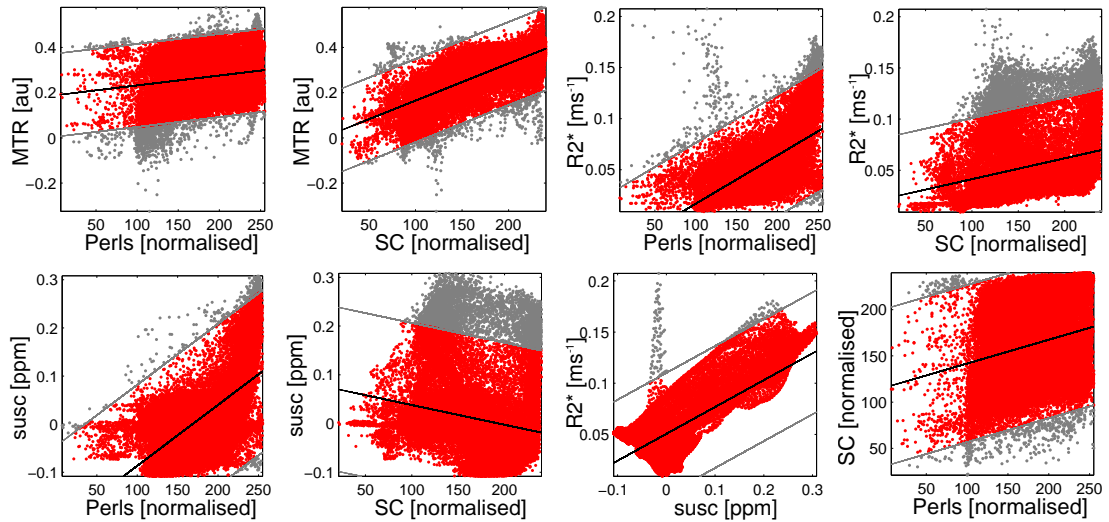
Figure 5.2.8: Plotted values of MTR, R_2^* and susceptibility versus Perls' and SC stains, and stains against each other, for HC2b sample within the whole-stem; black lines correspond to the fitted straight line and outliers ($\pm 2 \times$standard deviation) are plotted in grey.
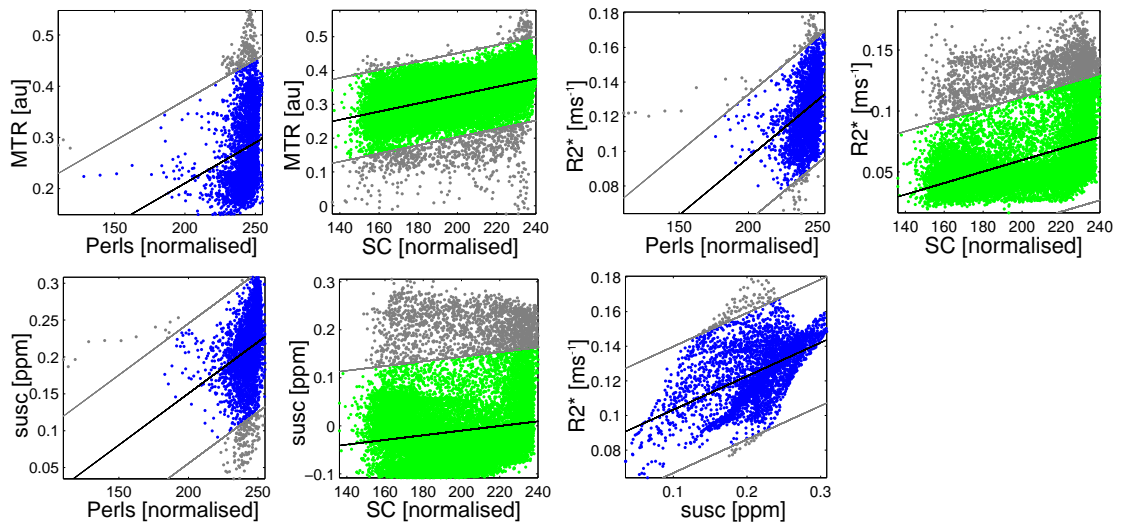
Figure 5.2.9: Plotted values of MTR, R_2^* and susceptibility versus SC and Perls stains, and stains against each other, for HC2b sample within the high-Perls and high-SC regions; black lines correspond to the fitted straight line and outliers ($\pm 2 \times$standard deviation) are plotted in grey.

	HC1	HC2a	HC2b
MTR vs Perls		$0.00^{\dagger}$	0.19
MTR vs SC		0.57	0.76
R_2^* vs Perls	0.69	0.60	0.65
R_2^* vs SC	0.33	0.14	0.29
susc vs Perls	0.69	0.63	0.62
susc vs SC	-0.04	-0.18	-0.20
R_2^* vs susc	0.85	0.85	0.74
SC vs Perls	0.19	0.05	0.25

Table 5.2.2: Summary of the correlation coefficients calculated for R_2^*, susceptibility and MTR maps versus Perls' and SC stained images in the PM samples for whole-stem; non-significant correlation is indicated with †.

Histograms of R_2^*, susceptibility and MTR, for high-Perls/-SC and the rest of the brain stem are presented in Figure 5.2.10.
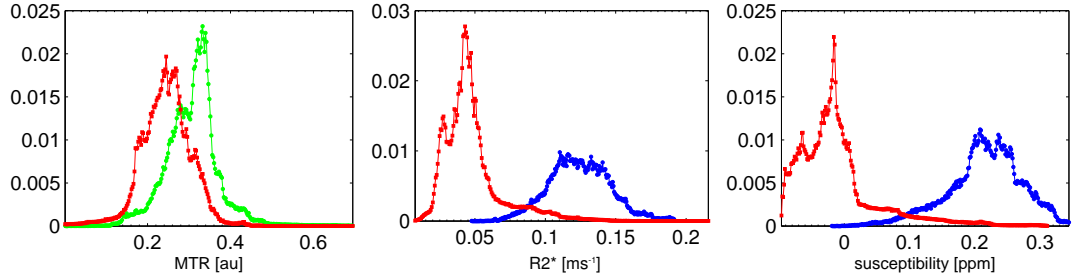
Figure 5.2.10: Normalised histograms of R_2^*, susceptibility and MTR values within high-Perls, high-SC and the rest of the stem, for HC2a sample; negative values of MTR were not shown in the plot, as they corresponded to the background region outside of the brain stem that was not removed by the mask.

Mean and standard deviation values were calculated within the high-Perls and high-SC masks and also in the remaining part of the brain stem for all the samples on R_2^*, susceptiblity and MTR, as summarised in Table 5.2.3.

| sample	image	high-Perls	high-SC	rest
HC1	R_2^*-w [au]	0.13 ± 0.03		0.47 ± 0.03
	susc [ppm]	0.36 ± 0.09		0.06 ± 0.09
HC2a	R_2^* [ms^{-1}]	0.12 ± 0.02		0.05 ± 0.02
	susc [ppm]	0.21 ± 0.06		-0.01 ± 0.06
	MTR [au]		1.34 ± 0.07	1.28 ± 0.07
HC2b	R_2^* [ms^{-1}]	0.12 ± 0.02		0.05 ± 0.02
	susc [ppm]	0.21 ± 0.05		0.00 ± 0.07
	MTR [au]		1.27 ± 0.06	1.15 ± 0.08

Table 5.2.3: Summary of the mean and standard deviation R_2^*, susceptibility and MTR values calculated for all three samples for the regions corresponding to high-Perls, high-SC and whole-stem.

STRUCTURE-ROIS ANALYSIS

Mean values of R_2^*, susceptibility and MTR obtained in vivo at 3T and 7T and PM at 7T, are presented for all the structures in bar plots in Figure 5.2.11; R_2^* and MTR values of all the structures for both field strengths in vivo are detailed in Table 5.2.4.
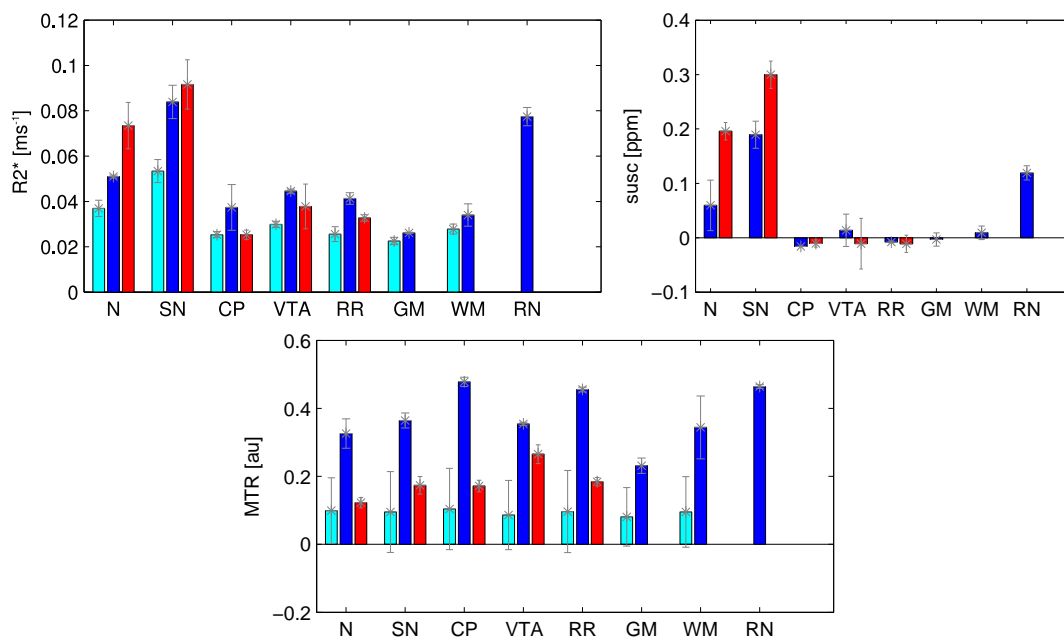
Figure 5.2.11: Mean values for all the structure-ROIs in R_2^*, susceptibility and MTR maps obtained in vivo in 3T, in vivo in 7T and PM in 7T.

	R_2^* [s^{-1}]		MTR [au]	
	3T	7T	3T	7T
nigrosome 1 (N)	36.9 ±3.6	51.0 ±0.7	0.099 ±0.10	0.330 ±0.040
substantia nigra (SN)	53.4 ±5.1	83.9 ±7.4	0.095 ±0.12	0.360 ±0.020
cerebral peduncle (CP)	25.3 ±1.3	37.4 ±10.0	0.104 ±0.12	0.480 ±0.010
ventral tegmental area (VTA)	29.9 ±1.4	44.6 ±0.9	0.086 ±0.10	0.354 ±0.005
periaqueductal tissue (PAT)	25.6 ±3.3	41.3 ±2.5	0.096 ±0.12	0.455 ±0.007
grey matter (GM)	22.6 ±1.6	26.2 ±0.2	0.081 ±0.09	0.230 ±0.020
white matter (WM)	27.8 ±2.2	34.0 ±4.9	0.095 ±0.10	0.340 ±0.090
red nucleus (RN)		77.5 ±4.0		0.460 ±0.005

Table 5.2.4: Mean values of R_2^* and MTR calculated for both field strengths across all the subjects using ROIs: N, SN, CP, VTA, PAT, GM,WM and RN.

Figure 5.2.12 presents a comparison of the mean normalised Perls' and SC stain values calculated within the structure-ROIs.
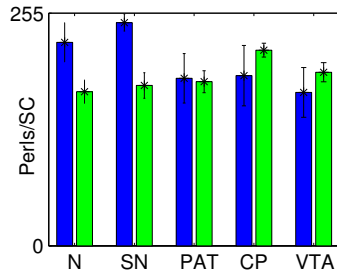
Figure 5.2.12: Mean values of normalised Perls' and SC stain intensity calculated within structure-ROIs.

Correlation of the stains with in vivo and PM MRI is presented in Figure 5.2.13 and the recorded correlation coefficients are summarised in Table 5.2.5.
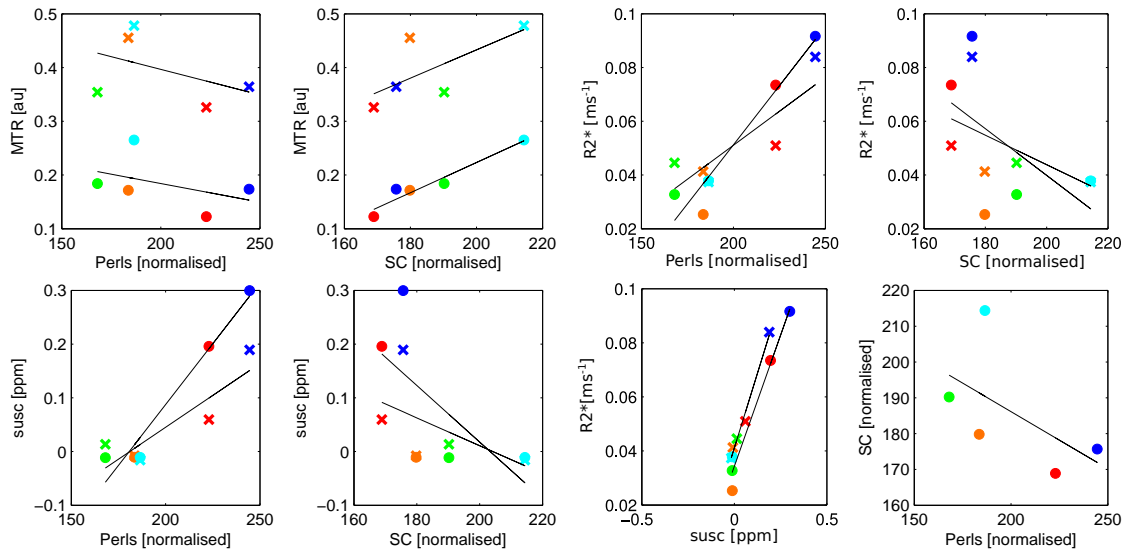
Figure 5.2.13: Plots showing correlation of 7T in vivo $\times$ and PM $\bullet$ R_2^*, susceptibility and MTR values with Perls' and SC stains, and stains with each other for corresponding structure-ROIs: N, SN, VTA, CP, PAT; correlation coefficients are presented in Table 5.2.5.

	in vivo	post mortem
MTR vs Perls	-0.45	-0.42
MTR vs SC	0.70	0.97*
R_2^* vs Perls	0.85†	0.96*
R_2^* vs SC	-0.52	-0.54
susc vs Perls	0.87*	0.98*
susc vs SC	-0.55	-0.64
R_2^* vs susc	0.99*	0.99*
SC vs Perls		-0.57

Table 5.2.5: Correlation coefficients for MRI and histology measures of iron and myelin calculated for post mortem and in vivo MR data; significant correlations were indicated with * and correlation with p=0.07 with †.

A summary of the gradient values from the linear fits from all the plots used in the

correlation analysis is presented in Table 5.2.6.

| | in vivo [$\times 10^{-3}$] | post mortem [$\times 10^{-3}$] | | |
	structure-ROIs	structure-ROIs	whole-stem	
MTR [au] vs Perls' [normalised]	-0.95	-0.69	0.22 ± 0.31	A_{PS}
MTR [au] vs SC [normalised]	2.63	2.81	1.36 ± 0.40	A_{SC}
$R_2^*[ms^{-1}]$ vs Perls' [normalised]	0.51	0.88	0.48 ± 0.01	B_{PS}
$R_2^*[ms^{-1}]$ vs SC [normalised]	-0.55	-0.87	0.16 ± 0.06	B_{SC}
susc [ppm] vs Perls' [normalised]	2.37	4.53	1.69 ± 0.55	C_{PS}
susc [ppm] vs SC [normalised]	-2.60	-5.27	-0.33 ± 0.17	C_{SC}
$R_2^*[ms^{-1}]$ vs susc [ppm]	221	194	276 ± 20	
SC [normalised] vs Perls' [normalised]		-318	176 ± 114	

Table 5.2.6: Summary of the gradients of the linear fits for all the correlations presented in Tables 5.2.2 and 5.2.5; the last column lists the names corresponding to the whole-stem coefficients, which are used further in the discussion of this section.

5.2.3 DISCUSSION

Two histochemical stains were used in this study: Perls' was used to investigate iron content in tissue and solochrome cyanine (SC) was used for myelin. Comparison of high-Perls and high-SC masks in Figure 5.2.5 revealed their partial overlap in the region of the pars reticulata of the SN (SNpr). This is possibly caused by lack the of sharp boundaries between the SNpr and cerebral peduncle (CP), so that CP myelinated fibres coexist with the high iron region of the SN in its most lateral part. Further histological investigation should confirm the source of this effect.

MTR AND MYELIN

It has previously been shown that MTR is a marker of the myelin content [50, 61]. MTR mapping is a technique widely used for monitoring demylineation and axonal damage in neurodegenerative diseases, especially in multiple sclerosis [10, 22, 25, 29] (also see Sections 6.1 and 6.2). However, other tissue properties related to inflammation have also been reported to affect MTR contrast [18, 54, 57].
Correlation of the PM MTR pixel values with the SC stain intensities across the whole-stem (Figures 5.2.7, 5.2.8 and Table 5.2.2) confirmed that MTR relates to the myelin distribution (as measured by the SC stain) in tissue within the healthy brain stem. Considering the structure-ROIs this correlation was significant in PM

data and tended towards significance in vivo (Figure 5.2.13 and Table 5.2.5), which is expected since the same samples were used for PM MRI/histology, but different samples were used in vivo. The correlation coefficient (R=0.97) was higher than the value previously reported (R=0.84) by Schmierer at el. [50] for PM MTR and myelin quantification measure based on a Luxol fast blue (LFB) stain. This is probably due to the high field MRI used here. When only the high-SC region was considered, a trend for a correlation between MTR and SC remained (Figure 5.2.9), suggesting that MTR reflects myelin variation even within the narrow range of myelin concentration values and that SC stain does not reach a level of full saturation.

There was no significant correlation between MTR and the Perls' stain within the whole-stem, the high-Perls region (Table 5.2.2, Figures 5.2.8 and 5.2.9) or the structure-ROIs (Table 5.2.5), suggesting that there is no dependence of the MTR contrast on iron. This implies that iron does not cause sufficient frequency shift to change MTR signal. However, comparing Figures 5.2.8 and 5.2.13 a trend for a negative correlation between MTR and Perls' stain calculated for the structure-ROIs can be seen, which was not present for the whole-stem. Since this was only seen for structure-ROIs it could possibly be explained by the choice of ROI representing structures of the brain stem of either high-iron and low-myelin (N, SN) or the opposite combination (CP, VTA), as presented in Figure 5.2.12.

Overlaying histograms of MTR values for the high-SC region and the rest of the stem, showed partial overlap, but two peaks were distinguishable confirming again the sensitivity of MTR to myelin content represented by the SC stain (Figure 5.2.10, Table 5.2.3).

R_2^*, SUSCEPTIBIITY AND IRON

The sensitivity of R_2^* contrast to the iron content within deep GM (dGM) structures previously shown both in vivo [20, 45, 46, 60] and post mortem [32] was confirmed in this study by the significant correlations between R_2^* maps and Perls' stained

images found PM within the whole-stem and within structure-ROIs (Figures 5.2.5, 5.2.8 and 5.2.13, Tables 5.2.2 and 5.2.5). Susceptibility values [59] (see Section 2.3.5) also correlated with the intensities of the Perls' stain, both PM and in vivo, as expected (Figures 5.2.6, 5.2.8, 5.2.13, Tables 5.2.2 and 5.2.5).

The trends corresponding to the whole-stem correlations were also present in high-Perls regions suggesting that both R_2^* and susceptibility are sensitive to the iron content variation and that the Perls' stain is not fully saturated within the narrow range of high-iron concentrations (Figure 5.2.9). Overlaying histograms of R_2^* and susceptibility values for high-Perls and the rest of the stem ROIs showed good distinction of these two regions in terms of R_2^* and susceptibility values (Figure 5.2.10, Table 5.2.2).

There was no significant correlation between the R_2^* or susceptibility values and the SC stain representing myelin content for whole-stem (Figures 5.2.5, 5.2.6 and 5.2.8). However there was a trend for a negative correlation for susceptibility and positive correlation for R_2^* (Table 5.2.2), which agrees with the previous results suggesting opposite effects of myelin on these two measures [34, 36].

R_2^* and susceptibility maps strongly correlated with each other, in vivo and PM, confirming that they both reflect the same tissue characteristics (Figure 5.2.8, 5.2.13). The linear dependence of these measures on the iron content suggested that within dGM their values are dominated by the effect of iron, which is in agreement with results of a recent in vivo study [12]. However, stronger correlations found between susceptibility and Perls' than between R_2^* and Perls' (Tables 5.2.2 and 5.2.5), the significance of the in vivo correlation between susceptibility and Perls' within the structure-ROIs (Table 5.2.5), and lack of correlation between susceptibility and SC values even within the high-SC region (Table 5.2.2) may suggest that in dGM susceptibility reflects iron content more accurately than R_2^*.

This study confirmed that R_2^* and susceptibility contrast are related to iron and that MTR corresponds to myelin content in tissue. Table 5.2.6 presents the gradient values of the lines fitted in the correlation analysis, summarising relations found between MRI measures and histological markers of iron and myelin content. Considering the whole-stem correlations as the most reliable indicator (calculated for the widest range of values and providing significant correlations, with one exception) and assuming that Perls' and SC are quantitative measures of iron and myelin, then the coefficients obtained for the linear fits can be used to parametrise the dependence of MTR, R_2^* and susceptibility on iron and myelin concentration, represented by x_m and x_i, respectively:

$$
\begin{cases}
MTR(x_m, x_i) = A_{SC}x_m + A_{PS}x_i + A \\
R_2^*(x_m, x_i) = B_{SC}x_m + B_{PS}x_i + B \\
\chi(x_m, x_i) = C_{SC}x_m + C_{PS}x_i + C
\end{cases}
\tag{5.1}
$$

where A, B and C represent intercept values of the linear fits combined with a contribution of the factors different than iron and myelin to the contrast. This approach could potentially provide a method for mapping iron and myelin content of in vivo, however there are several limitations which need to be overcome. First, this study focused on brain stem tissue, and the results are therefore valid only for brain stem structures and it needs to be confirmed that the same relationship holds in the rest of the brain. To extend these findings to the whole brain, investigation regarding other parts of the brain is necessary. Second, the number of PM samples used here was small and the analysis of more samples is needed to validate these results. Third, and most importantly, the intensities of the Perls' and SC stains used in this study are not truly quantitative measures and can not be easily converted to iron concentration values.

Comparison of the in vivo and PM, 3T and 7T R_2^* values in the structure-ROIs showed that in vivo R_2^* values were higher at 7T than 3T for all the structures (especially in high iron areas) as shown by the bar plots in Figure 5.2.11. This finding is in agreement with a previous study analysing the dependence of R_2^* contrast on the field strength [47]. Values recorded for the SN and nigrosome 1, N, were both high, therefore the hyperintense appearance of the nigrosome 1 on T_2^* weighted images at 3T and 7T is only an effect of the relative contrast with the neighbouring SN. Susceptibility values obtained at 7T were high in high iron structures (N, SN, RN) and close to zero in the remaining structures (relative to white matter). Susceptibility values were also higher PM than in vivo (except for the VTA, but for that structure both values were very small). MTR values obtained in vivo at 3T were low compared to 7T, because of the low MT sensitivity of the 3T sequence, compared to the 7T one, and PM 7T values were lower than in vivo 7T (but higher than 3T in all the structures), presumably due to changes in water content and proton exchange resulting from fixation.

This comparison also revealed that in high iron (SN and N) regions, 7T PM values of R_2^* were higher than those obtained in vivo. The increase of the iron concentration in a brain with age [28] can not explain this finding, as in vivo subjects in the study were not significantly younger than PM subject used for analysis (mean 39y.o. vs 46y.o.) compared to the trends of iron increase with age. These regions had also lower MTR values and higher susceptibility PM, so high R_2^* PM may be related to changes in water or myelin content, as well as directly or indirectly to iron. It could be due to the increase in iron content related to the changes in PM tissue, or due to increased heterogeneity in iron distribution, which was previously observed in PM T_2^*-w images compared to in vivo (see Figures 5.1.3 and 5.1.7). Another possible explanation would be a change in tissue absolute susceptibility, which can not be seen directly in our experimental measurements as only relative susceptibility is measured, but which can make iron-tissue differences bigger. Potentially, the results

may also be affected by the fact that both PM samples used for the calculations were taken from the same subject. Therefore further investigation involving more samples and additional high iron structures is necessary to understand origins of this finding.

5.3 Conclusions

Detailed anatomy of healthy and parkinsonian substantia nigra studied in Section 5.1 used in vivo and post mortem MRI data to identify nigrosome 1, the sub-structure of the SN suffering high loss of the dopaminergic neurons in PD. Further, in vivo investigation showed that this structure allows classification of the PD patients in 7T and possibly also 3T MRI.

The quantitative part of this chapter, Section 5.2, investigated properties of the healthy brain stem tissue in vivo and post mortem. Analysis focused on iron and myelin concentrations within the whole stem and within its particular structures showing correlations between MRI and histology measures. Susceptibility mapping was found to provide a better correlation with iron content than R_2^*. A potential approach for in vivo iron and myelin mapping was presented. These findings could be used to improve knowledge regarding brain stem tissue changes in Parkinson's disease as well as for the optimisation of MRI sequences used for imaging iron and myelin in deep grey matter.

Future work will include longitudinal and quantitative analysis of nigrosome 1 regarding its possible use as a disease progression marker and on developing in vivo method of iron and myelin mapping proposed in this study.

References

[1] D. P. Auer, *In vivo imaging markers of neurodegeneration of the substantia nigra.*, Experimental Gerontology, 44 (2009), pp. 4–9.

[2] F. Bagnato, S. Hametner, B. Yao, P. van Gelderen, H. Merkle, F. K. Cantor, H. Lassmann, and J. H. Duyn, *Tracking iron in multiple*

sclerosis: a combined imaging and histopathological study at 7 Tesla., Brain, 134 (2011), pp. 3602–15.

[3] N. P. S. BAJAJ, V. GONTU, J. BIRCHALL, J. PATTERSON, D. G. GROSSET, AND A. J. LEES, *Accuracy of clinical diagnosis in tremulous parkinsonian patients: a blinded video study.*, Journal of Neurology, Neurosurgery & Psychiatry, 81 (2010), pp. 1223–8.

[4] S. BARON AND D. WOOD, *Rec. 601 — the origins of the 4:2:2 DTV standard*, in EBU Technical Review, no. October, 2005, pp. 1–11.

[5] D. BERG, *Substantia nigra hyperechogenicity is a risk marker of Parkinson's disease: yes.*, Journal of Neural Transmission, 118 (2011), pp. 613–9.

[6] Z.-H. CHO, Y.-B. KIM, J.-Y. HAN, H.-K. MIN, K.-N. KIM, S.-H. CHOI, E. VEKLEROV, AND L. A. SHEPP, *New Brain Atlas — Mapping the Human Brain In Vivo with 7.0 T MRI and Comparison with Postmortem Histology: Will These Images Change Modern Medicine?*, International Journal of Imaging Systems and Technology, 18 (2008), pp. 2–8.

[7] Z.-H. CHO, S.-H. OH, AND J.-M. KIM, *Direct Visualization of Parkinson's Disease by In Vivo Human Brain Imaging Using 7.0T Magnetic Resonance Imaging*, Movement Disorders, 26 (2011), pp. 713–755.

[8] P. DAMIER, E. C. HIRSCH, Y. AGID, AND A. M. GRAYBIEL, *The substantia nigra of the human brain I. Nigrosomes and the nigral matrix , a compartmental organization based on calbindin D 28K immunohistochemistry*, Brain, 122 (1999), pp. 1421–1436.

[9] ——, *The substantia nigra of the human brain II. Patterns of loss of dopamine-containing neurons in Parkinson's disease*, Brain, 122 (1999), pp. 1437–1448.

[10] G. R. DAVIES, *Evidence for grey matter MTR abnormality in minimally disabled patients with early relapsing-remitting multiple sclerosis*, Journal of Neurology, Neurosurgery & Psychiatry, 75 (2004), pp. 998–1002.

[11] R. DE LA FUENTE-FERNÁNDEZ, *Role of DaTSCAN and clinical diagnosis in Parkinson disease.*, Neurology, 78 (2012), pp. 696–701.

[12] A. DEISTUNG, A. SCHÄFER, F. SCHWESER, U. BIEDERMANN, R. TURNER, AND J. R. REICHENBACH, *Toward in vivo histology: A comparison of quantitative susceptibility mapping (QSM) with magnitude-, phase-, and R2*-imaging at ultra-high magnetic field strength*, NeuroImage, 65 (2013), pp. 299–314.

[13] B. DRAYER, P. BURGER, R. DARWIN, S. RIEDERER, R. HERFKENS, AND G. A. JOHNSON, *MRI of brain iron.*, AJR. American journal of roentgenology, 147 (1986), pp. 103–10.

[14] B. DRAYER, P. BURGER, B. HURWITZ, D. DAWSON, AND J. CAIN, *Reduced signal intensity on MR images of thalamus and putamen in multiple sclerosis: increased iron content?*, American Journal of Roentgenology, 149 (1987), pp. 357–63.

[15] M. EAPEN, D. H. ZALD, J. C. GATENBY, Z. DING, AND J. C. GORE, *Using High-Resolution MR Imaging at 7T to Evaluate the Anatomy of the Midbrain*, American Journal of Neuroradiology, 32 (2011), pp. 688–694.

[16] J. M. FEARNLEY AND A. J. LEES, *Ageing and Parkinson's disease: substantia nigra regional selectivity*, Brain, 114 (1991), pp. 2283–2301.

[17] A. FRIEDMAN, J. GALAZKA-FRIEDMAN, AND D. KOZIOROWSKI, *Iron as a cause of Parkinson disease - a myth or a well established hypothesis?*, Parkinsonism & Related Disorders, 15 Suppl 3 (2009), pp. S212–4.

[18] P. J. GAREAU, B. K. RUTT, S. J. KARLIK, AND J. R. MITCHELL, *Magnetization Transfer and Multicomponent T2 Relaxation Measurements With Histopathologic Correlation in an Experimental Model of MS*, Journal of Magnetic Resonance Imaging, 11 (2000), pp. 586–595.

[19] K. Gellein, T. P. Flaten, K. M. Erikson, M. Aschner, and T. Syversen, *Leaching of trace elements from biological tissue by formalin fixation.*, Biological Trace Element Research, 121 (2008), pp. 221–5.

[20] N. Gelman, J. M. Gorell, P. B. Barker, R. M. Savage, E. M. Spickler, J. P. Windham, and R. a. Knight, *MR imaging of human brain at 3.0T: preliminary report on transverse relaxation rates and relation to estimated iron content.*, Radiology, 210 (1999), pp. 759–67.

[21] J. C. Gore, Y. S. Kang, and R. J. Schulz, *Measurement of radiation dose distributions by nuclear magnetic resonance (NMR) imaging.*, Physics in Medicine and Biology, 29 (1984), pp. 1189–97.

[22] M. Gozzi, D. M. Nielson, R. K. Lenroot, J. L. Ostuni, D. A. Luckenbaugh, A. E. Thurm, J. N. Giedd, and S. E. Swedo, *A Magnetization Transfer Imaging Study of Corpus Callosum Myelination in Young Children with Autism*, Biological psychiatry, 72 (2012), pp. 215–220.

[23] J. M. Graham, M. N. J. Paley, R. A. Gru, N. Hoggard, and P. D. Griffiths, *Brain iron deposition in Parkinson ' s disease imaged using the PRIME magnetic resonance sequence*, Brain, 123 (2000), pp. 2423–2431.

[24] P. D. Griffiths, B. R. Dobson, G. R. Jones, and D. T. Clarke, *Iron in the basal ganglia in Parkinson's disease. An in vitro study using extended X-ray absorption fine structure and cryo-electron microscopy*, Brain, 122 (1999), pp. 667–673.

[25] R. Grossman, *Magnetization transfer in multiple sclerosis*, Ann Neurol, 36 Suppl (1994), pp. S–97–9.

[26] E. M. Haacke, N. Y. C. Cheng, M. J. House, Q. Liu, J. Neelavalli, R. J. Ogg, A. Khan, M. Ayaz, W. Kirsch, and A. Obenaus, *Imaging iron stores in the brain using magnetic resonance imaging.*, Magnetic Resonance Imaging, 23 (2005), pp. 1–25.

[27] D. E. HAINES, *Fundamental Neuroscience for Basic and Clinical Applications*, 2006.

[28] B. HALLGREN AND P. SOURANDER, *The Effect Oof Age on the Non-heamin Iron in the Human Brain*, Journal of Neurochemistry, 3 (1958), pp. 41–51.

[29] S. J. HICKMAN, A. T. TOOSY, S. J. JONES, D. R. ALTMANN, K. A. MISZKIEL, D. G. MACMANUS, G. J. BARKER, G. T. PLANT, A. J. THOMPSON, AND D. H. MILLER, *Serial magnetization transfer imaging in acute optic neuritis.*, Brain : a journal of neurology, 127 (2004), pp. 692–700.

[30] M. JENKINSON AND S. SMITH, *A global optimisation method for robust affine registration of brain images*, Medical Image Analysis, 5 (2001), pp. 143–156.

[31] D.-H. KWON, J.-M. KIM, S.-H. OH, H.-J. JEONG, S.-Y. PARK, E.-S. OH, J.-G. CHI, Y.-B. KIM, B. S. JEON, AND Z.-H. CHO, *Seven-Tesla magnetic resonance images of the substantia nigra in Parkinson disease.*, Annals of Neurology, 71 (2012), pp. 267–77.

[32] C. LANGKAMMER, N. KREBS, W. GOESSLER, E. SCHEURER, F. EBNER, K. YEN, F. FAZEKAS, AND S. ROPELE, *Quantitative MR Imaging of Brain Iron: A Postmortem Validation Study*, Radiology, 257 (2010), pp. 455–462.

[33] C. LANGKAMMER, F. SCHWESER, N. KREBS, A. DEISTUNG, W. GOESSLER, E. SCHEURER, K. SOMMER, G. REISHOFER, K. YEN, F. FAZEKAS, S. ROPELE, AND J. R. REICHENBACH, *Quantitative susceptibility mapping (QSM) as a means to measure brain iron? A post mortem validation study.*, NeuroImage, 62 (2012), pp. 1593–9.

[34] J. LEE, K. SHMUELI, B.-T. KANG, B. YAO, M. FUKANAGA, P. VAN GELDEREN, S. PALUMBO, F. BOSETTI, A. C. SILVA, AND J. H. DUYN, *The contribution of myelin to magnetic susceptibility-weighted contrasts in high-field MRI of the brain*, NeuroImage, 59 (2012), pp. 3967–3975.

[35] S. Lehéricy, M. a. Sharman, C. L. D. Santos, R. Paquin, and C. Gallea, *Magnetic resonance imaging of the substantia nigra in Parkinson's disease.*, Movement Disorders, 27 (2012), pp. 822–30.

[36] C. Liu, W. Li, G. A. Johnson, and B. Wu, *High-field (9.4 T) MRI of brain dysmyelination by quantitative mapping of magnetic susceptibility*, NeuroImage, 56 (2011), pp. 930–938.

[37] A. K. Lotfipour, S. Wharton, S. T. Schwarz, V. Gontu, A. Schäfer, A. M. Peters, R. W. Bowtell, D. P. Auer, P. a. Gowland, and N. P. S. Bajaj, *High resolution magnetic susceptibility mapping of the substantia nigra in Parkinson's disease.*, Journal of Magnetic Resonance Imaging, 35 (2012), pp. 48–55.

[38] J. Maclaren, K. Lee, C. Luengviriya, O. Speck, and Z. M, *Combined prospective and retrospective motion correction to relax navigator requirements.*, Magnetic Resonance in Medicine, 65 (2011), pp. 1724–32.

[39] J. K. Mai and P. George, *The Human Nervous System*, Elsevier, 2nd ed., 2004.

[40] L. A. Massey and T. A. Yousry, *Anatomy of the substantia nigra and subthalamic nucleus on MR imaging.*, Neuroimaging Clinics of North America, 20 (2010), pp. 7–27.

[41] R. Meguro, Y. Asano, H. Iwatsuki, and K. Shoumura, *Perfusion-Perls and -Turnbull methods supplemented by DAB intensification for nonheme iron histochemistry: demonstration of the superior sensitivity of the methods in the liver, spleen, and stomach of the rat.*, Histochemistry and cell biology, 120 (2003), pp. 73–82.

[42] R. A. Menke, S. Jbabdi, K. L. Miller, P. M. Matthews, and M. Zarei, *Connectivity-based segmentation of the substantia nigra in*

human and its implications in Parkinson's disease, NeuroImage, 52 (2010), pp. 1175–1180.

[43] R. A. Menke, J. Scholz, K. L. Miller, S. Deoni, S. Jbabdi, P. M. Matthews, and M. Zarei, *MRI characteristics of the substantia nigra in Parkinson's disease: A combined quantitative T1 and DTI study*, NeuroImage, 47 (2009), pp. 435–441.

[44] L. Minati, M. Grisoli, F. Carella, T. D. Simone, M. G. Bruzzone, and M. Savoiardo, *Imaging Degeneration of the Substantia Nigra in Parkinson Disease with Inversion-Recovery*, AJNR, 28 (2007), pp. 309–313.

[45] R. J. Ordidge, J. M. Gorell, J. C. Deniau, R. A. Knight, and J. A. Helpern, *Assessment of Relative Brain Iron Concentrations Using T2-Weighted and T2*-Weighted MRI at 3 Tesla*, Magnetic Resonance in Medicine, 32 (1994), pp. 335–341.

[46] O. Peran, P. Celsis, C. Caltagirone, G. Spalletta, and U. Sabatini, *Volume and iron content in basal ganglia and thalamus.*, Human brain mapping, 30 (2009), pp. 2667–75.

[47] A. M. Peters, M. J. Brookes, F. G. Hoogenraad, P. a. Gowland, S. T. Francis, P. G. Morris, and R. Bowtell, *T2* measurements in human brain at 1.5, 3 and 7 T.*, Magnetic resonance imaging, 25 (2007), pp. 748–53.

[48] A. C. Ruifrok and D. A. Johnston, *Quantification of histochemical staining by color deconvolution*, Analytical & Quantitative Cytology & Histology, 23 (2001), pp. 291–299.

[49] M. Sasaki, E. Shibata, K. Kudo, and K. Tohyama, *Neuromelanin-Sensitive MRI*, Clinical Neuroradiology, 18 (2008), pp. 147–153.

[50] K. Schmierer, F. Scaravilli, D. R. Altmann, G. J. Barker, and

D. H. Miller, *Magnetization transfer ratio and myelin in postmortem multiple sclerosis brain.*, Annals of neurology, 56 (2004), pp. 407–15.

[51] M. Schrag, A. Dickson, A. Jiffry, D. Kirsch, H. V. Vinters, and W. Kirsch, *The effect of formalin fixation on the levels of brain transition metals in archived samples.*, Biometals, 23 (2010), pp. 1123–7.

[52] S. T. Schwarz, T. Rittman, V. Gontu, P. S. Morgan, N. Bajaj, and D. P. Auer, *T1-weighted MRI shows stage-dependent substantia nigra signal loss in Parkinson's disease.*, Movement Disorders, 26 (2011), pp. 1633–8.

[53] S. T. Schwrz, *Magnetisation Transfer contrast to enhance detection of neuromelanin loss at 3T in Parkinson's disease.*, in Proceedings of ISMRM 2013, Salt Lake City, Utah, USA, April 2013, p. 2848.

[54] S. Serrer, D. C. Anthony, Y. Jiang, S. J. Campbell, K. A. Broom, A. Khrapitchev, and N. R. Sibson, *Comparison of MRI signatures in pattern I and II multiple sclerosis models*, NMR in Biomdicine, 22 (2008), pp. 1014–1024.

[55] E. Sofic, P. Riederer, H. Heinsen, H. Beckmann, G. P. Reynolds, G. Hebenstreit, and M. B. H. Youdim, *Increased iron (III) and total iron content in post mortem substantia nigra of parkinsonian brain*, Journal of Neural Transmission, 74 (1988), pp. 199–205.

[56] J. P. van der Voorn, P. J. W. Pouwels, J. M. Powers, W. Kamphorst, J.-J. Martin, D. Troost, M. D. Spreeuwenberg, F. Barkhof, and M. S. van der Knaap, *Correlating quantitative MR imaging with histopathology in X-linked adrenoleukodystrophy.*, AJNR, 32 (2011), pp. 481–9.

[57] I. M. Vavasour, C. Laule, D. K. B. Li, A. L. Traboulsee, and A. L. MacKay, *Is the magnetization transfer ratio a marker for myelin in multiple sclerosis?*, Journal of magnetic resonance imaging, 33 (2011), pp. 713–8.

[58] A. J. WALSH, R. M. LEBEL, A. EISSA, G. BLEVINS, I. CATZ, J.-Q. LU, L. RESCH, E. S. JOHNSON, D. J. EMERY, K. G. WARREN, AND A. H. WILMAN, *Multiple Sclerosis: Validation of MR Imaging for Quantification and Detection of Iron*, 2Radiology, 267 (2013), pp. 531–42.

[59] S. WHARTON, A. SCHÄFER, AND R. BOWTELL, *Susceptibility Mapping in the Human Brain Using Threshold-Based k-Space Division*, 63 (2010), pp. 1292–1304.

[60] B. YAO, T.-Q. LI, P. VAN GELDEREN, K. SHMUELI, J. A. DE WART, AND J. H. DUYN, *Susceptibility contrast in high field MRI of human brain as a function of tissue iron content*, NeuroImage, 44 (2009), pp. 1259–1266.

[61] W. ZAARAOUI, M. DELOIRE, M. MERLE, C. GIRARD, G. RAFFARD, M. BIRAN, M. INGLESE, K. G. PETRY, O. GONEN, B. BROCHET, J.-M. FRANCONI, AND V. DOUSSET, *Monitoring demyelination and remyalination by magnetization transfer imaging in the mouse brain at 9.4T*, MAGMA, 21 (2008), pp. 357–362.

[62] W. ZHENG, H. NICHOL, S. LIU, Y.-C. N. CHENG, AND E. M. HAACKE, *Measuring iron in the brain using quantitative susceptibility mapping and X-ray fluorescence imaging*, NeuroImage, 78 (2013), pp. 68–74.

6

White and grey matter degeneration in Multiple Sclerosis

Conventional MRI techniques that are sensitive to white matter (WM) lesions, such as Fluid-Attenuated Inversion Recovery (FLAIR), T_2-weighted and post contrast T_1-weighted sequences, have become established methods for diagnosing and monitoring Multiple Sclerosis (MS) [59]. However, lesions detected using these methods show poor correlation with the clinical status of the disease and weak predictive value for its long-term prognosis [6, 36]. New quantitative MRI techniques and increased spatial resolution provided by high field MRI allow the detection of pathology in

normal appearing WM, as well as cortical and deep grey matter (GM), redefining MS no longer to be an exclusively WM disease [25]. More comprehensive knowledge of the involvement of grey matter could improve our understanding of the pathogenesis of MS and may provide new biomarkers for disease prognosis.

Oligodendrocytes are present in both GM and WM, where they are responsible for producing myelin, and can contain iron [45]. Increased iron concentration found in neurodegenerative diseases can therefore be considered a disease marker, but also as a measure of the neurodegeneration which is directly caused by (due to the toxicity of free radicals) or mediated by iron (for more details see Chapter 4).

This chapter presents an investigation of the MR markers in MS and clinically isolated syndrome (CIS) suggestive of MS (see Section 4.4 for more information), and related to them degeneration of WM as well as cortical and deep GM. The MRI data were acquired from two ongoing projects; the first, including MS and CIS patients and healthy controls (HCs), scanned with a protocol designed to look at WM, but with the field of view also covering the substantia nigra (SN), provided the material for studies described in Sections 6.1 and 6.3; the second, focusing on high resolution cortical imaging in MS patients and HCs, for the study of GM lesions, in Section 6.2.

6.1 Peri-lesional White Matter changes in CIS assessed using different MRI modalities

Many MR studies have reported changes in normal appearing white matter (NAWM) in MS using various MR contrasts such as T_1 [65], magnetization transfer ratio (MTR) [51, 57, 65], R_2'/T_2' [54, 60], diffusion weighted imaging [2, 14] and spectroscopy [2]. However, histological and MR evidence suggests that these changes are not uniform, but localized close to gross lesions, and involve different pathological processes depending on the distance from the lesion [2, 51]. Therefore the visible extent of the affected tissue surrounding the lesion might vary depending on the

MR imaging technique used [65]. Better identification of diffuse areas of damage in WM may be important in studying the progression of MS and possible responses to therapy. The first aim of this study was to compare different imaging techniques in terms of their ability to depict peri-lesional changes depending on the distance from the lesion boundary.

As was described in Section 2.3.3 MTR is a marker of the density of macromolecules including myelin, but the MT sequence can also be sensitized to NOE, the effect probably arising from lipids. Therefore MTR may provide a useful tool for accessing demyelination in close proximity to the WM lesions, with especially good sensitivity and high resolution in 7T images. T_1 maps, also sensitive to the changes in proton mobility and to some extent to iron, may provide an additional method to measure myelin loss. The occurrence of the rings of high iron content around the MS lesions has been shown in histological and MRI studies [17, 30, 32]. Here R_2^*-w images and quantitative susceptibility maps obtained from the phase component of the T_2^*-w datasets were applied to investigate iron content in peri-lesional tissue. T_2^*-w contrast and susceptibility mapping are considered established markers of iron content and have been used to measure iron in MS [1, 3, 32]. However, they can also be affected by myelin content with the opposite effect [44, 46]. Comparison of these two measures with MTR and T_1 values obtained for the tissue surrounding MS lesions may help to explain ongoing pathological processes, based on the myelin- and iron-related contrasts.

MS lesions can be classified according to their appearance in different MRI images, which correspond to time since the lesion occurred and degree of underlying pathology [53]. MRI characteristics of the changes in peri-lesional NAWM could potentially provide another way of distinguishing subgroups of lesions based on different pathological processes affecting the tissue. Moreover, investigating this in CIS patients could lead to a better understanding of the pathological mechanisms occurring in the early stages of MS and help to develop prognostic methods.

This section compares changes in the peri-lesional NAWM in patients with CIS

using myelin and iron sensitive, high resolution 7T images. Fitting functions were used to investigate the extent of penumbra around the lesion in different modalities. Moreover, an attempt at lesion classification based on the differences in the MR signal changes around the lesion with the distance from its boundary is presented.

6.1.1 MATERIALS AND METHODS

14 CIS patients (age=37.7±9.1, EDSS mean=2.0±0.9), selected from the project described in the introductory part of the chapter, were scanned in 7T Philips Achieva scanner equipped with a 16 channel receiver coil allowing SENSE reconstruction. Four different sequences were used: MT-TFE either with 20 off-res pulses applied at +1100Hz for APT and MT sensitivity (MT_1), 20 pulses applied at -1100Hz for NOE and MT sensitivity (MT_2), or no saturation (MT_0), T_1-TFE with seven different inversion times for T_1 measurement, high resolution T_2^*-w with phase data stored and MPRAGE optimised to provide maximum contrast between WM and GM. Details of the scan parameters are summarised in Table 6.1.1

name	resolution	slices	TR/TE	FA	additional	time
MT-TFE	0.86×0.86mm	2D 20×1.5mm	11/6.6 ms	8°	MTC=no/2×off (±1100Hz) BW=164.3Hz	9:06
T_1-TFE	1.25×1.25mm	3D 58×1.25mm	6.9/3.2ms	8°	TI=0,150,350,650,1050, 1650,2350, SENSE=2, BW=240.6Hz	14:49
T_2^*-w	0.5×0.5mm	3D 50×0.5mm	150/20ms	14°	4 stacks, SENSE=2, EPI=3, BW=80.4Hz	8:49
MPRAGE	0.6×0.6mm	3D 260×0.6mm	15/6ms	8°	SENSE=2, BW=114.9Hz	12:05

Table 6.1.1: Summary of the parameters of the acquired scans.

PRE-PROCESSING

MT_1 and MT_2 scans were co-registered to the MT_0 scans and processed to obtain MTR_1 and MTR_2 maps using method described in Section 2.3.3. Moreover, ASYM maps were calculated as a difference of MTR_2-MTR_1, such that they were assumed to be NOE-weighted. T_1 maps were created as presented in Section 2.3.2. Susceptibility maps were calculated from the phase data of the T_2^*-w images via k-space thresholding method (see Section 2.3.5). MPRAGE images were

bias corrected using SPM (`http://www.fil.ion.ucl.ac.uk/spm/`) and the other modalities (MTR, T_1, susceptibility maps and T_2^*-w) were linearly co-registered to the MPRAGE using FLIRT, FSL [35] (6 degrees of freedom). One subject was removed from the analysis due to a mis-registration error. The brain was extracted from all the images using masks obtained from MPRAGE by applying the BET, FSL tool [62]. Table 6.1.2 presents a summary of all the quantitative maps and images obtained from the original scans.

original scan	quantitative measures
MT-TFE	MTR_1 map, ASYM map (assumed to be NOE dominated)
T_1-FFE	$R_1 = 1/T_1$ map
T_2^*-w	R_2^*-w=$1/T_2^*$-w image, susceptibility map
MPRAGE	

Table 6.1.2: Summary of quantitative measures and images obtained from the original scans.

The white matter lesions (WML) were segmented manually on MPRAGE images using NeuRoi software (`http://www.nottingham.ac.uk/scs/divisions/clinicalneurology/software/neuroi.aspx`) by a trained radiologist, giving total of 237 lesions. Tissue segmentation of MPRAGE images was performed using SPM package (`http://www.fil.ion.ucl.ac.uk/spm/`) and resulting WM probability maps were thresholded to obtain NAWM masks. WM lesions were often classified as GM by SPM and therefore dilated lesion masks were added to the NAWM masks. The masks were then eroded to ensure all GM was removed and applied to the other images. The field of view (FOV) of the final results was limited by the data set with the smallest coverage (MTR) to allow comparison of all the modalities. An example set of preprocessed images is presented in Figure 6.1.1: MPRAGE, T_2^*-w images, susceptibility, T_1, MTR_1 and ASYM maps (dominated by NOE effect).
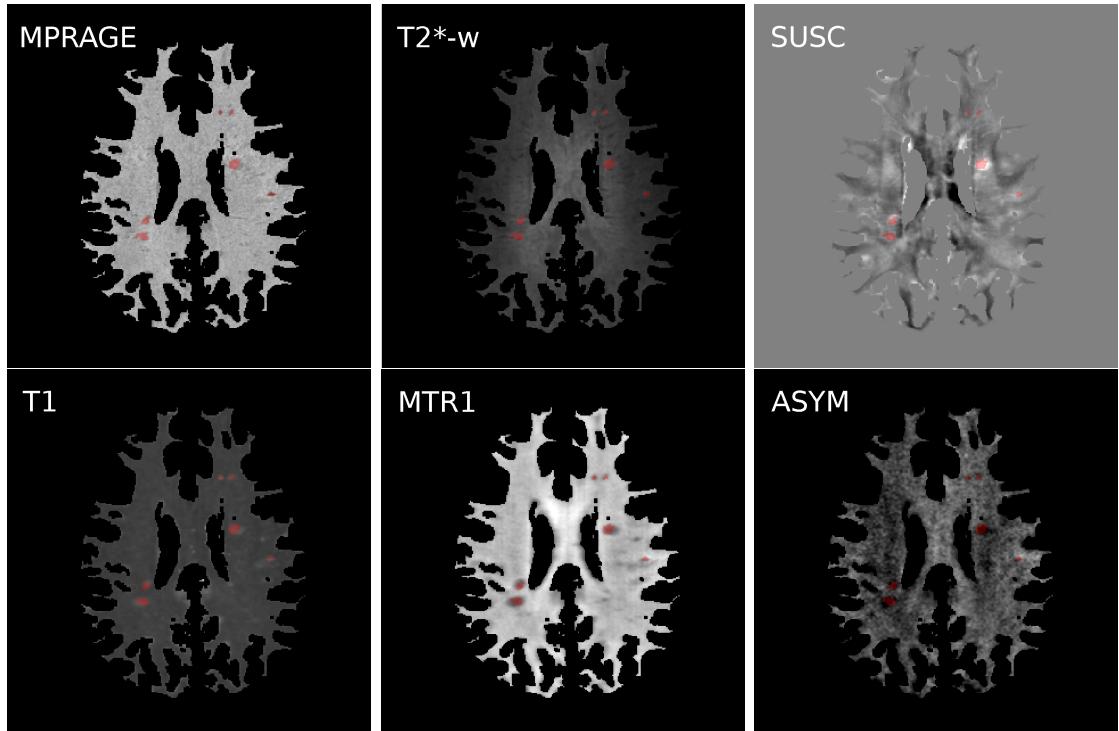
Figure 6.1.1: Example axial slices of one pre-processed dataset: MPRAGE corrected for bias, T_2^*-w image, susceptibility map (top row), T_1, MTR_1 and ASYM maps (bottom row), with overlapped lesions masks marked in red.

For each lesion separately two 3D distance maps were created with ImageJ plugin [22]: outside and inside of the lesion boundary. They were then combined to make distances smaller than 0 correspond to the lesion's inside and positive ones to its outside. The distances were re-scaled using a voxel size of the source images (0.6mm) to obtain maps of the distance expressed in millimetres. Figure 6.1.2 presents an example slice of a combined distance map of one lesion and a diagram illustrating values of the distance in relation to the lesion's boundary.
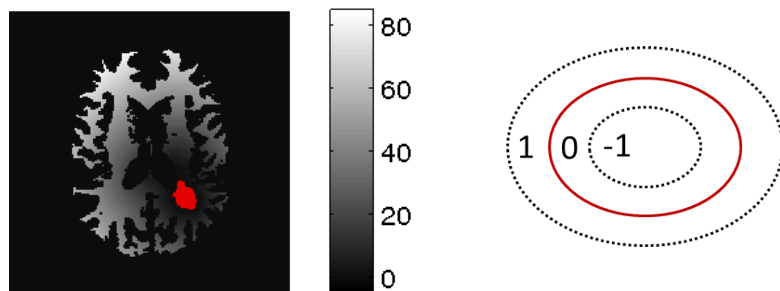

Figure 6.1.2: Example axial slice of a combined 3D distance map with overlapped mask of the lesion (red), where grey levels correspond to the distance from the lesion's boundary in mm (left); diagram illustrating distance values in relation to the lesion's boundary (right).

For every lesion, average intensities of each map or image within the distance bins of 1mm width were calculated to obtain *peri-lesional profiles* used for further analysis. During the calculations T_1 and T_2^*-w images were inverted to obtain R_1 maps and R_2^*-w images.

WM surrounding one particular lesion can be affected by other lesions located in the neighbourhood. In the pilot part of this study only the lesions with no other lesions lying within the particular distance from the lesion boundary were considered. The main aim was to investigate the general shape of the peri-lesional profiles and the extent of penumbra around the lesion, as measured with different modalities. The second part of the study used an alternative way of addressing the problem of the neighbouring lesions, the WM regions affected by more than one lesion were neglected in the analysis, allowing to increase the number of analysed lesions. The proximal and distal peri-lesional changes were distinguished based on the results of the pilot part of the study. Peri-lesional profiles were compared between different modalities and the attempt to profile-based lesion classification was performed.

Lesions with lesion-free neighbourhood

Two lesion-free distances were selected defining two subsets of lesions: (1) these with a lesion-free neighbourhood within 6mm distance in 3D (45 of 237 lesions) and (2) these with a lesion-free neighbourhood within 10mm distance in 3D (28 of 237 lesions). For these lesions the function $A(1-e^{-x/S_1})(1-\frac{x}{F})+B$, where x represents distance, was fitted to the peri-lesional profiles for 0-6mm in order to parametrize proximal changes in the rim of the lesion (S_1) and any distal changes further away from the lesion (F). Parameter constraints were applied, so that $S_1 \in [0,6]$mm and $F \in [-100, 100]$mm. Coefficient A represented amplitude and B corresponded to the signal value for $x = 0$. Figure 6.1.3 shows profiles of an example lesion with the fitted function and images of the corresponding lesion in all five modalities. For plotting purposes R_1 images were scaled by factor $\times 10^3$.
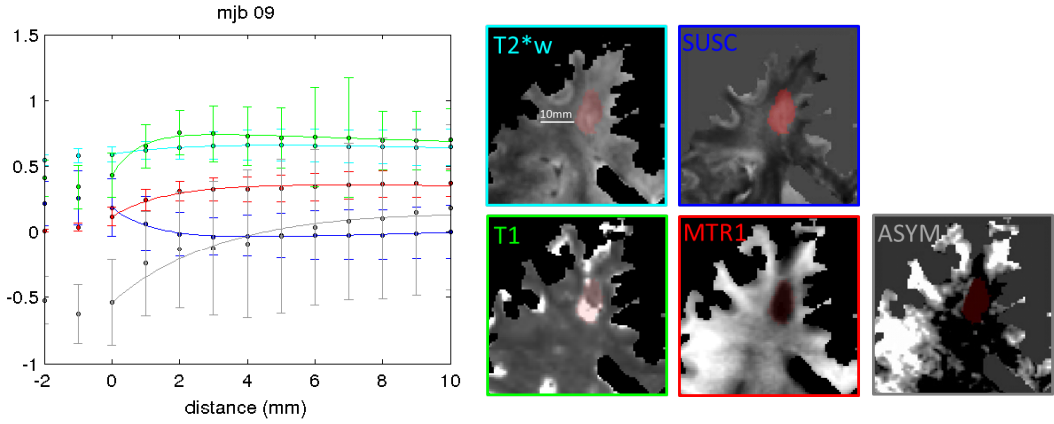
Figure 6.1.3: Profiles of the example lesion calculated on R_2^*-w=$1/T_2^*$-w [au], SUSC [ppm], R_1=$1/T_1$ [$ms^{-1} \times 10^3$], MTR_1 [au], ASYM [au] with the fitted function $A(1 - e^{-x/S_1})(1 - \frac{x}{F}) + B$ and error bars showing standard deviations of the values within each distance bin (left), and the images of this lesion in five modalities (right); colours of the images' labels correspond to the colours of the plotted profiles.

The same function was fitted to the profiles averaged across all the lesions from subsets (1) and (2) to compare how size of the lesion-free neighbourhood affects parameters of the fit.

LESIONS WITH NEIGHBOURHOODS' OVERLAP REMOVED

Lesions masks were dilated by 6mm (10 voxels) isotropically and then the parts of WM which belonged to more than one dilated lesion, i.e. regions that were within 10mm from two lesions, were removed. As many of the small lesions fell into the removed regions, this limited the number of lesions considered to 91 of the original 237.

The lesion profiles obtained in the pilot part of the study showed that changes further away from the lesion were sometimes linear in either positive or negative direction (Figure 6.1.4), apparently independently of proximal changes. However the first model had the effect of coupling the distal and proximal changes, so that the proximal fitted parameters would be affected by the fit to the distal part, making it difficult to compare proximal results between lesions. Therefore in the second model it was decided to split the function fitted to the peri-lesional profiles into two: the proximal-function $A(1 - e^{-x/S_2}) + B$ was fitted to the part of the profile

within 0-5mm and the linear distal-function $Dx + M$ was fitted to the part within 5-15mm. There was no constraints applied to the parameter D, but $S_2 \in [0, 15]$mm. The parameter S_2 of the proximal-function characterises the distance over which the tissue signal returns to normal around the lesion boundary, where D of the distal-function corresponds to signal changes further from the lesion in NAWM and can be positive or negative. The 5mm transition point was estimated from the average extent of proximal penumbra calculated in the pilot study. In order to normalise the resulting sum of square error estimate to allow χ^2 to be compared between the fits for different modalities, weights were applied equal to the average standard deviation across all the values used for calculation of the lesion profile in the particular image. Strictly, the weights would vary with distance since there will be more voxels included in average at larger radial distances. However given the biphasic nature of the fit and the underlying biological variability which will also vary in an unpredictable manner with distance from the lesion, a constant weighting with distance was assumed here. Figure 6.1.4 presents example profiles plotted with the fitted functions and the images showing the appearance of the corresponding lesions in all five modalities. The examples have been chosen to illustrate different sizes of lesions and extents of penumbra around the lesion boundary represented by the parameter S_2.
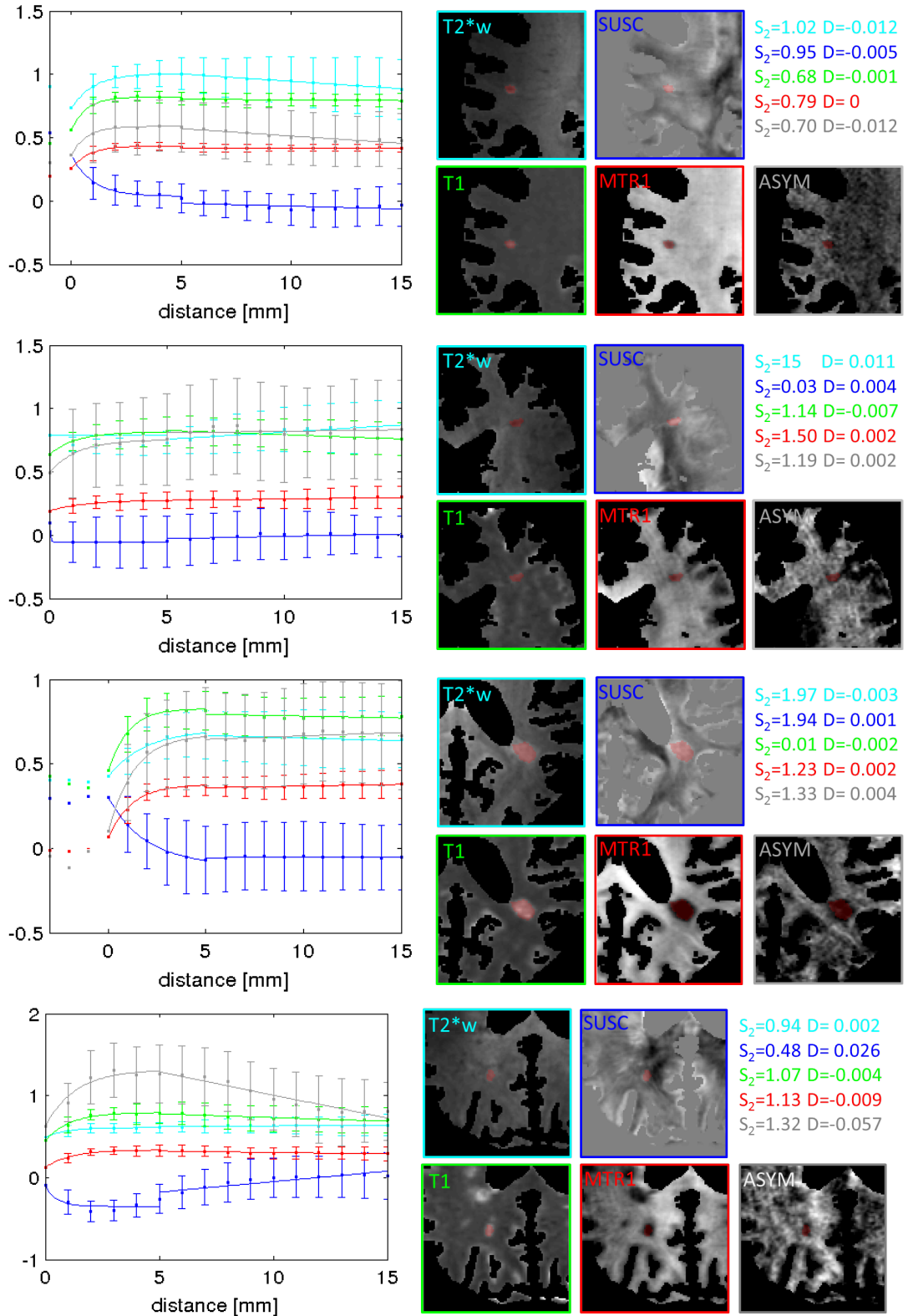
Figure 6.1.4: Lesion profiles of four example lesions with different values of S_2 and D parameters calculated on R_2^*-w=$1/T_2^*$-w [au], SUSC [ppm], R_1=$1/T_1$ [$ms^{-1} \times 10^3$], MTR_1 [au], ASYM [au] plotted together with the fitted functions: $A(1 - e^{-x/S_2}) + B$ for [0-5]mm and $Dx + M$ for [5-15]mm and error bars showing standard deviations of the values within each distance bin (left), and images of the same lesions (right); colours of the images' labels correspond to the colours of the plotted profiles.

The fitted functions were visually assessed and compared with the corresponding χ^2 values to define thresholds, χ^2=0.1, used to exclude lesions where the quality of the fits was insufficient for at least one modality. As a result, analysis of the coefficients of the fitted functions were performed only for 75 lesions in case of the proximal-function (0-5mm) and 91 lesions in case of the distal-function (5-15mm), which probably reflects increased biological and physical noise, as well reduced number of degrees of freedom at lower radii. Values of S_2 for each image were plotted against the lesion size and mean intensity inside the lesion to investigate possible correlations. S_2 and D coefficients were correlated between the different modalities to investigate possible relations between the lesion profiles of different sequences. Values of S_2 reaching an upper boundary of the defined constraints, $S_2 = 15$, were removed from the plots, as representing flat per-lesional profiles corresponding to the lack of penumbra.

CLUSTERING OF THE LESION PROFILES

Based on the fact that distances around the lesions over which the MR signal is affected were smaller in some lesions than in the others and that the characteristic distance (S_2) of the profile also differed between lesions, an attempt to distinguish subsets of lesions having similar characteristics was performed. Raw, unfitted peri-lesional profiles were divided into the clusters using agglomerative hierarchical clustering method. The algorithm computes a matrix of values of distance between each pair of the elements from the given set and iteratively merges the closest values into clusters until the required number of classes is reached. The complete-link version of the method was applied, where the maximum distance between the elements is compared. In this case the correlation between two profiles was used as the inter-profile distance measure to perform classification separately for the whole profiles 0-15mm and the profiles limited to the first 5mm, with required number of clusters C being 2,3 or 4. Figure 6.1.5 shows three example classification trees calculated for 15mm correlation between profiles, where the bottom level represents

the original set of profiles subsequently combined into the bigger clusters, moving up towards the root of the tree.
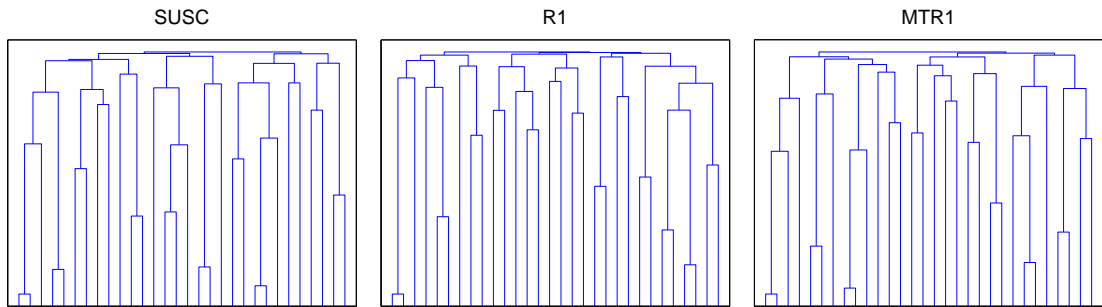

Figure 6.1.5: The example classification trees calculated for SUSC, R_1 and MTR_1 using 15mm correlation between profiles; the bottom level represents the original profiles, joined into the bigger clusters towards the root of the tree.

For each variant of the classification a co-occurrence matrix was created to count the numbers of lesion profiles falling into each cluster for every pair of modalities. The average profiles of lesions divided into the two classes (for classification with C=2) were plotted together for the comparison, with the error bars corresponding to the inter-class standard deviation. Classification based on each type of the image was used to group profiles.

INTER-MODALITY SCATTERS OF LESION PROFILES

The agreement between different modalities measuring properties of the tissue around the lesions was investigated by plotting lesion profiles against each other for every pair of images, so that the points corresponded to the values at different distances from a lesion boundary. A straight line was fitted to the points using an iterative procedure to exclude outliers: the data point lying furthest away from the fitted line was excluded if its removal improved the norm of residuals of the fit by at least 30%.

The gradients of the resulting fitted lines for each pair of modalities were averaged: (1) across all the lesions, (2) across the lesions of each subject, (3) across the 2 classes of lesions found using clustering of the 15mm profiles. For variant (3) additional one-way ANOVA testing with Tukey-Kramer correction for multiple comparisons

146

was performed to test differences between the groups corresponding to four possible combinations of classes to which two considered modalities belong.

6.1.2 Results

Lesions with lesion-free neighbourhood

The average profiles of two lesion groups used in the pilot study, with 6mm and 10mm lesion-free neighbourhood, were very similar, as shown in Figure 6.1.6.
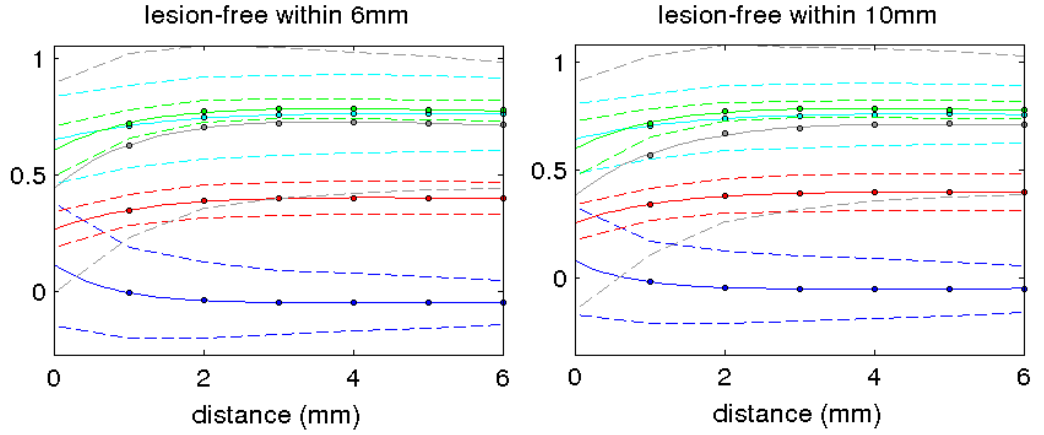
Figure 6.1.6: Average profiles calculated on R_2^*-w [au], SUSC [ppm], R_1 $[ms^{-1} \times 10^3]$, MTR_1 [au], ASYM [au] for the lesions with lesion-free neighbourhood within 6mm (left) and 10mm (right); dashed lines indicate standard deviations of the values across the lesions.

Summary of the coefficients of the function fitted to the averaged profiles for all the modalities is presented in Table 6.1.3.

	proximal recovery S_1 [mm]		distal gradient F [mm]	
lesion-free	6mm	10mm	6mm	10mm
R_2^*-w [au $\times 10^5$]	1.9	1.8	23.9	25.8
SUSC [ppm]	0.8	0.8	99.5	90.0
MTR_1 [au]	1.3	1.3	48.5	37.7
R_1 $[ms^{-1} \times 10^3]$	1.2	1.2	32.5	29.0
ASYM [au]	1.4	1.2	44.6	28.4
mean	1.3±0.4	1.3±0.4	49.8±29.5	42.2±27.1

Table 6.1.3: Coefficients of the function $A(1-e^{-x/S_1})(1-\dfrac{x}{F})+B$ fitted to the lesions profiles averaged across all lesions with 6mm and 10mm lesion-free neighbourhood; mean and standard deviation values calculated across all the modalities (bottom row).

Signal recovery close to the lesion boundary represented by S_1 and changes far from the lesion represented by F were similar in both groups. Values of S_1 coefficient

suggested that WM lying at least 2mm away from the lesion boundary in MPRAGE (on which lesions were originally segmented) can be considered as NAWM. Moreover S_1 was generally higher for R_2^* and lower for SUSC. Slightly higher F values for the group where there was only a 6mm lesion-free region around the lesion may be due to WM peripheral to the lesions being still affected by other lesions lying further away.

Lesions with neighbourhoods' overlap removed

Table 6.1.4 presents number of lesions used in the main study and their total volume for each of the analysed subjects.

subject	A	B	C	D	E	F	G	H	I	J	K	L	M	total
lesion count	9	9	2	2	2	11	4	2	10	10	13	10	7	91
lesion vol $[mm^3]$	156	1532	57	33	3324	416	85	181	4979	865	1657	434	139	13857

Table 6.1.4: Summary of numbers and total volumes of the lesions for all the subjects.

There was no systematic correlation between S_2 fitted to the first 5mm of the lesion profile and mean intensity within the lesion calculated for the same modality and between the parameter S_2 and size of the lesion (see Appendix 2, Figures A.1and A.2, respectively). Neither S_2 nor D coefficients, characterising the signal changes close to and far from the lesion boundary (respectively), correlated between different sequences (Figures A.3 and 6.1.7). However, there was a trend for positive correlation between D values measured on images related to myelin (MTR_1, ASYM, R_1) and on images related to iron (R_2^*, SUSC), and to negative correlation between myelin- and iron-dependent modalities.
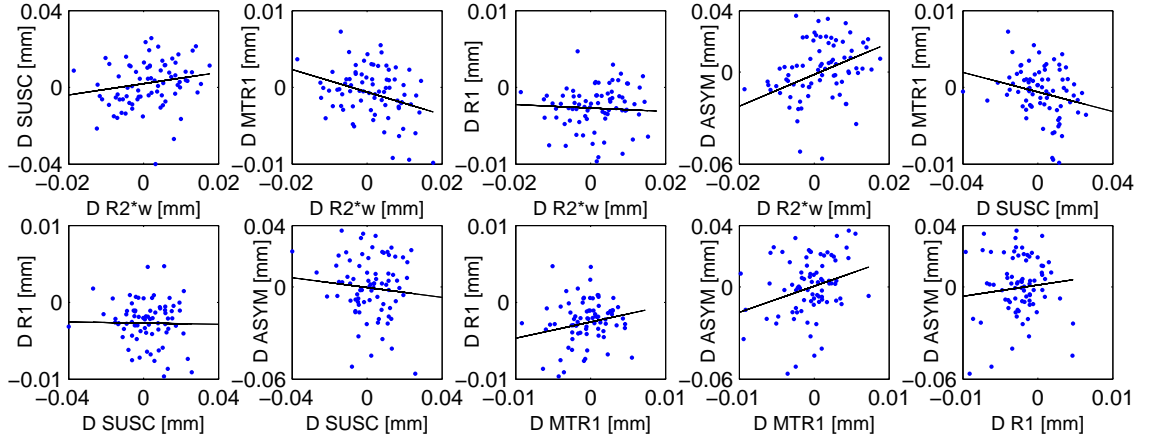
Figure 6.1.7: The coefficient D of the function fitted to the second part of the lesion profiles 5-15mm plotted for all the combinations of the pairs of the images with the fitted straight lines plotted in black.

CLUSTERING OF THE LESION PROFILES

Co-occurrence matrices calculated for each classification, for the number of clusters C=2,3,4, and for both 5 and 15mm, did not show any particular overlap between the classes in the pairs of modalities (see Appendix 2, Table A.1). Similarly, plots of the lesion profiles, averaged across two classes determined by the clustering based on the 15mm correlation, for each of five modalities revealed poor inter-classes separation (see Appendix 2, Figure A.4).

INTER-MODALITY SCATTERS OF LESION PROFILES

Figure 6.1.8 presents plots of one modality profile against another (so that each point represents a different distance from lesion boundary) for an example lesion, with a fitted straight line and any outliers that were removed to improve the fit marked in black.

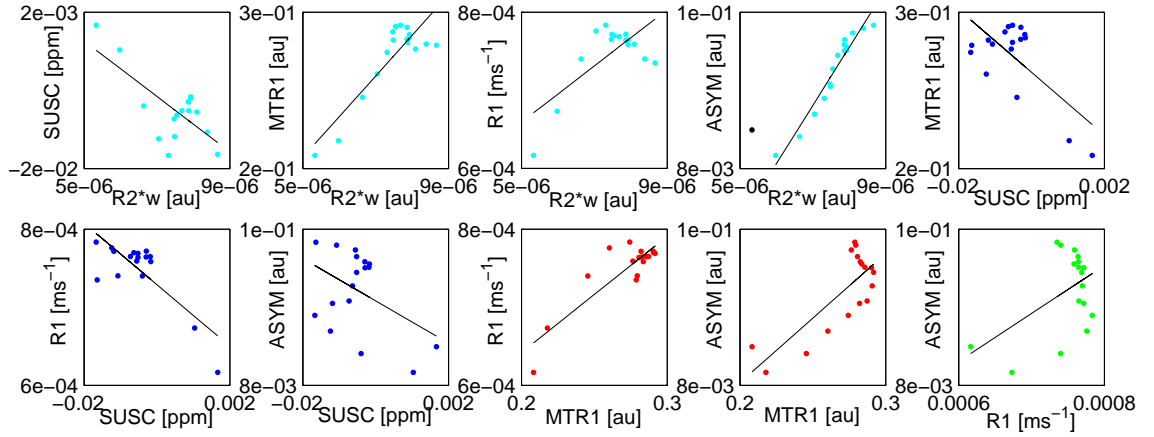**Figure 6.1.8:** Correlations of the profiles of the example lesion with the fitted first degree polynomial and outliers removed to improve the fit marked in black.

Table 6.1.5 summarises means and standard deviations of the gradient values of the fitted lines across all the lesions and the most frequent gradient signs. Large standard deviations from the average values of the gradients across the lesions corresponded to high variation of the correlation between the lesion profiles.

correlation gradient	mean ± std		−/+ gradient
SUSC [ppm] / R_2^*-w [au]	-4000 ± 22000		− (62%)
MTR_1 [au] / R_2^*-w [au]	23000 ± 46000		+ (69%)
R_1 [ms^{-1}] / R_2^*-w [au]	80 ± 90		+ (81%)
ASYM [au] / R_2^*-w [au]	15000 ± 25000		+ (84%)
MTR_1 [au] / SUSC [ppm]	-2.9 ± 4.0		− (75%)
R_1 [ms^{-1}] / SUSC [ppm]	-4.5 ± 5.8	$\times 10^{-3}$	− (80%)
ASYM [au] / SUSC [ppm]	-6.4 ± 15.0	$\times 10^{-1}$	− (71%)
R_1 [ms^{-1}] / MTR_1 [au]	1.2 ± 1.0	$\times 10^{-3}$	+ (91%)
ASYM [au] / MTR_1 [au]	0.3 ± 0.2		+ (95%)
ASYM [au] / R_1 [ms^{-1}]	150 ± 170		+ (89%)

Table 6.1.5: Summary of the gradients of plotted profiles of one modality against another averaged across all the lesions (mean and standard deviation) and the most frequent gradient direction (positive/negative, −/+) among all the lesions with a percentage.

Mean values of the gradient across all the lesions differed between the subjects as shown in Figure 6.1.9. High variation of the gradient values for different lesions within each subject (standard deviation) was also observed.
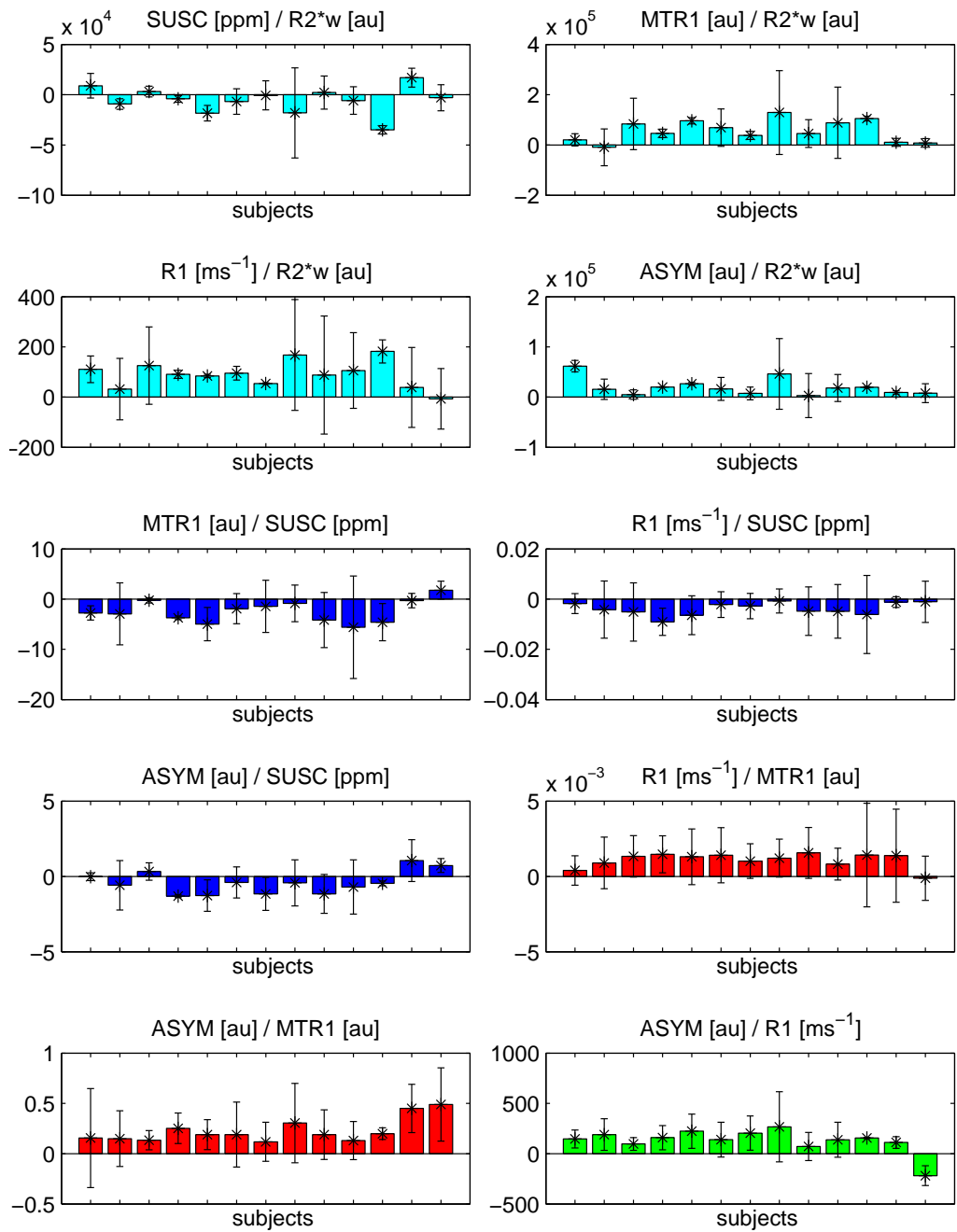
Figure 6.1.9: Mean values and standard deviation of the gradient values calculated across all the subject's lesions for all the correlations of the lesion profiles.

Figure 6.1.10 shows bar plots of the mean values of the gradients grouped based on the classification of the 15mm profiles into C=2 clusters. Each bar corresponds to one of four possible combinations of the classes to which correlated images belong. One-way ANOVA with Tukey-Kramer correction for multiple comparisons did not find any significant differences between the groups.

Figure 6.1.10: Each of the bar plots corresponds to one of the correlations between the lesion profiles. Each bar represents mean value of the gradient, where correlated images belongs to the given combination of the classes (1/1, 1/2, 2/1, 2/2). Classification was obtained using clustering of the lesion profiles within 15mm with two clusters. There was no significant differences between the groups.

6.1.3 DISCUSSION

Peri-lesional profiles of mean signal intensity values calculated for every bin of distance from the lesion boundary were used to characterise MR signal c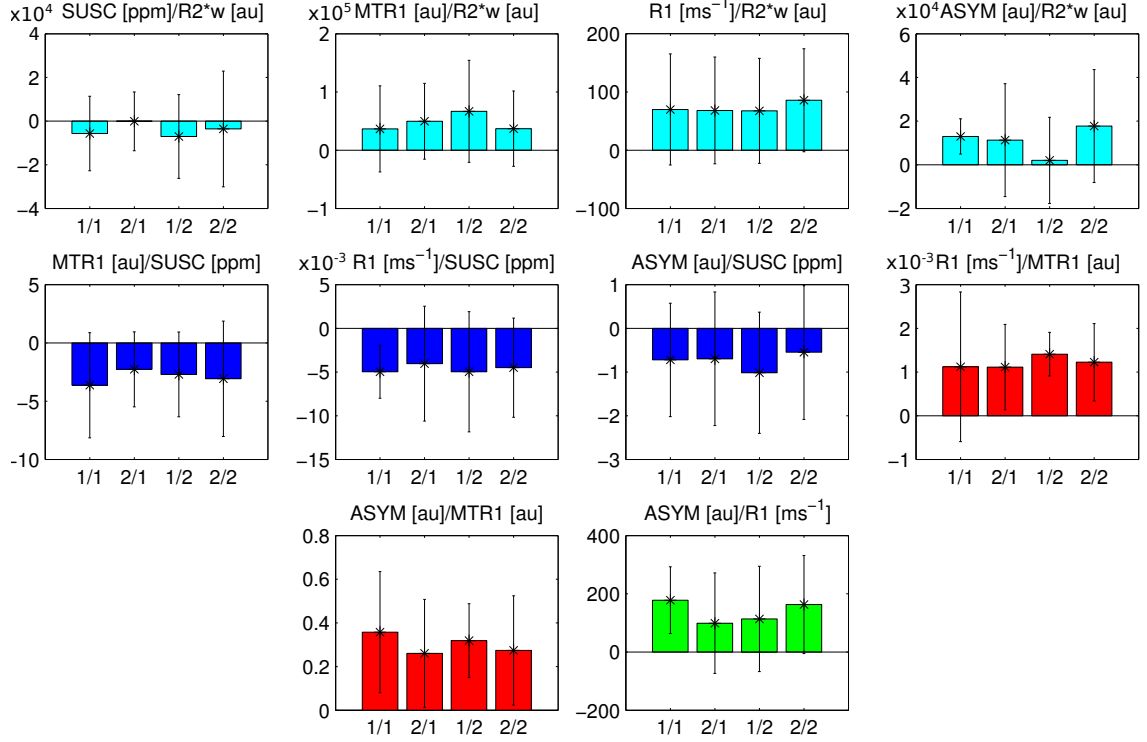hanges around the lesions in CIS patients. Five different modalities were used: R_2^*-w images, susceptibility, MTR, R_1 and ASYM maps. The negative values of ASYM found around the lesions showed that the z-spectrum was asymmetric in a manner that confirmed the initial assumption that they are NOE (not APT) dominated [52].

The coefficient S_1 of the function fitted to the average lesion profiles estimated the extent of penumbra around the lesion, allowing the conclusion that WM lying further than 2mm from an MPRAGE lesion boundary can be considered to be unaffected by significant inflammation for all the measures (Figure 6.1.6, Table 6.1.3). Based on that assumption, the transition value of 5mm was estimated and used to increase

stability of the fit by splitting lesion profiles into two parts: proximal to the lesion, where MR signal changes rapidly over the distance from the lesion boundary and distal to the lesion, where slower, approximately linear, signal change was observed. This result also suggested that lesions appear smaller in MPRAGE than in other analysed modalities indicating differences in their sensitivity to the same underlying biological changes.

S_1 value obtained for the average R_2^*-w profile was higher and S_1 calculated for susceptibility profile was lower than the average (Table 6.1.3), indicating different effects of iron and myelin content with the distance around the lesion boundary. Increasing myelin content around the lesion would cause gradual increase of R_2^* signal and decrease of the susceptibility values, however a simultaneously occurring decrease in iron content would cause slowing down of the R_2^* increase but speeding up of the susceptibility decrease. The narrow range of change in iron content accompanied by the wide range of change in myelin content could potentially indicate existence of iron rings around the lesions. However, the same set of lesion data was visually reviewed for another study finding no iron rings in susceptibility maps and T_2^*-w images, which would be expected for the CIS lesions representing an early stage of the disease. This effect must therefore be related to some other, not fully understood pathological processes. Possibly, changes in iron content leading to the creation of iron ring in the future may already occur in lesion proximity, being not significant enough to be visually identified.

The characteristic distance (S_2) of the proximal-function fitted within 0-5mm from the lesion boundary and corresponding to the range of the MRI detectable inflammation around the lesion was found to be independent of the size of the lesion as well as mean signal intensity measured within the lesion (Figures A.2 and A.1). Moreover there was no correlation of the characteristic distance coefficients (S_2) between different modalities (Figure A.3). These results indicated that in CIS patients the area of tissue affected pathological processes was similar for all the lesions, independent on their appearance in different modalities and size calculated

based on MPRAGE segmentation.

For the distal-function fitted to the 5-15mm part of the lesion profile, D values were relatively small, both positive and negative, corresponding to the slight increase and decrease (respectively) of the lesion profile in its distal part (Figure 6.1.7). This variation could be caused by the transition value chosen for two fitted functions possibly being too big and a range fitted being too large, so that the direction of the distal-function might have been driven by the data points which were missed from the distal-function (and included in the proximal-function).

The coefficients S_2 and D of the two functions fitted to the lesion profiles did not provide any information regarding possible sub-sets of lesions or dependence of different imaging measures on each other within the tissue surrounding the lesion. Another attempt to separate lesion groups based on the peri-lesional characteristics using an automatic clustering method with different configurations of the parameters (5mm and 15mm of the profile, expected number of clusters C=2,3,4) also did not achieve positive results. This can be clearly seen in the co-occurrence matrices (Table A.1) and in the comparison of the lesion profiles averaged within the classes (Figure A.4), indicating large uniformity or heterogeneity between lesions.

Values of the gradient of the straight line fitted to inter-modality scatters of the lesion profiles (Figure 6.1.8) confirmed a high variation of the characteristics of the peri-lesional tissue between the particular lesions (Table 6.1.5), subjects (Figure 6.1.9) and the classes obtained using the clustering method (Figure 6.1.10). No significant differences were found between the mean gradient values calculated for the groups obtained by clustering.

However, the signs of the straight line gradients, as summarised in Table 6.1.5, together with the percentage of the sign's occurrence reflected the general tendencies in the relations between the modalities within the peri-lesional tissue. The gradients for R_1, MTR1 and ASYM had positive direction in at about 90% of lesions, which would be expected as all three measures reflect myelin content. All of them had negative gradient values where plotted against SUSC but positive compared with

R_2^*-w (range of about 70-80%), which is likely to relate to the opposite dependence of SUSC and R_2^* on myelin [44, 46]. The negative gradient between SUSC and R_2^*-w would provide a confirmation of this finding, however it was true for only 62% of the lesions suggesting more complex contrast mechanisms, most likely related to the variable iron content in the peri-lesional region and the mixed effects of iron and myelin in R_2^*. Bar plots in Figure 6.1.9 clearly present the same trends within the particular subjects. Some indication of the similar trends was also found in correlations of the D values obtained for different images types (Figure 6.1.7). These results are in agreement with those presented in Section 5.2 of this thesis regarding brain stem tissue. Application of the proposed in vivo iron and myelin mapping method to the MS lesion surroundings could possibly provide better understanding of the pathological processes occurring in tissue around the lesions.

Investigation of the changes in myelin and iron content in a peri-lesional WM for the group of CIS patients presented in this section, using five MRI modalities and several different approaches, showed no behaviour indicating different types or classes of lesions or subjects. This lack of clear consistency may be due to either heterogeneity or uniformity of the lesion set. Uniformity may be caused by the early stage of the disease, where little recovery of lesion happening and therefore distinguishing lesion types based on the differences in pathology is not yet possible. On the other hand, the complex nature of the underlying pathological processes can cause high variation of the measures applied in this study making the lesion set heterogeneous. However this variation could also potentially result from the noise in the analysed data. Visual assessment of the lesions profiles and the fitted functions (see Figure 6.1.4) and relatively low χ^2 values suggested the fits were good and that it would more likely be caused by the biological heterogeneity of the lesions and therefore MRI characteristics. In future, Monte Carlo simulations propagating the measured physical noise would make it possible to determine the origin of the variation observed in the fits.

It is possible that the negative results obtained were related to over-fitting the data.

However this was more likely to be a problem for the model in the pilot part of the study where, although the number of degrees of freedom in the fits was generally larger, the components of the model were coupled such that noise in one part of the profile would have affected the fit in all of it. Furthermore by splitting the model into two components and fitting the signals separately, the problems of multiple comparisons become larger reducing the power of the study.

Other potential limitation of this study was the application of a geometrical measure of distance from the lesion boundary, while degeneration in the brain tissue might potentially spread along the WM tracts. However, given the short range of the distance considered, 15mm, the geometrical approximation seems sensible.

A future extension of this study would compare CIS lesions with lesions present in more advanced forms of MS in order to investigate differences in lesions characteristics. Moreover longitudinal monitoring of the same lesion combined with information about the potential conversion of the patient from CIS to MS will be performed. It would also be interesting to analyse tissue characteristic within the lesions in relation to the area of influence of the lesion around the lesion's boundary. Finally, the application of the iron and myelin mapping method proposed in Section 5.2 could possibly provide a better understanding of pathological processes occurring in the tissue surrounding lesions.

6.2 Detection of grey matter lesions in MTR and MPRAGE images

The majority of MRI studies of MS examine changes in white matter, although histopathological findings suggest that cortical lesions are very common in MS and might provide additional information regarding its pathogenesis [9, 38]. The most recent studies confirm that cortical lesions occur on early stages of the disease, are associated with the cognitive and physical impairment [12] and, rather than WM lesions, should be considered as a predictor of the disease progression [10, 13].

It was decided to extend the study described in section 6.1 to study the variations in NAGM about GM lesions. GM lesions are difficult to detect on MR due to their small size and the low levels of cortical myelin, however recently some success has been reported using T_2^*-weighted [48], FLAIR [39] and MPRAGE images at 7T and double inversion recovery (DIR) [63] or phase-sensitive inversion recovery (PSIR) [61] at 3T. Increased ability to detect GM lesions has been shown for the standard clinical protocols such as T_2-w, T_1-w and FLAIR in 7T compared with 3T [21]. This section presents a pilot part of the ongoing project comparing of the detection of GM lesions on high resolution 7T MTR maps and MPRAGE images.

6.2.1 Materials and methods

Eight MS (7 RRMS, 1 SPMS) patients (age mean=48±9) and four healthy controls (HC) (age mean=33±8) were recruited from Nottingham University Hospital Trust in accordance with local ethics committee approval and scanned on 7T Philips Achieva scanner using a 32-channel receive coil with SENSE reconstruction. The protocol included a high resolution MPRAGE sequence with a tailored inversion pulse to reduce effects of B1 inhomogeneities [34], optimised to produce maximum contrast between white and grey matter required for accurate tissue segmentation, and a MT-TFE acquisition with 20 off-resonance sinc pulses was applied to obtain saturation (bandwidth=300Hz, off-resonance=-1.0kHz (3.4ppm), 21ms between each pulse) and a Turbo-Field echo readout. Additionally T_2^*-w images were acquired with a 3D-FFE spoiled gradient echo sequence. Detailed parameters of all the scans are summarised in Table 6.2.1

name	resolution	slices	TR/TE/TI	FA	additional	time
MPRAGE	0.5x0.5mm	3D 280 x 0.5mm	15/7/1070ms	8°	BW=95.3Hz	11:20min
MT-TFE	0.5x0.5mm	3D 80 x 1.0mm	12/6.4ms	8°	MTC=no/off, BW=100.7Hz, SSi=10s	8:45min
T_2^*-w	0.5x0.5mm	3D 180 x 0.5mm	150/20ms	16°	4 stacks, BW=79.6Hz	9:37min

Table 6.2.1: Summary of the parameters of the acquired scans.

Preprocessing of the data was performed by Dr. Olivier Mougin. MPRAGE images were bias field corrected using SPM and the cortical grey matter ribbon (CGMR)

was segmented using Freesurfer to ensure the observers had no knowledge of any WM lesions, to attempt to blind them to clinical status. The mask of the CGMR was dilated by one pixel to compensate for the registration and tissue classification errors, and then manually corrected for any missegmentation (e.g. due to the mixed lesions laying partially in the WM). Finally the CGMR mask was visually checked to ensure the reviewers would remain blinded (does not include any WM abnormalities). High resolution MTR maps were calculated using a method described in Section 2.3.3. MTR maps and T_2^*-w images were co-registered to MPRAGE via FLIRT, FSL [35] and the CGMR mask was applied to them all.

Two MRI physicists (OM and AB, the author of this thesis), one experienced in GM lesions segmentation (OM), and one neurologist (NM) reviewed example lesions in MTR, MPRAGE and T_2^*-w images and reached consensus on the lesion definition. A tissue abnormality was considered as a lesion if it was hypointense on MTR and MPRAGE and hyperintense on T_2^*-w, lying within the cortex, of the longest dimension in the x-y plane bigger than 4 voxels, present in at least two consecutive slices, which was not a result of a partial volume effect or movement artefact on the cortex boundaries. This definition was then applied by AB to manually segment lesions, separately in MTR and MPRAGE images and additionally on 4 randomly chosen T_2^*-w scans (2 controls and 2 MS) using ITKSnap software. The image sets were all presented in random order to prevent the observer using mutual information between two modalities when finding lesions. Segmentation was reviewed post-hoc by OM comparing raw images (i.e. including also WM) of all three modalities to confirm lesion identification and to separate cortical and mixed lesions (i.e. those that lie in both GM and WM). Numbers of lesions identified for each subject were counted. Masks of the local normal appearing GM (LNAGM) surrounding each lesion were obtained by subtracting two masks created by dilating the lesions masks by 2 and then 9 voxels. Contrast between the LNAGM and lesion was calculated for each lesion on MTR and MPRAGE (normalised by dividing by the mean of LNAGM).

6.2.2 RESULTS

Figure 6.2.1 presents a CGMR of the example subject masked on MPRGE, MTR and T_2^*-w as it was presented to the observer performing lesions segmentation task.
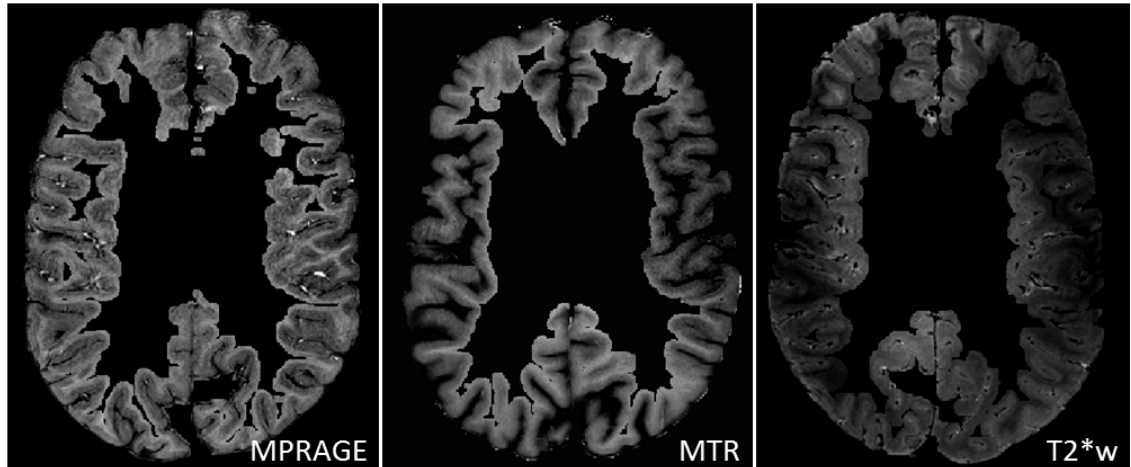
Figure 6.2.1: Example CGMR masked on MPRAGE, MTR and T_2^*-w images.

Figure 6.2.2 shows examples of both lesion types in MPRAGE and MTR.
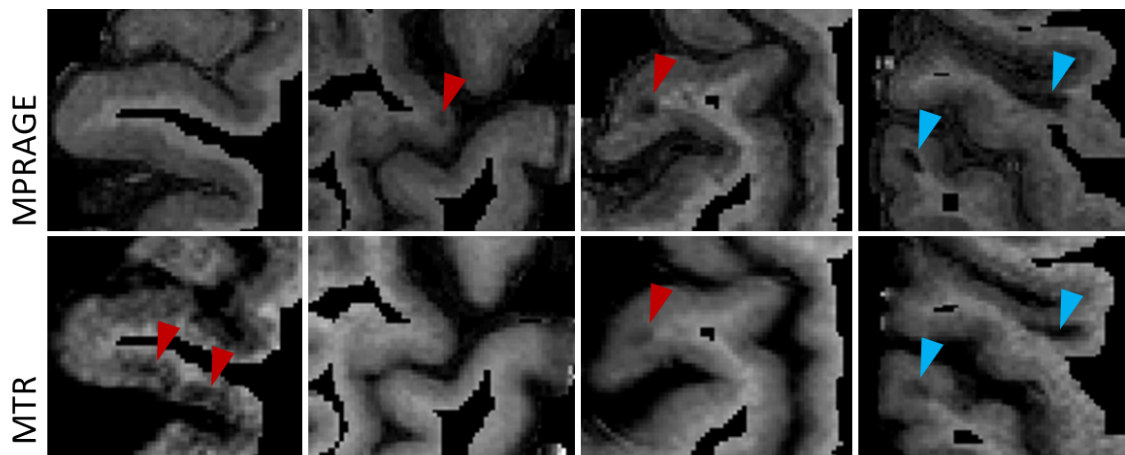
Figure 6.2.2: Example lesions in MPRAGE (top row) and MTR (bottom row). Cortical lesions detected only in MTR or only in MPRAGE and mixed lesions detected in both images.

Figure 6.2.3 and Table 6.2.2 summarize the number of detected lesions, and show that GM abnormalities were significantly more commonly found in MS patients than HC.

Figure 6.2.3: Total number of lesions (combined cortical and mixed) for each HC and MS subject in MTR versus MPRAGE.

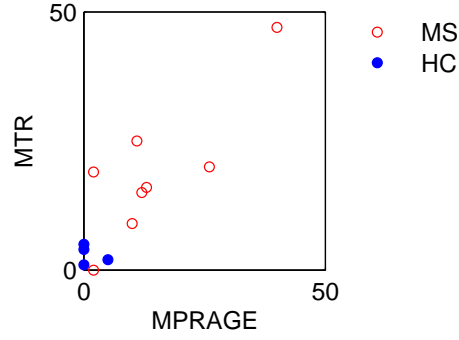|	MPRAGE		MTR		MPRAGE & MTR	
	cortical	mixed	cortical	mixed	cortical	mixed
MS (N=8)	79	37	129	22	16	18
HC (N=4)	5	0	12	0	0	0

Table 6.2.2: Summary of the lesion detection in 12 subjects: total number of cortical and mixed lesions identified in MTR and MPRAGE images, together with the number of the additional lesions found post-hoc by the second observer, and number of lesions found in both modalities.

MTR detected almost twice as many cortical lesions as MPRAGE on average, but was less efficient in case of mixed ones. Relatively few lesions were detected jointly on both sequences. MTR and MPRAGE contrast between lesion and LNAGM were plotted in Figure 6.2.4 for both cortical and mixed lesions.
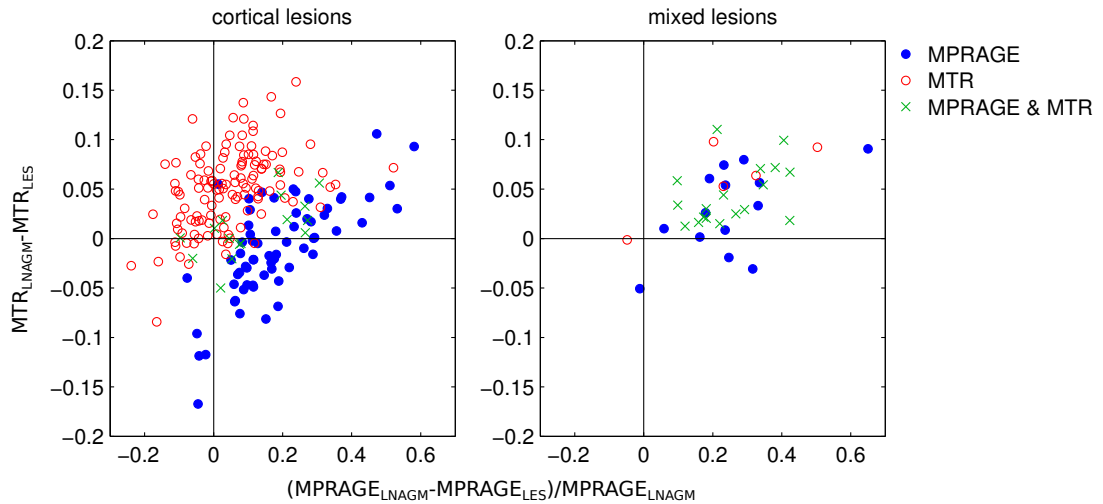

Figure 6.2.4: Scatter plots of contrast between lesions and LNAGM in MTR and MPRAGE for lesions detected in MPRAGE, MTR and MPRAGE & MTR. Left: cortical and right: mixed lesions.

In 4 randomly chosen cases (2 controls and 2 MS) T_2^*-w scans were examined and

showed only 8 lesions in total between them compared to 52 for MTR and 38 for MPRAGE.

6.2.3 DISCUSSION

Increased rate of detection of intracortical lesions was found for MTR compared to MPRAGE at 7T, but MPRAGE was more sensitive in detecting mixed leukocortical lesions. Only very few lesions were detected on HC, which agrees with previous reports [10, 61] and makes it unlikely that artefacts were misinterpreted as lesions. Both MPRAGE and MTR were better at detecting cortical lesions than T_2^*-w scans, previously shown to provide a good contrast for GM lesions in the post mortem [58] and in vivo [48] work. However, the scans used in this study were optimised to detect small lesions and therefore the T_2^*-w images were obtained with 3D sequence of slice thickness 0.5mm (compared to 1.0mm in [48]) increasing sensitivity to shimming variations and movement. The high spatial resolution made it possible to localize the position of the cortical lesions precisely, for instance as purely intracortical, which was not possible in previous studies using DIR results [27].

Since the cortical levels of myelin are low, demyelination is difficult to detect in the GM. High specificity of MTR to demyelination may explain why more lesions were detected with MTR than with MPRAGE, despite the fact that the MTR maps are noisier than the MPRAGE images and require intrinsic registration. Moreover, the pathological processes underlying occurrence of cortical lesions differ from those causing WM degeneration in MS and are not yet well understood [11, 40]. Demyelination in cortical lesions involves microglial cells and is not associated with inflammation [8, 56]. The longitudinal relaxation time (to which MPRAGE is sensitive) is related to different tissue characteristics compared to MTR, such as inflammation or iron content, which may explain its sensitivity to the mixed lesions. For a small subset of detected lesions, values of the peri-lesional contrast (Figure 6.2.4), calculated for the same modality in which these lesions were identified, were surprisingly low or negative. This was due to the compromises of the contrast

measure used. LNAGM surrounding the lesion was selected automatically by dilating the lesion mask, so that in some cases remainings of CSF tissue were also included in the calculations. This problem can be solved either by correcting CGMR segmentation to remove all CSF or by selecting a LNAGM based on the profile of tissue intensity around the lesion. After improvements this method could possibly assist a future automation of lesion segmentation using contrast difference to define lesion boundary, which could be used in longitudinal MS studies.

This preliminary study proved MTR was superior to MPRAGE for the cortical lesion detection at 7T and motivated continuation of the project, in which the author of this thesis is no longer involved, using bigger number of patients and including different protocols for the comparison. This study will compare the results regarding GM lesions with the clinical progress of the patients on the longitudinal manner and will relate these results to the changes in white matter, with the special interest in the regions laying close to the GM lesions. This project can therefore provide better understanding of the MS as a disease involving degeneration of WM but also, not yet fully understood, cortical GM pathology.

On the other hand, peri-lesional contrast calculations performed in this pilot study are potentially promising for further development of automatic or semi-automatic lesion detection or lesion characterisation.

6.3 Increase in the iron content of the SN and RN in MS and CIS: a 7T MRI study

Iron deposition in deep grey matter (dGM) structures in the MS has been monitored using T_2- and T_2^*-weighted MRI scans [4, 15, 23, 37, 55, 67, 68] or R_2 and R_2^* maps which provide more quantitative measures [43]. However these NMR relaxation based parameters are also sensitive to the other tissue properties like myelin content and water concentration [28] which can also change in MS. Recent studies used the phase data to obtain information more specifically related to iron content [32].

Susceptibility weighted images (SWI) combine phase and T_2^*-weighted signals with the aim of achieving higher sensitivity to iron density [29, 69].

However the phase maps are distorted compared to the underlying susceptibility distribution in the tissue. This is because there is a non-local relationship between the susceptibility distribution and the resulting magnetic field distortion, which leads to spatial distortions in both phase and SWI data. Therefore in this work we used quantitative susceptibility mapping [66] which converts phase data into magnetic susceptibility maps that are not spatially distorted. We also used T_2^*-weighted magnitude images since the effect of iron on T_2^* is mediated by magnetization dephasing which depends on the spatial distribution of iron as well as the absolute content; furthermore the use of T_2^*-weighted images allowed results to be compared with previous studies.

Neurodegeneration within the brainstem is common in MS and is associated with poor prognosis [18, 64], possibly due to the location of the crucial motor and sensory pathways in the brainstem. Iron accumulation is often associated with neurodegeneration and MRI changes suggestive of increased iron content have been consistently reported for most of the dGM structures in MS [1, 15, 69], but results for the substantia nigra (SN) and red nucleus (RN) remain inconsistent. While some studies reported a difference between MS and healthy subjects in both structures [43, 55, 68], others found increased iron only in the SN [16, 30] or only in the RN [5] and some studies reported no difference in either [23, 67].

Changes in the RN and SN may be particularly important in MS. The RN is involved in motor control; lesions of the RN including demyelinating plaques within it or affecting its connection to the cerebellum may cause a characteristic rubral tremor [41]. In addition, involvement of the SN in MS has been demonstrated through the detection of lesions on transcranial sonography [33] and decreased levels of proteins associated with myelin, neuronal development and axonal growth indicating demyelination of the SN [16] have been found in the SN of MS patients.

This study investigated changes in iron deposition in the SN and RN in two groups of

patients, with Relapsing-Remitting MS (RRMS) and Clinically Isolated Syndrome (CIS), a condition indicating the earliest clinical stage of demyelinating disease, hypothesising that iron deposition in the SN and RN might ultimately provide a marker of clinical progression in MS. Previous MRI studies of iron accumulation in dGM structures in CIS did not examine SN and RN [1, 15], although we have recently reported significant differences in iron content of the dGM structures, caudate nucleus, putamen, globus pallidus, thalamus and pulvinar, between CIS patients and healthy controls, using phase data from 7T MRI to produce quantitative susceptibility maps [1]. We acquired the data using a 7T MR scanner, as the field shifts due to magnetic susceptibility perturbations scale with the field strength providing both higher precision in susceptibility maps and increased sensitivity to iron content in T_2^*-w data [68].

The T_2^*-w MRI scans were also examined post-hoc in order to identify nigrosome 1, the largest of the subgroups of dopamine-containing neurons identified in calbindin-negative zones within the SNpc [19]. It has previously been shown using histology data that the nigrosomes suffer preferential dopaminergic cells loss in Parkinson's disease [20] and recent studies have shown that nigrosome 1 can be detected in vivo using 7T MRI [7] (also see Section 5.1), and that this structure cannot be seen in Parkinon's disease [7, 42]. Therefore the presence of nigrosome 1 was assessed in CIS and RRMS patients, since in the late stages of MS, the pathology is not particularly disease specific, but is similar to that found in other neurogenerative diseases (Alzheimer's or vascular changes) [26].

The aim of this work was to asses iron content in the SN and RN of patients with CIS and RRMS compared to healthy controls (HC), using susceptibility mapping and T_2^*-weighted signals measured at 7T. Ventral (SNv) and dorsal (SNd) parts of the SN were analysed separately based on the reported changes in iron distribution in other neurogenerative diseases [24]. Moreover, the effect of CIS on RRMS on the visibility of nigrosome 1 on MRI scans was also investigated.

6.3.1 Materials and methods

14 patients with relapsing-remitting multiple sclerosis (RRMS: age=42.4 ± 11.3, range 20-56 y.o.) and 21 with clinically isolated syndrome (CIS: age=37.2 ± 8.8, range 24-57 y.o.) together with 27 age-matched healthy controls (HC: age=36.4 ± 8.8, range 21-58 y.o.) were recruited from Nottingham University Hospital in accordance with local ethics committee approval. Expanded Disability Status Scale (EDSS) assessment giving values between 0 and 10 (death due to MS) was performed by a trained physician for all of the patients.

MR images were acquired on a 7T Philips Achieva scanner with 16-channel receive coil and head-only volume transmit coil. A T_2^*-weighted 3D GRE sequence was acquired with TR/TE=150/20ms, flip angle 14°, SENSE factor 2, EPI factor 3, number of acquisitions 1, scan time 8.5min. Four interleaved stacks parallel to the AC-PC line with coverage 192x164x25 mm were acquired for each scan, where the overlap between stacks was 5mm. Spatial resolution of the data was 0.5x0.5x0.5mm. Susceptibility maps were generated from the phase data using the k-space threshold method [66]. For each subject, the 5 slices of each T_2^*-w image where both structures were most visible were chosen and then circular ROIs of diameter 3mm were drawn using ITKSnap software (`http://www.itksnap.org`), separately on left and right RN, ventral and dorsal SN (Figure 6.3.1).
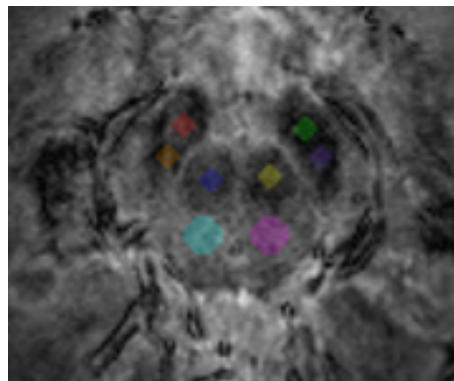

Figure 6.3.1: T_2^*-weighted image showing ROIs placed in the SNv (red and green), SNd (orange and purple) and RN (blue and yellow). The two ROIs in cyan and magenta are WM regions used for normalisation.

All of the SN ROIs were positioned to avoid touching ventral and medial boundaries

of the structure. Two further ROIs of diameter 5mm were placed on the white matter (WM) in the same slices and used to provide reference values for the susceptibility measurement.

Matlab [49] was used for further processing of the data. Mean values of $1/T_2^*$-w (used instead of R_2^* maps in absence of the multiecho data) and susceptibility were calculated for SNv, SNd and RN ROIs, averaging the values obtained from the left and right hand sides. The results were normalised using the mean intensity of the WM region, taking the difference between the ROI and WM region for susceptibility and ratio for the ROI to the WM region for $1/T_2^*$-w. Moreover the product of negative logarithm of the normalised T_2^*-w signal (which should be linear in $1/T_2^*$ and hence iron concentration) and normalised susceptibility signal (Susceptibility-T_2^* product) was determined for each structure, to increase sensitivity in a similar manner to the SWI signal but using susceptibility maps to overcome the problems of non-local phase effects in SWI data.

Presence of nigrosome 1 within the SN was assessed visually by a trained expert, separately on each side of the SN, using the criteria stated in the previous study [7]. Normality was checked using the Kolmogorov-Smirnov test. One-way ANOVA test with the Tukey-Kramer correction for multiple comparisons was performed to examine differences in susceptibility and $1/T_2^*$-w values between the CIS, RRMS patients and HC for each structure. Left and right parts of the structures were also compared using one-way ANOVA. Scatter plots of susceptibility and $1/T_2^*$-w signal were overlaid with ellipses indicating the HC, CIS and RRMS population distributions ($\pm$ 1.5 s.d.). Dependence of the $1/T_2^*$-w, susceptibility and product values on age was tested for healthy controls and dependence on the EDSS score for the CIS and RRMS patients.

6.3.2 Results

Mean EDSS results obtained for two groups of patients were 2.8±0.7 for RRMS and EDSS=1.6±1.0 for CIS. There was a trend for susceptibility in all of the structures

to increase between HC, CIS and RRMS patients (Figure 6.3.2) and the differences between HC and RRMS in SNd and RN were significant (p<0.05).
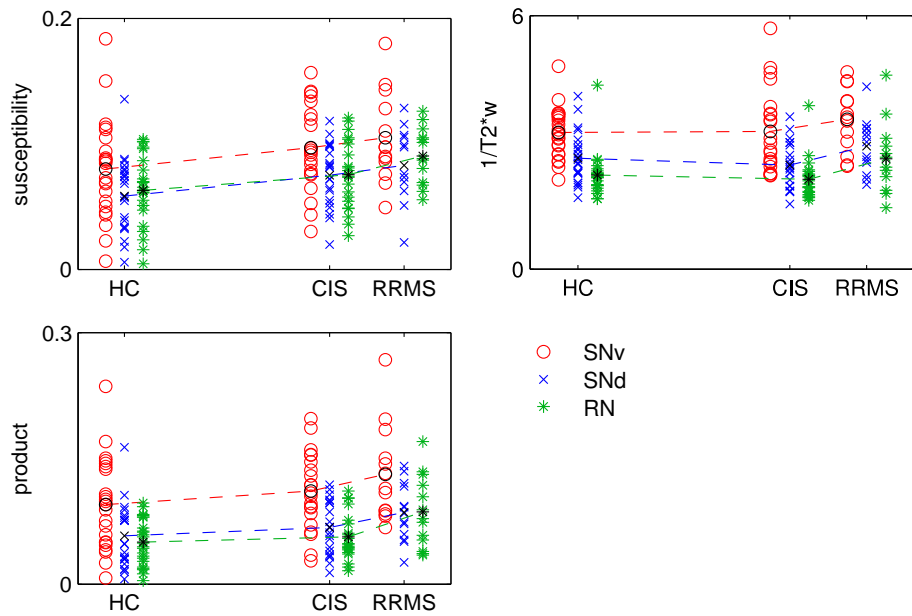
Figure 6.3.2: Mean susceptibility, $1/T_2^*$-w and product in SNv, SNd and RN for HC, CIS and RRMS patients.

No difference was seen in SNv although this may be because the data for this region was more scattered. The $1/T_2^*$-w signal in both parts of the SN and RN was unchanged for CIS patients compared to HC and higher for RRMS patients, although differences were not significant (Figure 6.3.2). The Susceptibility-T_2^** product increased separation of the RRMS versus HC (p<0.01) and RRMS versus CIS groups (p<0.05) in RN, however the difference between the groups for SNd was no longer significant.

Scatter plots in Figure 6.3.3 show that there is relatively weak correlation between susceptibility and $1/T_2^*$-w signal in all ROIs for all subject groups.
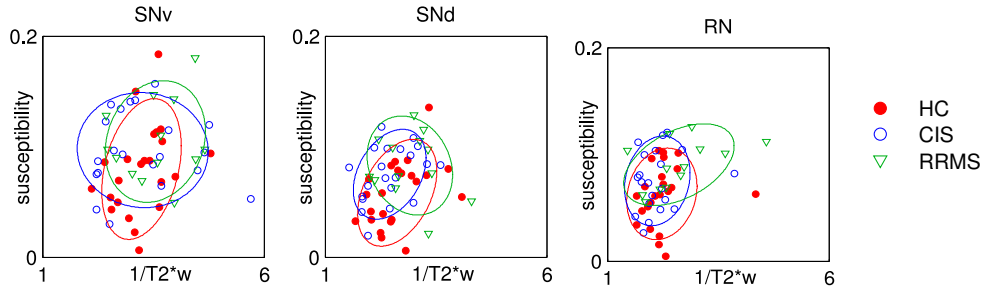
Figure 6.3.3: Scatter plots of susceptibility versus $1/T_2^*$-w in SNd, SNv and RN. Ellipse indicate populations of the HC, CIS and RRMS centred at the mean value, outlined by the 1.5 of the standard deviation and oriented parallel to the best fit slope.

Susceptibility, $1/T_2^*$-w and the product did not show a significant correlation either with the patients' EDSS score (Figure 6.3.4) or age for HC and no significant differences between the left- and right side- structures were found.

Figure 6.3.4: Values of susceptibility, $1/T_2^*$-w and product in SNv, SNd and RN plotted against their EDSS scores.

Examination of the subjects' scans in order to identify nigrosome 1 did not show significant difference between the groups as it is presented in Table 6.3.1.

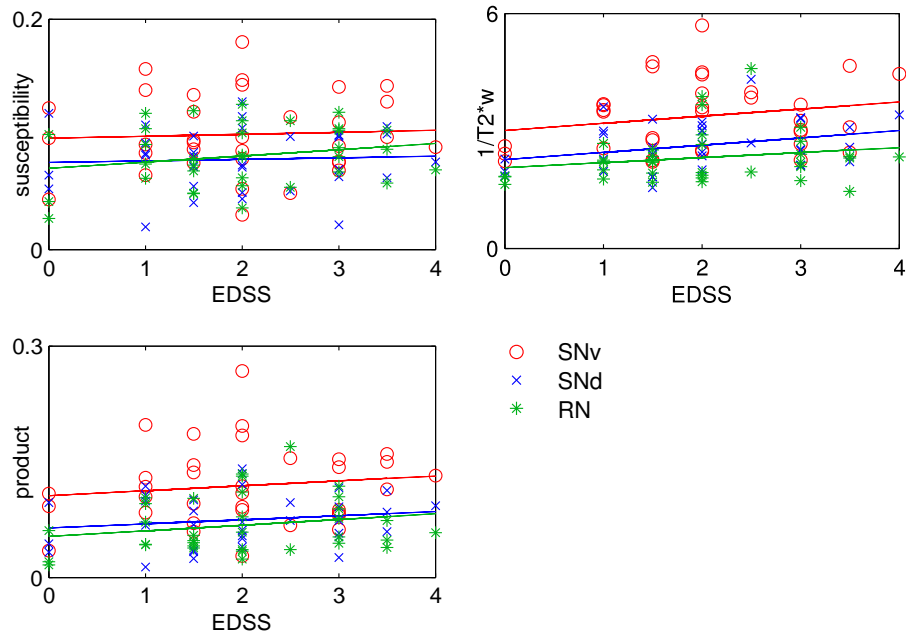| | subjects | | nigrosome 1 | | | |
	total	excl*	L+R	L/R	none	%
HC	27	3	21	2	1	87.50
CIS	21	3	16	0	2	88.89
RR	14	1	11	0	2	84.62
						87±2

Table 6.3.1: The summary of identification of nigrosome 1 in healthy (HC) subjects and patients (CIS, RR). *Datasets excluded from the analysis were either of not sufficient quality (4 cases) or not sufficient coverage to include lower part of the SN (3 cases).

Seven datasets were excluded, three due to insufficient coverage (did not include the lower part of the SN containing nigrosome 1) and four due to the quality not reaching the diagnostic level. Average percentage of subjects with nigrosome 1 present on both sides was equal 87±2%.

6.3.3 DISCUSSION

Changes consistent with increased iron content in the SNd and RN were found in RRMS patients compared to HCs using susceptibility mapping at 7T (Figure 6.3.2). There was a trend for the CIS patients to have higher values than HC in all three ROIs, although the differences were not significant. These results suggest a relationship between iron deposition and disease progression and agree with the previous work applying the same quantitative susceptibility mapping method to the other dGM structures for the same CIS patients [1]. $1/T_2^*$-w signal did not show significant changes between the patients and HC groups, but there was a trend for a small change between CIS and RRMS patients (Figure 6.3.2). The difference between the trends found for susceptibility and $1/T_2^*$-w values affected the third measure we used, the Susceptibility-T_2^* product. The values of this product increased the separation of the RRMS and HC groups in comparison to susceptibility, but did not show significant differences for the CIS versus HC (as may be expected from the results on $1/T_2^*$-w alone) (Figure 6.3.2). Nonetheless, the combined measure of iron concentration could have an advantage over susceptibility alone in monitoring the diagnosed MS patients.

The effects of iron accumulation on susceptibility maps and T_2^*-w images are

different. Susceptibility will depend on the total iron content within a voxel [28]. On the other hand T_2^*-w signal decay will depend on both the total iron content of the tissue and also its distribution (ie whether or not the iron is aggregated into 'clumps'. Therefore a trend for susceptibility to change in earlier demyelinating diseases (CIS) than T_2^*-w might suggest that iron accumulation is initially uniform but becomes more heterogeneous later. However susceptibility and T_2^*-w signal also depend on myelin content [28] and hence demyelination may also explain the observed differences in the changes in T_2^*-w and susceptibility between groups. Myelin is diamagnetic (negative susceptibility) whereas iron is paramagnetic (positive susceptibiltiy). Hence, both demyelination and increased iron content would be manifest as a net increase in susceptibility. In contrast, myelin generaly reduces T_2 so demyelination will cause a decrease in $1/T_2^*$-w where as increased iron will cause an increase in $1/T_2^*$-w. Further work, possibly including magnetization transfer (MT) measures are required to separate these effects but either way the early changes may make susceptibility mapping potentially useful in the future for monitoring progression of CIS. It has been recently reported that the nigrosome is visible on 7T MRI [7] of healthy controls but not of Parkinson's disease patients [7, 42]. Post hoc examination of the data acquired here found no change in frequency of nigrosome detection between RRMS and CIS patients and controls (average frequency of detection in data sets with sufficient coverage and image quality was 87±2%).

Previous results on the accumulation of iron in the SN and RN in MS were inconsistent. Most of the work was based on the T_2-w contrast [5, 15, 23, 37, 55, 67, 68] which is affected not only by the iron content, but also by the other tissue properties like water concentration or myelin content [28]. Alternatively the phase component of the signal was used separately [32] or combined with the magnitude in form of SWI [29, 69] to provide signals more specific to iron content, but as discussed above without performing susceptibility mapping (as carried out here) the phase signal is distorted in a way which is likely to increase scatter in the results.

Interestingly, in our study greater differences in susceptibility were found in SNd compared to SNv. Variation across the SN may partially explain the lack of consistency in previous results using images acquired at lower field strengths, as high resolution imaging at 7T allowed specific ROIs to be defined within the SN. It could also suggest a similar pattern of the iron accumulation in SN to that previously found in Parkinson's disease in histology [24] and T_2^*-w images [47], which is in agreement with the gradient of neurodegeneration found SN in PD patients using MRI [50].

In PD it has previously been shown in histology [19] and in vivo MRI [7, 42] that iron is preferentially deposited in nigrosome 1 and nigrosome 1 cannot be detected in vivo in patients. On the other hand, presence of nigrosome 1 at the same rate in both healthy subjects and patients does not support that hypothesis, as our previous study showed the absence of this structure in the Parkinson's patients [7].

The lack of variation in iron content over the age range used in our study (20-58y) agrees with previous histological measurements [31]. As in previous studies of dGM iron in MS patients, we also found no correlation between iron and EDSS, possibly due to a relatively low range of EDSS scores [67, 68].

The quantitative susceptibility mapping used in this work is a robust method providing a more direct measure of the spatial iron distribution by the actual susceptibility values overcoming the problem of non-local phase and susceptibility relationship [66]. Although the susceptibility maps are rather sensitive to noise, the increase of the signal-to-noise ratio in the images obtained from 7T magnetic field is sufficient to acquire good quality data.

Due to the orientation dependence of the susceptibility measurements the choice of WM as the reference regions may be a limitation of results of this study based on the susceptibility mapping. However, as CSF is affected by flow, WM is the most robust choice.

This is the first study using quantitative susceptibility mapping to analyse iron accumulation in SN and RN in CIS and RRMS patients. 'Future work will include

R_2^* and MT measurements to better understand the mechanisms underlying changes in iron and possibly myelin content found here. Longitudinal data will be analysed to investigate whether these measures can predict conversion from CIS to RRMS, which would be important for studying the disease progression.

6.4 Conclusions

This chapter presented three separate studies investigating different aspects of the neurodegeneration in MS, using 7T MRI.

Peri-lesional WM tissue in CIS patients was analysed in Section 6.1, in order to gain a better understanding of the pathological processes leading to, and underlying, the disease, by studying iron and myelin coupling in the proximity of the lesions. However, the results obtained failed to provide more insight into these effects. The attempt to classify lesions based on the MR characteristics of their surroundings was not successful, but lesion profile analysis allowed to estimate of the value of the distance from lesion boundary, where the NAWM can be considered unaffected (2mm for lesion segmented on MPRAGE). Comparison of the profiles obtained for different modalities confirmed a high variation of the MR lesion characteristics, but agreed with the previous results regarding dependence of the particular contrasts on myelin and iron. Application of the iron and myelin mapping method proposed in Section 5.2 could provide an additional input for the interpretation of these results.

The second study, presented in Section 6.2, compared MTR and MPRAGE images in terms of their usability for GM lesion detection in MS patients and found MTR to be a better sequence for segmentation of purely cortical lesions. Moreover, the method of calculating peri-lesional contrast used in this study could potentially be developed into an automatic or semi-automatic lesion segmentation tool.

Section 6.3 described analysis of the iron content and visibility of nigrosome 1 (see Section 5.1) in the SN and RN, in MS and CIS patients compared to HCs. Increased iron content was found in patients using susceptibility mapping in the RN and a dorsal part of the SN, with higher values recorded for RRMS than for CIS suggesting

iron accumulation with the disease progresion. There was no evidence of nigrosome 1 loss in MS patients in contrast to the results obtained in Parkinson's disease(see Section 5.1).

REFERENCES

[1] A. M. AL-RADAIDEH, S. J. WHARTON, S.-Y. LIM, C. R. TENCH, P. S. MORGAN, R. W. BOWTELL, C. S. CONSTANTINESCU, AND P. A. GOWLAND, *Increased iron accumulation occurs in the earliest stages of demyelinating disease: an ultra-high field susceptibility mapping study in Clinically Isolated Syndrome.*, Multiple Sclerosis, (2012), pp. 1–8.

[2] Y. ANIK, A. DEMIRCI, H. EFENDI, S. S. D. BULUT, I. CELEBI, AND S. KOMSUOGLU, *Evaluation of normal appearing white matter in multiple sclerosis: comparison of diffusion magnetic resonance, magnetization transfer imaging and multivoxel magnetic resonance spectroscopy findings with expanded disability status scale.*, Clinical neuroradiology, 21 (2011), pp. 207–15.

[3] F. BAGNATO, S. HAMETNER, B. YAO, P. VAN GELDEREN, H. MERKLE, F. K. CANTOR, H. LASSMANN, AND J. H. DUYN, *Tracking iron in multiple sclerosis: a combined imaging and histopathological study at 7 Tesla.*, Brain, 134 (2011), pp. 3602–15.

[4] R. BAKSHI, R. H. B. BENEDICT, R. A. BERMEL, S. D. CARUTHERS, S. R. PULI, C. W. TJOA, A. J. FABIANO, AND L. JACOBS, *T2 Hypointensity in the Deep Gray Matter of Patients With Multiple Sclerosis*, Archives of Neurology, 59 (2002), pp. 62–68.

[5] ——, *T2 Hypointensity in the Deep Gray Matter of Patients With Multiple Sclerosis*, Archives of Neurology, 59 (2002), pp. 62–68.

[6] F. BARKHOF, *MRI in multiple sclerosis: correlation with expanded disability status scale (EDSS)*, Multiple Sclerosis, 5 (1999), pp. 283–286.

[7] A. I. Blazejewska, S. T. Schwarz, A. Pitiot, M. C. Stephenson, J. Lowe, N. Bajaj, R. W. Bowtell, D. P. Auer, and G. P. A, *Visualization of nigrosome 1 and its loss in PD: Pathoanatomical correlation and in vivo 7T MRI.*, Neurology, 81 (2013), pp. 534–540.

[8] L. Bø, C. Vedeler, H. Nyland, B. Trapp, and S. Mø rk, *Intracortical multiple sclerosis lesions are not associated with increased lymphocyte infiltration*, Multiple Sclerosis, 9 (2003), pp. 323–331.

[9] B. Brownell and J. T. Hughes, *The distribution of plaques in the cerebrum in multiple sclerosis*, Journal of Neurology, Neurosurgery and Psychiatry, 265 (1962), pp. 315–320.

[10] M. Calabrese, N. De Stefano, M. Atzori, V. Bernardi, I. Mattisi, L. Barachino, A. Morra, L. Rinaldi, C. Romualdi, P. Perini, L. Battistin, and P. Gallo, *Detection of cortical inflammatory lesions by double inversion recovery magnetic resonance imaging in patients with multiple sclerosis.*, Archives of neurology, 64 (2007), pp. 1416–22.

[11] M. Calabrese, A. Favaretto, V. Martini, and P. Gallo, *Grey matter lesions in MS. From histology to clinical implications*, Prion, 7 (2013), pp. 20–27.

[12] M. Calabrese, V. Poretto, A. Favaretto, S. Alessio, V. Bernardi, C. Romualdi, F. Rinaldi, P. Perini, and P. Gallo, *Cortical lesion load associates with progression of disability in multiple sclerosis*, Brain, 135 (2012), pp. 2952–2961.

[13] M. Calabrese, C. Romualdi, V. Poretto, a. Favaretto, a. Morra, F. Rinaldi, P. Perini, and P. Gallo, *The changing clinical course of multiple sclerosis: A matter of grey matter.*, Annals of neurology, (in press).

[14] A. Ceccarelli, M. a. Rocca, A. Falini, P. Tortorella, E. Pagani, M. Rodegher, G. Comi, G. Scotti, and M. Filippi, *Normal-appearing*

white and grey matter damage in MS. A volumetric and diffusion tensor MRI study at 3.0 Tesla., Journal of neurology, 254 (2007), pp. 513–8.

[15] A. Ceccarelli, M. a. Rocca, M. Neema, V. Martinelli, A. Arora, S. Tauhid, A. Ghezzi, G. Comi, R. Bakshi, and M. Filippi, *Deep gray matter T2 hypointensity is present in patients with clinically isolated syndromes suggestive of multiple sclerosis.*, Multiple sclerosis, 16 (2010), pp. 39–44.

[16] S. Chen, F. F. Lu, P. Seeman, and F. Liu, *Quantitative proteomic analysis of human substantia nigra in Alzheimer's disease, Huntington's disease and Multiple sclerosis.*, Neurochemical research, 37 (2012), pp. 2805–13.

[17] W. Craelius, M. W. Midgral, C. P. Luessenhop, A. Sugar, and I. Mihalakis, *Iron deposits surrounding multiple sclerosis plaques*, Archives of Patholgy & Laboratory Medicine, 106 (1982), pp. 397–399.

[18] A. Damasceno, F. Von Glehn, C. O. Brandão, B. P. Damasceno, and F. Cendes, *Prognostic indicators for long-term disability in multiple sclerosis patients.*, Journal of the neurological sciences, 324 (2013), pp. 29–33.

[19] P. Damier, E. C. Hirsch, Y. Agid, and A. M. Graybiel, *The substantia nigra of the human brain I. Nigrosomes and the nigral matrix , a compartmental organization based on calbindin D 28K immunohistochemistry*, Brain, 122 (1999), pp. 1421–1436.

[20] ——, *The substantia nigra of the human brain II. Patterns of loss of dopamine-containing neurons in Parkinson's disease*, Brain, 122 (1999), pp. 1437–1448.

[21] W. L. de Graaf, I. D. Kilsdonk, A. Lopez-Soriano, J. J. M. Zwanenburg, F. Visser, C. H. Polman, J. a. Castelijns, J. J. G. Geurts, P. J. W. Pouwels, P. R. Luijten, F. Barkhof, and M. P. Wattjes, *Clinical application of multi-contrast 7-T MR imaging in multiple sclerosis: increased lesion detection compared to 3 T confined to grey matter.*, European radiology, 23 (2013), pp. 528–40.

[22] R. Dougherty and K.-H. Kunzelmann, *Computing Local Thickness of 3D Structures with ImageJ*, in Microscopy and Microanalysis, vol. 13, Aug. 2007, pp. 1678–1679.

[23] B. Drayer, P. Burger, B. Hurwitz, D. Dawson, and J. Cain, *Reduced signal intensity on MR images of thalamus and putamen in multiple sclerosis: increased iron content?*, American Journal of Roentgenology, 149 (1987), pp. 357–63.

[24] J. M. Fearnley and A. J. Lees, *Ageing and Parkinson's disease: substantia nigra regional selectivity*, Brain, 114 (1991), pp. 2283–2301.

[25] M. Filippi, M. A. Rocca, N. De Stefano, C. Enzinger, E. Fisher, M. A. Horsfield, M. Inglese, D. Pelletier, and G. Comi, *Magnetic Resonance Techniques in Multiple Sclerosis*, Archives of Neurology, 68 (2011), pp. 1514–1520.

[26] J. M. Frischer, S. Bramow, A. Dal-bianco, C. F. Lucchinetti, H. Rauschka, M. Schmidbauer, H. Laursen, P. S. Sorensen, and H. Lassmann, *The relation between inflamination and neurodegeneration in multiple sclerosis brains*, Brain, 132 (2009), pp. 1175–1189.

[27] J. J. G. Geurts, S. D. Roosendaal, M. Calabrese, O. Ciccarelli, F. Agosta, D. T. Chard, a. Gass, E. Huerga, B. Moraal, D. Pareto, M. a. Rocca, M. P. Wattjes, T. a. Yousry, B. M. J. Uitdehaag, and F. Barkhof, *Consensus recommendations for MS cortical lesion scoring using double inversion recovery MRI.*, Neurology, 76 (2011), pp. 418–24.

[28] E. M. Haacke, N. Y. C. Cheng, M. J. House, Q. Liu, J. Neelavalli, R. J. Ogg, A. Khan, M. Ayaz, W. Kirsch, and A. Obenaus, *Imaging iron stores in the brain using magnetic resonance imaging.*, Magnetic Resonance Imaging, 23 (2005), pp. 1–25.

[29] E. M. Haacke, J. Garbern, Y. Miao, C. Habib, and M. Liu, *Iron stores and cerebral veins in MS studied by susceptibility*, International Angiology, 29 (2010), pp. 149–157.

[30] E. M. Haacke, M. Makki, Y. Ge, M. Maheshwari, V. Sehgal, J. Hu, M. Selvan, Z. Wu, Z. Latif, Y. Xuan, O. Khan, J. Garbern, and R. I. Grossman, *Characterizing iron deposition in multiple sclerosis lesions using susceptibility weighted imaging.*, JMRI, 29 (2009), pp. 537–44.

[31] B. Hallgren and P. Sourander, *The Effect Oof Age on the Non-heamin Iron in the Human Brain*, Journal of Neurochemistry, 3 (1958), pp. 41–51.

[32] K. E. Hammond, M. Metcalf, L. Carvajal, D. T. Okuda, R. Srinivasan, D. Vigneron, S. J. Nelson, and D. Pelletier, *Quantitative in vivo magnetic resonance imaging of multiple sclerosis at 7 Tesla with sensitivity to iron.*, Annals of neurology, 64 (2008), pp. 707–13.

[33] S. Horowski, U. K. Zettl, R. Benecke, and U. Walter, *Sonographic basal ganglia alterations are related to non-motor symptoms in multiple sclerosis.*, Journal of neurology, 258 (2011), pp. 195–202.

[34] A. C. Hurley, A. Al-Radaideh, L. Bai, U. Aickelin, R. Coxon, P. Glover, and P. a. Gowland, *Tailored RF pulse for magnetization inversion at ultrahigh field.*, MRM, 63 (2010), pp. 51–8.

[35] M. Jenkinson and S. Smith, *A global optimisation method for robust affine registration of brain images*, Medical Image Analysis, 5 (2001), pp. 143–156.

[36] L. Kappos, D. Moeri, E. W. Radue, a. Schoetzau, K. Schweikert, F. Barkhof, D. Miller, C. R. Guttmann, H. L. Weiner, C. Gasperini, and M. Filippi, *Predictive value of gadolinium-enhanced magnetic resonance imaging for relapse rate and changes in disability or impairment in multiple sclerosis: a meta-analysis. Gadolinium MRI Meta-analysis Group.*, Lancet, 353 (1999), pp. 964–9.

[37] M. Khalil, C. Enzinger, C. Langkammer, M. Tscherner, M. Wallner-Blazek, M. Jehna, S. Ropele, S. Fuchs, and F. Fazekas, *Quantitative assessment of brain iron by R(2)* relaxometry in patients with clinically isolated syndrome and relapsing-remitting multiple sclerosis.*, Multiple Sclerosis, 15 (2009), pp. 1048–54.

[38] D. Kidd, F. Barkhof, R. McConnell, P. R. Algra, I. V. Allen, and T. Revesz, *Cortical lesions in multiple sclerosis.*, Brain, 122 (Pt 1) (1999), pp. 17–26.

[39] I. D. Kilsdonk, W. L. de Graaf, a. L. Soriano, J. J. Zwanenburg, F. Visser, J. P. a. Kuijer, J. J. G. Geurts, P. J. W. Pouwels, C. H. Polman, J. a. Castelijns, P. R. Luijten, F. Barkhof, and M. P. Wattjes, *Multicontrast MR Imaging at 7T in Multiple Sclerosis: Highest Lesion Detection in Cortical Gray Matter with 3D-FLAIR.*, AJNR, 34 (2013), pp. 791–6.

[40] R. Klaver, H. E. De Vries, G. J. Schenk, and J. J. G. Geurts, *Grey matter damage in multiple sclerosis: a pathology perspective.*, Prion, 7 (2013), pp. 66–75.

[41] M. Koch, J. Mostert, D. Heersema, and J. De Keyser, *Tremor in multiple sclerosis.*, Journal of neurology, 254 (2007), pp. 133–45.

[42] D.-H. Kwon, J.-M. Kim, S.-H. Oh, H.-J. Jeong, S.-Y. Park, E.-S. Oh, J.-G. Chi, Y.-B. Kim, B. S. Jeon, and Z.-H. Cho, *Seven-Tesla magnetic resonance images of the substantia nigra in Parkinson disease.*, Annals of Neurology, 71 (2012), pp. 267–77.

[43] R. M. Lebel, A. Eissa, P. Seres, G. Blevins, and A. H. Wilman, *Quantitative high-field imaging of sub-cortical gray matter in multiple sclerosis.*, Multiple Sclerosis, 18 (2012), pp. 433–41.

[44] J. Lee, K. Shmueli, B.-T. Kang, B. Yao, M. Fukanaga, P. van Gelderen, S. Palumbo, F. Bosetti, A. C. Silva, and J. H. Duyn, *The contribution of myelin to magnetic susceptibility-weighted contrasts in high-field MRI of the brain*, NeuroImage, 59 (2012), pp. 3967–3975.

[45] S. M. LeVine and W. B. Macklin, *Iron-enriched oligodendrocytes: a reexamination of their spatial distribution.*, Journal of Neuroscience, 26 (1990), pp. 508–12.

[46] C. Liu, W. Li, G. A. Johnson, and B. Wu, *High-field (9.4 T) MRI of brain dysmyelination by quantitative mapping of magnetic susceptibility*, NeuroImage, 56 (2011), pp. 930–938.

[47] A. K. Lotfipour, S. Wharton, S. T. Schwarz, V. Gontu, A. Schäfer, A. M. Peters, R. W. Bowtell, D. P. Auer, P. a. Gowland, and N. P. S. Bajaj, *High resolution magnetic susceptibility mapping of the substantia nigra in Parkinson's disease.*, JMRI, 35 (2012), pp. 48–55.

[48] C. Mainero, T. Benner, a. Radding, a. van der Kouwe, R. Jensen, B. R. Rosen, and R. P. Kinkel, *In vivo imaging of cortical pathology in multiple sclerosis using ultra-high field MRI.*, Neurology, 73 (2009), pp. 941–8.

[49] MATLAB, *version 7.10.0 (R2010a)*, The MathWorks Inc., Natick, Massachusetts, 2010.

[50] L. Minati, M. Grisoli, F. Carella, T. D. Simone, M. G. Bruzzone, and M. Savoiardo, *Imaging Degeneration of the Substantia Nigra in Parkinson Disease with Inversion-Recovery*, AJNR, 28 (2007), pp. 309–313.

[51] N. M. Moll, A. M. Rietsch, S. Thomas, A. J. Ransohoff, J.-C. Lee, R. Fox, A. Chang, R. M. Ransohoff, and E. Fisher, *Multiple Sclerosis Normal-Appearing White Matter: Pathology- Imaging Correlations*, Annals of Neurology, 70 (2011), pp. 764–773.

[52] O. Mougin, M. Clemence, A. Peters, A. Pitiot, and P. Gowland, *High-resolution imaging of magnetisation transfer and nuclear Overhauser effect in the human visual cortex at 7T.*, NMR in biomedicine, (2013).

[53] M. Neema, J. Stankiewicz, A. Arora, Z. D. Guss, and R. Bakshi, *MRI in multiple sclerosis: what's inside the toolbox?*, Neurotherapeutics, 4 (2007), pp. 602–17.

[54] D. Paling, D. Tozer, C. Wheeler-Kingshott, R. Kapoor, D. H. Miller, and X. Golay, *Reduced R2' in multiple sclerosis normal appearing white matter and lesions may reflect decreased myelin and iron content.*, Journal of neurology, neurosurgery, and psychiatry, 83 (2012), pp. 785–92.

[55] S. Pawate, L. Wang, Y. Song, and S. Sriram, *Analysis of T2 intensity by magnetic resonance imaging of deep gray matter nuclei in multiple sclerosis patients: effect of immunomodulatory therapies.*, J Neuroimaging, 22 (2011), pp. 137–44.

[56] J. W. Peterson, L. Bo, S. Mork, A. Chang, and B. D. Trapp, *Transected neurites, apoptotic neurons, and reduced inflammation in cortical multiple sclerosis lesions*, Annals of Neurology, 50 (2001), pp. 389–400.

[57] G. B. Pike, N. De Stefano, S. Narayanan, K. J. Worsley, D. Pelletier, G. S. Francis, J. P. Antel, and D. L. Arnold, *Multiple sclerosis: magnetization transfer MR imaging of white matter before lesion appearance on T2-weighted images.*, Radiology, 215 (2000), pp. 824–30.

[58] D. Pitt, A. Boster, W. Pei, E. Wohleb, A. Jasne, C. R. Zachariah, K. Rammohan, M. V. Knopp, and P. Schmalbrock, *Imaging cortical lesions in multiple sclerosis with ultra-high-field magnetic resonance imaging.*, Archives of neurology, 67 (2010), pp. 812–8.

[59] C. H. Polman, S. C. Reingold, B. Banwell, M. Clanet, J. a. Cohen, M. Filippi, K. Fujihara, E. Havrdova, M. Hutchinson, L. Kappos,

F. D. LUBLIN, X. MONTALBAN, P. O'CONNOR, M. SANDBERG-WOLLHEIM, A. J. THOMPSON, E. WAUBANT, B. WEINSHENKER, AND J. S. WOLINSKY, *Diagnostic criteria for multiple sclerosis: 2010 revisions to the McDonald criteria.*, Annals of Neurology, 69 (2011), pp. 292–302.

[60] L. Y. REITZ, M. INGLESE, J. FIEHLER, J. FINSTERBUSCH, B. HOLST, C. HEESEN, R. MARTIN, AND S. SCHIPPLING, *Quantitative T2' imaging in patients with clinically isolated syndrome.*, Acta neurologica Scandinavica, 126 (2012), pp. 357–63.

[61] V. SETHI, T. A. YOUSRY, N. MUHLERT, M. RON, X. GOLAY, C. WHEELER-KINGSHOTT, D. H. MILLER, AND D. T. CHARD, *Improved detection of cortical MS lesions with phase-sensitive inversion recovery MRI.*, Journal of neurology, neurosurgery, and psychiatry, 83 (2012), pp. 877–82.

[62] S. M. SMITH, *Fast robust automated brain extraction.*, Human brain mapping, 17 (2002), pp. 143–55.

[63] E. C. TALLANTYRE, P. S. MORGAN, J. E. DIXON, A. AL-RADAIDEH, M. J. BROOKES, P. G. MORRIS, AND N. EVANGELOU, *3 Tesla and 7 Tesla MRI of multiple sclerosis cortical lesions.*, JMRI, 32 (2010), pp. 971–7.

[64] M. TINTORE, A. ROVIRA, G. ARRAMBIDE, R. MITHANA, J. RIO, C. AUGER, C. NOS, E. MC, J. CASTILLO, A. HORGA, F. PEREZ-MIRALLES, E. HUREGA, M. COMBELLA, J. SASTRE-GARRIGA, AND X. MONTALBAN, *Brainstem lesions in clinically isolated syndromes.*, Neurology, 75 (2010), pp. 1933–8.

[65] H. VRENKEN, J. GEURTS, D. KNOL, C. POLMAN, J. CASTELIJNS, P. POUWELS, AND F. BARKHOF, *Normal-Appearing White Matter Changes Vary with Distance to Lesions in Multiple Sclerosis*, AJNR, (2006), pp. 2005–11.

[66] S. WHARTON, A. SCHÄFER, AND R. BOWTELL, *Susceptibility Mapping in the*

Human Brain Using Threshold-Based k-Space Division, Magnetic Resonance in Medicine, 63 (2010), pp. 1292–1304.

[67] Y. ZHANG, L. M. METZ, V. W. YONG, AND J. R. MITCHELL, *3T deep gray matter T2 hypointensity correlates with disability over time in stable relapsing-remitting multiple sclerosis: a 3-year pilot study.*, Journal of the neurological sciences, 297 (2010), pp. 76–81.

[68] Y. ZHANG, R. K. ZABAD, X. WEI, L. M. METZ, M. D. HILL, AND J. R. MITCHELL, *Deep grey matter "black T2" on 3 tesla magnetic resonance imaging correlates with disability in multiple sclerosis.*, Multiple Sclerosis, 13 (2007), pp. 880–3.

[69] R. ZIVADINOV, M. HEININEN-BROWN, C. V. SCHIRDA, G. U. POLONI, N. BERGSLAND, C. R. MAGNANO, J. DURFEE, C. KENNEDY, E. CARL, J. HAGEMEIER, R. H. B. BENEDICT, B. WEINSTOCK-GUTTMAN, AND M. G. DWYER, *Abnormal subcortical deep-gray matter susceptibility-weighted imaging filtered phase measurements in patients with multiple sclerosis: a case-control study.*, NeuroImage, 59 (2012), pp. 331–9.

7

CONCLUSIONS

The work presented in this thesis involved the application of MRI methods to investigation of the properties of brain tissue in healthy and diseased brain, focusing on iron and myelin. Chapter 3 presented simulations aimed at producing a better understanding of the effects of the microscopic characteristics of iron stores on the MR signal. Subsequently two experimental chapters described studies investigating two neurodegenerative diseases: Parkinson's disease (PD) in Chapter 5 and multiple sclerosis (MS) in Chapter 6.

Simulations presented in Chapter 3 provided insight into the dependence of T_2^*-w contrast on the shape and concentration of oriented inclusions of high susceptibility, which can potentially correspond to various forms of high-iron biological objects present in tissue (particles, proteins etc.).

Qualitative comparison of in vivo and post mortem (PM) MR data with histology in healthy controls (HCs) and PD patients presented in Chapter 5 led to the identification of nigrosome 1 in T_2^*-w images of HCs obtained at 7T. This low-iron sub-structure lying within the high-iron substantia nigra (SN) was also found to disappear in in vivo images of PD patients, potentially providing a classifying factor for distinguishing between patients and HCs. A small study on healthy subjects proved that nigrosome 1 can also be identified at 3T and therefore the presence of this structure could potentially be used in the diagnosis of PD in the clinical setting.

The second part of the chapter focused on healthy brain stem tissue, including nigrosome 1, and confirmed magnetization transfer ratio (MTR) as a marker of myelin content and susceptibility as well as R_2^* as markers of iron content. Susceptibility was slightly more sensitive to iron concentration than R_2^* and they both were also affected by myelin content, but in opposite senses. These findings were used to propose a quantitative method of iron and myelin mapping in in vivo data.

Chapter 6 described an analysis of neurodegeneration taking place in MS, in white matter (WM) and grey matter (GM). MR characteristics of the penumbra around the WM lesions were analysed in patients with clinically isolated syndrome (CIS), suggestive of MS. The analysed lesions could not be classified on the basis of their peri-lesional profiles, but the analysis which was performed provided insight into some lesion features. The dependence of the different types of contrast on myelin and iron content found in Chapter 5 was could be used to explain the results of this study of peri-lesional WM tissue. The extent of the penumbra which was visible in the images formed using the different modalities was found to be up to approximately 2mm large for the lesion boundary seen on MPRAGE data.

Analysis of GM lesions in MS patients presented in the second part of Chapter 6 led to the conclusion that MTR provides a better tool for identification of the cortical lesions than MPRAGE image contrast.

The last part of Chapter 6 described the finding of increased iron content in the dorsal part of the SN and in the red nucleus (RN) of CIS and MS patients compared to HCs, based upon susceptibility mapping. The increase was higher in MS than in CIS subjects suggesting that iron accumulates with disease progression. The differences found using $1/T_2^*$-w images were not significant, which is in agreement with the conclusion of Chapter 5 about the greater sensitivity of susceptibility than R_2^* to iron content. Different effects found in susceptibility and $1/T_2^*$-w contrast need further investigation. As both modalities are also affected by myelin content, additional use of an MR marker of myelin (such as MTR) may lead to better understanding of these dependencies. There was no evidence of nigrosome loss in MS and CIS patients in contrast to PD studies presented in Chapter 5.

FUTURE WORK

The simulations part of the thesis will be extended to include comparison of these results with experiments regarding microscopic tissue structure. Moreover, simulations incorporating the effect of diffusion will be performed.

In order to investigate the possible use of nigrosome 1 as a disease progression marker, future work should include longitudinal comparisons of PD patients, HCs and subjects at risk of developing PD. Quantitative approaches should be applied to measure the rate of nigrosome loss and correlate these results with the stage of disease development. Application of the in vivo method of iron and myelin mapping may provide additional information about the disease related changes occurring in tissue. In parallel, further studies using clinically available 3T data should be conducted on PD patients and HCs.

Future work regarding peri-lesional WM in CIS will include longitudinal studies comparing development of the same lesions with time. MS patients will be also studied along with CIS subjects to investigate WM pathology at different stages of the disease. Moreover, a method of iron and myelin mapping described in Chapter 5 will be applied to the peri-lesional tissue, to provide a better understanding of the

complex mixture of iron and myelin content changes around lesions.

The continuation of the study analysing GM lesions will include studying bigger group of patients, comparing appearance of the lesions in wider range of modalities and relating these results to the WM degeneration as well as to the clinical progress of the disease. The method of measuring peri-lesional contrast presented here needs some improvement, but could be potentially used in future studies to assist lesion segmentation by helping to find their boundaries in an automatic or semi-automatic way.

The study of the deep GM in MS will be extended to use the longitudinal data acquired for this project obtained with one and two years follow up to investigate changes of the iron content in dGM structures with the disease progression, especially in the patients who converted from CIS to RRMS. Moreover different quantitative measures such as MTR and R_2^* will be applied in the future for better understanding of iron and myelin content changes in the analysed structures.

In order to check if two ellipsoids overlap the following method was used [1]. Assuming that each ellipsoid is algebraically represented by the general equation of the second order algebraic surface given as:

$$Ax^2 + By^2 + Cz^2 + Dxy + Eyz + Fxz + Gz + Hy + Jz + K = 0,$$

where A, B, C, D, E, F, G, H, J, K are constants. This can be transformed to the matrix representation:

$$XSX^T = 0,$$

where

$$X = \begin{bmatrix} x & y & z & 1 \end{bmatrix}$$

and

$$S = \frac{1}{2} \begin{bmatrix} 2A & D & F & G \\ D & 2B & E & H \\ F & E & 2C & J \\ G & H & J & 2K \end{bmatrix}$$

For the ellipsoid we can calculate:

$$\frac{(x - x_c)^2}{a^2} + \frac{(y - y_c)^2}{b^2} + \frac{(z - z_c)^2}{c^2} - 1 =$$

$$= \frac{1}{a^2}x^2 + \frac{1}{b^2}y^2 + \frac{1}{c^2}z^2 - \frac{2x_c^2}{a^2}x - \frac{2y_c^2}{b^2}y - \frac{2z_c^2}{c^2}z + \frac{x_c^2}{a^2} + \frac{y_c^2}{b^2} + \frac{z_c^2}{c^2} - 1 =$$

$$= \begin{bmatrix} \dfrac{1}{a^2} & 0 & 0 & -\dfrac{x_c^2}{a^2} \\ 0 & \dfrac{1}{b^2} & 0 & -\dfrac{y_c^2}{b^2} \\ 0 & 0 & \dfrac{1}{c^2} & -\dfrac{z_c^2}{c^2} \\ -\dfrac{x_c^2}{a^2} & -\dfrac{y_c^2}{b^2} & -\dfrac{z_c^2}{c^2} & \dfrac{x_c^2}{a^2} + \dfrac{y_c^2}{b^2} + \dfrac{z_c^2}{c^2} - 1 \end{bmatrix} X^T = XSX^T$$

Algebraic condition for the separation of two ellipsoids can be formulated as following:

For given ellipsoids $\mathcal{A} : XAX^T = 0$ and $\mathcal{B} : XBX^T = 0$ their *characteristic equation* is defined as:

$$f(\lambda) = det(\lambda A + B) = 0$$

(1) $\mathcal{A}$ and $\mathcal{B}$ are *separated* iff $f(\lambda)=0$ has two distinct positive roots,

(2) $\mathcal{A}$ and $\mathcal{B}$ *externally touch* each other iff $f(\lambda)=0$ has positive double root.

In case of discrete coordinates *externally touching* means heaving common point (pixel), what may be considered as overlapping.

To calculate roots of the characteristic equation, assume that:

$$A = \begin{bmatrix} a_{11} & a_{12} & a_{13} & a_{14} \\ a_{21} & a_{22} & a_{23} & a_{24} \\ a_{31} & a_{32} & a_{33} & a_{34} \\ a_{41} & a_{42} & a_{43} & a_{44} \end{bmatrix}, B = \begin{bmatrix} b_{11} & b_{12} & b_{13} & b_{14} \\ b_{21} & b_{22} & b_{23} & b_{24} \\ b_{31} & b_{32} & b_{33} & b_{34} \\ b_{41} & b_{42} & b_{43} & b_{44} \end{bmatrix},$$

and x_i^c is i-th row of the matrix X, where c-th element was removed. Characteristic equation can be written as following:

$$f(\lambda) = det(\lambda A + B) =$$

$$= \sum_{c=1}^{4} sgn(-1)^c \left(\lambda^4 a_{4c} \begin{vmatrix} a_1^c \\ a_2^c \\ a_3^c \end{vmatrix} + \lambda^3 \left(b_{4c} \begin{vmatrix} a_1^c \\ a_2^c \\ a_3^c \end{vmatrix} + a_{4c} \begin{vmatrix} a_1^c \\ a_2^c \\ b_3^c \end{vmatrix} + a_{4c} \begin{vmatrix} a_1^c \\ b_2^c \\ a_3^c \end{vmatrix} + a_{4c} \begin{vmatrix} b_1^c \\ a_2^c \\ a_3^c \end{vmatrix} \right) + \right.$$

$$+ \lambda^2 \left(b_{4c} \begin{vmatrix} a_1^c \\ a_2^c \\ b_3^c \end{vmatrix} + b_{4c} \begin{vmatrix} a_1^c \\ b_2^c \\ a_3^c \end{vmatrix} + b_{4c} \begin{vmatrix} b_1^c \\ a_2^c \\ a_3^c \end{vmatrix} + a_{4c} \begin{vmatrix} a_1^c \\ b_2^c \\ b_3^c \end{vmatrix} + a_{4c} \begin{vmatrix} b_1^c \\ a_2^c \\ b_3^c \end{vmatrix} + a_{4c} \begin{vmatrix} b_1^c \\ b_2^c \\ a_3^c \end{vmatrix} \right) +$$

$$\left. + \lambda \left(b_{4c} \begin{vmatrix} a_1^c \\ b_2^c \\ b_3^c \end{vmatrix} + b_{4c} \begin{vmatrix} b_1^c \\ a_2^c \\ b_3^c \end{vmatrix} + b_{4c} \begin{vmatrix} b_1^c \\ b_2^c \\ a_3^c \end{vmatrix} + a_{4c} \begin{vmatrix} b_1^c \\ b_2^c \\ b_3^c \end{vmatrix} \right) + b_{4c} \begin{vmatrix} b_1^c \\ b_2^c \\ b_3^c \end{vmatrix} \right)$$

REFERENCES

[1] W. WANG, J. WANG, AND M.-S. KIM, *An algebraic condition for the separation of two ellipsoids*, Computer Aided Geometric Design, 18 (2001), pp. 531–539.

The following figures present additional, negative results of the study described in Section 6.1. Figures A.1, A.2 and A.3 show correlation scatters of the fitting coefficients obtained for lesions with neighbourhoods' overlap removed.
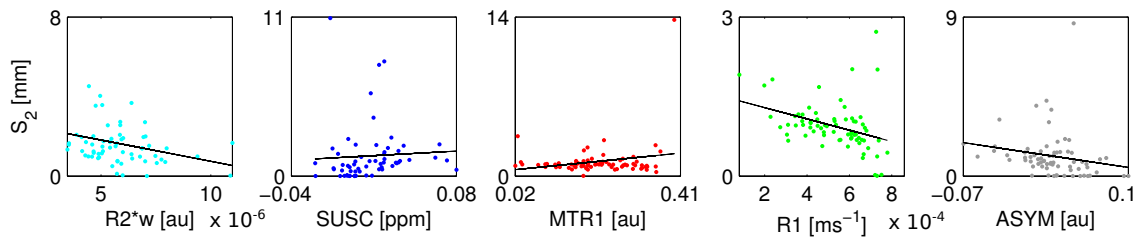

Figure A.1: Characteristic distance (S_2) of the function fitted to the first part of the lesion profiles 0-5mm plotted against the lesions mean intensity in all the modalities: R_2^*-w, SUSC, MTR_1, R_1, ASYM; the number of the data points for which S_2=15mm removed from the plots is N=11,14,2,3,4, respectively; the fitted straight lines are plotted in black.

Figure A.2: Plots of the characteristic distance (S_2) of the function fitted to the first part of the lesion profiles 0-5mm against the lesion size; two data points representing very big lesions have been removed to provide better clarity of the plots; R_2^*-w, SUSC, MTR_1, R_1, ASYM; the number of the data points for which $S_2 = 15$mm removed from the plots is N=11,14,2,3,4, respectively; the fitted straight lines are plotted in black.
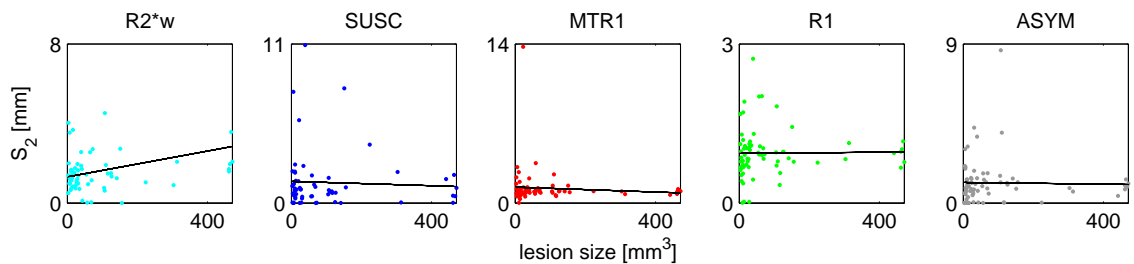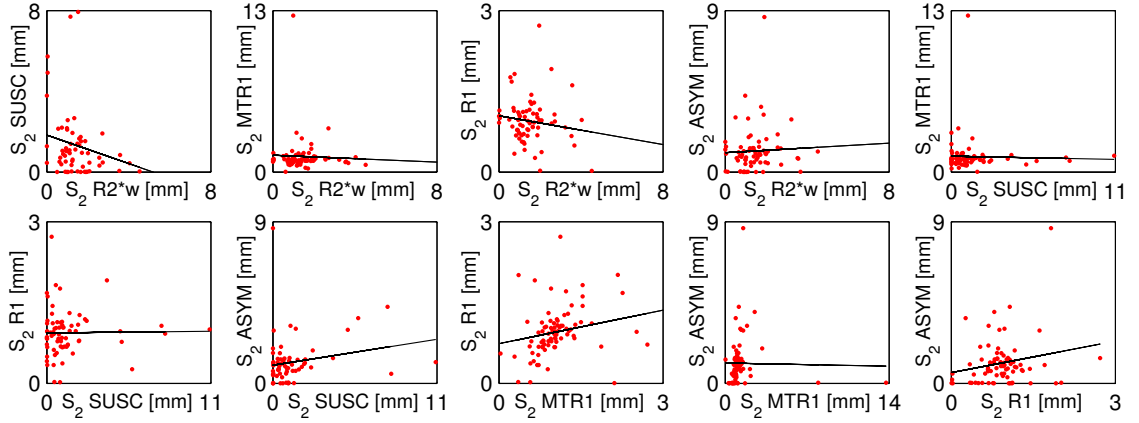
Figure A.3: The characteristic distance (S_2) of the function fitted to the first part of the lesion profiles 0-5mm plotted for all the combinations of the pairs of the images with the fitted straight lines plotted in black; the number of the data points for which $S_2 = 15$mm removed from the plots is N=11,14,2,3,4, for R_2^*, SUSC, MTR_1, R_1 and ASYM, respectively;

Table A.1 presents the example set of the co-occurrence matrices resulting from the C=2 clusters classification of the whole 15mm profiles. No clear overlap between the classes in the pairs of modalities was found.

		ASYM		R_1		MTR_1		SUSC	
		1	2	1	2	1	2	1	2
R_2^*	1	3	21	8	16	16	8	9	15
	2	8	59	16	51	33	34	25	42
SUSC	1	5	29	10	24	14	20		
	2	6	51	14	43	35	22		
MTR_1	1	5	44	11	38				
	2	6	36	13	29				
R_1	1	4	20						
	2	7	60						

Table A.1: Co-occurrence matrix for C=2 obtained from the clustering of the whole profiles (within 15mm).

Figure A.4 shows plots of the lesion profiles, averaged across two classes determined by the clustering based on the 15mm correlation, where large error bars corresponding to the standard deviation of the profile values indicate high intraclass variance.
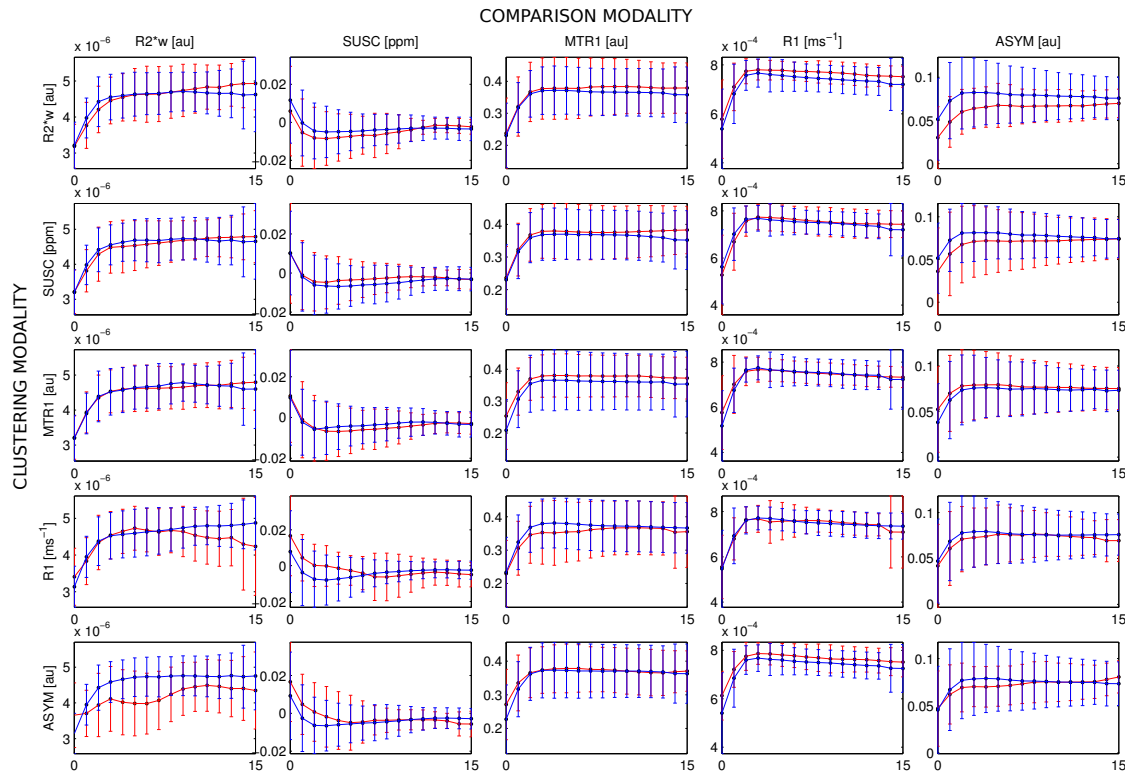
Figure A.4: Average lesion profiles calculated for two classes determined by 15mm correlation, plotted together for the comparison in red and blue. Rows' labels correspond to the source images used for the classification (clustering modality), and columns represent images from which the average profiles were calculated (comparison modality). In each plot, the x-axis shows distance in mm.